FRACTURE TOUGHNESS BASED MODELS FOR THE PREDICTION OF POWER CONSUMPTION, PRODUCT SIZE, AND CAPACITY OF JAW CRUSHERS

JAMES G. DONOVAN

Dissertation submitted to the Faculty of the Virginia Polytechnic Institute and State University in partial fulfillment of the requirements for the degree of

DOCTOR OF PHILOSOPHY

IN

MINING AND MINERALS ENGINEERING

DR. MARIO G. KARFAKIS
DR. GREG ADEL
DR. NORM DOWLING
DR. TOM NOVAK
MR. HUGH RIMMER
DR. ERIK WESTMAN

JULY 2003
BLACKSBURG, VA

KEYWORDS: Size reduction, Fracture toughness, Jaw crusher, Comminution modeling

FRACTURE TOUGHNESS BASED MODELS FOR THE PREDICTION OF POWER CONSUMPTION, PRODUCT SIZE, AND CAPACITY OF JAW CRUSHERS

James G. Donovan

(ABSTRACT)

There is little process control employed at aggregate crushing plants and essentially no optimization at the primary or jaw crushing stage. Jaw crusher selection is very dependent on the subjective judgment/experience of individuals, the characterization of rock material using inadequate and unrepresentative tests, and the desire to limit secondary breakage, resulting in the conservative selection and operation of jaw crushers. A method for predicting the power consumption, product size, and volumetric capacity of jaw crushers based on fracture toughness has been proposed in this study. A new fracture toughness test, the Edge Notched Disk Wedge Splitting test, has been developed and verified in order to rapidly assess the fracture toughness of six quarry rocks. A High Energy Crushing Test system has been used to simulate the operational settings of a jaw crusher so that comparison of fracture toughness, specific comminution energy, and breakage distribution could be performed. The results indicate that the specific comminution energy required to reduce a rock particle to a given size increases with fracture toughness. The breakage distribution has also been shown to be dependent upon fracture toughness as long as the elastic modulus is taken into account. Laboratory jaw crushing experiments show that the capacity of a jaw crusher is dependent upon fracture toughness and the elastic modulus. Models for the prediction of power consumption, breakage function/product size, and volumetric capacity have been developed based on these results. At the experimental level, the models were able to predict the specific comminution energy to within 1% and t_{10} (characteristic crushing parameter) to within 10%. Prediction of the product size distribution produced by a lab-scale jaw crusher, for four different rocks, was within ± 5% (in terms of percent passing). The models allow for the selection of a jaw crusher based on the nature of the rock being broken and the average amount of size reduction done on the feed material. The models can also be used to optimize feed and operational settings, as well to determine the product size produced for a given rock and reduction ratio.

ACKNOWLEDGEMENTS

I want to thank the Department of Mining and Minerals Engineering for allowing me to continue my graduate studies and conduct this unsupported research. I am grateful for the financial support, as well as the opportunity to be a part of such a fine department.

I want to recognize the support provided by *Luck Stone Corporation*, who donated all seven rock samples in the form of drill core and bulk samples taken from their production sites. I'd also like to thank Bob Stansell for answering all my crushing questions in regards to *Luck Stone's* operations and in general. And I want to thank Bruce Faison for accompanying me on my site visits and helping me acquire rock samples.

I want to acknowledge the contributions and involvement of my advisor, Dr. Mario Karfakis. He provided the motivation for this project but gave me complete liberty in developing, and executing, my research approach. He provided constant support along the way and was always available as a sounding board for ideas and suggestions. I feel fortunate to have been his student for the past six years.

I want to also thank the rest of my committee members, Dr. Adel, Dr. Dowling, Dr. Novak, and Dr. Westman, for their guidance and support. This work would not be the same if not for their participation and input. I was lucky to have such an informed and knowledgeable group of people at my disposal. I want to also thank Hugh Rimmer for stepping in as a last minute addition to my committee, as well as for making possible the use of the High Energy Crushing Test system in this study. I am pleased to have demonstrated how beneficial his donation of the HECT system can be.

Finally, I'd like to personally recognize the two people that make all things possible, and all things bearable, for me: my wife, Erin, and my son, Quinn. To Quinn, you make me realize everyday just how unimportant the material on the following pages is. To Erin, I couldn't be given enough pages, enough words, or enough time to properly express what you mean to me, and what you've done for me the past four years. In the same time it took me to write this dissertation you have defined me in the two most important ways, as a husband and a father, and that will always be the first thing I recall when thinking about this time in our lives.

TABLE OF CONTENTS

LIST OF FIGURES

LIST OF TABLES

CHAPTER 1. INTRODUCTION

The size reduction of brittle materials is the most essential mechanical operation within the raw material processing, i.e. mining, industry. It is also an inefficient, energy intensive process that consumes billions of kilowatt-hours of electricity per year (approximately 3-5% of all electricity consumed on the national level (Hofler, 1990; Duthoit, 2000)). In fact only 1% of the total energy input into size reduction processes is used in fragmentation and the creation of smaller particles, with most of the energy manifesting in the form of heat and noise. How has a process so fundamental, and costly, to the mining industry remained so inefficient? In a large part because the scientific research required to lay down the theoretical foundations of particle size reduction has lagged behind the actual achievements of technology, resulting in the design and operation of crushing equipment based on standards that fail to adequately describe the entire particle breakage process (Beke, 1964). Since the technology is already in place, improvements in comminution are dependent upon optimizing the application and operation of that technology. In fact, the United States National Materials Advisory Board estimated that improving the energy efficiency of comminution processes, using practical approaches, could result in energy savings of over 20 billion kilowatt-hours per year (Napier-Munn et al., 1999).

The failure to optimize the selection and operation of large, costly crushing equipment affects the entire mining industry. However, the aggregate industry is particularly burdened by the utilization of inefficient crushers due to the absolute dependence on the crushing plant to provide a finished product that provides all the revenue for the mining operation (Svensson and Steer, 1990). Aggregate producers are reliant on crushers to produce low value materials at high-throughputs that also must meet stringent quality standards (i.e., particle size and shape for *Superpave* mix design). Furthermore, the design of aggregate crushing processing plants requires rugged, massive, and expensive equipment, and misjudgments in design are difficult, if not impossible, and expensive to correct (Duthoit, 2000). In today's crushing environment the need for optimization of primary crusher selection and operation to meet the economics of quarrying requirements has become imperative (DeDiemar, 1990). The benefits of optimization include reduced capital costs, reduced unit operating costs, increased throughput, and improved performance of downstream processes as a result of improved feed size specification (Napier-Munn et al., 1999).

Much work has been done in the area of size reduction with regards to developing a theory, or criterion, that can be used to select and evaluate crushing equipment. Various theories have been proposed, none of which is completely satisfactory. Von Rittinger, Kick, and Bond proposed theories that constitute the three "laws" of comminution, all of which primarily demonstrate a relationship between the size reduction ratio of a material and the necessary energy input. The inherent problem with each of these "laws" is that they are empirically based laws that only fit experimental data over a limited range of

variables and only in certain cases (Choi, 1982). Furthermore, the relevance of these laws to primary crushing equipment processing large particle feed sizes is questionable. Eloranta (1997) calculated the expected power consumption of a crusher using Bond's "theory" and found that the actual power consumption was 240% higher than the expected consumption. In fact, crusher manufacturers and design engineers rely on a host of other methods to size and select crushing equipment for aggregate operations. Unfortunately these methods often lend themselves to the subjective judgment of an individual, resulting in the conservative over-design of crushing plant equipment (Bearman et al., 1990).

The importance of Von Rittinger, Kick, and Bond's work is that it indicates some relationship between the energy required to decrease the size of a particle and the resultant size of the broken particle. Bond's work in particular highlights the importance of selecting and evaluating crushing equipment, and determining power requirements, based on product size and some measure of a materials resistance to fracture. Over the last three decades more research has focused on the physics of particle fracture during the crushing process and the material characteristics related to fragmentation. Advancements in comminution theory have been made during this time by conducting single particle breakage tests, the goal of which is to relate the pattern of breakage, and the resultant fragment size distribution, with the nature of the material broken (Arbiter et al., 1969). Single particle breakage studies are now used to develop mathematical models, or functions, that describe the size reduction process of different materials. The trend in single particle breakage analysis now is to further relate the fracture energy and product size distribution to some physical property of the material. The ultimate purpose is to be able to assess the fracture properties of a material, and the requirements of any device used to break that material, using a single, easily determined physical property.

There is evidence that a link may exist between characteristic rock properties and the energy consumption, and performance, of primary crushing equipment. Berry at al. (1984) has related a number of common rock strength parameters to the performance of a laboratory scale crusher. Bearman et al. (1991) performed tests that lead to the development of empirical relationships between a number of rock strength parameters and the power consumption, and product size, of a cone crusher. It has been suggested that a material's fracture properties should be characterized in terms of particle strength, specific breakage energy, and the breakage fragment size distribution of the material (Bourgeois et al., 1992). In this case the strength is measured in terms of the tensile strength because particles of brittle materials break in tension under compressive loads due to the pre-existence of natural flaws within the material. However, the tensile strength does not fully describe the fracture process, it is only a measure of a particle's resistance to an applied load. It does not account for the inherent flaws present in brittle materials, or the magnitude of the stresses around these flaws when the material is loaded, and their effect on the fracture process. Thus, the particle strength should be replaced by another, more descriptive measure of a material's ability to withstand fracture.

Fracture toughness is an intrinsic material property expressing a material's resistance to crack propagation, and it is a measure of the energy required to create a new surface in a material. More specifically, fracture toughness is a critical value of the stress intensity factor, a quantity that characterizes the severity of the crack situation within a material as affected by crack size, stresses near the crack tip, and the geometry of the crack, material specimen, and loading configuration (Dowling, 1999). Given its sound theoretical foundation, evolving from the study of fracture mechanics and Griffith's theory of fracture, fracture toughness may offer a fundamental basis for describing size reduction processes. It is already used as an index for rock fragmentation processes such as tunnel boring and scale model blasting, as a key element in modeling rock cutting and blasting, and in the stability analysis of rock structures (Whittaker et al., 1992). Furthermore, Bearman (et al, 1989) has shown that a strong correlation exists between the fracture toughness of a material and the power consumption of a laboratory crusher used to crush the material, indicating that fracture toughness may have practical application in the evaluation of crushing equipment.

The major drawback in using fracture toughness as a parameter for crushing equipment evaluation is that the tests required to measure the property are difficult and expensive to perform, particularly in the case of brittle materials such as rock. The complexity of existing tests is an immediate problem when considering the application of fracture toughness to gauge size reduction processes (Bearman, 1998). This includes the standard testing techniques established by the International Society of Rock Mechanics (ISRM), tests that, although employing core-based specimens, require a chevron-notch to be machined into each specimen, a tedious and difficult process, especially for a large number of specimens. Thus, another method for fracture toughness testing of rocks is necessary, one that will give a representative toughness value and yet be simple, requiring neither pre-cracking, nor crack-length, displacement measurements, or sophisticated evaluation techniques (Ouchterlony, 1989).

Based on the premise that fracture toughness fully characterizes a rock's resistance to fracture, it is proposed to examine the potential of fracture toughness to function as a predictive means for rock crushability, and to develop fracture toughness based models for the selection and optimization of primary jaw crushers. The models will be developed by investigating the relationships among fracture toughness, breakage energy, and fragment size distributions of various aggregates. Fracture toughness will be measured using a newly developed fracture toughness test, and the energy and particle size distributions will be measured using a unique single particle breakage system. The ability of the laboratory derived models to predict the power draw and product size of jaw crushers will be examined using a lab-scale jaw crusher, and if possible, with the working conditions of large-scale primary crushers operated by *Luck Stone Corporation*.

1.1 PROJECT OBJECTIVES

Black and Hoek (1967) outlined the general methods of applied science used when approaching problems involving rock mechanics. Following their outline the objectives of this project are:

1. *Observe the natural phenomena in question as they occur and if possible quantify the observations*: Primary crushing equipment used in the aggregate industry is inefficient and over-designed. The proper selection and optimization of primary crushing equipment should be based on the energy required for rock breakage, the desired product size, and the desired production capacity, all of which are dependent upon a proper physical characterization of the rock being crushed.

2. *Propose a model or theory to explain the phenomena observed*: The fragmentation of rock in any size reduction process relies on the propagation of internal flaws within the rock. The resistance of a rock to crack propagation can be quantified using fracture toughness; it is a measure of the energy required to cause extension of flaws present within the rock. The power consumption, product size distribution, and capacity of a jaw crusher are dependent on the distribution of flaws within the rock being broken. It follows that fracture toughness can be used to optimize the selection and performance of a jaw crusher.

3. *Test and develop the model through laboratory experimentation*: The fracture toughness of various rock types will be determined using a newly developed procedure that utilizes a core-based specimen and allows for the rapid estimation of fracture toughness. The High Energy Crush Test (HECT) system will be used to determine the specific comminution energy and breakage function of the same rock types. Regression analysis of the data will be used to develop models for the prediction of power consumption and breakage function based on fracture toughness. Laboratory scale jaw crusher experiments will be used to redefine the current model for volumetric capacity taking into account fracture toughness.

4. *Use the model to predict behavior in similar circumstances*: Dolomitic limestone will be tested in the HECT system in order to test the applicability of the specific comminution energy and breakage function models. A laboratory scale jaw crusher will be used to test the ability of the breakage function model to predict the product size for a given set of operational settings.

5. *Insure by measured experiment or observation that the predictions made are valid, or that deviations from the behavior can be accounted for*: In addition to the laboratory scale crusher, jaw crushers currently in use at *Luck Stone Corporation's* quarrying operations will be evaluated. The effects of specimen size, crusher throughput, feed conditions, and effects of blasting will be considered

CHAPTER 2. LITERATURE REVIEW

2.1 PRIMARY CRUSHING

The first stage of rock breakage in any mining application is blasting. The purpose of blasting is to produce rock fragments small enough to be accepted by the processing plant. Blasted rock is "delivered" to the processing plant and subjected to the first stage of mechanical breakage, primary crushing. Primary crushers are large, rugged machines capable of handling large quantities of material and are used to reduce the size of blasted rock to sizes suitable for feeding secondary crushers. They typically handle feed sizes up to 1.5 meters with reduction ratios (ratio of particle feed size to product size) ranging from 3 to 10 (King, 2001).

Crushing in general is an energy intensive process. Primary crushing in particular consumes large amounts of energy due to the significant amount of size reduction taking place. In addition to the amount of size reduction, the energy required for breakage in crushing applications is dependent upon the physical properties of the material and the quantity of material being crushed. The rate of energy input is dependent upon the type of crushing machine used since the application of the crushing force changes with machine type.

Primary crushers apply breakage forces by means of compression or impact. Jaw and gyratory crushers are the most common types of primary compression crushers. Each applies a compressive force to rock particles as they come in contact with the crushing surfaces. The force is applied slowly (in comparison to impact machines) resulting in abrasion and cleavage fracture. Impact crushers apply a high-speed impact force to rock particles using hammers or blow bars. The rate of energy input is much higher causing particles to shatter. Impact crushers can achieve higher reduction ratios than jaws and gyratory's but are limited by high rates of abrasive wear and thus are restricted to somewhat softer rocks (Duthoit, 2000). In the aggregate industry, for tonnage outputs less than 1000 metric tons per hour, jaw crushers are the dominant type of primary crusher.

2.1.1 JAW CRUSHERS

Jaw crushers have been around for almost 175 years. All jaw crushers are distinguished by the presence of two plates, one of which is fixed and one that swings open and then closes, concurrently trapping and crushing material between the two surfaces. There are three types of jaw crushers: Blake, Dodge, and Universal. They are classified according to the location of the pivot point of the swinging jaw. The most common type of jaw crusher today is the Blake crusher, patented by Eli Whitney Blake in 1858 (Weiss, 1985). The Blake crusher pivots at the top and comes in two forms: the double toggle and the single toggle. The single toggle is taking over most new applications due to lower cost

and higher capacity (Stansell, 2003). Figure 2.1 is a cross-section through a *Nordberg* C Series single toggle jaw crusher.

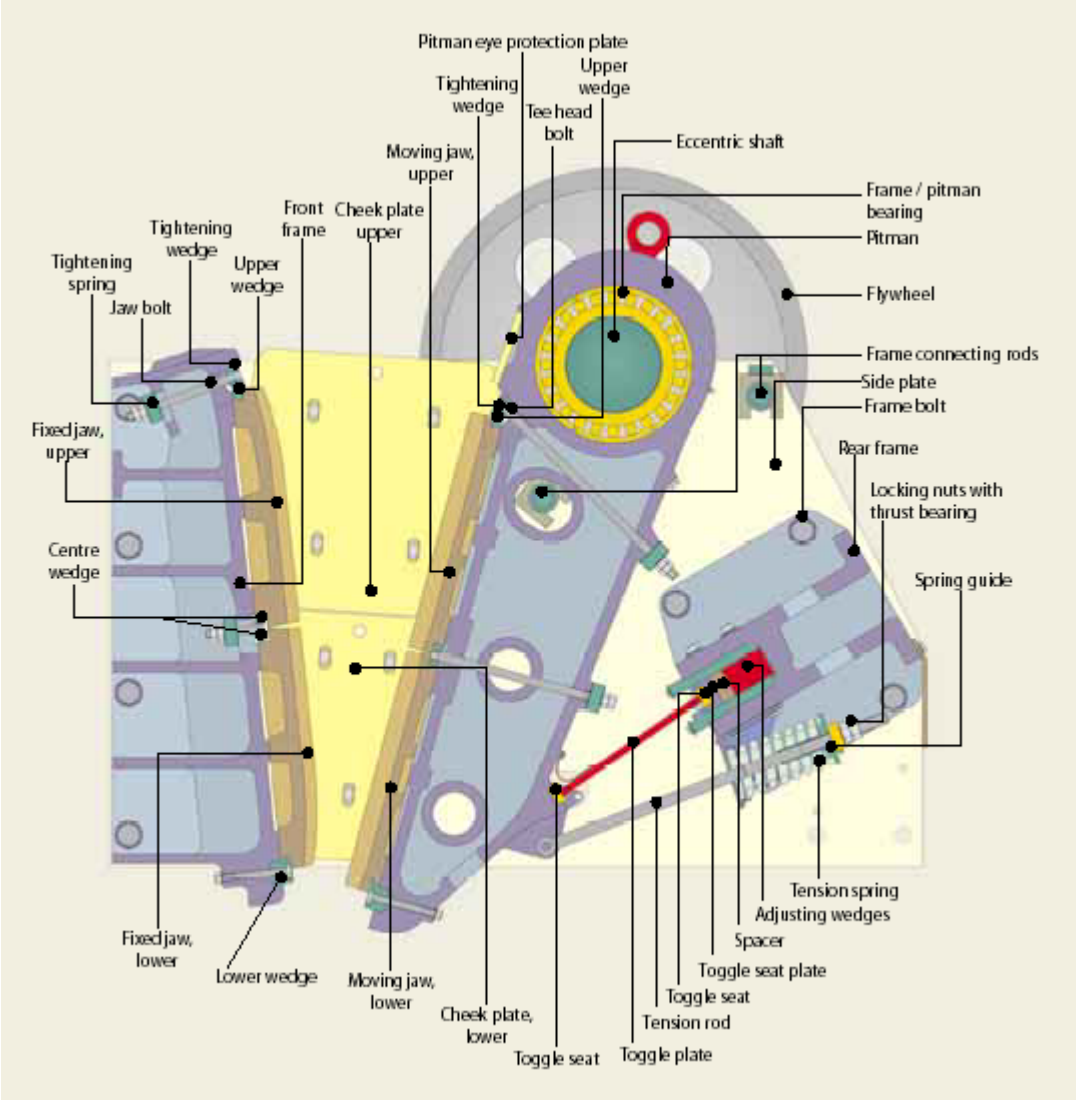

Figure 2.1 Cross-section of *Nordberg* C Series jaw crusher
(*From Metso-Minerals 2003*)

From Figure 2.1 it can be seen that the swing jaw is suspended from the eccentric shaft, allowing it to move vertically as the eccentric shaft rotates. The elliptical motion of the swing jaw assists in pushing rock through the crushing chamber and results in the single-toggle machine's higher capacity (Wills, 1992). The toggle mechanism moves the swing jaw towards the fixed jaw, and along with the eccentric supplies the force required for crushing. The flywheel is responsible for the momentum required to maintain a constant speed during the crusher cycle.

Dimensions and operating parameters

When considering the jaw crusher of Figure 2.1, there are variables of the feed that define the important machine dimensions (Napier-Munn et al., 1999). The feed particle sizes of interest are:

- The size of particle that enters the crusher
- The size of particle that can be nipped
- The size of particle that can fall through the chamber at any time
- The size of particle that can fall through the chamber when the jaws are open as wide as possible.

The dimensions defined by those particle sizes are (Fig 2.2):

- The gape - the distance between the jaws at the feed opening
- The closed side set (CSS) - the minimum opening between the jaws during the crushing cycle (minimum discharge aperture)
- The open side set (OSS) – the maximum discharge aperture
- The throw – the stroke of the swing jaw and the difference between OSS and CSS.

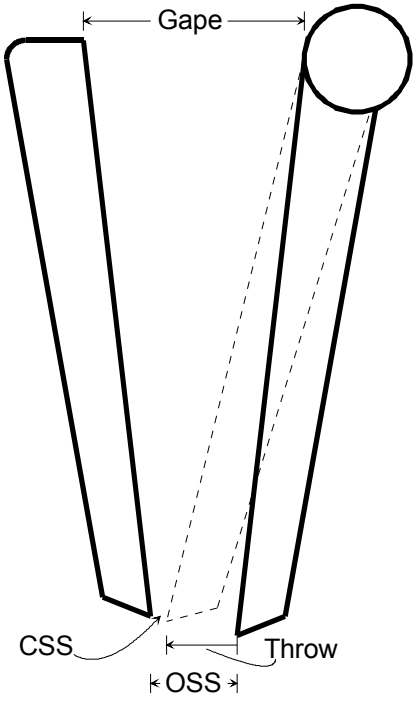

Figure 2.2 Schematic of crusher dimensions

Jaw crushers are rated, or designated, according to the maximum dimensions of their feed opening, defined by the gape and the width of the plates. Feed openings can vary from 250 mm by 500 mm (10 in × 20 in) to 1524 mm by 2032 mm (60 in × 80 in). It is common practice to limit the largest particle of rock entering the jaw to be no more than 80% of the rated gape (Weiss, 1985).

The size distribution of the product is influenced mainly by the open and closed side settings of the crusher. The discharge opening of a jaw crusher is commonly listed in terms of the closed side set. Closed side sets can range from 19 mm (0.75 in) up to 711 mm (28 in). Crusher sets can be changed on-site, either manually or automatically, usually in order to compensate for jaw liner wear (King, 2001). The capacity of a jaw crusher is function of the feed size and the settings of the crusher. Crusher manufacturers typically produce capacity tables for their various sized machines in terms of the closed side set (Table 2.1).

Table 2.1 Capacities for various Nordberg C Series jaw crushers
(*After Metso Minerals, 2003*)

CSS *mm*	**C63** 440 × 630	**C100** 760 × 1000	**C110** 850 × 1100	**C140** 1070 ×1400	**C160** 1200 ×1600	**C200** 1500 ×2000
40	40			∗Capacities in metric tons per hour∗		
50	55					
60	65					
70	80	150	190			
80	95	170	210			
90	110	190	235			
100	120	215	255			
125		265	310	385		
150		315	370	455	520	
175		370	425	520	595	760
200		420	480	590	675	855
225				655	750	945
250				725	825	1040
275					900	1130
300					980	1225

The throw of a jaw crusher is dependent upon the type of crushing required. For coarse crushing a long stroke is used and for fine crushing a short stroke is employed, resulting in a range from 9.5 mm (0.375 in) up to 50 mm (2 in) (Weiss, 1985).

The speed of the crusher is another important operating parameter (expressed in terms of the flywheel rpm). Single toggle jaw crushers can range in speed from 200 rpm to 350 rpm, and speeds do not typically fall below the 200 rpm threshold. The crusher speed decreases with increasing machine size and most large single toggle jaw crusher run at speeds near 225 rpm.

Crushing process

It was previously noted that jaw crushers are compression machines and that under the action of the eccentric shaft and the toggle, very powerful crushing forces are generated. In order to fracture a particle the crushing forces must be high enough to exceed the fracture strength of the particle. When a particle is nipped between the plates of a jaw

crusher tensile stresses are induced in the particle. Thus, the compressive force applied by the jaw plates causes the rock particle to fail in tension (Fig 2.3).

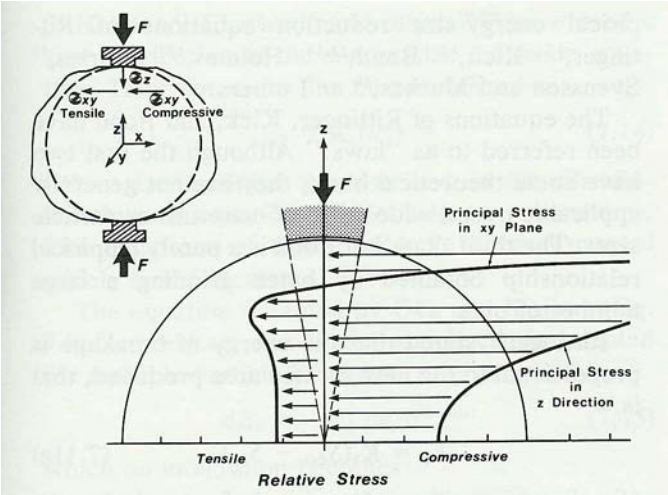

Figure 2.3 Stress distribution in particle under localized compressive loading
(*After Oka and Majima, 1970*)

After a particle is nipped and fails in tension, the resulting fragments drop down to new positions within the crushing chamber before being nipped again. Particles continue to drop down and are either repeatedly nipped by the jaws or pass through the discharge opening (when small enough). This is referred to as arrested crushing, where crushing is by the jaws only. The increasing stroke of the swing jaw at the discharge end allows material to leave at a rate sufficient enough to leave space for the particles above, preventing choking of the crusher. Since particles smaller than the discharge opening are free to pass through the crushing chamber at any time, the breakage process within the crusher operates simultaneously with a classification process (Fig 2.4).

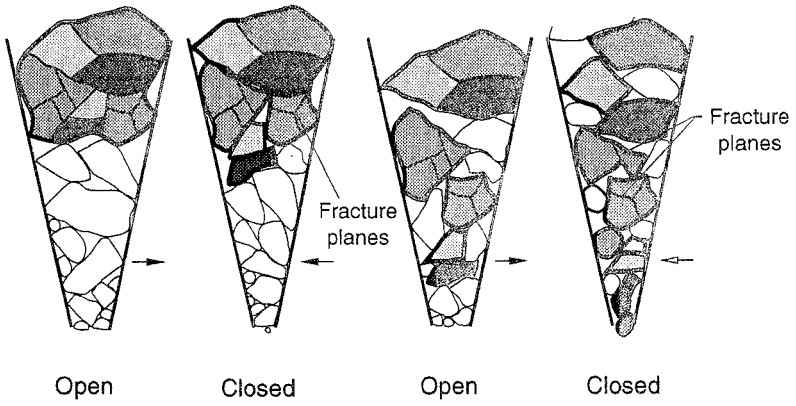

Figure 2.4 Breakage and classification in a jaw crusher
(*After Lynch, 1977 and Napier-Munn et al., 1999*)

2.1.2 JAW CRUSHER SELECTION

An operator's control over the crushing process is mainly limited to the selection of the proper crushing equipment. The main factors that influence the selection of aggregate primary jaw crushers are (Duthoit, 2000; Weiss, 1985; Metso Minerals 2003a):

- The petrographic nature of the rock
- The abrasion index of the aggregate
- The mechanical strength of the rock
- The work index, or impact crushability, of the rock
- The brittleness of the rock
- The flakiness of the rock
- The feed size
- The desired product size (or reduction ratio)
- The throughput to be crushed (tons per hour)
- The capital cost
- The long term operating costs.

The petrographic nature of the rock and its resistance to crushing forces (characterized by strength, work index, etc.) are used first to determine what type of crusher is needed and then in part to determine the power requirement of the crusher. When a jaw crusher is selected outright, the physical properties of the rock can be used to determine the mechanical features of the jaw crusher, but for the most part they are used along with the feed size and desired throughput to determine the size of the jaw crusher and its power requirement.

Usually the feed size range or the desired throughput dictates the selection of specific jaw crusher. The current trend is to go to the largest feed opening that is economically feasible in order to avoid as much secondary breakage as possible (Stansell, 2003). Once a crusher is selected it can be determined whether or not the crusher will provide the desired reduction ratio or product size distribution. As was noted previously the size of a jaw crusher's discharge opening controls the product size distribution. Thus, determining whether a specific jaw can produce the desired product is dependent upon whether or not that crusher can have its discharge opening set to the required dimension.

Based on the previous discussion, crusher selection can be simplified down to a process of employing screen analysis graphs (Fig 2.5) and capacity charts (Table 2.1). *Metso Minerals* has developed a computer program to aid in the selection of its Nordberg C Series jaw crushers. The *Bruno* program uses input information regarding rock type, feed gradation, and the desired crusher to simulate expected capacities and product size distribution curves (Metso Minerals, 2003). Wagner (1990) has proposed a crusher efficiency index number based on crusher manufacturer's published data and the crushability factor of the rock. However graphs, charts, and other data are usually based on a standard rock type and although deviations from the standard rock can be accounted for, there is a level of uncertainty due to the inhomogeneous nature of rock (Bearman et

al., 1990). In order to properly characterize the nature of the rock to be crushed various laboratory tests are usually performed.

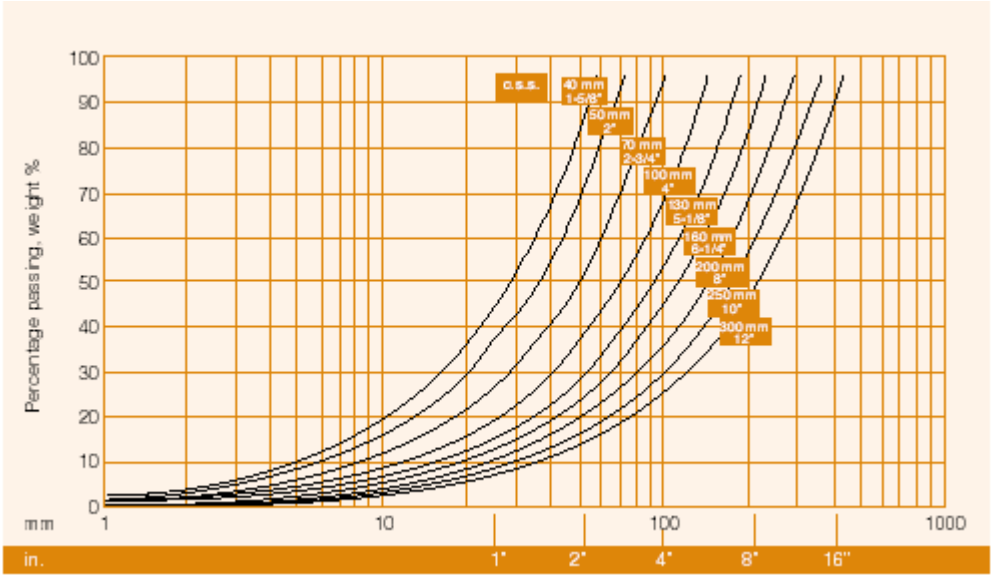

Figure 2.5 Product size distributions based on CSS
(*From Metso Minerals, 2003*)

Rock material classification
Crusher manufacturers perform tests on rock material in order to rank rocks based on their mechanical properties and to help aid in the determination of crusher power draw. The main properties used are listed on page 10 but the following discussion focuses on the most utilized for jaw crushers, compressive strength and the work index.

Compressive Strength
The compressive strength is typically used to rank a rock material's hardness. It is also sometimes used to determine a material's homogeneity and in the selection of the type of crusher used (i.e, jaw or gyratory).

Testing for compressive strength follows the standard procedure set forth by the American Society for Testing and Materials (ASTM D2938). A cylindrical specimen with a length to diameter ratio of at least 2 is loaded axially (Figure 2.6). The peak load required to cause failure is then used to determine the compressive strength of the rock specimen. A number of tests are performed in order to obtain a representative average value used to rank the material. However, adjustments to the ranking value are sometimes performed using a ratio of the highest measured value to the average value (Nordberg, 1995). When the ratio is greater than 175%, the rock is considered to have a higher than normal variation in its hardness. In this instance crusher manufacturers tend to the conservative side and use the maximum value to rank the material. Table 2.2 lists rankings based on compressive strength values.

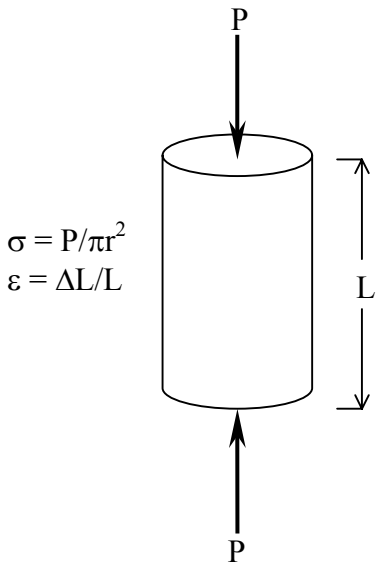

Figure 2.6 Specimen and loading configuration for compressive strength

Table 2.2 Material hardness rankings based on compressive strength

Compressive Strength	Ranking
Less than 69 MPa	Material is soft. Can be processed by all equipment at low power consumption. Equipment will be volume limited.
69 to 138 MPa	Material is average. Can usually be processed by all equipment. Can consume full power of equipment.
138 to 276 MPa	Material is hard. Require heavy duty equipment and full power draw.
Greater than 276 MPa	Material is extremely hard.

Using compressive strengths to rank materials and/or aid in the selection and design of jaw crushers has its limitations. The test itself is not representative of the breakage process occurring inside an actual jaw crusher. As discussed in section 2.1.1, nipping of a particle between the jaw plates induces tensile stresses within the particle. Thus the particle fails in tension, a failure process that does not occur during an unconfined compression test where shear failure dominates. Furthermore, tensile stresses in rocks tend to propagate, or open, inherent flaws in the material, "promoting" failure, while compressive stresses result in crack closure.

In addition to not representing the breakage process occurring within a jaw crusher, compressive strength alone is not adequate in ranking materials. Peak loads do not fully describe a rock material's stress-strain behavior, an important aspect when considering the amount of energy required to crush or break a material. This can be seen in Figure 2.7. Three rock types tested in unconfined compression are compared via their stress-strain curves. Rock A and Rock B have equal unconfined compressive strengths and

rank as hard materials according to Table 2.2. However, Rock B undergoes more deformation when loaded to failure and thus more work, or energy, is required to break it

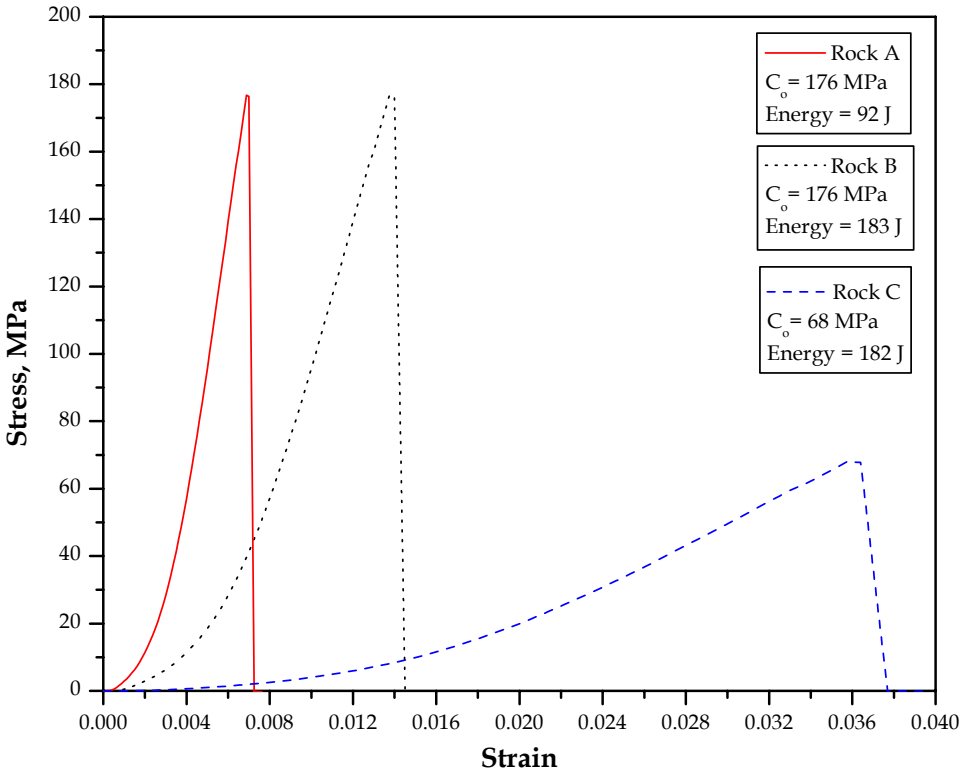

Figure 2.7 Stress-strain behavior of three different rocks

(where work is force time distance). The power draw of a jaw crusher used to reduce the size of Rock A cannot be expected to match that of one crushing Rock B. This point is further elucidated by Rock C; ranked soft and able to be processed at low power consumptions (based on compressive strength) it would require full power draw due to its ability to tolerate a large amount of deformation before fracturing.

Work Index and the crushability test

The work index was developed by Fred Bond (1952) in order to provide a method for sizing crushing equipment, specify motor sizes, and determine the energy requirements of the equipment. The Bond crushability test, sometimes referred to as the impact crushability test, is used to determine the work index.

A particle of rock (representative of what is seen in the actual crushing process) approximately 75 mm by 50 mm (3 in × 2 in) is mounted between two opposing 13.6 kg (6 lb) hammers that are used to strike the particle simultaneously. The hammers are repeatedly dropped from increasing heights until the particle breaks. The impact crushing strength (ICS) is the height from which the hammers were dropped times their weight divided by the thickness of the particle. An average value is obtained by testing

between 10 and 15 particles, and the work index (in kilowatt-hours per metric ton) is determined from the following formula:

$$WI = 53.49 \frac{ICS}{SG} \quad [2.1]$$

where, *ICS* is the impact crushing strength is in Joules per millimeter
SG is the specific gravity of the rock.

The impact crushability test is functional and its greatest advantage is that it can be used to differentiate between materials previously ranked in the same "category" according to strength test results. It also includes an energy measurement and a "crack" length measurement, essentially tying the energy input to the "amount" of size reduction, or the area of new surfaces created. However, only the maximum drop height is used to determine the ICS although every previous drop contributed to the fracture event and, in the same vane, it is assumed that the final drop propagated a crack equal to the specimen thickness in fact each previous drop was contributing to crack growth and fracture damage. This tends to underestimate the *ICS*, as more energy is required to cause complete fracture than is indicated by the final drop height.

2.1.3 Predicting Jaw Crusher Performance

The performance of a jaw crusher is most aptly defined using the product size, the capacity or throughput, and the power consumption. The main object of size reduction in the aggregate industry is to generate a well-shaped product within a specified size range with a minimum of fines. It is also desirable to maintain target production rates and to crush the rock material as efficiently as possible.

There are various methods for the prediction of crusher performance. As noted previously in the discussion of crusher selection, technical literature provided by crusher manufacturers can be used to determine capacities and product size. Adjustments can be made to account for physical variations in feed materials using the aforementioned laboratory tests. When the actual performance of a jaw crusher is difficult to determine or unclear to the manufacturer, laboratory tests using small-scale jaw crushers are sometimes conducted in order to predict the performance of full capacity machines. The normal procedure is to test crush a representative sample of the feed material and determine the product size distribution. Comparison of the product distribution and associated properties of the feed material to other materials is used to estimate overall crushing performance, power requirements, and to detect characteristics that may require special design considerations. These tests provide an opportunity to evaluate the effects of various crusher settings, speeds, feeding methods, and the physical characteristics of the material (Pennsylvania Crusher Corporation, 2003).

In addition to charts, graphs, and lab-scale crushing tests, jaw crushers can also be evaluated using mathematical modeling techniques. Mathematical techniques are usually derived from laboratory data and can be used to predict crusher performance and possibly

improve selection and design procedures (Rimmer et al., 1986). Models/equations are typically used to determine the product size, power draw, and capacity of crushers. The advantage of models is that they reduce complex operations to a few numbers or parameters and can provide guidance to improved performance and decision making (Napier-Munn et al., 1999).

Modeling of product size

Section 2.1.1 covered the crushing process that occurs as feed material passes between the plates of a jaw crusher. It was noted that the breakage process within the crusher operates simultaneously with a classification process. Feed material entering the crusher is first classified, with particles smaller than the CSS of the crusher avoiding breakage and moving on as product. Particles larger than the OSS of the crusher "report" to breakage and will undoubtedly be broken, while particles in between the CSS and OSS report to breakage but with a probability of being broken that decreases with size. This

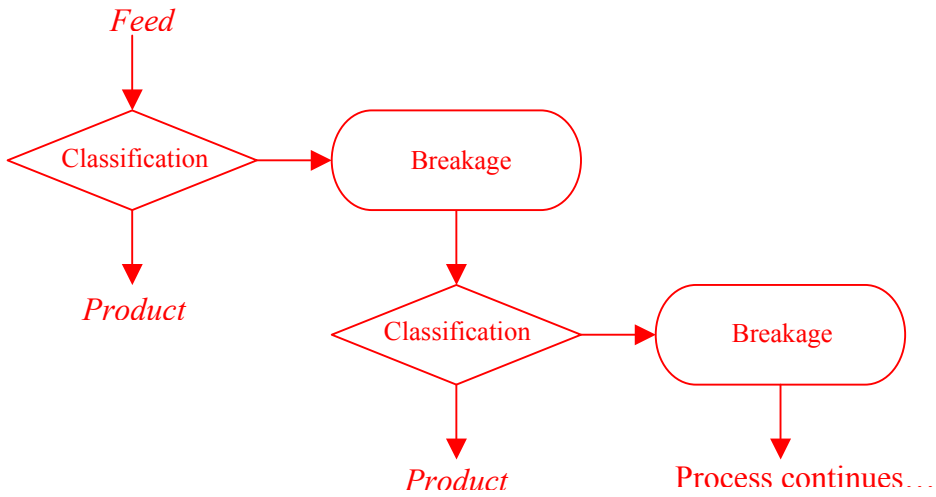

Figure 2.8 Flowchart of classification and breakage process
(*After Napier-Munn et al., 1999*)

process continues with each cycle of the swing jaw and is illustrated as a flowchart in Figure 2.8.

Considering the classification and breakage of particles in a jaw crusher as a closed circuit process reduces Figure 2.8 to the flow path shown in Figure 2.9, a schematic of the Whiten crusher model (Whiten, 1972). Mass balance equations written about each node of Figure 2.9 describe the repetitive process of classification and breakage and are expressed as (Kojovic et al, 1997):

$$x = f + Bx \qquad [2.2]$$

$$x = p + Cx \qquad [2.3]$$

where, x is a vector representing the amount in each size fraction entering the crusher
f is the feed size distribution vector
p is the product size distribution vector
C is the classification (diagonal) matrix

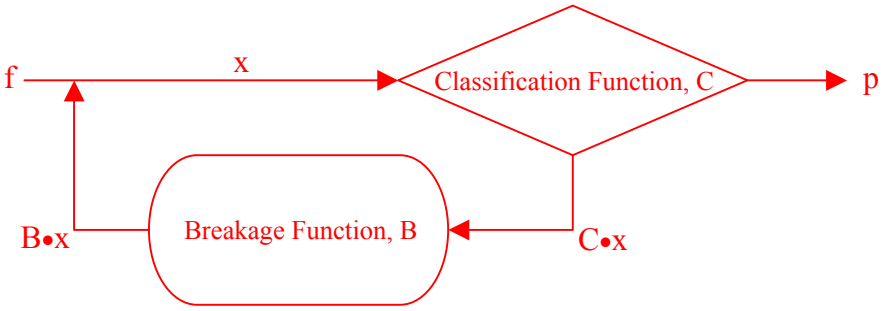

Figure 2.9 Whiten crusher model

B is the breakage distribution (lower triangular) matrix.

The classification matrix describes the proportion of particles in each size interval entering the crushing zone. The breakage distribution matrix gives the relative distribution of each size fraction after a breakage event. Equations 2.2 and 2.3 can be combined resulting in the Whiten crusher model equation (Whiten, 1972):

$$p = (\mathrm{I} - C) \bullet (\mathrm{I} - BC)^{-1} \bullet f \qquad [2.4]$$

where, I is the unit matrix. Equation 2.4 can be used to determine the product size of a jaw crusher given the feed size, classification function, and the breakage function.

The classification function has, in some respect, been defined in the discussion of the crushing process. The classification function is the probability of a particle being selected for breakage, which of course is dependent upon particle size. For example, a particle smaller than the CSS of the crusher probably will not be broken, or has only a small probability of being selected for breakage. Whiten used the following set of functions to describe the classification function (Whiten, 1972a):

$$\begin{aligned} C(x) &= 0 && \text{for } x < K1 \\ C(x) &= 1 - \left(\frac{K2 - x}{K2 - K1} \right)^{K3} && \text{for } K1 < x < K2 \\ C(x) &= 1 && \text{for } x > K2 \end{aligned} \qquad [2.5]$$

K1 is the particle size below which all particles will "by-pass" breakage and go directly to the product, and *K2* is the size above which all particles will be broken. These two parameters are expected to be functions of the crusher sets, *K1* being dependent upon CSS and *K2* upon OSS. As an exponent *K3* describes the shape of the classification function for particles between the *K1* and *K2* sizes (Figure 2.10).

Research has shown that *KI* and *K2* are, in addition to closed and open side set, functions of feed size, throughput, crusher throw, and plate liner characteristics with exact relationships being found empirically using actual operating conditions/parameters (Napier-Munn et al., 1999; Whiten 1984; Karra, 1982; Andersen, 1988; Andersen and Napier-Munn, 1990). The same work has shown that *K3* remains fairly constant among

various instances with a value around 2.3. An initial estimate of the classification function sets *K1* equal to the CSS, *K2* to the largest particle in the product (should be close to OSS), and *K3* equal to 2.3.

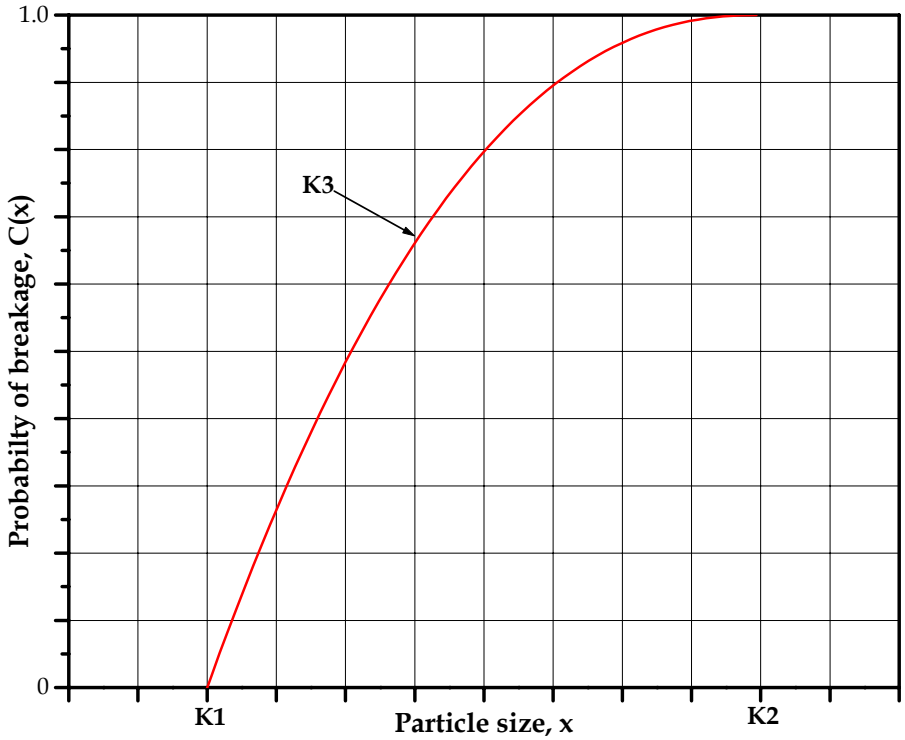

Figure 2.10 Whiten classification function

The breakage function is determined from single particle breakage testing (section 2.4). It is a size distribution dependent upon the nature of the material broken and to some extent the operating conditions of a crusher. Within a jaw crusher, a large number of single particle breakage events are occurring simultaneously, with a portion of the products of breakage undergoing subsequent crushing. The breakage distribution mathematically describes this process as it considers breakage in terms of a series of single particle fracture events (Kelly and Spottiswood, 1982). A more detailed discussion of the breakage function can be found in section 2.4.3.

Csoke (et al., 1996) developed an empirical method for determining the product size of "preliminary" crushers, i.e. jaw crushers and gyratory crushers. The product size resulting from breakage of the material larger than the CSS of the crusher can be modeled using the following function:

$$P(d) = \left(\frac{r}{r_{\max}} \right)^{m} \qquad [2.6]$$

with,

$$r = \frac{d_p}{Gap}$$

$$r_{\max} = \frac{d_{pMAX}}{Gap}$$

where, m is exponent describing the product size distribution

d_p is the particle size

d_{pMAX} is the largest size in the product (OSS)

the *Gap* is the CSS of the crusher.

Based on operating data found in the literature Equation 2.6 fits the product size of a jaw crusher with r_{max} equal to 1.223 and m of 0.842.

King (2001) outlined a model for the prediction of product size based on data from a crusher manufacturer. The main concept is that the size distribution of the product is characterized by the particle size relative to the OSS and by the product type, P_t, which is the fraction of the product smaller than the OSS. P_t is related to the nature of the material and is distinguished by the work index and a qualitative description of the material. The size distribution given by this model is determined from the following equations:

$$P(d) = 1 - e^{\left(-\left(\frac{r}{K_u}\right)^{1.5}\right)} \qquad \text{for } r > 0.5$$

$$P(d) = 1 - e^{\left(-\left(\frac{r}{KL}\right)^{0.85}\right)} \qquad \text{for } r < 0.5 \qquad [2.7]$$

with,

$$r_i = \frac{D_i}{OSS}$$

$$K_u = \left[\ln\left(\frac{1}{1-P_t}\right)\right]^{-0.67}$$

$$K_l = 0.5\left[\ln\left(\frac{1}{1-P_b}\right)\right]^{-1.18}$$

$$P_b = 1 - e^{\left(-\left(\frac{0.5}{K_u}\right)^{1.5}\right)}$$

Equation 2.7 should only be used when the size at which half of the feed material passes is greater then the OSS.

Modeling of power draw

The most popular method of determining the power draw or consumption of size reduction equipment is Bond's method. Bond's theory states that the work input is proportional to the new crack tip length produced in particle breakage and is equal to the

work represented by the product minus the work represented by the feed (Bond, 1952). Based on this theory the equation for determining the work input (kWh/metric ton) is:

$$W = 10 \times WI \times \left(\frac{1}{\sqrt{P_{80}}} - \frac{1}{\sqrt{F_{80}}} \right) \quad [2.8]$$

where, WI is the work index in kWh/metric ton (see section 2.1.2)
P_{80} is the size at which 80% of the product passes
F_{80} is the size at which 80% of the feed passes.

Using Equation 2.6 the power draw of a size reduction machine can be found for a given feed throughput from:

$$P = W \times T \quad [2.9]$$

where T is the throughput in metric tons per hour.

Although Bond's equation applies reasonably well to grinding conditions (i.e., ball mills and rod mills) its relevance to primary crushing equipment processing large feed sizes is questionable. Bond's "law" is an empirical law that only fits experimental data over a limited range of variables and only in certain cases (Choi, 1982). It can be corrected for other operating conditions but even with this correction it has been shown that the power consumption of a jaw crusher can be as much as 240% greater than the expected consumption based on Bond's equation (Eloranta, 1997). Rose and English have suggested a relationship for power consumption based on Bond's work index but take into account the material density and machine characteristics, i.e., gape, throw, CSS, etc. (Lowrison, 1974).

A more recent approach to predicting power consumption has focused on the power required by laboratory breakage devices to achieve the same size reduction as seen in actual crushers (Andersen and Napier-Munn, 1988; Morrell et al., 1992). The power required by the lab device, in this case the twin pendulum or the drop-weight (see section 2.4.2), is related to the actual power drawn by a crusher using the following expression:

$$P_c = AP_p + P_n \quad [2.10]$$

where, P_c is the power drawn by the crusher under load in kW
P_p is the pendulum power in kW
P_n is the power drawn by the crusher under no load in kW
A is scaling factor specific to a crusher (from regression analysis).

The process for determining the pendulum power is based on the classification and breakage functions described previously and will not be covered here. It can be expressed as the total energy required to reduce the crusher feed size to the product size as if all the reduction took place in the laboratory device (Napier-Munn et al., 1999).

Estimating capacity

The capacity of a jaw crusher is dependent upon the machine characteristics, the feed, and the nature of the rock material. The volumetric capacity of a jaw crusher can be estimated from the following equations (Sastri, 1994):

$$V = 60Nw\left(CSS + 0.5T\right)\left(\frac{DT}{G-\left(CSS+T\right)}\right) \qquad \text{at low speeds}$$
$$V = 60Nw\left(CSS + 0.5T\right)\left(\frac{450g}{N^2}\right) \qquad \text{at high speeds} \qquad [2.11]$$

where, N is the speed of the crusher in rpm
w is the width of the jaws in m
CSS is the closed side set in m
T is the throw in m
D is the vertical depth between the jaws in m
G is the crusher gape in m
g is gravitational acceleration in m/s^2 .

Equation 2.11 gives volumetric capacity under ideal conditions. At low crusher speeds the material falls down the chamber due to gravity flow, and the distance of the fall is dependent on the geometry of the machine. At higher speeds there is less time between strokes/revolutions and movement of material down the chamber is constricted and controlled by the speed of the machine (Hersam, 1923).

In order to determine the actual capacity of a jaw crusher, Equation 2.11 needs to be corrected by accounting for the feed size, the degree of compaction resulting from vibration, and the nature of the material. Equation 2.12 gives the estimated capacity using these parameters (Sastri, 1994):

$$V = 60Nw\left(CSS + 0.5T\right)\left(\frac{DT}{G-\left(CSS+T\right)}\right)K_1K_2K_3 \qquad \text{at low speeds}$$
$$V = 60Nw\left(CSS + 0.5T\right)\left(\frac{450g}{N^2}\right)K_1K_2K_3 \qquad \text{at high speeds} \qquad [2.12]$$

with,

$$K_1 = 0.85 - \left(\frac{F_{avg}}{G}\right)^{2.5}$$
$$K_2 = 1.92 \times 10^{\frac{-6.5T}{G}} \qquad [2.13]$$

where, F_{avg} is the average feed size in m
K_3 is a parameter related to the nature of the material.

The parameter K_3 does not have a suggested value but is considered to increase with increasing hardness or toughness.

2.1.4 CONCLUSIONS

Jaw crushers are large, heavy-duty machines capable of crushing large quantities of tough, abrasive materials. They are typically employed as primary crushers within aggregate processing plants. Jaw crushers are most commonly defined by gape size,

open and closed side sets, and capacity. There are a wide range of jaw crusher sizes for varying production and product size requirements.

The plates of a jaw crusher are used to apply compressive forces that induce tensile stresses within particles, causing fracture. Particles are repeatedly nipped until they pass through the crushing chamber. The breakage process occurring between the jaw plates acts simultaneously with a classification process. The classification process defines whether or not a particle will be subjected to crushing and is dependent upon the settings of the crusher and particle size.

The selection of a jaw crusher for application in the aggregate industry is primarily based on technical literature provided by crusher manufacturers, experience, and cost. Charts and graphs provide data on electric power requirements, crusher size (gape), as well as expected capacities for a given material and closed side set. These charts and graphs have also been incorporated into computer programs to aid in crusher selection. In order to account for material variations manufacturers rely on a suite of laboratory tests. The uniaxial compression and Bond impact crushability test are two of the most common tests used to rank materials relative to their hardness/crushability. Each of these tests has limitations and neither adequately describes a material's resistance to fracture. Although jaw crushers are used extensively, the lack of understanding relative to their operational characteristics, as well as a reliance on an inappropriate, single set of material properties, makes selection of a proper machine difficult. Jaw crusher selection is also heavily influenced by the subjective judgment/experience of individuals, which can result in the conservative selection and operation of jaw crushers.

The prediction of crusher performance is typically concerned with the size distribution of the product exiting the crusher, the machine's power draw, and the capacity. The capacity of a jaw crusher is dependent upon the operating characteristics of the machine and influenced by the feed size and the nature of the material. It can be determined fairly easily but there has been difficulty in accounting for the variable nature of rock materials. Bond's theory or equation has long been used to determine the power draw and motor requirements of size reduction machines. However, its relevance to jaw crushers handling large feed sizes has been questioned. The recent trend has been to calculate power draw based on laboratory crushing tests. The modeling of crusher performance has focused mainly on the prediction of the product size distribution. The product size distribution of a crusher can be determined using the Whiten model given the feed size, the classification function, and the breakage function. The classification function is dependent upon the operating parameters of the crusher, namely the closed side and open side set. The breakage function considers breakage in terms of a series of single particle fracture events and is dependent upon the nature of the material. It is determined from a series of laboratory single particle breakage tests.

There is significant room for improvement when it comes to selecting and optimizing jaw crushers. The enhancement of crusher selection and the prediction/optimization of

its performance are dependent upon the operating parameters of the machine and the physical properties of the material being broken. Early attempts at establishing relationships between these components focused on the energy consumed by a crushing machine and the resultant size reduction. Energy-size relationships themselves require an awareness of the mechanisms of fracture, the fundamentals of which are covered in the following section.

2.2 PHYSICS OF PARTICLE FRACTURE

The breakage of particles in any comminution or crushing machine is a difficult process to understand. Comprehending the sub-processes that occur prior to material failure can provide a basis for evaluating the limitations of crushing machines or set the direction for potential improvements (Schoenert, 1972). Knowledge of the mechanisms of fracture provides information about the final stages of strain within a particle, namely the formation and propagation of cracks (Tkacova, 1989). This provides a basis for how to properly characterize materials, i.e., which mechanical properties are representative of the fracture process.

The mechanisms of fracture also affect the distribution of resultant particle sizes. Different methods of breakage produce different product sizes based on the amount of energy input and process of loading. A perception of the expected distribution of resultant particle sizes can be ascertained simply based on fracture physics.

2.2.1 PARTICLE BEHAVIOR

Rocks are brittle materials and the amount of strain within a particle under load is proportional to the applied stress. Recalling that jaw crushers induce tensile stresses within particles, it is the tensile strength of rock materials that must be exceeded in order for the material to fracture. Theoretically the tensile strength of an ideal brittle material should be approximately:

$$\sigma_t = \frac{E}{10} \qquad [2.14]$$

where, E is Young's modulus.
In reality the actual tensile strength of a rock is well below the estimate given by Equation 2.12, usually at least 100 times lower. This decrease in strength is due to the presence of pre-existing flaws or cracks within the rock.

Pre-existing flaws and cracks within rocks act as stress concentrators. Inglis (1913) provided a solution for the case of an elliptical hole in a stressed plate (Fig 2.11). He found that the stress concentration near the tip of the ellipse was proportional to the size of the ellipse and the ellipse radius. Inglis' stress concentration factor can be written as:

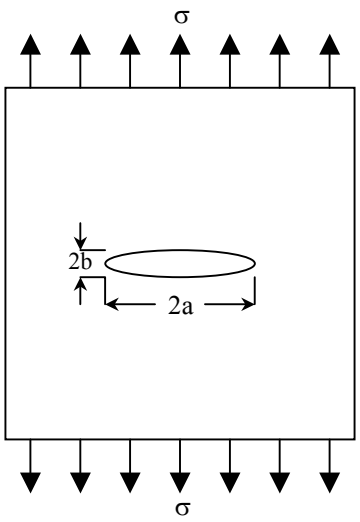

Figure 2.11 Elliptical hole in an infinite plate

$$k = \left(1 + 2\sqrt{\frac{a}{\rho}}\right) \qquad [2.15]$$

where, a is the half-length of the ellipse

ρ is the tip radius of the ellipse.

Griffith (1921) extended Inglis' work by hypothesizing that pre-existing cracks in brittle materials would act like Inglis' ellipse causing stresses to concentrate at the crack tips. Griffith used Inglis' stress analysis to establish a relationship between fracture stress and crack size using an energy balance approach. Griffith established that the fracture of brittle materials is due to the existence of pre-existing flaws and is an energy-controlled process.

2.2.2 GRIFFITH'S THEORY

Griffith's proposed that the failure of a brittle solid is caused by the extension of inherent cracks resulting in a new crack surface that absorbs energy supplied by the work done by an external force or by the release of stored strain energy from within the solid (failure occurs when the energy supplied by an external force or by the release of stored strain energy is greater than the energy of the new crack surface). This implies that the more energy a material absorbs, the more resistant it is to crack extension.

Two important criterions must be met in order for brittle failure to occur according to Grifffith's theory (I. Chem. E. Report, 1974).

1. There must be a mechanism for which crack propagation can occur. At some point in the material, the local stress must be high enough to overcome the

molecular cohesive strength of the material. This is accomplished through stress concentration around "Griffith" cracks or inherent flaws.

2. The process must be energetically feasible. Enough potential energy must be released in order to overcome the material's resistance to crack propagation. This can be accomplished by increasing the work done by external forces acting on the material.

As noted previously Griffith used Inglis' stress analysis in his energy balance approach. Thus the total energy for infinite plate (Fig 2.11) with an elliptical crack can be written as:

$$U = U_t + U_c - W + U_s \qquad [2.16]$$

where, U_t is the initial elastic strain energy of an uncracked plate

U_c is the elastic energy release caused by the introduction of a crack

W is the work done by external forces

U_s is the change in the elastic surface energy due to the new crack surfaces.

Using elastic theory expressions, the four energy components can be determined, yielding the following equation (Whittaker et al., 1992):

$$U = \frac{\sigma^2 A}{2E'} - \frac{\pi\sigma^2 a^2}{E'} - \frac{\sigma\varepsilon A}{2} + 4a\gamma_s \qquad [2.17]$$

where, A is the infinite area of the plate

E' is the effective Young's modulus (E for plane stress; $E/(1-\nu^2)$ for plane strain)

ε is the strain

γ_s is the specific surface energy.

Griffith defined the fourth energy component, where γ_s is a constant material property representing the energy required to create a unit area of new crack surface.

According to Griffith the crack will propagate when an increase in its length does not change the net energy of the plate, when dU/da equals zero. Differentiating Equation 2.14 with respect to a results, and setting the result equal to zero, gives:

$$4\gamma_s - \frac{2\pi\sigma^2 a}{E'} = 0 \qquad [2.18]$$

Equation 2.18 can be arranged to determine the fracture stress required to cause crack initiation and more importantly the strain energy release rate, G:

$$G = \frac{\pi\sigma^2 a}{E'} \qquad [2.19]$$

G characterizes the energy per unit area required to extend the crack and is expected to be a fundamental physical property controlling the crack (Dowling, 1999).

Modifications of Griffith's theory have since followed, mainly in order to compensate for plastic deformation near the crack tip. In fact, due mainly to plastic deformation, the energy required for crack extension has been found to be 10 times higher than that predicted by Griffith. Plastic deformation acts to relax strain energy since energy is

consumed in deforming the material ahead of the crack tip. The high stress that would ideally exist near the crack tip is effectively spread over a larger region or redistributed, resulting in a lower stress near the crack tip that may be resisted by the material. Orowan (1949) and Irwin (1948) took this into account and included the work of plastic deformations in calculations of the energy balance of fracture.

Despite the definition of a characteristic material property that describes crack propagation, the importance of Griffith's work, in particular reference to particle breakage, really lies in the connection made between the stress required for fracture and the presence and size of cracks or flaws. Any criterion used to define or distinguish the crushability of rock material needs to account for the presence of flaws and their influence on the work required to initiate fracture.

Influence of particle size

Griffith's theory indicates that fracture is dependent upon the presence of inherent flaws. Rocks, due to their geologic nature and inhomogeneity, contain a large number of flaws and cracks, both on the macro and microscopic level. Thus in addition to the mere presence of flaws controlling fracture, the distribution of flaws also affects the fracture of particles. In order to describe, and even compensate for, the distribution of flaws within brittle materials statistical approaches are generally employed.

The most well known statistical description of flaw distribution and its effect on particle fracture is Weibull's (1939) model. Weibull's weakest link theory assumes that the fracture of a particle is dependent only on the local strength of its weakest flaw from which the most severe crack will propagate and is independent of all other flaws. Weibull's model shows that the presence of this weakest flaw becomes less probable with decreasing particle size. This is in agreement with experimental results that indicate strength increases with decreasing particle size. As particle size decreases critical flaws are essentially "used up" in order of their significance.

Particle size effect can also be explained using energy considerations. Recalling that failure of a brittle solid occurs when the energy supplied by an external force or by the release of stored strain energy is greater than the energy of the new crack surface, smaller particles, which have less capacity for storing elastic energy (U_t is proportional to volume), will require more work by external forces, or higher stresses, in order to fracture. Smaller particles also exhibit a more plastic response than larger ones. The high stress levels in small particles result in irreversible deformations that modify the stress distribution within the particle and result in coarser fragments upon fracture (Schoenert, 1972).

The effects of size on particle fracture call in to question the applicability of strength parameters to crushing resistance. A jaw crusher sees a wide range of particle sizes. It also must re-crush smaller particles produced from the crushing of larger ones. The smaller particles will require higher stresses as the flaw distribution changes with a

decrease in particle size. Since tensile strength mostly controls fracture initiation of particles in a jaw crusher, characterization of a rock material using a laboratory based tensile strength test would require either a large number of samples of varying size or statistical rock mechanics in order to analyze size effects. A more appropriate method of characterizing rock materials would be one that compensates for size effects. For example rearranging Equation 2.18 into:

$$\sigma\sqrt{\pi a} = \sqrt{2E'\gamma_s} \qquad [2.20]$$

indicates that, according to Griffith's criterion, fracture will occur when $\sigma\sqrt{\pi a}$ reaches a constant critical value determined by the characteristic material properties E, ν, and γ_s. Higher stresses are normalized by the smaller flaw size, a, around which they are concentrating. When considering fracture physics as it pertains to crushers, resistance to fracture should account for the stresses required for breakage, the presence of flaws, and be independent of particle size.

2.2.3 FRACTURED SIZE DISTRIBUTION

The fracture process due to the point contact loading that occurs between the plates of a jaw crusher and a particle is illustrated in Figure 2.12. The induced tensile stress along

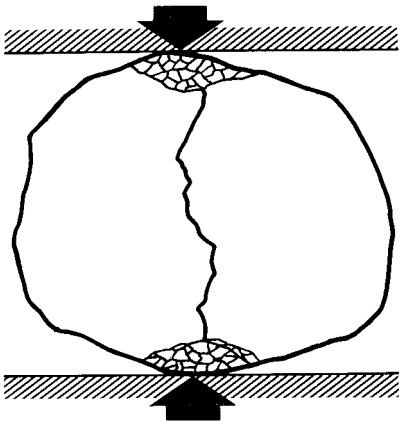

Figure 2.12 Fracture caused by compression crushing
(*After Kelly and Spottiswood, 1982*)

the axis of the particle results in fracture by cleavage. The areas directly below the loading contacts fail in compression producing abrasion fracture. Abrasion can be thought of as type of shatter fracture (shatter is the third type of fracture – common in impact breakers). Shatter occurs when there is excess energy input and a large number of flaws are stressed almost simultaneously or before the weakest flaw is unloaded. Abrasion is localized shatter. There is not enough energy to shatter the entire particle but the impact of the jaw plates on the particle does produce attrition at the load point.

Coarse progeny particles are a result of cleavage fracture and finer sized progeny are a result of abrasion/shatter. A comparative display of the distribution of progeny sizes

after particle failure is represented in Figure 2.13. Since two mechanisms of fracture

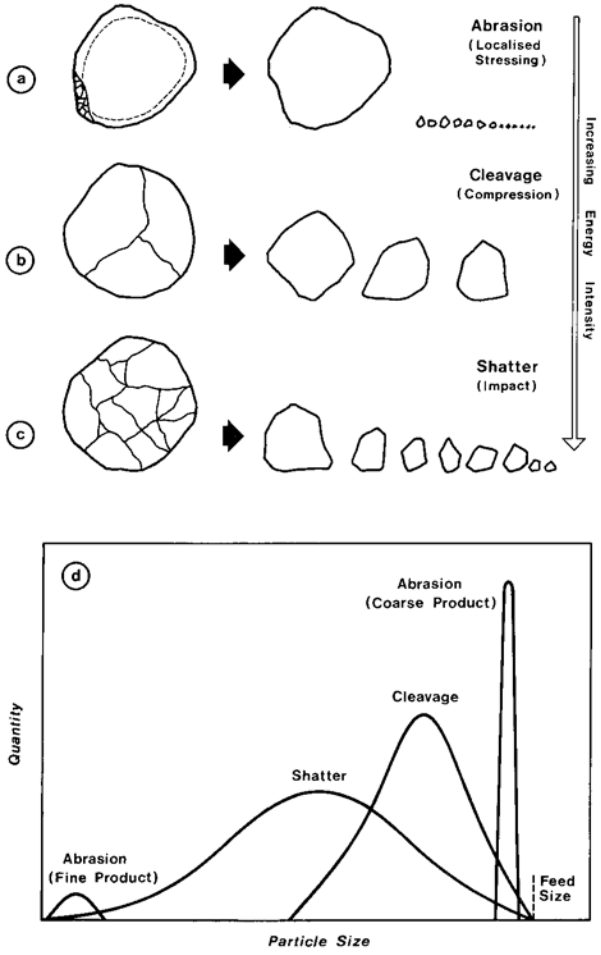

Figure 2.13 Size distributions occurring due to mechanisms of fracture
(*From Bowers et al., 1991*)

occur during point contact loading, resultant size distributions from jaw crushers are expected to be bimodal. Lynch (1977) attributed the two components as being a result of localized fracture against the crusher face (fine size distribution) and main fracture of the particle (coarse distribution).

The distribution of particle sizes after fracture is dependent on the fracture mechanisms occurring as a result of particle loading. The mechanisms occurring during fracture are controlled by the intensity of energy applied to the particle. The physics of fracture and quantification of the energy required for fracture have been explained by Griffith's theory. Since the same mechanisms control product size, there is expected to be a relationship between the distribution of progeny sizes and a particle's resistance to fracture (characterized by some form of Griffith's criteria).

2.2.4 CONCLUSIONS

A thorough understanding of fracture physics and the mechanisms that drive fracture initiation is necessary in the evaluation and improvement of jaw crushing operations. It is also important to be aware of fracture mechanisms when using material properties or indexes to describe the particle breakage process or determine crusher performance.

Brittle materials fail at stress levels well below what is predicted based on stress-strain behavior (Young's modulus). The presence of cracks accounts for the markedly lower strength. Rocks are brittle materials and by their nature also contain inherent flaws (i.e., grain boundaries, voids/pores, etc.) on both small and large scales. These cracks act as stress concentrators, with the increase in stress at these locations being proportional to the length of the crack and the crack tip radius.

Griffith used Inglis' stress analysis of an elliptical crack in an infinite plate to determine a relationship between crack size and fracture stress. Griffith hypothesized that fracture occurs when the energy supplied by an external force, or by the release of stored strain energy, is greater than the energy of the new crack surface. Using an energy balance approach Griffith was able to define the strain energy release rate G, a material property that characterizes the energy per unit area required to a crack. Griffith's work also defined a constant critical value of $\sigma\sqrt{\pi a}$ that when met will result in fracture. The importance in terms of crushing operations is that fracture is dependent on applied loads and the presence and size of flaws, and both need to be accounted for when characterizing a rock materials' resistance to fracture.

It has been shown that, for a given material, as particle size decreases strength increases. This is due to the distribution of flaws within the material. Weibull's weakest link theory states that the strength of a particle is dependent upon its most critical flaw. Fracture initiates from that flaw independently of all other flaws within the particle. As the size of the particle becomes smaller the existence of such a critical flaw becomes less probable, thus the increase in strength with decreasing particle size. Defining a material's resistance to fracture should account for the effect of size or be independent of it.

Since the mechanisms of fracture also control the distribution of progeny particle sizes and specific fracture mechanisms produce specific fragment sizes, particle physics is the foundation for the first models/equations used to describe size reduction processes. Energy-size reduction relationships are related to Griffith's energy criterion and the presence of Griffith cracks. The energy criterion states that enough potential energy must be released in order to overcome a material's resistance to crack propagation, requiring an increase in the work done by external forces acting on the material. This is the amount of energy input into reducing the size of a particle. The amount of size reduction, or the size distribution resulting from fracture, is dependent upon the presence and distribution

of Griffith cracks. Energy-size reduction relationships are a natural progression of the physics of particle fracture and form the principles of comminution.

2.3 FRACTURE ENERGY AND SIZE REDUCTION

Relationships between energy and size reduction are concerned with the amount of energy input by a comminution machine and the degree of size reduction attained. It was pointed out in section 2.2.2 that different sized particles require different amounts of energy in order to be fractured. The effect of particle size on energy input was used to develop the first relationships between energy and size reduction.

It is now generally accepted that established relationships between energy and size reduction can be expressed using the following singular equation (Charles, 1957):

$$\mathrm{d}E = -K\frac{\mathrm{d}d}{d^n} \qquad [2.21]$$

where, E is the specific energy necessary to supply the new surface energy
K is a constant
d is the particle size
n is a value describing different size ranges.

Equation 2.21 is the general form energy-size relationships proposed by various researchers. The principles behind their suggestions and their specific equations follow.

2.3.1 LAWS OF COMMINUTION

The work of Von Rittinger, Kick, and Bond constitute what are commonly referred to as the "laws" of comminution. Von Rittinger (1867) stated that the breakage energy is proportional to the area of the new surfaces produced and that the energy requirement remains constant for a unit of surface energy produced. Von Rittinger's law is:

$$E = K\left(A_2 - A_1\right) \qquad [2.22]$$

where, A_1 is the specific surface area of the initial particle
A_2 is the specific surface area of the final particle.

Since the specific area is inversely proportional to the diameter, Equation 2.22 can be rewritten as:

$$E = K\left(\frac{1}{d_2} - \frac{1}{d_1}\right) \qquad [2.23]$$

where, d_1 is the initial particle diameter (mean size for a distribution of particles)
d_2 is the final particle diameter (mean size for a distribution of particles).

Von Rittinger's theory is similar to Griffith's since it relates the energy input into creating new surfaces (cracks) to the surface area of the cracks. However, it only accounts for the energy required to pull apart molecular bonds, and as Griffith showed there are many other energy aspects to overcome.

Kick (1883) postulated that the energy required for breakage is proportional to the size or volume of the particle and that the energy requirement remains constant for equivalent geometrical changes. Kick's equation is:

$$E = K \ln \frac{d_1}{d_2} \qquad [2.24]$$

The problem with Kick's law is that it assumes the energy required to achieve a certain degree of size reduction will remain constant for equivalent changes in particle volume. The effect of size on the amount of energy required for fracture, as discussed in section 2.2.2, is not considered by Kick. But smaller particles will require more energy to fracture and the energy requirement will increase as particle volume decreases.

Bond stated that the energy input is proportional to the new crack tip length produced and is equal to the work represented by the final particle size minus the work represented by the initial particle size. His law of comminution is in fact an empirically derived relationship based on a series of grinding tests. A specific form of Bond's equation is given on page 19 in Equation 2.8. A general form in relation to Von Rittinger's and Kick's is:

$$E = K\left(\frac{1}{\sqrt{d_2}} - \frac{1}{\sqrt{d_1}}\right) \qquad [2.25]$$

In some respects Bond's law resolves Kick and Von Rittinger's theories. Bond argued that crushing is concerned with both surface area (Von Rittinger) and particle volume (Kick). The volume of the particle is proportional to the amount of stress absorbed and stresses concentrate on the surface, which eventually propagate into cracks. Bond's work attempted to follow Griffith's theory since the premise is that when local deformation exceeds the critical strain a crack tip forms, the surrounding stress energy flows to it, and fracture follows (Pryor, 1974). However, Austin and Brame (1983) found that Bond's work has no factually based relation to Griffith's theory. Bond did introduce the effect of material properties though, noting that different materials will have different resistances to a reduction in their size (Equation 2.6 included the work index, *WI*, of the material being crushed).

The three laws of comminution have been shown to be applicable over different size ranges (Figure 2.14). For particle sizes encountered during crushing Kick's law is most applicable. Von Rittinger's law fits fine size reduction fairly well and Bond's empirical "law" of course corresponds to the grinding range. Despite the inability of each law to fully characterize an energy-size reduction relationship for the entire spectrum of size ranges, they do recognize some important aspects (Manca et al., 1983):

a. The relative importance of the energy expended
b. The importance of reduction ratio
c. The importance of the feed and product size distribution

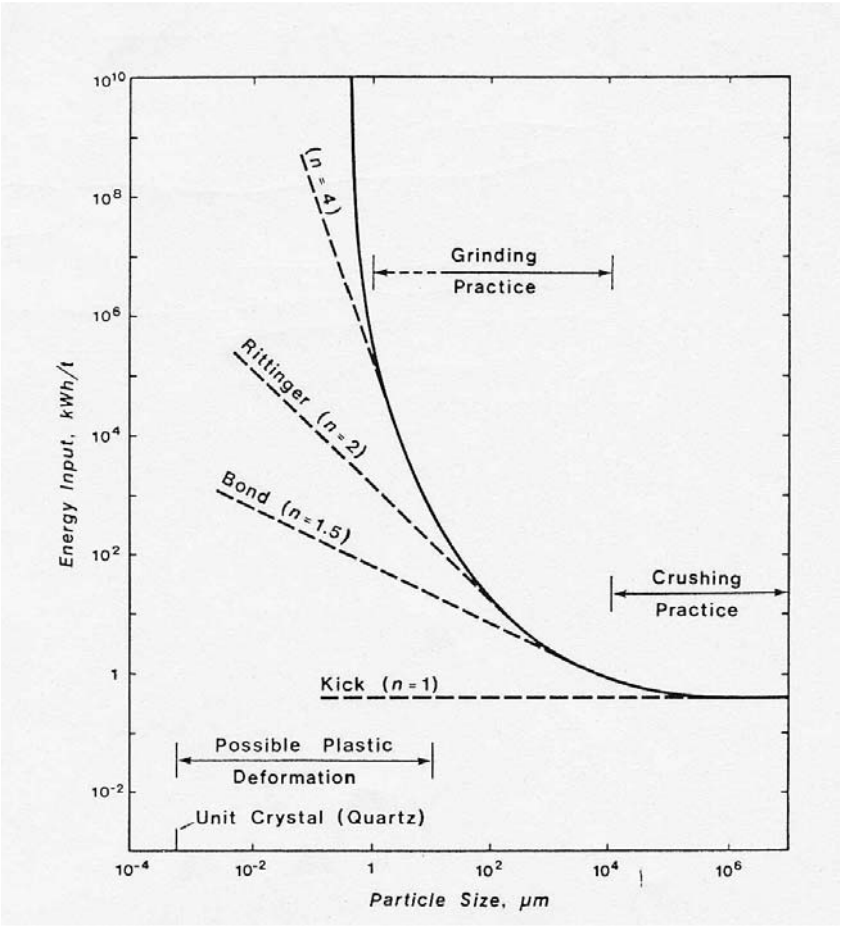

Figure 2.14 Size ranges applicable to Von Rittenger, Kick, and Bond equations
(*After Hukki, 1961*)

d. The effects of different conditions of stress application for different size reduction devices
e. The influence of the characteristics of the material.

Advancement of the three laws has included relating energy requirements to non-uniform particle size distributions as well accounting for changes in particle strength. Holmes (1957) modified Kick' law in order to account for elastic deformation and the effect of reduced particle size on strength. For a given reduction ratio and product size, Holmes' considers the exponent *n* in Equation 2.21 a measure that expresses the degree of variation in particle strength with variations in size, and is specific to the material and the manner of stress application. Von Rittinger, Kick, and Bond assumed that the shape of the size distribution remains fairly constant, which is not the case, particularly for crushers (Napier-Munn et al., 1999). Charles (1957) included the size modulus from the Schuhmann distribution function in his equation for energy. His equation relating energy requirement to product size distribution reduction is:

$$E = \frac{K}{n-1}\left(\frac{\kappa^{1-n}}{\alpha - n + 1} - \frac{1}{\alpha d^{n-1}}\right) \qquad [2.26]$$

where, κ is the Schumann size modulus

α is a constant in Schumann's distribution function

d is the particle size.

Equation 2.26 describes the relationship between energy and size reduction and includes all the parameters upon which energy input is dependent on, but it only applies to simple comminution systems and falls short of being applicable over a wide range of sizes. Although Charles' equation itself is not universally applicable, it also offers the theoretical proof that a general law valid for all comminution processes cannot exist and that every rock fragmentation process requires the derivation of a specific analytical expression (Manca et al., 1983).

2.3.2 CONCLUSIONS

A number of researchers have investigated the relationship between energy input and size reduction in an attempt to establish an equation or model capable of predicting the energy requirements of comminution machines (for a given degree of size reduction). The laws of Von Rittinger, Kick, and Bond do not describe the energy-size reduction relationship for all size ranges but each has been found to pertain to some particle size class.

The three laws are related to Griffith's theory and seem to be founded in fracture physics. However, Von Rittinger's law only considers surface area, thus its application is to fine sizes where volume effects are minimal. Kick's law considers particle volume but disregards the effect of flaws or cracks on particle strength, the distribution of which tends to decrease with size, making smaller particles more difficult to fracture. Kick's law is applicable to coarse particle sizes. Bond considered both surface area and volume in his theory and actually argued that it was related to Griffith's theory. That argument has been shown to have no basis, but since Bond's equation was empirically derived from grinding tests his model fits particle sizes typically found in that application.

Bond introduced the concept of work index to compensate for the reality that different materials exhibit different resistances to a reduction in their size. Additional work demonstrates that energy-size relationships need to account for non-uniform size distributions as well as variability in particle size, strength, and load application. Yet inclusion of these factors still does not provide a singular relationship capable of predicting energy requirements for any range of size reduction. In reality a common law valid for all size reduction processes probably does not exist and empirically derived models need to be fully developed for particular breakage processes.

The complexity of the energy-size reduction relationship has lead investigators to seek an alternative method of assessing the energy requirements and product distribution of size reduction devices. In the past 40 years a method has been developed in order to

investigate the science of size reduction. The method is based on the fracture physics discussed in section 2.2 and focuses on: fracture mechanisms, crushing under controlled conditions, packed bed crushing, measurement of energy needed for fracture, fragment size distribution, new surface area produced, mathematical simulation of crushing processes, and practical applications (Rumpf, 1966). The approach used to investigate these issues is referred to as single particle breakage analysis.

2.4 SINGLE PARTICLE BREAKAGE ANALYSIS

The breakage process occurring in a crusher, or any comminution device, is a series of single particle crushing events. A particle is loaded and fractures only under the stresses applied to it. The product coming out of the crushing device is just a collection of progeny particles from numerous single particle events. An understanding of single particle fracture, which is the fundamental process of comminution, is of great benefit. Additionally it provides a means to separate a material's fracture behavior from the operating conditions of comminution machines. The three laws discussed previously are limited to certain methods of comminution and include characteristics of those methods (Krogh, 1980). Characterization of a material's fracture behavior (i.e, by determining values like fracture energy, fragment size) should be independent of the eventual method of comminution used.

Although the concept of applying fracture physics, through single particle breakage, to comminution processes was pioneered by Rumpf beginning in the 1960's, the first single particle tests where conducted in the 1930's (Carey and Bosanquet, 1933). The purpose of these tests was to determine the energy necessary to reduce coal and gypsum particles (ranging from 2 to 50 mm) to a certain size. But most of the work at this time focused on the validation or refutation of Kick's and Von Rittenger's theories. Using compression devices (to calculate input energy) and gas adsorption techniques (to determine surface area), the relationships suggested by Kick and Von Rittenger were tested. But since Rumpf's proposal that the fundamental areas of comminution to be studied should include fracture physics and the material characteristics related to breakage, a great deal of progress has been made in employing results from single particle breakage analysis to improvements in actual crushing and comminution applications. The following outlines the concepts behind single particle breakage, the test methods employed, and the related data used to characterize a material's response to fracture.

2.4.1 CONCEPTS OF SINGLE PARTICLE BREAKAGE

Single particle breakage (SPB) is the study of fracture physics (section 2.2). The state of stress arising in a particle loaded by a comminution machine is dependent on the size and distribution of cracks or flaws within the material and the deformation behavior of the material. The flaw size and distribution are dependent on particle size and its

homogeneity. And the type of breakage device affects the type, direction, and number of contact forces acting on the particle, and the velocity at which they are applied. Figure 2.15 shows the number of "events" occurring during the breakage of a particle and their interdependence.

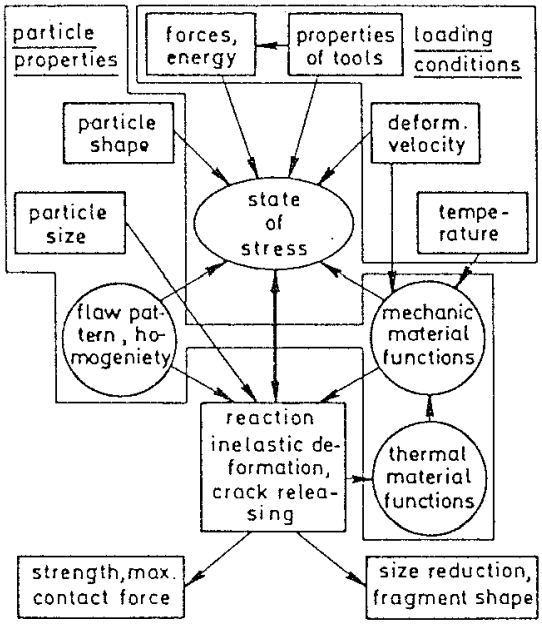

Figure 2.15 Phenomena that effect single particle fracture
(*After Schoenert, 1987*)

The presence and effect of flaws on particle fracture has been discussed in detail, as has the effect of particle size (section 2.2.2). It is important to note again though that rock materials are inherently flawed and only at very small particle sizes will the presence of flaws be less critical. At those fine sizes the behavior of the particle becomes inelastic. In terms of single particle breakage, since the determination of progeny size distribution is of great importance, the importance of flaws is two-fold. In addition to its influence on fracture, the crack pattern arising out of flaw propagation will determine the size and the shape of the progeny fragments and the new surfaces created (Schoenert, 1979).

One aspect of the behavior of a stressed particle that has not previously been discussed is the effect of deformation rate. Although single particle breakage isolates the material behavior from comminution machine operating parameters, there is some differentiation between slow compression and impact compression. The deformation rate in a crusher is between 0.1 and 10 m/s, as compared to an impact mill that might deliver a rate between 20 and 200 m/s. Single particle breakage analysis applicable to jaw crusher processes is generally considered slow compression (but only in a relative sense, a more appropriate classification might be slow impact). In slow compression elastic waves

arising from load contact do not affect the breakage of the particle, nor does the deformation rate, as long as the particle behaves mainly elastically (Schoenert, 1991).

The stress field generated in single particle crushing is dependent upon the direction and number of forces applied. The stress field arising in a particle under load has been studied mainly for the case of an elastic sphere since the stress-strain behavior of irregularly shaped particles cannot be calculated. When an elastic particle is loaded by a contact force, the area underneath the contact develops a cone-shaped zone of stress concentration in which particle degradation is severe compared to the space outside the zone (Prasher, 1987). Fine fragments originate mainly from these cone-shaped zones, with coarse fragments coming from the zones away from the contact area. This corresponds to the situation of a particle under localized compression (Figure 2.3) and the resultant fracture pattern (Figure 2.12). When multiple forces act on a particle the result is more fracture since cracks grow under the contact areas and propagate towards other contacts. Since jaw crushers perform arrested crushing particle stressing is through two contacts only, between the jaw plate and particle (see section 2.1.1).

Figure 2.12 does not take into account what occurs after initial breakage. Since the throw (crushing stroke) of a jaw crusher is fixed, particles are often loaded beyond the point of first fracture. It is important in single particle breakage to distinguish between the first stage of primary fracture and the second stage in which a group of fragments are compressed; with fragmentation continuing until the reaction stress of the fragments is equal to the applied stress (Schoenert, 1987). The amount of fragment particles crushed in the second stage is dependent on the material hardness (harder materials will have fragments that leave the crushing chamber at higher velocities) and the loading velocity.

2.4.2 TEST METHODS

There are basically three ways to reduce the size of particle, by slow compression, impact, and abrasion/shear. Since size reduction processes are carried out in various ways there are different methods of conducting single particle breakage (SPB) analysis, including: impact by falling media, dropping the particle on a surface, and slow compression (Krough, 1980). Single particle breakage analyses utilizing slow compression and impact crushing are most applicable to the conditions of jaw crushing and are the focus here. The distinction between slow compression and impact is the rate of load application. Slow compression tests occur over a time scale of approximately 1 to 10 seconds, while impact tests can take as little as 1×10^{-5} seconds to complete (Peters Rit et al., 1983).

Slow compression is simple and has the advantage of being easy to execute (Mehrim and Khalaf, 1980). More recently, single particle tests used to determine the behavior of rock have evolved to include pendulum and drop weight tests (Bearman et al., 1997). The Comminution Center at the University of Utah has made variations to these tests, developing the Ultrafast Load Cell Apparatus. The Julius Kruttschnitt Mineral Research

Center (JKMRC) has also specialized in the use of similar methods (Narayanan and Whiten, 1988).

Slow compression

Slow compression tests are essentially compressive strength tests but with slightly faster loading rates (i.e., uniaxial compressive strength test might be run at 0.001mm/s while slow compression for single particle breakage might be 0.1 mm/s). A particle is placed between two surfaces, an axial force is applied, and the particle is loaded until failure. A typical set-up employs a materials testing system to measure the force and displacement (using a load cell and linear voltage displacement transducer).

Slow compression was developed as a method of single particle breakage analysis because it breaks particles in the most efficient manner possible. No more energy than is required to fracture the particle is applied. Bergstrom conducted experiments in which 95% of the applied energy was determined to be strain energy being absorbed by the particle (Bergstrom et al., 1962; Bergstrom and Sollenberger, 1962).

Although some researchers have conducted slow compression SPB tests on cylindrical core specimens, that particle shape is not representative of what is seen in commercial applications, and due to the large loading surface area of a cylinder the induced stress field is not that same as seen under point contact loading. Most research using slow compression has been conducted using spheres or irregularly shaped particles (Hanish and Schubert, 1986; Yashima and et al., 1979; Arbiter et al., 1969). In those cases the particle size ranged from 2.5 mm up to 30 mm.

Data collection is straightforward. The energy required for fracture is determined from load-displacement data collected during testing. The fragmented particle distribution is determined from sieve analysis of the tested particles. For irregular particles it is difficult, if not impossible, to determine the particle strength. For spheres elastic theory can be used to relate the applied load to the stress field induced in the particle.

Slow compression tests have given way to impact tests such as the drop weight, pendulum, and falling media because of a need to achieve higher deformation rates and because breakage devices that supply excess energy are more analogous to commercial applications. A great deal of research has focused on single particle breakage relative to ball mills and grinding mills, thus the development of various impact crushing tests. Despite the misnomer as slow compression machines, jaw crushers apply loads over a time period of between 0.2 to 0.3 seconds (based on typical operating rpm's). The corresponding rate of deformation (dependent also on the stroke) is much faster relative to previous slow compression SPB research, and can more readily be simulated using impact type single particle breakage tests.

Ultrafast load cell

The Ultrafast Load Cell (UFLC) was developed in order to mimic the loading and fracture of particles in a tumbling mill, which occurs within a very short period of time and from a wide range of drop heights (Hofler, 1990). The device was developed at the Comminution Center at the University of Utah (Weichert and Herbst, 1986).

The UFLC has a sampling rate of 2 μs enabling it to pick up data from impacts that typically occur over a period less than 1500 μs. The UFLC uses the propagation of elastic waves to measure the force acting on a particle under impact loading. A drop weight impacts a particle resting on top of a steel rod resulting in compressive strain wave that propagates through the rod (Figure 2.16). Strain gages on the rod are used to

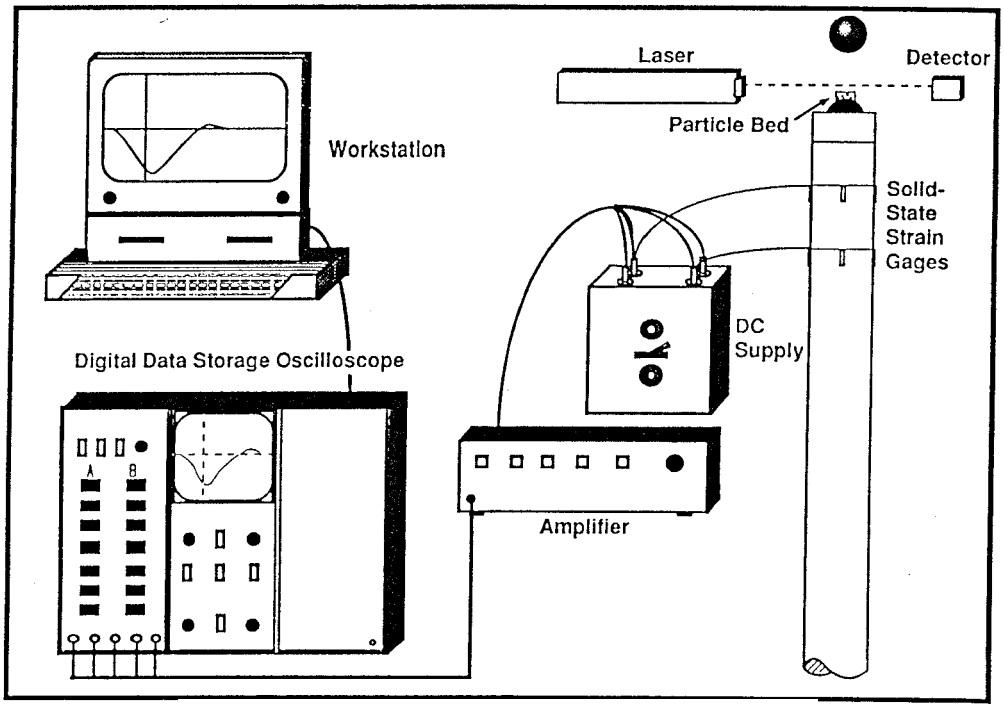

Figure 2.16 Ultrafast load cell configuration
(*From Herbst and Lo, 1992***)**

transmit a signal to a digital oscilloscope. A computer is then used to calculate the force versus time trace.

The energy consumption is determined in the same manner as a slow compression test, by integrating the force-displacement plot. The fragmented particles are collected and sieved in order to determine the progeny size distribution. The particle strength can be determined from the maximum force applied (assuming the particle is essentially a sphere).

The UFLC has been employed successfully in SPB testing. Bourgeois (et al., 1992) broke 100 particles in the 3.35 to 4 mm range in order to determine the mass specific breakage energy, breakage function, and particle strength. But these tests are relevant to ball mill conditions and there has been no application of the UFLC to slower velocity impacts seen in crushers.

Hopkinson pressure bar

The Hopkinson Pressure Bar (HPB) was originally employed to simulate the energy levels commonly encountered in cone crushers (Napier-Munn et al., 1999). The purpose of the HPB is to enable the resolution of the force experienced by a rock as it is dynamically loaded in compression (Briggs and Bearman, 1995). It is also used to measure the energy required to initiate failure in a particle.

The HPB is similar to the UFLC but is aligned horizontally. Figure 2.17 shows the test set-up. A horizontally aligned steel bar with a rock sample attached on its end is

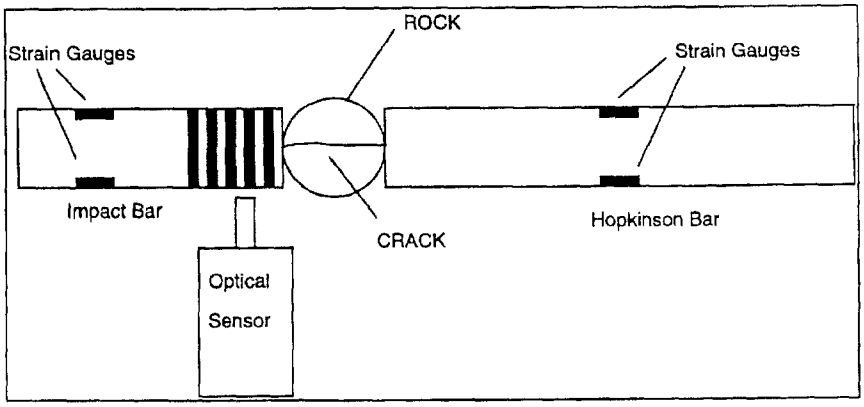

Figure 2.17 Hopkinson pressure bar experimental set-up
(*From Briggs and Bearman, 1995)*

impacted by a smaller bar. A spring mounted on the small bar is compressed to a known distance allowing for control of the impact velocity. An optical sensor is used to measure the speed of the impact bar at the point of impact. As with the UFLC strain gage bridges are used to resolve the force versus time trace.

Since both bars are fitted with strain gages, the lost strain energy can be subtracted from the input energy, allowing for the calculation of actual fracture energy. Additionally the particle strength can be determined from the time at which a sudden drop in force is observed on the force versus time plot. Currently the HPB is used to determine the energy required for breakage and although it has not been used specifically for single particle breakage analysis it may aid in crusher design (Napier-Munn, 1999).

Other investigators have employed HPB type methods. Shockey (et al., 1974) used a "gas gun" to develop an approach for predicting the fragment size distribution in rock resulting from dynamic loads. Santurbano and Fairhurst (1991) employed a similar

device in order to develop a mechanistic explanation of fragmentation by impact. The "rock gun" uses pneumatic air instead of a spring to accelerate a rock particle down a hollow cylinder from which it discharges and impacts a Hopkinson bar. The velocity of the particle is determined using paired photocells and reflectors. The study by Santurbano and Fairhurst considered the energy required for fracture and observations were made about the resultant fracture patterns but no determination of fragment size distribution was made.

Drop weight tests

Drop weight tests are the simplest of the single particle breakage tests. Various types of drop weight devices have been employed due to their simple configuration (Fairs, 1954; Arbiter et al., 1969; Jomoto and Majima, 1972; Jowett and Van Der Waedern, 1982; Pauw and Mare, 1988).

A weight is dropped from a known height onto a particle resting on a hard surface. The kinetic energy is determined from the mass of the drop weight, the height from which it was dropped, and gravity. The potential energy of the weight is transmitted to the particle, and if high enough the particle fractures. By adjusting the drop height and/or the mass of the drop weight the input energy level can be altered. The JKRMC uses combinations of drop height and drop weight mass that represent an energy range of 0.001 to 50 kWh/t. Figure 2.18 depicts the JKRMC drop weight test set-up.

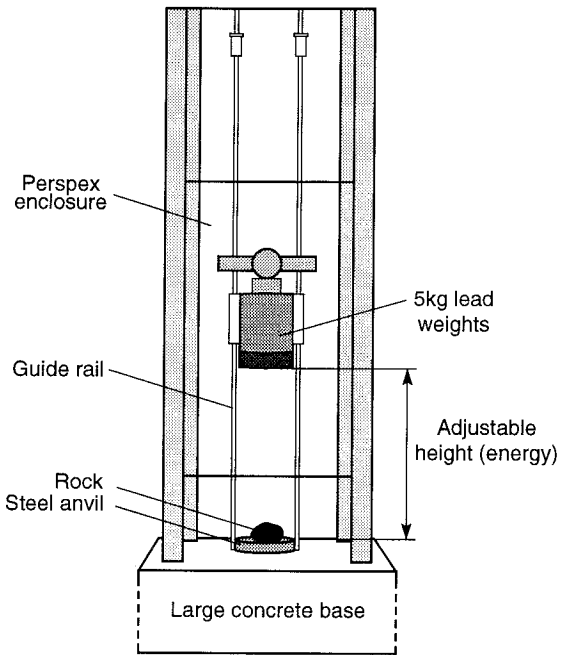

Figure 2.18 JKRMC drop weight test set-up
(*From Napier-Munn, 1999)*

Since the drop weight comes to rest on top of crushed fragments after breakage, the actual applied energy is the initial potential energy of the drop weight minus the potential energy it retains at the offset height. The progeny fragments are retained for determination of cumulative size distribution.

Pendulum tests

Pendulum tests employ twin pendulums. The input pendulum is released from a certain height and impacts a particle attached to the rebound pendulum. Figure 2.19 illustrates a twin pendulum set-up. The specific fracture energy is the calculated by determining the

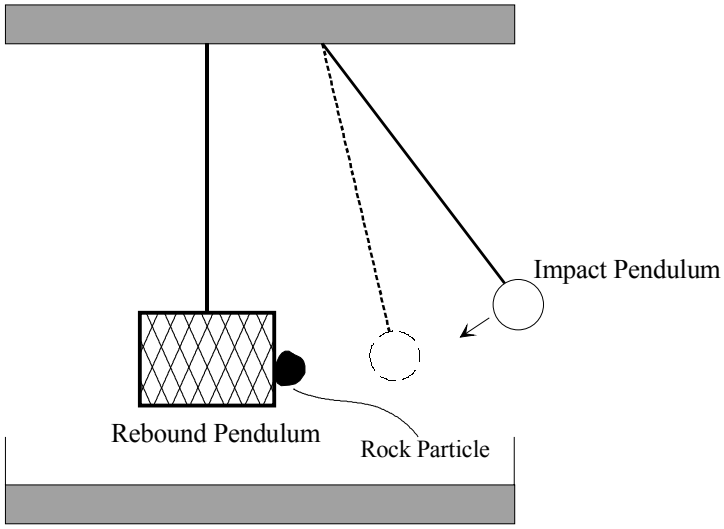

Figure 2.19 Twin pendulum test set-up

difference in the energy of the input pendulum before impact and the energies of the rebound and input pendulum after impact (Narayanan, 1985).

Bond's crushability test for determining the work index is a twin pendulum test (section 2.1.2). Gaudin and Hukki (1946) extended the use of the pendulum test to determine the size distribution of fragmented particles. At the JKRMC two twin pendulum devices were developed in order to determine the energy available for breakage and the resultant size distribution for a wide range of input energy levels (Narayanan, 1985). A twin pendulum device was also developed by Allis-Chalmers, and found to accurately predict rock crushability and crusher product size distribution (Moore, 1982). However, Napier-Munn (et al., 1999) has found that twin pendulum devices are restricted in their energy and particle size range, and that operating the device is time consuming.

2.4.3 DATA COLLECTION

The analysis of single particle breakage is concerned with characterizing the "crushing" characteristics of a material and relating those characteristics to the energy required to

fracture the material. A material's crushing characteristics are measured using some parameter of material strength or resistance to fracture and the fragmented size distribution, which are in turn used to develop energy-based relationships. Schoenert (1991) has recommended that the fracture properties of a material should be characterized in terms of three fundamental properties: particle strength, mass specific breakage energy, and breakage fragment size distribution. Ultimately these characteristic and their inter-relationships can be used, in conjunction with comminution machine parameters, to predict and optimize the performance of size reduction processes. The following discussion focuses on some of the parameters obtained through SPB used to describe the three fundamental fracture properties.

Product size distribution

Fracture of a single particle results in a collection of daughter fragments. A number of SPB tests are conducted on particles of the same material in order to group the fragments together and determine their size distribution. Figure 2.13 showed the distribution of fragments that results from each of the three fracture mechanisms: cleavage, shatter, and abrasion (section 2.2.3). Based on those distributions early researchers attempted to use mathematical expressions to describe size distributions. Gilvarry (1961) derived a Poisson distribution based on the Griffith flaws associated with fracture of a particle. The Gilvarry equation for product size resulting from single particle fracture is:

$$y = 1 - e^{-\left[\left(\frac{x}{k}\right)+\left(\frac{x}{j}\right)^2+\left(\frac{x}{i}\right)^3\right]} \qquad [2.27]$$

where, k is the average spacing of activated edge flaws

j^2 is the average amount of surface containing one activated surface flaw

i^3 is the average volume corresponding to an activated volume flaw.

When surface and volume flaws are ignored the Gilvarry equation reduces to the well-known Rosin-Rammler distribution, and for very small values of particle size, x, it simplifies to the Schumann equation (Gilvarry and Bergstrom, 1962).

Other researchers have proposed similar mathematical expressions. Gaudin and Meloy (1962) derived a size distribution expression for single particle fracture using the binomial distribution. Klimpel and Austin (1965) combined the approaches of Gilvary and Gaudin and Meloy and developed a general expression for product size distribution. Despite the attempts to describe the size distribution of a single particle fracture event on theoretical bounds, none of these models reproduce the size distribution and most researchers now agree that empirically derived functions are adequate (King, 2001).

Empirically derived expressions for product size resulting from SPB are called breakage functions. Kelsall and Reid (1965) used a breakage function that produced a nearly straight line on a log-log scale and that had a distribution modulus near 1. Herbst and Fuersternau (1972) generated a distribution that deviated from a straight line but did find that fine particle sizes were characterized by the Schumann distribution and a distribution modulus of 0.72. Based on these, and similar findings, the breakage function

has been shown to be dependent only on the ratio of the progeny fragment sizes to the initial particle size:

$$B(d_i, d_1) \propto \left(\frac{d_i}{d_1}\right)^n \qquad [2.28]$$

where, B is the breakage function
d_i is the particle size
d_1 is the initial particle size
n is the distribution modulus.

The concept behind the breakage function is that the progeny population is made up of a mixture of separate populations (the populations occurring as a result of cleavage, shatter, and abrasion) and that it is independent of initial particle size. Different values of n account for the larger fragments produced by induced tensile stresses, the smaller fragments produced by compressive stresses directly under the area of loading, and/or the fragments produced by abrasion.

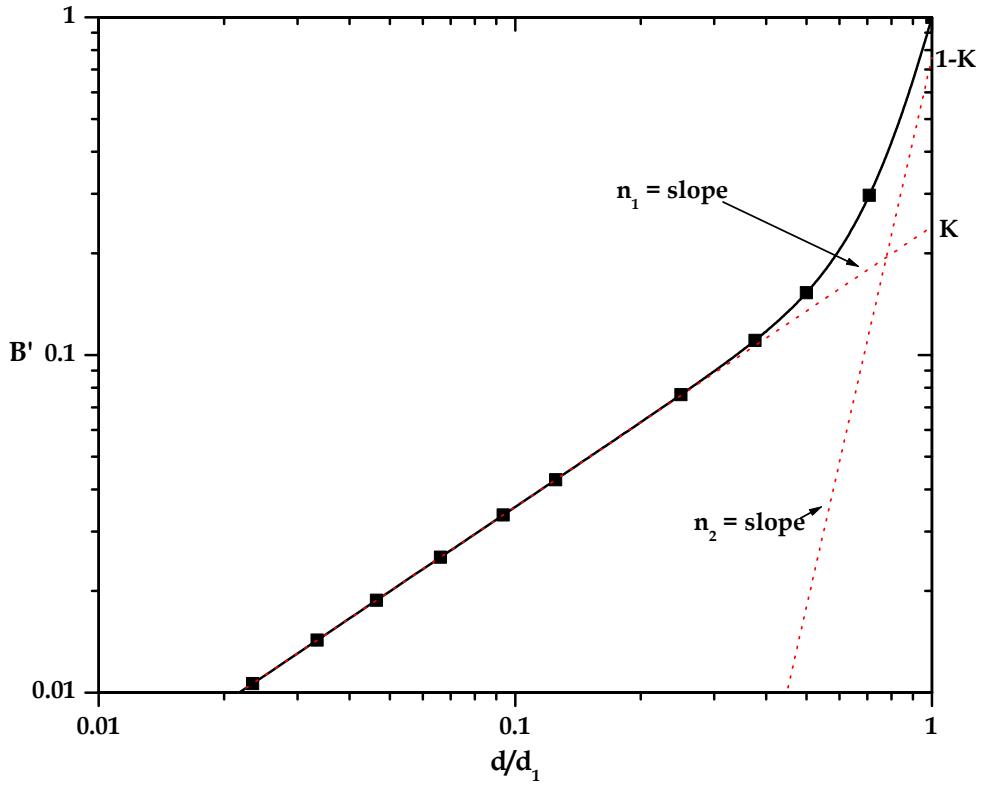

Figure 2.20 A typical breakage function and corresponding parameters

A typical product size distribution resulting from SPB is shown in Figure 2.20. The breakage function modeled to fit the distribution in Figure 2.20 has two components, a fine distribution resulting from localized fracture of the particle against the loading surface and a coarse distribution resulting from main fracture of the particle (Lynch,

1977). For a $\sqrt{2}$ size fraction the breakage function of Figure 2.20 can be fit with the following expression:

$$B(d_i, d_1) = K\left(\frac{d_i}{d_1}\right)^{n_1} + (1-K)\left(\frac{d_i}{d_1}\right)^{n_2} \qquad [2.29]$$

where K is the fraction of progeny fragments that contribute to the finer fraction. Typical measured values of n_1 lie between 0.6 and 1.3 while values of n_2 have been shown to be in the range of 2.5 to 5 (Arbiter et al., 1969; Kelly and Spottiswood, 1990).

If a measured breakage function becomes bimodal, which sometimes occurs with large particles that have a tendency to chip rather than shatter, a third distribution modulus can be used to properly model the breakage function. Additionally, if size distributions are determined for various parent particles of the same material and the breakage functions do not normalize (i.e., show a dependency on initial particle size), then the fraction K must be determined as a function of the parent size.

More recently the JKRMC has developed the one-parameter family of curves method to represent SPB breakage data (Narayanan and Whiten, 1988). The parameter is the percent of progeny particles passing a size one-tenth of the initial original particle size, or t_{10}. t_{10} is employed as a characteristic size reduction parameter and is determined primarily by the energy absorbed during a SPB test. For crushing applications t_{10} is usually in the range of 10% to 20% and for tumbling mills t_{10} ranges between 20% and 50% (Napier-Munn, et a., 1999). Figure 2.21 shows a plot of the one-parameter family of curves for a given material. Each t_n value (% passing 1/n of the original particle size) is

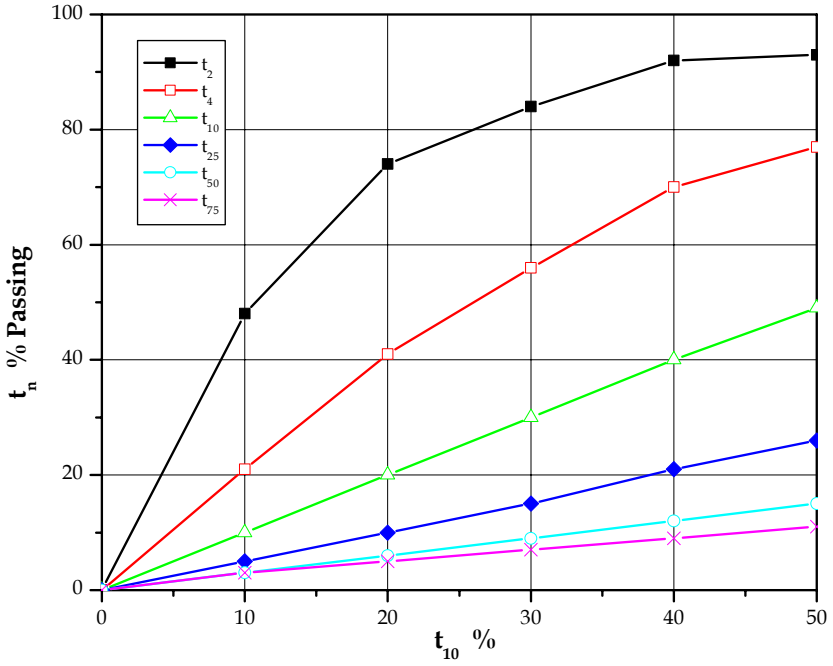

Figure 2.21 One-parameter family of curves
(After Naravanan, 1985)

uniquely related to t_{10}. Each vertical line represents a complete size distribution and if a value of t_{10} is given the full product size distribution can be reconstructed. An alternative to the one-parameter family of curves is to use standard truncated distribution functions (i.e., Rosin-Rammler, logistic, log-normal) that are dependent on t_{10} and one or two other parameters (King, 2001).

Fracture energy

The calculation of fracture energy is dependent upon the method of testing but in each case it is usually determined as a mass specific energy (i.e., kWh/t). There are few "types" of specific energy that should be differentiated. The specific energy required to initiate fracture is called the specific breakage energy. The specific breakage energy is a material property since it represents the energy stored in the particle due to elastic strain, and it represents the minimum amount of energy required to cause fracture. Measurement of the specific breakage energy requires the use of sophisticated devices like the Ultrafast Load Cell. The specific comminution energy is the energy required to produce a certain amount of size reduction or the characteristic size reduction parameter t_{10}. The specific comminution energy is determined in drop weight or pendulum tests where there is no way to discern the time of first fracture. Specific comminution energy is more applicable to actual operating conditions since size reduction machines commonly supply excess amounts of energy.

SPB testing has indicated that the breakage function is related to the specific fracture energy and the specific comminution energy. In general more energy results in a larger portion of daughter fragments in the fine size range. This is particularly true with specific comminution energy since the excessive amount of energy input into breakage is dissipated through secondary fracture. Figure 2.22 illustrates the relationship between specific comminution energy and product size (recalling that larger values of t_{10} indicate a finer size distribution). From Figure 2.22 it can be also be seen that t_{10} can be related to specific comminution energy using the following function:

$$t_{10} = t_{10\max}\left(1 - e^{-bE_c}\right) \qquad [2.30]$$

where, t_{10max} is a material specific limiting value of t_{10}

E_c is the specific comminution energy

b is a material specific parameter.

Mehrim and Khalaf (1980) fit their test results with a similar exponential relationship between size distribution and energy input. They also found that the relationship was linear at lower levels of input energy and deviated from linear at high levels of input energy (similar to what is occurring in Figure 2.23).

Bergrstrom (et al., 1962; 1965) found that the specific energy is inversely proportional to the size modulus of the product distribution and confirmed that the relationship holds for impact crushing and slow compression, as well as for irregularly shaped particles and spheres. Since smaller size moduli describe finer particle distributions this inverse relationship indicates that more applied energy produces smaller

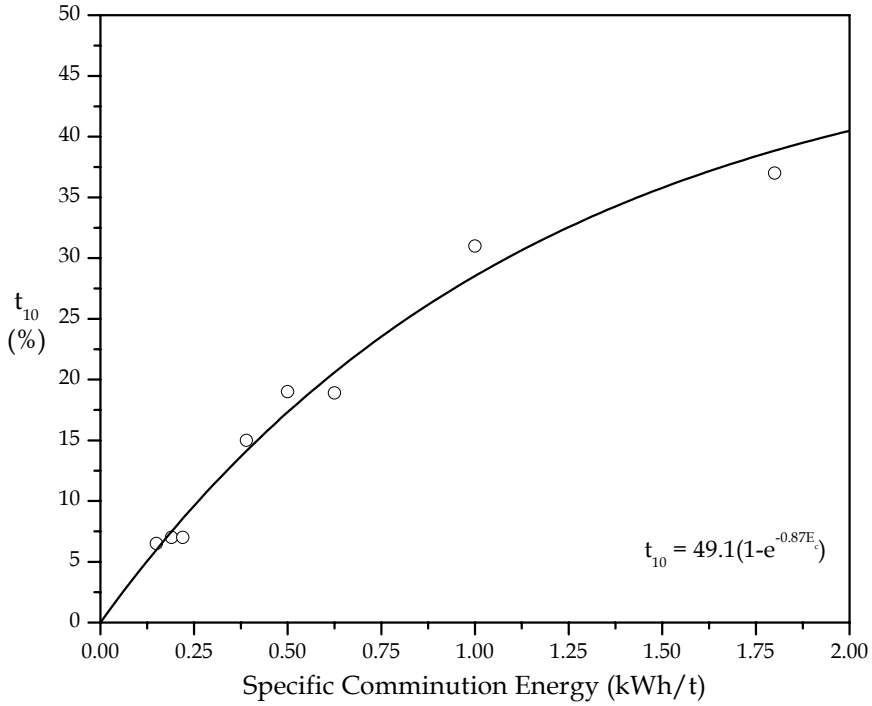

Figure 2.22 Relationship between product size and specific comminution energy (*After Napier-Munn, 1999*)

fragments and also proves, once again, that smaller particles require more energy for fracture than larger ones. Another important aspect of this relationship is that although increased energy results in a finer product size distribution, only the proportion of material in the fine size range is changing (i.e., *K* from Equation 2.29) not the distribution modulus ($n_{1,2}$ remain unchanged). Hanisch and Schubert (1986) confirmed this using slow compression tests, stating that the distribution moduli are essentially not influenced by stress conditions or comminution energy, and that only the mass fractions of the product depend strongly on the comminution energy.

Particle strength

In studies of single particle fracture particles break in tension under compressive loads. This is in agreement with the breakage processes occurring in most comminution machines, particularly crushers. The stress distribution determined by Oka and Majima (1970) (Figure 2.3) for localized compressive loading is essentially the distribution determined by Hondros (1959) for the case of a disk subject to short strip loadings. The maximum tensile strength can easily be determined using these distributions if the applied load is known as well as the specimen dimensions.

For disk specimens the tensile strength can be determined from the following equation:

$$\sigma_t = \frac{2P}{\pi D t} \qquad [2.31]$$

where, P is the compressive load, at failure, applied over a small, localized area
D is the disk diameter
t is the disk thickness.

It is more common in SPB testing to test irregularly sized particles. In this case the tensile stresses cannot be determined from elastic theory. It is assumed that the contact area is a certain fraction of the particle cross-section and that the stress resulting in fracture is simply the compressive force acting on that fractional area. Equation 2.29 is then used to determine particle strength.

$$\sigma_t = \frac{4P}{\pi D^2} \qquad [2.32]$$

where, D is the particle diameter. Hiramatsu and Oka (1966) used photoelastic methods to show that a sphere, prism, and cube all have a similar stress states when subjected to a pair of concentrated compressive forces. They obtained the following expression for the tensile strength of an elastic sphere:

$$\sigma_t = \frac{2.8P}{\pi D_p^{\,2}} \qquad [2.33]$$

In this case D_p is the distance between the loading contacts but in practice it is assumed to be equal to the particle diameter. Jomoto and Majima (1972) and Oka and Majima (1970) have suggested similar equations for determining the tensile strength of irregular particles.

Experimental results indicate that particle strength is related to both energy input and the breakage distribution. Yashima (et al., 1979) found that the reciprocal of the size modulus of the fragmented product size was proportional to the compressive strength of spheres by a power of 1.7 (for slow compression testing). Jomoto and Majima (1972) suggested, based on drop weight tests, that the square of the tensile strength is proportional to energy input and it could be used as a useful criterion under conditions of impact crushing. Shockey (et al., 1974) measured both dynamic tensile strength and fracture toughness of Arkansas novaculite and found that making quantitative predictions of rock fragmentation based on the knowledge of a few determinable rock strength properties is feasible.

2.4.4 CONCLUSIONS

Single particle breakage analysis provides a method for studying the most fundamental process occurring in a size reduction machine. It is a physical representation of the fracture physics associated with the breakage of a particle under loading conditions typically seen in comminution machines. There are a multitude of factors that affect even the breakage of one single particle and they are inter-dependent. The loading condition is dependent on the machine type, which controls the number and direction of contact forces, the deformation velocity, and the stress state of the particle. The stress field

induced in the particle also depends on its shape, the presence and distribution of flaws, its homogeneity, and the particle's stress-strain behavior. An understanding of how to properly represent single particle breakage at the experimental level can be acquired if proper consideration is given to these factors.

Several methods exist for the testing of single particles. Slow compression tests were the first tests to be used and have now given way to tests capable of applying large amounts of energy at high impact velocities (or deformation rates). The Ultrafast Load Cell, Hopkinson Pressure Bar, pendulum tests, and drop weight tests are the most common. The drop weight tests are the most simplistic but do allow for a wide range of input energies to be applied representing basically all comminution applications. The Ultrafast Load Cell has the ability to collect data very rapidly and allows for the differentiation between the energy required to initiate fracture and the total energy input.

The purpose of SPB analysis is to characterize a material's "crushability" and relate it to the energy required to fracture the material. A material's crushability is described using the breakage function, an empirically derived function that expresses the distribution of progeny particles that result form particle fracture. The breakage function is considered to be independent of initial particle size and is a mixture of separate size populations. When its discrete values are put in matrix form it can be used to help predict/optimize the product size emerging from an actual crushing machine. The JKRMC has popularized the use of t_{10}, the characteristic size parameter. For a given t_{10} the one-parameter family of curves can be used to develop the entire breakage function of a material. t_{10} can also be used with standard truncated size distributions in order to develop a full product size distribution.

t_{10} is determined primarily by the energy absorbed during a single particle breakage test, as are the proportions of coarse and fine material. The specific energy is inversely proportional to the size modulus of the product distribution but has no effect on the distribution modulus. Thus for a given material an increase in energy intensity changes only the proportion of fine and coarse fragments in the progeny distribution. An exponential relationship has been suggested for determining the size distribution, or t_{10}, resulting from a certain level of specific comminution energy.

Schoenert has proposed that the fracture properties of a material should be characterized in terms of three fundamental properties: particle strength, mass specific breakage energy, and breakage fragment size distribution. Despite the realization that some measure of a material's resistance to fracture should be intimately related to a particle's behavior in SPB, there have been only minor attempts to include particle strength along with other SPB data. Most of these attempts have focused on the tensile strength since tensile stresses control breakage in comminution processes. Even though there is evidence that the nature of a material is related to the energy required to fracture it and the resultant breakage distribution, it is generally thought that standard rock mechanics tests or properties do not provide useful information for the design and

optimizations of size reduction processes. But the role of standard tests and properties in understanding and optimizing comminution is likely to increase in the future if a link can be made between a material's crushability as described by SPB analysis and its mechanical response to fracture.

The breakage function determined from SPB testing is dependent upon the energy input and the nature of the material broken. Since the energy input of a comminution device is related to the method and rate of load application, the breakage function parameters are most likely dependent upon some operational characteristics (such as closed side set and speed or frequency), as well as the nature of the material broken. A rapid method of establishing the breakage function for a given crushing process and material may be possible if SPB is used to determine the breakage function and the energy input for a certain set of operational settings, and those measures are related to an inherent property that describes a material's resistance to fracture.

2.5 ROCK FRACTURE MECHANICS AND FRACTURE TOUGHNESS

Modifications to Griffith's theory have led to the development of the field of fracture mechanics. Fracture mechanics deals with facture initiation and crack propagation, and provides quantitative methods for characterizing the behavior of an intact material as it fractures due to crack growth. The extension of fracture mechanics to rock is understandable since rock masses contain cracks and discontinuities. States of stress around these flaws cannot be predicted using macroscopic failure criteria (i.e. Mohr-Coulomb, ultimate strength theories). In order to deal with crack propagation, particularly in terms of "intentional" fracturing as in size reduction processes, rock fracture mechanics must be used.

Although fracture mechanics has an undeniable place in rock mechanics applications, it was not developed for geomaterials. It should be recognized that differences exist between fracture mechanics for man-made materials (metals) and rock fracture mechanics, particularly in basic material response and engineering application. Whittaker (et al., 1992) gave a comprehensive list and explanation of these differences, which can be summarized as:

1. *Stress state* – Many rocks structures are subjected to compressive stresses as opposed to tensile stresses. However, in comminution and crushing the induced stress state is tensile (from point-load compression) and thus tensile fracture is seen in rock.
2. *Rock fracture* – Rock materials usually fracture in a brittle or quasi-brittle manner and usually do not exhibit plastic flow.
3. *Fracture process zone (FPZ)* – Non-elastic behavior ahead of a crack tip in rock takes the form of micro-cracking as opposed to excessive shear stresses and the resultant plastic process zone seen in metals. If the size of the FPZ is small then linear elastic fracture mechanics applies.

4. *Crack surface* – Crack surfaces in rock can be non-planar with friction and inter-locking occurring, but linear elastic fracture mechanics assumes that no forces are transmitted across the surface of a smooth planar crack
5. *Crack propagation* – In rocks there is a tendency for crack propagation to "wander" along grain boundaries or planes of weakness. The area of newly created surface is then larger then the assumed fracture area.
6. *Rock fracture mechanics applications* – In rock mechanics, as in (man-made) materials engineering, the prevention of failure by fracture growth is a concern. But the optimizing the generation and propagation of cracks is also a concern as in size reduction processes. Thus the application dictates how material parameters should be determined and used.
7. *Influence of scale* – Due to the complicated geologic nature of rock masses, the characterization of a rock mass is high. For the prevention of crack growth and failure, parameters measured experimentally are of secondary importance but for rock fragmentation applications, experimentally measured properties are of primary importance.
8. *Heterogeneity* – Changes in local structure and strength ahead of a crack tip affects the continuity of crack growth.
9. *Presence of discontinuities* – Pre-existing discontinuities affect the local stress states and crack propagation.
10. *Anisotropy* – Rocks can be anisotropic affecting measured fracture parameters as a function of crack orientation.

Recognition of these variations has led to more practical and developed concepts of fracture mechanics as it applies to rock behavior, with principles of linear elastic fracture mechanics being extended even to rocks that behave non-linearly and much of the focus centering on the measurement of fracture toughness.

The most fundamental aspect of rock fracture mechanics is the establishment of a relationship between rock fracture strength and the geometry of the flaws that result in fracture. Through this relationship an intrinsic material property that describes a materials' resistance to crack propagation can be measured. This property is called fracture toughness. The application of fracture toughness in size reduction processes is clear. Fracture toughness represents a critical level above which crack extension and fracture occurs. When individual rock particles are subjected to the applied forces of size reduction, it is most likely that the intrinsic tensile property measured as the fracture toughness will control breakage (Bearman, 1998). Since the amount of energy input into a size reduction process and the amount of size reduction achieved (i.e., the fractured size distribution) are related to the type of loading and the crack pattern in the material, there should be a relationship between these parameters and fracture toughness.

2.5.1 LINEAR ELASTIC FRACTURE MECHANICS

In section 2.2.2 Equation 2.20 was presented as a size independent expression characterizing the resistance of a material to fracture based on the stresses required for

breakage and the presence of flaws. It showed that fracture initiation in a brittle solid is controlled by the product of a far-applied stress and the square root of the flaw length which reaches a critical value determined by the characteristic material properties E, ν, and γ_s. This critical value is called the critical stress intensity factor and is denoted K_c.

Irwin (1957) used a stress intensity approach to relate the critical strain energy release rate G_c to the critical stress intensity factor K_c. Rather than follow Griffith's global approach, Irwin considered the crack tip region, which is small compared to the rest of the body (or plate, in reference to section 2.2) but large enough with respect to atomic dimensions such that linear elastic theory applies (Knott, 1972). Irwin determined the work required to close up a small portion of a crack by superimposing tensile forces along the crack surfaces and hypothesized that this work is equal to the energy released when the crack extends. Thus the work required to close a unit length of the crack is the strain energy release rate and, based on the stresses and displacements occurring as a result of the tensile forces, is equal to:

$$G = \frac{\left(1-\nu^2\right)K^2}{E} \qquad [2.34]$$

Since crack propagation occurs when G reaches a critical value, the critical value of stress intensity can be defined as:

$$K_c = \sqrt{\frac{G_c E}{\left(1-\nu^2\right)}} \qquad [2.35]$$

By demonstrating the equivalence of K and G, Irwin provided the basis for the development of Linear Elastic Fracture Mechanics (LEFM). In LEFM the crack tip stresses, strains, and displacements can be characterized by K as long as inelastic yielding ahead of the crack tip is small. The advantage of LEFM is that it provides a universal approach for determining a material's resistance to fracture, as defined by K_c. As long as an explicit function for the stress intensity near a crack tip is known for a given crack geometry and loading configuration, K_c can be measured experimentally.

2.5.2 Stress Intensity Factor

The stress intensity factor K, alluded to in the previous section, characterizes the severity of the crack condition as affected by crack dimension, stress, and geometry (Dowling, 1999). Determining K is based on a linear-elastic approach (hence LEFM), which assumes the material in which the crack is located is isotropic and behaves according to Hooke's Law.

Different loading configurations at a crack tip lead to different modes of crack tip displacement. The different types of crack deformation are generalized using three basic modes (Figure 2.23). Mode I is the opening mode due to tension, where the crack surfaces move directly apart; Mode II is the sliding mode due to shearing, where the crack surfaces move over one another in a direction perpendicular to the crack front;

Mode III is the tearing mode also due to shearing, where the crack surfaces sliding over one another but in a direction parallel to the crack front. The three basic modes can also

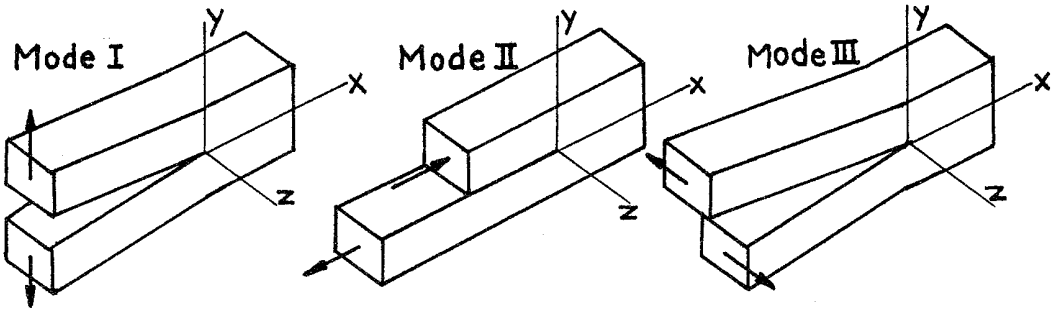

Figure 2.23 The three basic modes of crack surface displacement
(*After Tada et al., 2000*)

occur in combination as "mixed-mode" loading with the superposition of the modes sufficient to describe most general three-dimensional cases of local crack tip stress and deformation fields (Tada et al., 2000). Mode I is the most commonly encountered mode in engineering applications and is also the easiest to analyze, produce experimentally on laboratory specimens, and apply (Schmidt and Rossmanith, 1983).

Using theory of elasticity, namely the stress analysis methods of Muskhelishvili (1963) and Westergaard (1939), the crack tip stress and displacement fields (and hence *K*) for each mode of loading can be determined (for a complete derivation see Pook, 2000). With Figure 2.24 representing the coordinate system measured from the leading edge of a crack, the Mode I stress components are given according to the following equations:

$$\sigma_x = \frac{K_I}{\sqrt{2\pi r}}\cos\frac{\theta}{2}\left[1-\sin\frac{\theta}{2}\sin\frac{3\theta}{2}\right]$$

$$\sigma_y = \frac{K_I}{\sqrt{2\pi r}}\cos\frac{\theta}{2}\left[1+\sin\frac{\theta}{2}\sin\frac{3\theta}{2}\right]$$

$$\tau_{xy} = \frac{K_I}{\sqrt{2\pi r}}\cos\frac{\theta}{2}\left[\sin\frac{\theta}{2}\cos\frac{3\theta}{2}\right] \qquad [2.36]$$

$$\sigma_z = \nu\left(\sigma_x + \sigma_y\right), \text{ for plane strain}$$

$$\sigma_z = 0, \text{ for plane stress}$$

$$\tau_{xz} = \tau_{yz} = 0$$

where K_I is the stress intensity factor for Mode I. The displacements at the crack tip can be found by substituting Equations of 2.36 into Hooke's Law.

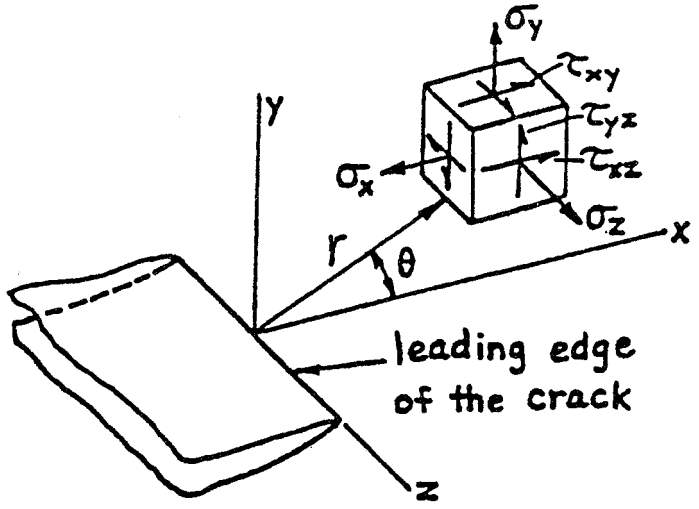

Figure 2.24 Coordinate system for a crack tip
(*After Tada et al., 2000*)

It can be seen from Equations 2.36 that at the crack tip (as r approaches zero) the stresses approach infinity, as has already been indicated by Inglis' solution for stresses around an elliptical hole in a stressed plate (section 2.2.1). Since no value of stress at the crack tip can be given, and all non-zero stresses of Equation 2.36 are proportional to K_I, with the remaining factors varying only with r and θ, the stress field near the crack tip can be determined by giving the value of K_I, which has a formal definition of (Dowling, 1999; Pook, 2000):

$$K_I = \lim_{r,\theta \to 0} \sigma_y \sqrt{2\pi r} \qquad [2.37]$$

It was noted earlier that K_I is affected by the crack size, stress, and geometry. In order to account for different geometries Equation 2.37 can be rewritten as:

$$K_I = F\sigma\sqrt{2\pi a} \qquad [2.38]$$

where, F is a dimensionless constant dependent on the geometric configuration
σ is the stress averaged over the gross area
a is the half-crack length.

F can generally be described as a function of loading geometry and a/w where w is defined as the maximum possible crack length. When F is determined for a given geometry the critical value of stress intensity, or fracture toughness, can be determined as long as inelastic yielding ahead of the crack tip is small and the conditions for LEFM are met. Equations and values of F for a wide range of crack, specimen, and loading geometries are determined using analytical, numerical, and experimental methods and have been compiled in various handbooks (see Tada et al., 2000; Murakami, 1987; Rooke and Cartwright, 1976; Sih, 1973).

2.5.3 MODE I FRACTURE TOUGHNESS TESTING

The critical value of stress intensity factor, K_{Ic}, is determined by testing a prepared specimen that has a crack in it. There are no standardized test methods for the measurement of Mode I rock fracture toughness. The earliest applications of rock fracture roughness testing employed the ASTM standard method (ASTM-E399) for metals. Although ASTM-E399 seemed to be effective for rock testing, the general consensus for rock testing has become that an ideal method would yield a representative fracture toughness value and yet be simple, requiring neither pre-cracking, nor crack length and displacement measurements, nor sophisticated evaluation techniques (Ouchterlony, 1989). In reference to these requirements ASTM-E399 is cumbersome, and most testing methods for rock now employ core-based specimens. The International Society of Rock Mechanics (ISRM) has suggested two methods be established as standardized tests in order to obtain accurate, compatible, and reproducible K_{Ic} values for rocks (ISRM, 1988).

Before covering the actual test methods used to determine fracture toughness, consideration needs to be given to some factors that influence the applicability of measured values and the testing procedures.

Fracture process zone

The application of linear elasticity has been shown to be valid even in cases of plastic yielding ahead of the crack tip, as long as the amount of yielding is small relative to the geometry of the crack and other characteristic dimensions (specimen thickness, length). When the non-elastic field is large and dominates the crack behavior before failure, then LEFM is not applicable and other methods of fracture analysis must be employed. Based on the size of the non-elastic field, specimen and crack size requirements have been developed to ensure that measured values of fracture toughness are not underestimated (as is the case when LEFM is applied to non-linear conditions).

The fracture process zone (FPZ) in rocks is the region ahead of the crack tip that experiences non-linear behavior. The FPZ is formed by the initiation and propagation of micro-cracks in the vicinity of the crack tip (Figure 2.25). Models used to determine the size and shape of the FPZ are based on the models used to describe the plastic zone in metals. Schmidt (1980) used a maximum normal stress criterion to describe the shape of the FPZ and found that the size of the FPZ can be given as:

$$r(\theta) = \frac{1}{2\pi}\left(\frac{K_I}{\sigma_t}\right)^2 \cos^2\frac{\theta}{2}\left(1+\left|\sin\frac{\theta}{2}\right|\right)^2 \qquad [2.39]$$

where, σ_t is the tensile strength of the rock material.

r, θ are defined by the coordinate system in Figure 2.26.

An illustration of the FPZ is shown in Figure 2.26. The characteristic size of the FPZ is defined when θ is equal to zero and is identical to the plastic zone in metals under plane stress conditions. The maximum size of the FPZ is defined when θ is equal to 60°.

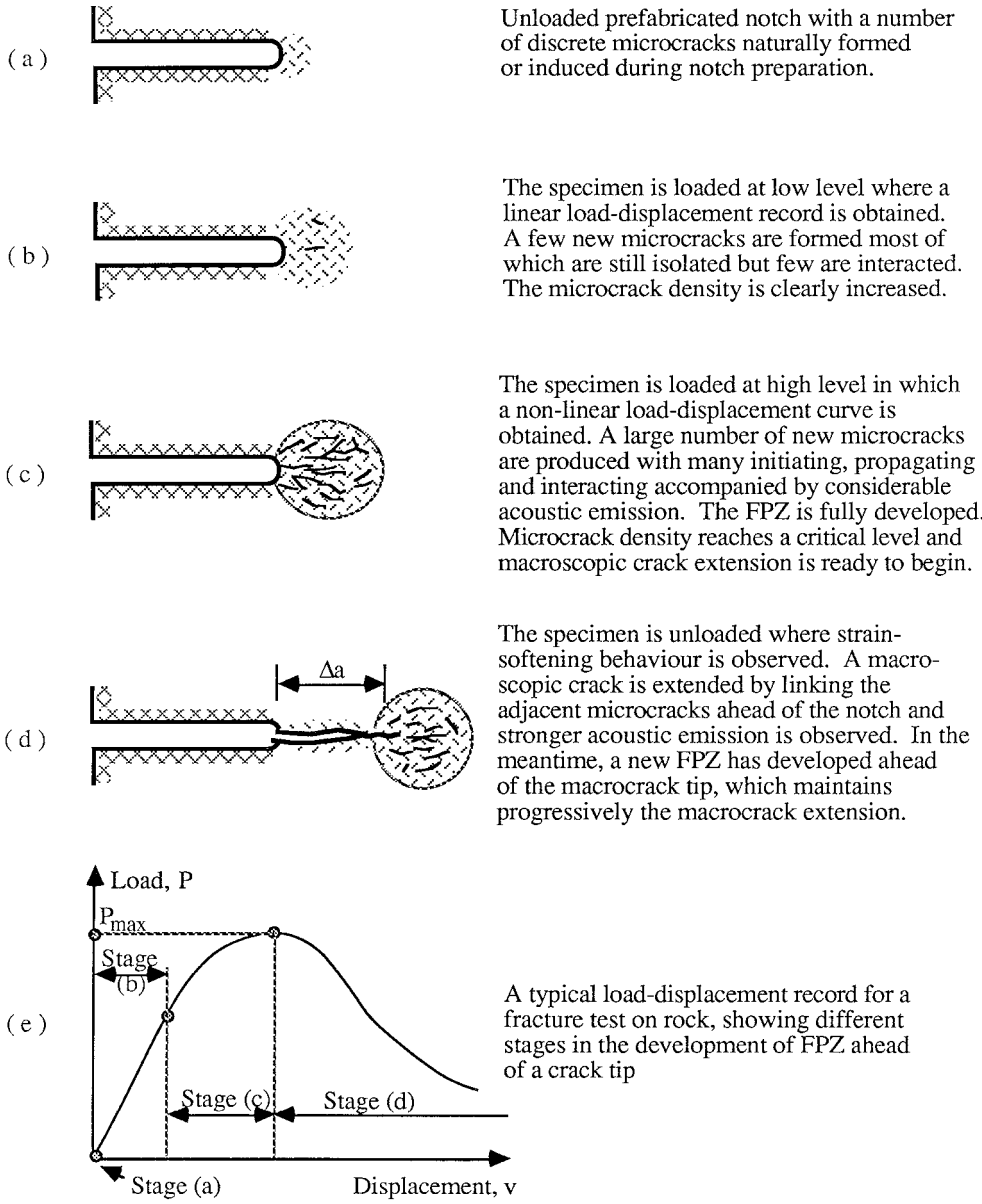

Figure 2.25 Development of the FPZ
(*After Hoagland et al., 1973 and Whittaker et al., 1992*)

Based on the previous analysis the size and shape of the fracture process zone is independent of either plane stress or plane strain conditions. Nolen-Hoeksema and Gordon (1987) proved this experimentally using dolomite, showing that the FPZ is the same for a crack on a free surface (plane stress) and for a crack located within the rock (plane strain). In comparison to the plastic zone of metals, the FPZ, and fracture toughness accordingly, is not affected by specimen thickness (but it cannot be subjectively small). It is however dependent upon the crack length and ligament width (uncracked length). Lim (et al., 1994) compiled a list of minimum crack lengths required

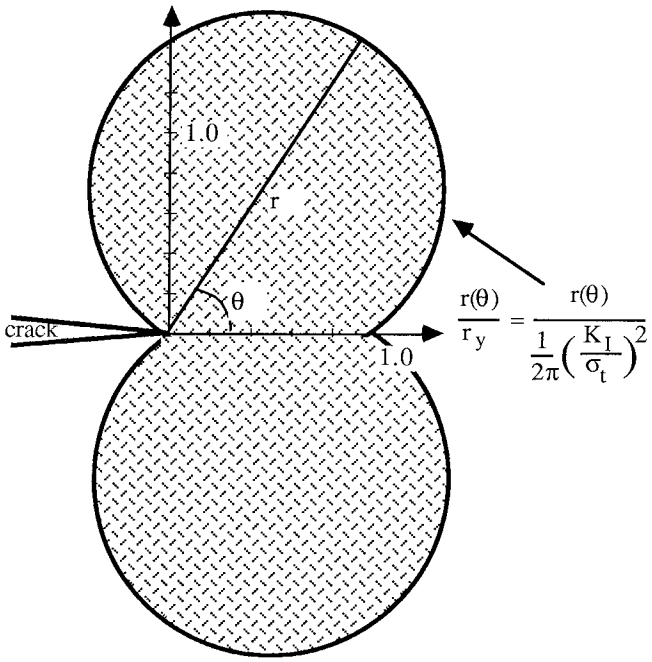

Figure 2.26 Size and shape of the FPZ
(*After Schmidt, 1980*)

for valid fracture toughness testing of different rocks, citing that minimum crack length depends on both material type and testing technique. However it is generally accepted that Equation 2.39 along with aspects from the plastic zone of metals can be used to define the specimen dimensions required to give representative fracture toughness values (Schmidt, 1980; Barton, 1983). The requirements are:

$$\left.\begin{matrix} a \\ w-a \end{matrix}\right\} \geq 2.5\left(\frac{K_{Ic}}{\sigma_t}\right)^2$$
$$t \geq \frac{27}{32\pi}\left(\frac{K_{Ic}}{\sigma_t}\right)^2 \qquad [2.40]$$

where, w-a is the uncracked length
t is the specimen thickness.

The requirements of Equation 2.40 are conservative, and other factors have been proposed, but in general if the requirements given are not met the measured fracture toughness value (i.e., the apparent fracture toughness) is considered invalid, or outside the bounds of LEFM.

Micro-cracking ahead of the crack tip, and subsequent FPZ development, is influenced by the microstructure or grain size of the rock. Minimum ratios of the smallest specimen dimension to the grain size have been suggested in order to make certain representative values of K_{Ic} are measured. A minimum ratio of 10:1 is

recommended by the ISRM for the two suggested standard methods of testing (ISRM, 1988).

Crack requirements

In order to determine fracture toughness a specimen needs to be "cracked". The crack should be representative of a natural crack, one that is sharp and free from the effects of residual stresses, specimen boundaries, and pre-fabricated notches (Whittaker et al., 1992). In metals, specimens are usually pre-cracked by fatigue in order to obtain a naturally sharp crack. In rocks fatigue pre-cracking is difficult since the loads required to produce fatigue crack growth are usually too high (they approach catastrophic failure levels) and care is required in order to prevent further propagation of the pre-crack after it has been initiated.

Other methods are required to pre-crack rock materials, the simplest being to notch the rock with a thin saw-cut. Despite the ease of notching there is evidence that notched specimens tend to underestimate fracture toughness. Sun and Ouchterlony (1986) showed that apparent fracture toughness values measured using notched specimens are invariably lower than those measured from pre-cracked specimens (for the same rock type), concluding that the use of notch length in the calculation of K_{Ic} ignores micro-crack growth prior to crack extension. Fenghui (2000) has proposed a model, based on the size of the FPZ and notch radius, that can be used to determine the fracture toughness based on the measured fracture toughness of a notched specimen as long as the notch radius is not greater than the average grain size of the rock.

The most widely accepted method of pre-cracking rocks employs a chevron-notch. The chevron-notch is a V-shaped notch that allows the length of the crack front to increase as the crack propagates. Further propagation of the crack requires an increase in the load, which is the condition of stable propagation, and inherent monotonic pre-cracking is produced during testing (Sun and Ouchterlony, 1986). A sharp natural crack is automatically formed and the resistance to propagation becomes fully developed after initial crack growth. But the chevron-notch is not particularly easy to produce in comparison to standard or straight-through saw-cut notches, and the decision to use one or the other is based on the "level" of testing required.

Testing level

The ISRM (1988) has defined two testing levels in order to let researchers decide what combination of screening and accuracy is best for the given application of the measured fracture toughness values. Level I testing can be performed using portable equipment and requires only the registration of maximum load. The associated value of fracture toughness has the nature of an index property more so than of a material property. Level I testing is more appropriate for screening purposes or for the rapid estimation and comparison of fracture toughness values.

Level II testing requires load and displacement measurements, and thus is laboratory based and intrinsically more complicated to perform. It is recommended for the determination of accurate, compatible, and reproducible fracture toughness values.

Loading rate

Various loading rates have been prescribed for rock fracture testing, ranging from 0.01 to $0.03\ MPa\sqrt{m}/s$ (Barton, 1983). For the ISRM recommended tests, the loading rate is not supposed to be greater than $0.25\ MPa\sqrt{m}/s$ or such that failure occurs within 10 seconds (ISRM, 1988). Although rock strength properties exhibit loading rate dependency, there is no consensus on whether or not K_{Ic} is affected by an increase in loading rate. Based on the FPZ it is logical to expect that *dynamic* loading will result in underestimated values of fracture toughness since fracture will occur before the FPZ is fully developed. But by testing in accordance with the recommendations of the ISRM it has been shown that loading rate has a negligible effect on measured fracture toughness (Khan and Al-Shayea, 2000).

Calculating fracture toughness

A material's resistance to crack propagation can be quantified using fracture toughness, K_{Ic}, the critical stress intensity factor. When the stress intensity factor, K_I, in the region of a crack tip exceeds K_{Ic}, fracture initiates and propagates until the stress intensity factor decreases below K_{Ic}. From Equation 2.38, fracture toughness is related to the applied stress and crack length, and the function F, which is a dimensionless function dependent on the crack and specimen geometry, and the loading configuration. When working with applied loads and planar geometries, as is this case in rock testing, the critical stress intensity factor is determined from the critical applied load, P_Q, and the corresponding crack length at failure, a_c. The measured fracture toughness value is termed the apparent fracture toughness, K_Q. After K_Q has been measured it is checked against the specimen size requirements of Equation 2.40 in order to verify its validity.

There are various methods for the determination of P_Q and a_c, and they are dependent upon the test method and the test results (for a comprehensive review see Whittaker et al., 1992). For example, with notched specimens the critical crack length at failure is equal to the original notch length and the critical applied load is equal to the maximum load applied. Frequently some type of load-displacement curve is used to determine P_Q and a_c. These load-displacement curves are usually in the form of applied load, P, versus either Load Point Displacement (LPD) or, if possible, P versus Crack Mouth Opening Displacement (CMOD). Again various methods can be employed using P vs. LPD/CMOD curves (i.e., 5% Secant Approach, Compliance Calibration). An additional function of P vs. LPD/CMOD curves is that they can be used to observe and even account for non-linear behavior at the crack tip, allowing for the extension of LEFM analysis to rocks that exhibit some non-elasticity.

After a series of K_Q measurements have been validated using Equation 2.40, K_{Ic} can be determined by extrapolating the K_Q versus crack length curve until K_Q becomes a constant. Since K_{Ic} is independent of specimen dimensions it is a limiting value of K_Q (which has been shown to increase with crack length).

Test methods

As mentioned previously there are two test methods suggested by the International Society for Rock Mechanics for the determination of rock fracture toughness. They are the Chevron Edge Notched Round Bar in Bending (CB) and the Chevron Notched Short Rod (SR). The motivation for developing the suggested methods was to provide testing methods that consistently yield accurate and precise K_{Ic} values (ISRM, 1988). Each method is also core based, the only viable specimen alternative as rock is often available in the form of core pieces (Ouchterlony and Sun, 1983).

Another commonly employed test method is the Semi-Circular Bend (SCB) test. The SCB can be prepared from rock cores and is especially adaptable to small, compact samples that require duplicate samples to test parameters that may affect K_{Ic} such as loading rate, specimen thickness, and crack length (Karfakis et al., 1986; Chong, 1980). Despite the suggested standard methods of the ISRM and the popularity of the SCB, various other methods, each with its own advantages, are still used to determine rock fracture toughness. Whittaker (et al., 1992) provides an exhaustive review of these alternative methods.

Chevron edge notched round bar in bending

Figure 2.27 shows the specimen configuration and test set-up for the CB test. The CB test employs a bend specimen test with a chevron-notch cut perpendicular to the core axis (Ouchterlony, 1980). The specimen rests on roller supports and a compressive load is applied causing crack growth and transverse splitting of the specimen. For a complete review and background of the test see Sun and Ouchterlony (1986), ISRM (1988), Ouchterlony (1989), Ouchterlony (1989a), and Whittaker (et al., 1992).

The core based specimen, chevron-notch, stable crack growth, ability to account for non-linearity, and multiple testing levels (Level I and II) are the main advantages of the CB test. However, as can be seen from Figure 2.27 the specimen geometry and loading configuration are not simple. And despite the advantage of the chevron-notch it is still a rather difficult pre-crack to machine. Furthermore, the advantages of the CB test seem only to be significant in terms of Level II testing. If Level I testing is sufficient then other more straightforward techniques are available for the rapid estimation of fracture toughness.

Chevron Notched Short Rod

Figure 2.28 shows the configuration and test set-up for the SR test. The SR test specimen has a chevron-notch that is cut parallel to the core axis. A tensile load is applied at the notch mouth causing crack growth and lengthwise splitting of the specimen. For a

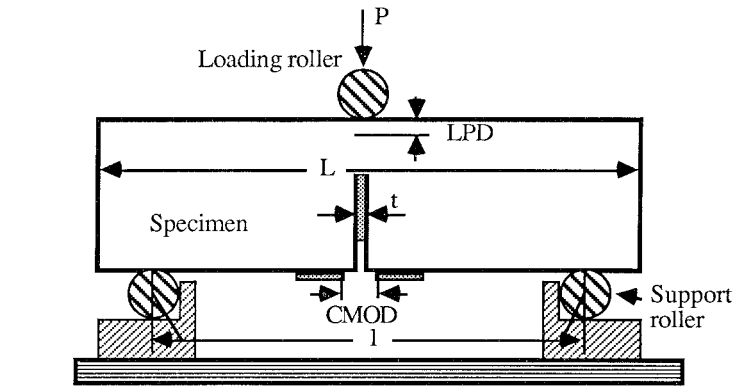

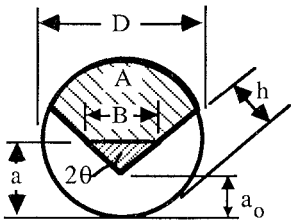

Notations:
A = Ligament area
D = Specimen diameter
l = Loading span, 3.33D
a = Crack length
a_o = Chevron tip distance from specimen surface, 0.15D
h = Depth of cut in notch flank
B = Crack front width
t = Notch width
L = Specimen length
P = Applied load
2θ = Chevron angle, 90°

Figure 2.27 The CB specimen and testing configuration
(*After ISRM, 1980 and Whittaker et al., 1992*)

complete background review and detailed analysis see Barker (1977), Bubsey (et al., 1982), Sun and Ouchterlony (1986), ISRM (1988), Ouchterlony (1989), Ouchterlony (1989a), and Whittaker (et al., 1992).

The advantages of the SR test are the same as those for the CB test. The SR method also uses a smaller sized specimen and according to the ISRM, two SR specimens can be obtained from one fractured CB test (since the length to diameter requirement of the CB test is 4:1 and for the SR it is 1.45:1). This saves material and allows for the measurement of fracture toughness using two crack orientations. Again, the disadvantages of the SR are that the specimen, notably the chevron-notch, is difficult to reproduce consistently and that for Level I type testing it is too complex.

Semi-Circular Bend

Figure 2.29 depicts the specimen geometry and loading configuration of the SCB test. The SCB test was developed and proposed by Chong and Kuruppu (1984) in order to provide a test method that was simple to fabricate and load. The pre-crack can be a saw-cut notch that is fatigued loaded in order to produce a natural crack, a chevron-notch, or a very thin saw-cut notch. The kinematics of the test are similar to that of the CB test since a vertical compressive load produces three-point bending and transverse splitting of the

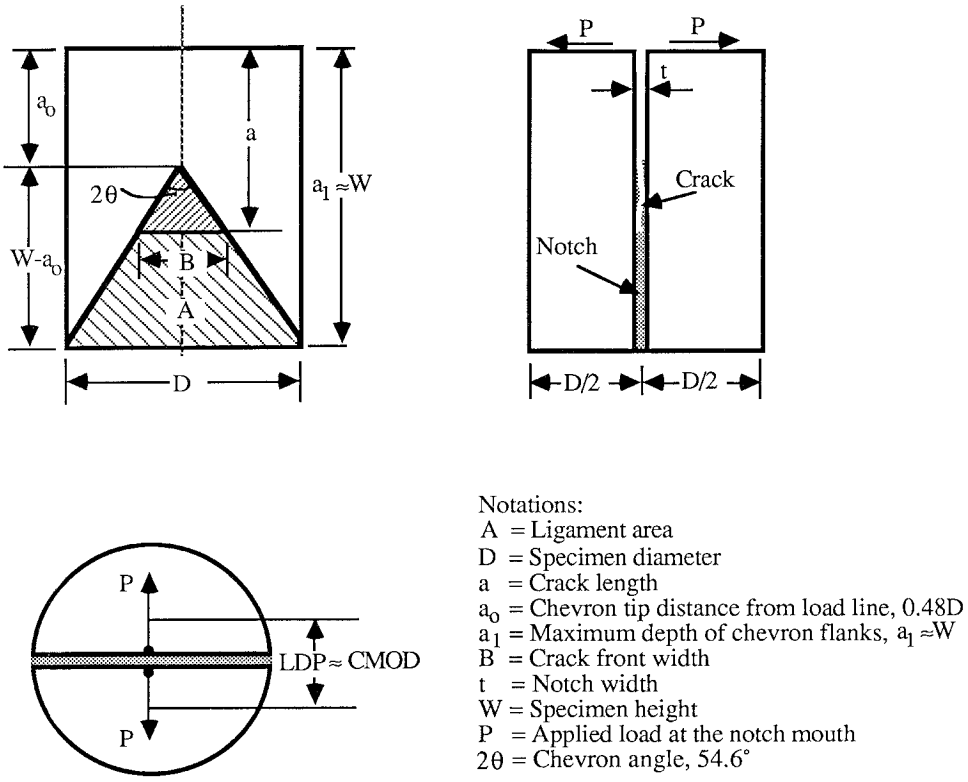

Notations:
A = Ligament area
D = Specimen diameter
a = Crack length
a_o = Chevron tip distance from load line, 0.48D
a_1 = Maximum depth of chevron flanks, $a_1 \approx W$
B = Crack front width
t = Notch width
W = Specimen height
P = Applied load at the notch mouth
2θ = Chevron angle, 54.6°

Figure 2.28 The SR specimen and test configuration
(*After ISRM, 1988 and Whittaker, et al., 1992*)

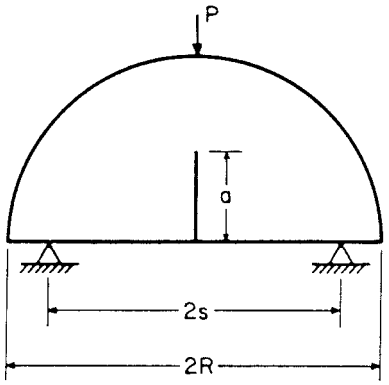

Figure 2.29 The SCB specimen and test configuration
(*After Karfakis et al., 1986*)

specimen (Akram, 1991). A detailed description of the test is given by Chong and Kuruppu (1984), Karfakis et al., 1986, Chong (et al., 1987), and Whittaker (et al., 1982).

Testing of the SCB specimen is simple and does not require sophisticated equipment, and a large number of samples can be tested rapidly and accurately. But the test is

difficult to perform on standard NX core specimens (approximately 50 mm in diameter) and larger diameter specimens are usually required in order to obtain stable loading and crack growth.

2.5.4 APPLICATIONS OF ROCK FRACTURE TOUGHNESS

Because of the complicated nature of rocks and rock formations, the application of fracture mechanics to rock fragmentation has not been straightforward. But recently (within the last 25 years) there has been an effort to employ aspects of fracture mechanics, particularly fracture toughness, to various types of rock breakage analyses. This work has been able to correlate fracture toughness, the intrinsic material property expressing a material's resistance to crack propagation, with various rock fragmentation processes such as blasting, tunnel boring and rock cutting.

The process of rock cutting involves forcing a cutting tool into rock in order to "break out" fragments from the surface. Since cutting is achieved by a fracture process it is logical to expect that differences in cuttability of various rocks is related to the variation of fracture material properties among the rocks (Nelson and Fong, 1986). Deliac (1986) analyzed the chip formation due to drag picks and found that for sharp, rigid picks operating in brittle rocks the cutting force can be expressed as a function of the fracture toughness of the rock and the cutting depth. Guo (1990) related the fracture toughness to the penetration rate of a diamond-coring machine and found that rocks with higher fracture toughness are harder to penetrate resulting in lower penetration rates. Ingraffea (ey al., 1982) has proposed using the fracture toughness of different rocks encountered during three tunnel boring projects to predict the performance of the TBM's (Tunnel Boring Machines). Preliminary testing showed that fracture toughness, in general, showed less variability than other material properties (uniaxial strength, tensile strength, and point load strength) and that fracture toughness appears to be an ideal measure to relate to TBM performance. It has been shown that the critical energy release rate, G, is related linearly to the penetration rates of TBM's. Since G is related to fracture toughness by Poisson's ratio and the modulus of elasticity, it follows that the penetration rate could also be predicted by fracture toughness (Clark, 1987).

The connection of fracture toughness to some common fragmentation processes indicates that fracture toughness could also be correlated to crushing processes. Bearman (et al., 1991) correlated various rock strength parameters to power consumption of a laboratory cone crusher with a statistical significance of 99.9% and fracture toughness was among those parameters. The same study also showed that fracture toughness could be related to product size with a significance of 95% and that K_{Ic} also could be correlated with energy-size relationships derived from single particle breakage tests. The same correlations and level of confidence should hold true for laboratory scale primary crushing equipment (jaw and gyratory crushers) and optimistically for actual, large-scale industrial crushers employed at processing plants.

2.5.5 CONCLUSIONS

Irwin's modifications to Griffith's theory, and his demonstration that the strain energy release rate is related to the stress intensity factor, led to the development of the field of fracture mechanics. Fracture mechanics provides quantitative methods for characterizing the behavior of an intact material as it fractures due to crack growth. Although fracture mechanics was developed for metallic or man-made materials its extension into rock mechanics is natural due to the presence of inherent flaws and discontinuities within geologic materials. These flaws control the fracture of rocks, and establishing a relationship between flaw geometry and fracture strength is the most fundamental aspect of fracture mechanics.

Irwin's work provided the basis for Linear Elastic Fracture Mechanics. In LEFM the crack tip stresses and displacements can be characterized by the stress intensity factor K as long as plastic, or non-linear, deformation ahead of the crack tip is small. The stress intensity factor characterizes the magnitude of the stresses near a crack tip in a linear-elastic, homogeneous, and isotropic material. LEFM provides a universal approach for determining a material's resistance to fracture since crack propagation occurs when K reaches a critical value.

There are three general modes of crack tip displacement that are used to describe most cases of local crack tip stress and deformation fields. Mode I is the opening mode and it is the dominant mode in rock fragmentation. Using theory of elasticity a general form of the Mode I stress intensity factor has been determined and shown to be a function of the applied stress, the crack length, and a dimensionless constant, which itself is a function of loading and specimen geometry. In order to determine fracture toughness an explicit function that describes the stress intensity near a crack tip for a given crack geometry and loading configuration needs to be known. Once this function is defined the fracture toughness can be determined experimentally based on the loading condition, crack geometry, and specimen configuration.

Fracture toughness testing of rock specimens is influenced by the development of a fracture process zone (FPZ) ahead of the crack tip. The FPZ is formed by the initiation and propagation of micro-cracks near the crack tip. The FPZ is similar to the plastic zone that forms ahead of a crack tip in metals, and likewise is used to define specimen dimension requirements, ensuring that the amount of non-elastic behavior ahead of the crack tip is small enough so that LEFM remains applicable. Fracture toughness testing of rock can also be influenced by the microstructure/grain size of the rock, the type of crack used, the testing "level", and the loading rate.

There are currently no standardized test methods for the determination of Mode I rock fracture toughness. The main requirements of any test method are that it be core based, require simple specimen preparation, be easy to load, have a straightforward fracture toughness calculation, and yield representative and reproducible values. The ISRM has

suggested two methods for standardization, the Chevron Edge Notched Round Bar in Bending (CB) and the Chevron Notched Short Rod (SR). The Semi-Circular Bend (SCB) test is also commonly employed. Each of these tests has its advantages yet none are used exclusively. The CB and SR specimens require a chevron-notch, which is difficult to reproduce consistently, and the SCB test is difficult to apply to standard NX size rock cores.

Rock fracture toughness has found wide application in processes of rock fragmentation. Researchers have been able to correlate fracture toughness with the penetration rates of tunnel boring machines and rock cutters. In the field of comminution fracture toughness has been related to the power consumption and product size distribution of a cone crusher. Based on these results it is expected that fracture toughness can be related to the power consumption, product size, and capacity of jaw crushers. When individual rock particles are subjected to the applied forces of size reduction the amount of energy input and the amount of size reduction achieved are related to the type of loading and the crack pattern in the material. Fracture toughness measures a material's resistance to fracture based on the applied load and flaw geometry within the rock, thus the same characteristics that control the operating parameters of jaw crushers also control an intrinsic material property. However, in order to investigate the use of fracture toughness in crusher applications a new test method for the rapid estimation and comparison of fracture toughness values needs to be developed.

CHAPTER 3. EXPERIMENTAL PROGRAM

In order for any size reduction process to be fully characterized, material properties, or physical expressions describing the nature of the material broken, should be related to the pattern of breakage and resultant fragment size distribution created by crushing. It has been suggested that a material's fracture properties should be characterized in terms of particle strength, specific breakage energy, and the breakage fragment size distribution of the material. It is proposed that the particle strength should be replaced by another, more descriptive measure of a material's ability to withstand fracture. Fracture toughness fully characterizes a rock's resistance to fracture and is dependent on the fracture strength of the rock as well as the presence of flaws within the rock. Therefore, it is proposed that the potential of fracture toughness to function as a predictive means for rock crushability, and to develop fracture toughness based models for the selection and optimization of primary jaw crushers be examined. The aim of the models is to predict the power consumption, product size, and capacities of jaw crushers. Using the "technique" of single particle breakage, discussed in section 2.4, the specific comminution energy and fragment size distributions of various aggregates will be determined. The associated fracture toughness of each rock type will be measured using a newly developed fracture toughness test. Finally, a lab-scale jaw crusher will be used to test the strengths of the laboratory-based models, and, if possible, to determine if "scale-up" regression analysis between the laboratory results and actual operating conditions is necessary.

3.1 ROCK SPECIMENS

Luck Stone Corporation, the 12th largest producer of crushed stone products in the United States, with operations in Maryland, Virginia, and North Carolina, has provided rocks from five of their aggregate quarries: Boscobel, Charlottesville (Shadwell), Culpeper, Leesburg and Spotsylvania (Figure 3.1). Additional rock was also provided from a sixth site not currently under production, identified as the Thornburg property (located near the Spotsylvania operation). Rock from the Culpeper site classifies into two groups, by color (red and gray), and although the properties of each are expected to be the same, they are to be tested independently in this study.

Each of the rock types originates in the same physiographic province. Virginia contains five physiographic provinces: the Coastal Plain, Piedmont, Blue Ridge, Valley and Ridge, and Appalachian Plateaus (east to west in Figure 3.2). The six *Luck Stone* rocks are found in the Piedmont. The Piedmont extends eastward from the Blue Ridge to the Fall Line, where unconsolidated sediments of the Coastal Plain cover Paleozoic-age and older igneous and metamorphic rocks. The Piedmont is characterized by deeply weathered, poorly exposed bedrock, and a high degree of geological complexity (DMME, 2003). Crystalline rocks are sprinkled with a few areas of much younger, unmetamorphosed, sedimentary and volcanic rocks found in rift basins, with the largest

being the Culpeper Basin. A more specific geologic description of each rock type to be tested follows and has been provided by *Luck Stone* (*Luck Stone, 2003*).

Figure 3.1 Location of rock quarries that provided specimens
(*From Luck Stone, 2003*)

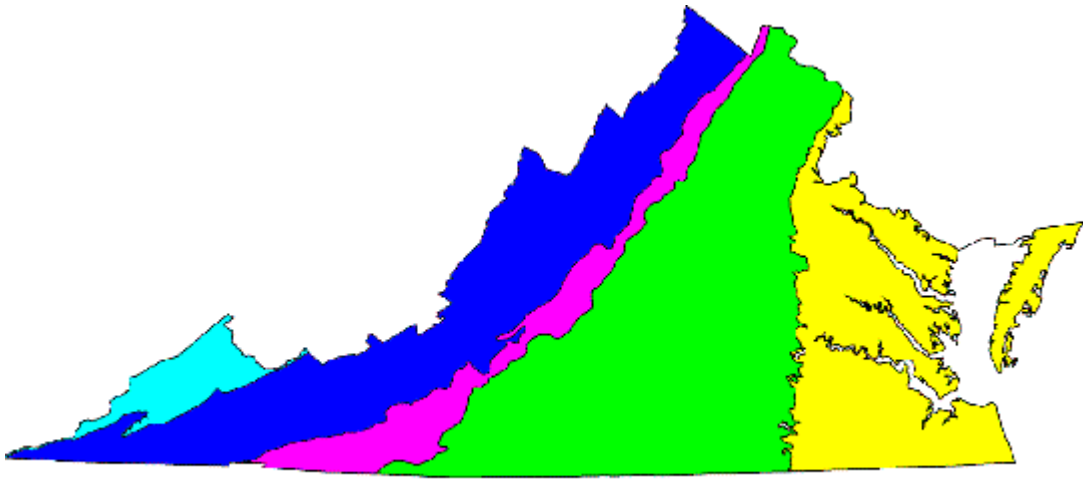

Figure 3.2 Physiographic provinces of Virginia (Piedmont is green, 2nd from right)
(*From VA DMME, 2003*)

Boscobel Granite (BG)

The Boscobel operation quarries Petersburg Granite, an igneous formation about 330 million years old. The rock was formed from a molten mass and has a pink, multi-

colored appearance. Quart, orthoclase, plagioclase, muscovite, and small amounts of dark colored minerals combine to give the granite its multi-colored appearance.

Shadwell Metabasalt (SMB)
The Shadwell operation (just outside of Charlottesville) mines Catoctin Greenstone, formed by lava flows over 500 million years ago. The greenstone originated as basalt and contains plagioclase and pyroxene minerals. Epidote and chlorite infused the formation during mountain building giving the green color.

Culpeper Siltstone (CGS and CRS)
The Culpeper quarry produces sedimentary siltstone, sandstone, and shale. Siltstone is the main rock, but the formation does grade down in particle size to shale and up in size to fine-grained sandstone. Sediments eroded from western uplands were deposited in the low-lying Culpeper Basin, which was formed as a result of continental land masses pulling apart. Deposition of the sediments took place 200 million years ago, with lower sediments gradually hardening under the effects of weight and pressure. The red colored rock (found at greater depth) results from the hematite-cementing agents that bound the sediment grains into rock. The upper, gray colored rock occured as a result of a lack of oxygen during deposition that prevented the cementing agent from becoming red in color.

Leesburg Diabase (LD)
The Leesburg quarry produces diabase, sometimes referred to as traprock. The diabase is a dense, igneous rock with greenish-black to bluish-black color. Formed by hot magma over 200 million years ago, the rock contains mainly pyroxene and plagioclase.

Spotsylvania Granite (SG)
The Spotsylvania operation quarries a complex blend of igneous and metamorphic rock types (Po River Metamorphic Suite). The rock types at Spotsylvania are granite-gneiss and biotite-gneiss, and are about 400 million years old. The granite-gneiss is a white to gray color and the biotite-gneiss is dark gray to black.

Thornburg Granite (TG)
The rock formation at the Thornburg property is similar to that of the Spotsylvania granite. Formed by a later igneous intrusion, the rock is different in its appearance than the Spotsylvania granite. It is a reddish granite with large mineral crystals that contrasts with the surrounding rock. Figure 3.3 depicts each of the seven rocks to be tested.

3.1.1 ROCK PROPERTIES

A series of standard laboratory tests have been conducted on the rock types in order to determine their mechanical properties and to provide a basis for comparison among typical rock properties and fracture toughness as they relate to the selection of jaw crushers. The uniaxial compressive strength, indirect tensile strength, and elastic modulus of each rock was determined pursuant to ASTM standard test method

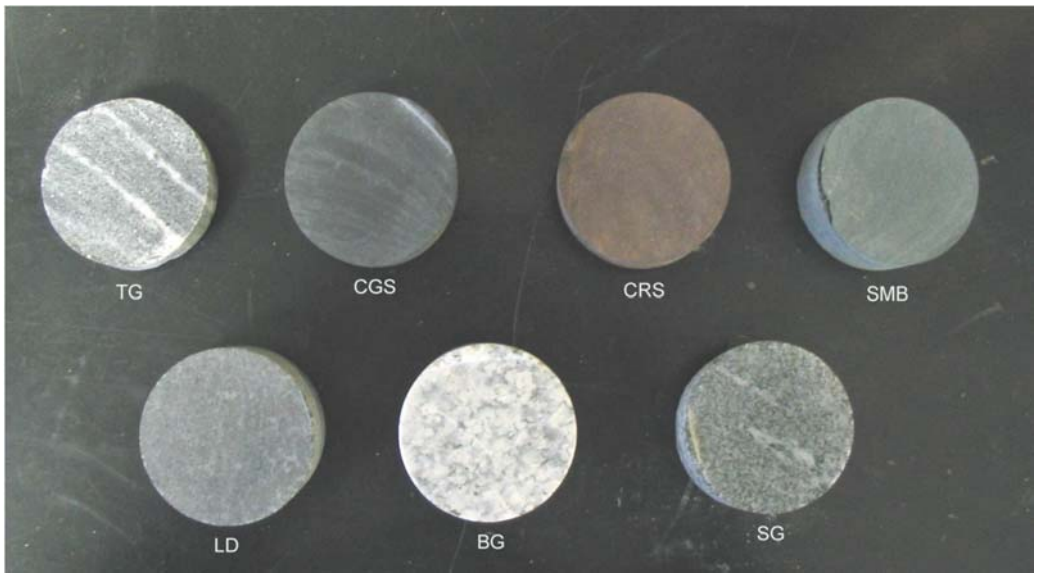

Figure 3.3 Seven quarry rocks to be tested

procedures (ASTM D2938-95: Standard Test Method for Unconfined Compressive Strength of Intact Rock Core Specimens; ASTM D3967-95: Standard Test Method for Splitting Tensile Strength of Intact Rock Core Specimens). The testing was conducted in the Department of Mining and Minerals Engineering Rock Mechanics Laboratory at Virginia Tech. Table 3.1 summarizes the test results.

Table 3.1 Mechanical properties of tested rocks

Rock Type	**Compressive Strength** *MPa*	**Tensile Strength** *MPa*	**Elastic Modulus** *GPa*
Shadwell Metabasalt	142.0	18.72	29.79
Boscobel Granite	59.2	7.76	16.76
Culpeper Grey Siltstone	185.3	21.94	25.93
Culpeper Red Siltstone	155.0	22.08	23.65
Leesburg Diabase	225.7	17.61	29.51
Thornburg Granite	142.6	13.36	27.03
Spotsylvania Granite	114.3	12.44	25.38

3.2 FRACTURE TOUGHNESS TESTING

Although the International Society of Rock Mechanics has suggested that the Chevron Notched Short Rod and Chevron Notch Round Bar in Bending be adopted as recommended fracture toughness tests (see section 2.5.3), the use of these tests for rock characterization and indexing purposes is not widespread. The complexity of these existing tests is an immediate problem when considering the application of fracture

toughness to gauge size reduction processes. Thus, another method for fracture toughness testing of rocks is necessary, one that will give a representative toughness value (in accordance with Level I testing) and yet be simple, core based, with easily reproducible crack geometry, and requiring only straightforward data collection and evaluation techniques.

It is proposed that a wedge test utilizing an edge notched disc (END) be employed in order to acquire fracture toughness values suitable for rapid indexing and comparative purposes. The test will enable a large number of rock types to be tested so that relationships among breakage energy, fragment size distribution, and fracture toughness can be investigated in order to develop a crushing index capable of predicting and evaluating primary crushing equipment performance. The development and experimental verification of the END wedge splitting test, using trial rocks, is covered in the following section.

3.2.1 DEVELOPMENT OF THE EDGE NOTCHED DISC WEDGE SPLITTING TEST

Stress intensity factors for edge notched disk

Recalling section 2.5, a material's resistance to crack propagation can be quantified using fracture toughness, K_{Ic}, the critical stress intensity factor. When the stress intensity factor, K_I, in the region of a crack tip exceeds K_{Ic}, fracture initiates and propagates until the stress intensity factor decreases below K_{Ic}. Equation 2.38 showed the relationship between fracture toughness, the applied stress, crack length, and F, a dimensionless constant dependent on the geometric configuration. When working with applied loads and planar geometries, as is this case in rock testing, the stress intensity factor can be expressed according to:

$$K_I = F_p \frac{P}{t\sqrt{w}} \qquad [3.1]$$

where, P is the applied load

t is the specimen thickness

w is the uncracked ligament length (or the maximum possible crack length)

F_p is a new dimensionless geometry factor, defined as:

$$F_p = f_p\left(geometry, a/w\right) \qquad [3.2]$$

For the testing and calculation of rock fracture toughness using an edge notched disk, the stress intensity factor and F_p must be determined. In reference to the specimen geometry and loading configuration given in Figure 3.4, Isida et al. (1979) and Gregory (1979) have independently characterized the stress-strain region enclosing the crack tip using stress field analysis for the two dimensional case, assuming linear-elastic behavior and small-scale yielding (Murakami, 1987). For an edge cracked circular plate subject to concentrated forces acting at symmetrical points, Isida (et al., 1979) employed the boundary collocation method and found the stress intensity factor, F to be:

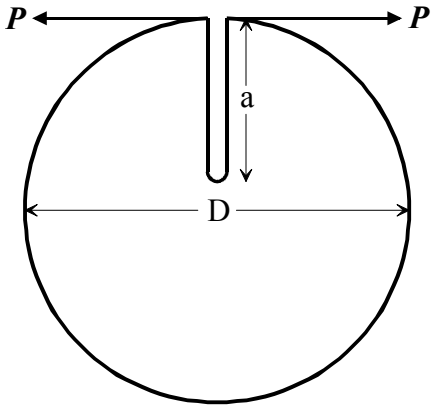

Figure 3.4 Edge notched disk specimen and loading configuration

$$F_{Isida} = \frac{K_I D}{P\sqrt{\pi a}} \qquad [3.3]$$

Isida (et al., 1979) give values of F for a/D ratios ranging from 0.1 to 0.6 (Table 3.2).

Table 3.2 Values of *a/D* and corresponding value of *F* from Isida (et al., 1979)

a/D	0.1	0.2	0.3	0.4	0.5	0.6
F	11.488	7.721	7.051	7.451	8.636	10.990

Gregory's F equation was derived using stress functions and it is a closed form solution. It is applicable to an edge cracked circular disk subjected to "pin" loading at the crack mouth. F can be written as:

$$F_{Gregory} = \frac{K_I \sqrt{2a}}{2P\sqrt{D}} \qquad [3.4]$$

Gregory gave the function that defines F so the stress intensity factor for any a/D ratio can be calculated directly. The expression for F is:

$$F_{Gregory} = \frac{a}{0.355715\left(D-a\right)^{3/2}} + \frac{1}{0.966528\left(D-a\right)^{1/2}} \qquad [3.5]$$

A plot of F_p (as defined in Equations 3.1 and 3.2) versus a/D was developed in order to compare the two solutions (Figure 3.5). F_p in terms of Isida' and Gregory's F was created by normalizing Equations 3.3 and 3.4 against Equation 3.1 resulting in the following expressions:

$$F_{P-Isida} = \sqrt{\frac{\pi a}{D}} F_{Isida} \qquad [3.6]$$

$$F_{P-Gregory} = \frac{2D}{\sqrt{2a}} F_{Gregory} \qquad [3.7]$$

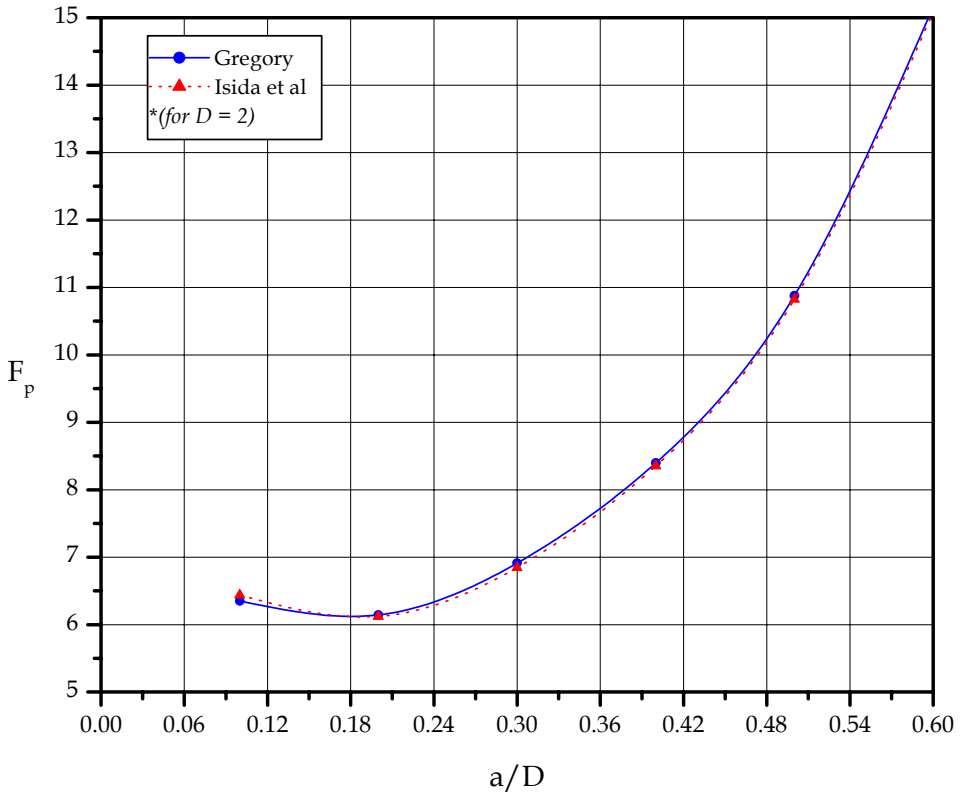

Figure 3.5 Comparison of independent solutions of F_p vs. *a/D* for an END

Figure 3.5 shows that the two solutions are almost identical for *a/D* ratios varying from 0.1 to 0.6, and either can be used to determine the stress intensity factor for the END. For application in rock fracture toughness testing it was determined that Gregory's solution provides the easiest method for determining K_I since a direct expression for F is given, and K_I can be determined precisely for any *a/D* ratio.

Load application

The previous stress analysis requires the edge notched disk to be loaded at the crack mouth by equal and opposing forces. This loading configuration can be achieved rather simply by using a wedge. The splitting force of the wedge, P_{sp}, is the horizontal component of the force acting on the crack mouth edge and can be determined from force equilibrium analysis (Figure 3.6 and Appendix V). Equation 3.8 shows the splitting force in terms of the applied vertical force, P_v, acting on the wedge, the wedge angle α, and the coefficient of interface friction μ.

$$P_{sp} = \frac{P_v}{2\tan\left(\alpha/2\right)} \cdot \frac{1-\mu\tan\left(\alpha/2\right)}{1+\mu\cot\left(\alpha/2\right)} \qquad [3.8]$$

The wedge provides a mechanical advantage, an advantage that increases as the wedge angle decreases. For wedging of a crack in rock the amount of friction between

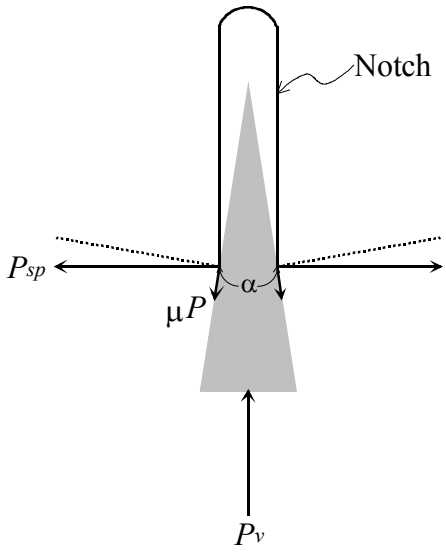

Figure 3.6 Forces acting at the crack mouth

the wedge material and the rock can be substantial and frictional losses may occur. The coefficient of friction needs to be quantified for each rock type tested in order to account for frictional losses. A tilt test can be used to determine μ, where the angle of sliding is ϕ and tan ϕ is equal to μ. The coefficients of friction between four rock types and hardened steel are shown in Table 3.3 (rock types and wedge material used during END wedge test development).

Table 3.3 Values of ϕ and μ from tilt test on hardened steel

	Large grained granite	Fine grained granite	Dolomitic limestone	Sioux quartzite
ϕ	18.5°	18.9°	19.7°	22.8°
μ	0.335	0.342	0.358	0.420

Test Specimen

The test specimen can be prepared from standard rock core, resulting in the geometry shown in Figure 3.4. Specimens are cut using a diamond wheel saw and the sides of the disk ground until parallel (or to within ± 0.125 mm) to each other. The edge notch is cut using a diamond wheel saw (with a thickness of 1.5 mm) and requires a fixture that holds the disk and ensures that the notch is cut along the centerline of the disk.

Minimum specimen dimensions for the END are investigated in the following section, but guidelines for rock fracture testing have already been discussed (section 2.5.3). In general, values of rock fracture toughness do not show the same type of dependency on specimen size, namely thickness, as seen in testing of metallic materials. But the size cannot be too small and the thickness must not be smaller than the width of the fracture process zone. The requirements given by Equation 2.40 are used for rock fracture testing and these are "checked" after an apparent fracture toughness value has

been measured. Since the specimens will be prepared from NX rock core the diameter will typically be around 50 mm. The proposed thickness is approximately 25.4 mm. Various notch lengths were proposed initially in order to investigate any relationship between fracture toughness results and specimen size.

Wedging device

The wedging device used to apply the splitting force along the crack mouth edge consists of hardened steel. The wedge angle is 11°. The wedge, with approximate dimensions, is shown in Figure 3.7.

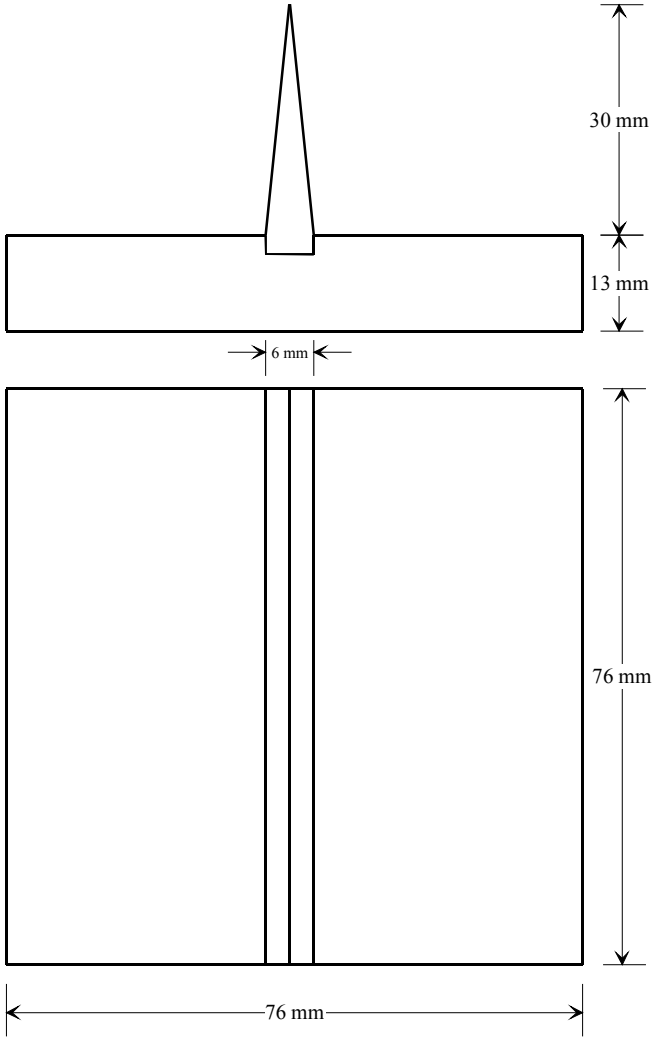

Figure 3.7 Wedge configuration

Test set-up, loading, and measurement

The END specimen is placed on the wedge (Figure 3.8). The vertical force is applied under displacement control by an MTS 810 closed loop servo-hydraulic materials testing

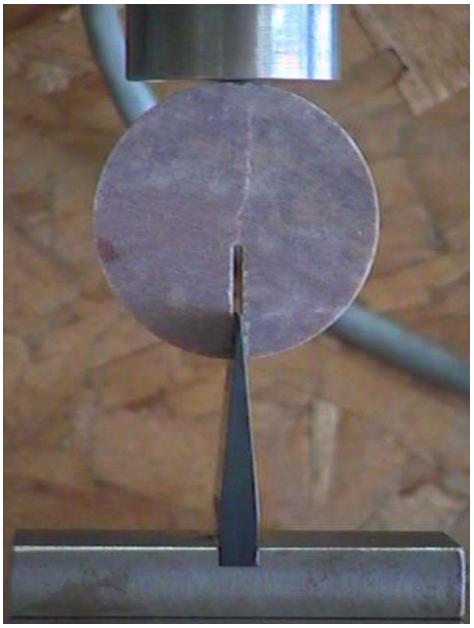

Figure 3.8 Test set-up for END wedge test
(*After Donovan and Karfakis, 2003*)

system affixed with an 8896 N load cell. Load and load-line displacement data are recorded digitally by a PC and also with an X-Y recorder (for back-up).

Various loading rates, usually in terms of stress intensity per second, have been prescribed for rock fracture testing (see section 2.5.3). The loading rate in terms of stress intensity cannot be determined until after testing. Different rates were tested, by varying the load-line displacement, in order to investigate any dependency of the results on loading rate. The loading rate for the END wedge test is discussed in the following section.

In accordance with Level I rock fracture toughness testing only the maximum load needs to be recorded in order to calculate K_{Ic}. However, the load-displacement data should be recorded in order to verify that the maximum load is the critical applied load that results in crack propagation. For the END wedge test this involves an approximation of the crack mouth opening displacement (CMOD). There are no plans to measure the CMOD directly but it can be calculated from the wedge angle and the load-line displacement. The 5% secant approach for determining the critical load has been shown to be satisfactory for rock testing, although smaller specimens may give lower K_{Ic} values. This method, along with direct observation of the load-displacement curve (i.e., looking for non-linear behavior), was used to verify that the maximum load was the critical load when testing trial rocks using the END wedge test.

Calculation of K_{Ic}

The calculation of fracture toughness using the END wedge test is straightforward. The critical load, if not the maximum load, is determined from the load and the calculated CMOD curve (Figure 3.9). The apparent fracture toughness is calculated using the following equation, by substituting for P in Gregory's stress analysis of the END specimen (Equations 3.4 and 3.5) with the splitting force, P_{sp}, applied by the wedge (Equation 3.8):

$$K_q = 2\sqrt{\frac{D}{2a}}\left(\frac{P_v}{2\tan\left(\alpha/2\right)}\cdot\frac{1-\mu\tan\left(\alpha/2\right)}{1+\mu\cot\left(\alpha/2\right)}\right)\left(\frac{a}{0.355715\left(D-a\right)^{3/2}}+\frac{1}{0.966528\left(D-a\right)^{1/2}}\right) \quad [3.9]$$

The apparent fracture toughness value is considered valid (i.e., equal to K_{Ic}) after checking that the specimen size requirements are met.

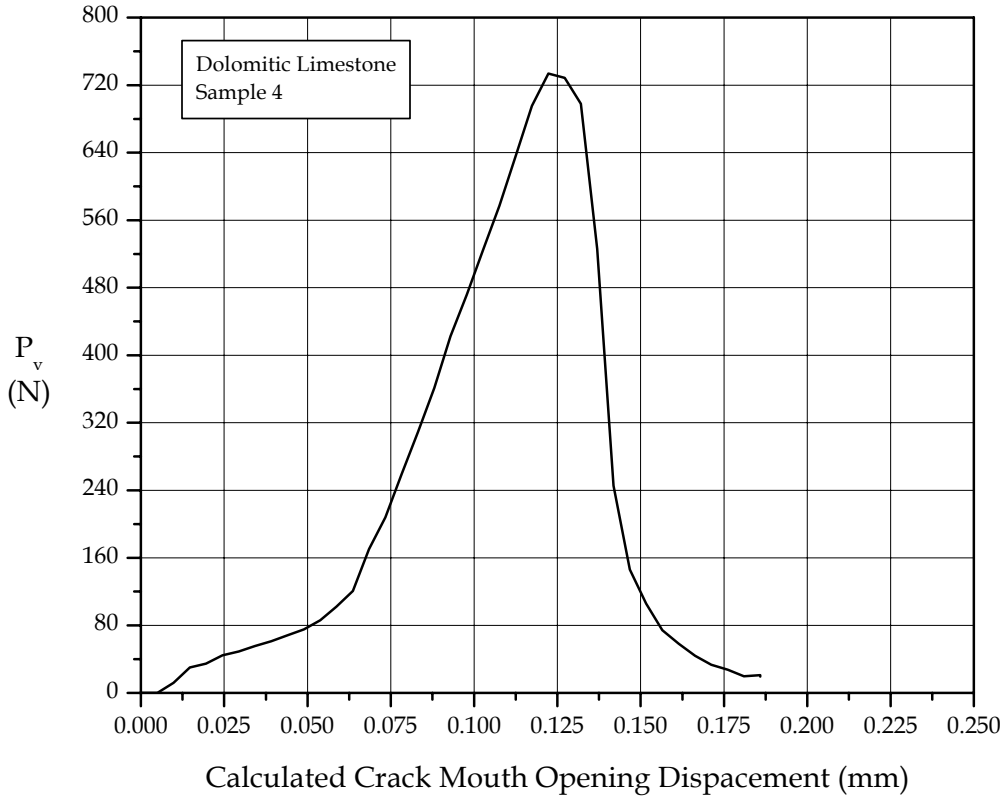

Figure 3.9 Example vertical load vs. calculated CMOD curve

3.2.2 EXPERIMENTAL VERIFICATION OF THE END WEDGE SPLITTING TEST

Four rock types were tested in order to test the validity of the END specimen and test configuration: fine-grained granite, large-grained granite, dolomitic limestone, and Sioux quartzite. These rocks were chosen because samples of the fine-grained granite, limestone, and the quartzite each had previously been tested using a common fracture

toughness test, the Semi-Circular Bend test (see section 2.5.3), providing a basis for comparison (Akram, 1991). The large-grained granite was included in order to investigate the influence of notch length and loading rate on fracture toughness.

Fifty-four samples were prepared in accordance with the previous section. A 15 cm diameter, diamond bladed, radial arm saw was used to cut 25 mm thick disks from 50 mm diameter rock cores. The disk sides were ground flat and parallel to each other using a diamond surfaced grinding wheel. A 1.5 mm thick diamond blade was used to cut a straight through edge notch along the centerline of the disc. The notch lengths varied from 10.57 mm to 28.35 mm. Cutting, grinding, and notching of the samples took less than 3 hours, resulting in a preparation time of approximately 3 minutes per specimen.

Testing of the specimens was done using an MTS 810 closed loop servo-hydraulic materials testing system affixed with an 8.896 kN load cell. The tests were performed under load line displacement control. The load-line displacement rate was 0.025 mm/s for the limestone and quartzite, either 0.003 mm/s or 0.001 mm/s for the fine-grained granite, and varied among the previous three rates for the large-grained granite. After testing the loading rates were determined in terms of stress intensity. The maximum stress intensity-loading rate occurred with the limestone and was $0.0986\ MPa\sqrt{m}/s$. The minimum occurred with the large-grained granite and was $0.0011\ MPa\sqrt{m}/s$. Possible effects of loading rate on fracture toughness are discussed later.

The load-displacement data was collected and converted into splitting force (P_{sp})-calculated CMOD data in order to verify that the maximum load was also the critical load. This required the measurement of the frictional coefficient between the rock and the hardened steel of the wedge. For all 54 samples the critical applied load resulting in crack propagation was also the maximum load.

After testing, all specimen dimensions were tested against Equation 2.40 to verify that dimension requirements were met (tensile testing of the same rock types was performed in order to determine σ_t). Of the 54 samples tested, 1 fine-grained granite sample and 3 limestone samples did not meet the minimum requirement for crack length (one of the 3 limestone samples also did not meet the thickness specification). These samples were disregarded.

Fracture toughness results

Table 3.4 shows the results of the END wedge splitting and those of the Semi-Circular Bend test (Akram, 1991). Statistical analysis of the results for each individual rock type indicates that the mean values of fracture toughness from both tests are not significantly different (at a confidence level of 99%). From the initial analysis it seems reasonable to expect the END wedge split test to yield representative fracture toughness values, particularly in terms of indexing and for comparative purposes.

Table 3.4 Fracture toughness values from the END test and SCB test

Rock Type	END		SCB	
	# of Specimens	K_{Ic} $MPa\sqrt{m}$	# of Specimens	K_{Ic} $MPa\sqrt{m}$
Fine grained granite	13	0.914 ± 0.093	6	0.884 ± 0.022
Large grained granite	27	0.621 ± 0.101	NA	NA
Dolomitic limestone	9	1.398 ± 0.186	6	1.331 ± 0.080
Sioux quartzite	4	1.241 ± 0.031	6	1.244 ± 0.071

Based on the test results, there is some dependency on grain size. The larger grained rocks had the lowest fracture toughness values, and this follows the general observation that rocks with smaller grains tend to have higher values of fracture toughness (Whittaker et al., 1992). Generally, for rock testing, the ratio of smallest specimen dimension to grain size should be at least greater than 10:1. The END specimens in this case satisfied that requirement, but there is some question as to the effect of notch thickness. The maximum notch width should also be considerably larger than the grain size. In this case a notch thickness of 1.5 mm was used, which may not be large enough relative to the granite rocks.

Crack length effects

Figure 3.10 shows fracture toughness values versus *a/D* for the two granite rocks tested.

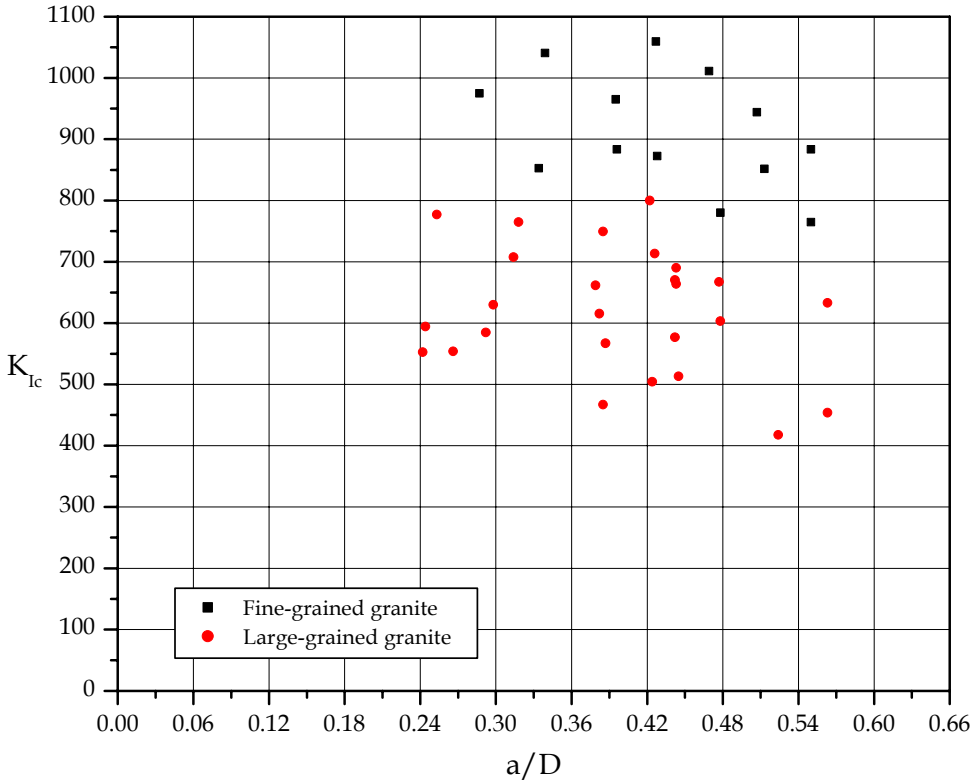

Figure 3.10 Fracture toughness vs. *a/D*

There is some dependency of K_{Ic} on crack length (D was constant at approximately 50 mm). Usually when the crack length is long enough, the fracture process zone becomes fully developed before failure, resulting in the consumption of more energy and a higher fracture toughness value. Figure 3.10 seems to contradict this, as K_{Ic} seems to decrease slightly with increasing crack length, but the amount of scatter in the data requires that a wider range of crack lengths be tested before suggesting a relationship between K_{Ic} and crack length for the END test.

Effect of loading rate

It was previously noted that the loading rate was varied among 0.025, 0.003, and 0.001 mm/s for the large-grained granite. In terms of stress intensity, the corresponding loading rates were 0.0283, 0.0032, and 0.0011 $MPa\sqrt{m}/s$. At least 8 samples were tested at each rate so that an analysis of variance could be performed to quantitatively assess any effect of loading rate on K_{Ic}. At a confidence interval of 99% there is no significant difference between the fracture toughness values determined at different loading rates. For the END wedge split test it is recommended that the load line displacement be no greater than 0.025 mm/s.

Test limitations

In section 2.5.3 it was stated that fracture toughness specimens employing a notch instead of a sharp crack tend to underestimate K_{Ic}. This is the biggest drawback to using the END specimen. However, the purpose of the END test is to provide representative values of fracture toughness for use in indexing different rocks quickly and easily, in regards to sample preparation and testing. From this standpoint the limiting effect of a notch does not seem to be an issue since the results of the END tests compared so favorably to the Semi-Circular Bend tests. For application to Level II testing it would be worthwhile to investigate the use of a sharp crack (i.e., a chevron notch) with the END specimen.

3.2.3 APPLICATION OF THE END WEDGE SPLITTING TEST

The Edge-Notched Disc Wedge Splitting test gives a representative toughness value (in accordance with Level I testing) and is a simple, core based specimen, requiring only straight-through notch and straightforward data collection for the determination of K_{Ic}. The END test can be used for indexing and comparative purposes. The test will enable a large number of rock types and specimens to be tested so that relationships among breakage energy, fragment size distribution, and fracture toughness can be investigated, leading to the development of an improved method for prediction and evaluation of crushing equipment.

For this study the testing procedure follows the one used in the development and verification of the END test. A loading rate of 0.001 mm/s is to be used to ensure slow, stable crack growth. Ten specimens of each rock type are to be tested. The average

specimen dimensions for each rock, along with the coefficient of friction between the wedge and rock, are given in Table 3.5.

Table 3.5 Average specimen dimensions and coefficient of friction for tested rocks

Rock Type	D *mm*	a *mm*	t *mm*	μ
Shadwell Metabasalt	47.422	21.946	24.696	0.384
Boscobel Granite	47.483	22.007	25.354	0.410
Culpeper Grey Siltstone	47.597	20.668	25.042	0.386
Culpeper Red Siltstone	47.589	22.289	25.166	0.372
Leesburg Diabase	47.597	21.763	25.776	0.350
Thornburg Granite	47.160	21.237	25.588	0.398
Spotsylvania Granite	47.468	21.989	25.197	0.394

3.3 SINGLE PARTICLE BREAKAGE TESTING

In any size reduction process the breakage of any individual particle occurs simultaneously with that of many other particles. However, each individual particle breaks only as a result of the stresses applied to it, thus isolation of the single particle fracture event represents the most elementary process in size reduction and its study is of great importance. The characteristics of crushing that need to be measured are force applied at fracture, total fracture energy, specific fracture energy (taking into account the mass of the particle), and the product size distribution. The product size distribution is used to determine the breakage function, which is influenced by the material properties of the particle, the nature of the stress application, and the energy input. The purpose of single particle breakage in this study is to derive crushing energy and product size distribution data for the seven rock types, data which will ultimately be compared to the fracture toughness of the those rock types.

The most common devices used for single particle breakage studies were described in section 2.4.2. None of those testing systems will be used in this study. Single particle breakage tests will be carried out using the Allis-Chalmers High Energy Crushing Test (HECT) system. The HECT system is a specially configured MTS materials testing system that is capable of simultaneously measuring crushing force and actuator displacement in order to accurately calculate the net energy utilized in particle crushing (Allis-Chamlers, 1985). Additionally the HECT system allows for flexible control of the force or displacement during a test so that a pre-specified profile can be followed. It is capable of running under displacement control at 2 m/sec, using an inverted haversine profile permitting close simulation of the crushing cycle in an actual crusher. The HECT system can simulate a wide range of crusher sets, speeds, and throws, a range that includes essentially all crusher operating conditions, consequently distinguishing itself

from other testing systems. The Department of Mining and Minerals Engineering Rock Mechanics Laboratory at Virginia Tech is equipped with a HECT system.

3.3.1 CONCEPTS OF THE HIGH ENERGY CRUSHING TEST

The purpose of the HECT test is to obtain the breakage functions for various feed sizes over a range of crushing energies or size reduction levels. A number of pieces of material are broken, the crushing energy is recorded for each piece, and the products pooled together. The size distribution of the pooled pieces is determined by sieve analysis and the breakage function is determined in accordance with the methods outlined in section 2.4.3.

Since the crushing energy is dependent upon the amount of size reduction and the mechanical properties of the material, the range of HECT tests is defined by various reduction ratios. The reduction ratio is the ratio of the geometric feed size to the closed side set of the HECT device. Allis-Chalmers recommends that HECT tests be run for reduction ratios between 1.6 and 3.3. It is also recommended that various feed sizes, representing what might be seen in an actual crusher, be tested.

The HECT system is very flexible and can accommodate a wide range of crusher conditions. The HECT system requires the specification of three conditions: the closed side set, the throw, and the speed (or frequency). These parameters are set to match the operating conditions of the crusher application in question.

The HECT system itself measures only two parameters during testing, the crushing force and the displacement of the hydraulic actuator. A linear variable differential transducer (LVDT) measures the displacement of the hydraulic ram, which carries the test material up towards a fixed platen. A load cell affixed to the upper platen measures the crushing force. These two signals are recorded digitally by a data acquisition system.

The following section outlines the exact HECT test procedure, set-up, data acquisition and analysis, and specimen geometry used in this study.

3.3.2 HECT TEST SET-UP AND PROCEDURE

Test specimens

Luck Stone provided core boxes of the rock types to be used in this study. Therefore the specimen geometry for the HECT test is limited by the cylindrical geometry of rock cores. Normally single particle breakage is performed using irregular shaped particles or, in some instances, spherical particles are used. There is no evidence in the literature that cylindrical specimens have been used previously for single particle breakage. The main limitation of any specimen with a uniform, geometric shape is that it is not representative of the irregular particles fed to an actual crusher. However, the state of stress within a particle under point contact loading is essentially independent of the particle shape and,

as with irregular particles, cylindrical particles fracture due to induced tensile stresses that act along the load-line.

Table 3.6 gives the average specimen dimensions for each rock tested using the HECT system. A cylindrical specimen with a thickness approximately half of the diameter was chosen. The specimens are cut using a radial armed saw outfitted with a diamond wheel blade. Approximately 20 specimens, or at least enough to exceed 2000 g by mass (total), are prepared for each test (i.e., varying reduction ratios) per rock type.

Table 3.6 Average HECT test specimen dimensions

Rock Type	Reduction Ratio 1			Reduction Ratio 2		
	D	t	Mass	D	t	Mass
	mm	*mm*	*g*	*mm*	*mm*	*g*
Shadwell Metabasalt	47.477	25.883	126.8	47.481	26.109	128.8
Boscobel Granite	47.492	25.668	117.0	47.464	26.041	117.5
Culpeper Grey Siltsone	47.624	26.601	128.3	47.621	25.575	124.0
Culpeper Red Siltsone	47.631	26.034	127.6	47.605	25.740	125.5
Leesburg Diabase	47.587	26.575	141.2	47.608	26.038	139.1
Thornburg Granite	47.174	26.728	125.1	47.192	26.064	119.9
Spotsylvania Granite	47.454	26.673	128.3	47.431	26.069	125.2

Test equipment and set-up

The HECT system is a uniquely designed MTS 810 materials testing system (Figure 3.11). It is a closed loop servo-hydraulic materials testing system affixed with a 250 kN load cell. The force-generating device in the HECT system is a high velocity hydraulic actuator. The actuator, or ram, is capable of speeds up to 2 m/s and has a maximum stroke length of 152 mm. The actuator is rated at 150 kN. The displacement of the ram is measured by an LVDT mounted inside the hydraulic piston.

The closed side set, throw, and speed are the only parameters that need to be defined for the HECT. The closed side set is determined based on the required amount of size reduction. For this study it is proposed that tests be run at two different reduction ratios, with the closed side set for reduction ratio 1 being 31.75 mm and for reduction ratio 2, 16.00 mm. Based on the average dimensions given in Table 3.6, the average reduction ratios are 1.50 and 2.97. The throw (the linear distance traveled by the actuator) is fixed at 50.8 mm in accordance with Allis-Chalmers' direction that all tests be run at that throw (Allis-Chalmers, 1985). The speed of the test is to be representative of an actual jaw crusher. 225 rpm is an average speed/frequency for a single-toggle jaw crusher and the tests outlined here will be run close to that speed. The HECT system requires that the speed be entered as a frequency, thus the test is set-up at a crushing frequency of 3.8 Hz (228 rpm).

Figure 3.11 HECT system

The test is run under displacement control with the actuator displacement following an inverted haversine profile, shown in Figure 3.12. The combination of the given throw and frequency results in an average loading rate of 386 mm/s. Breakage of one particle takes 0.26 seconds with full-scale displacement occurring at 0.13 seconds.

Each particle is placed inside the crushing zone, as defined by the small platen affixed to the load cell (Figure 3.13). The crushing chamber is surrounded by a plastic enclosure that is closed and locked after a particle is loaded. The particle is then broken. After breakage the particle fragments are cleaned from the chamber and transferred to a plastic bag.

Data acquisition

A digital acquisition system accompanies the HECT system (upper left hand corner in Figure 3.11) and records and analyzes the "raw" data sent to it during each test. The raw data is the displacement as measured by the LVDT and the load as measured by the load cell. The *DATA 6000 Waveform Analyzer* acquires this data during testing and is also capable of processing it after testing. The *DATA 6000* has a sampling rate of 10 μs.

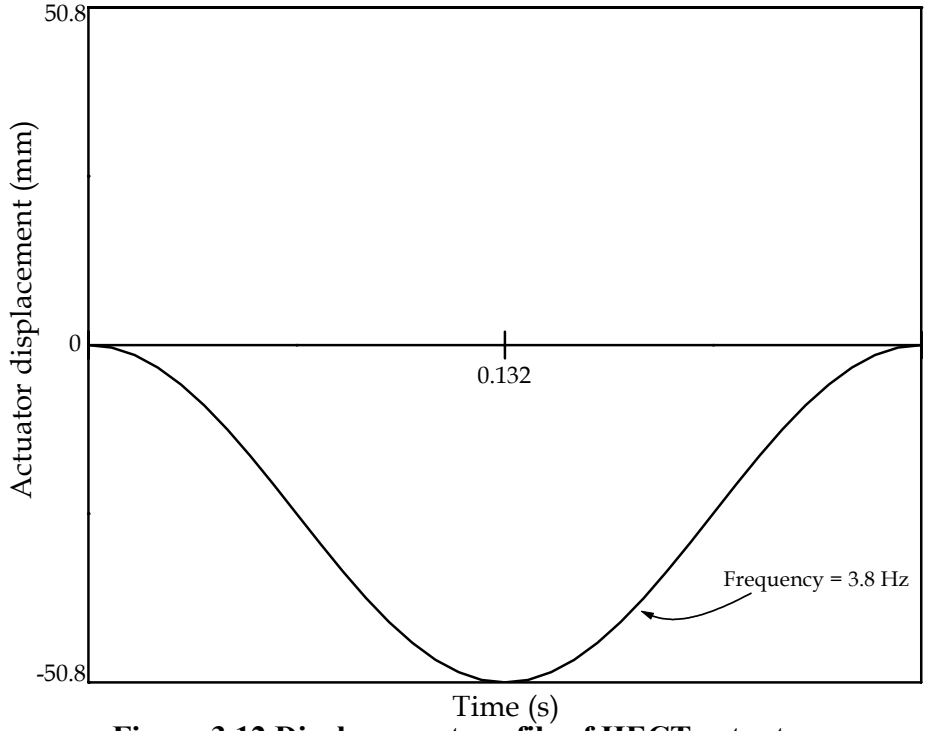

Figure 3.12 Displacement profile of HECT actuator

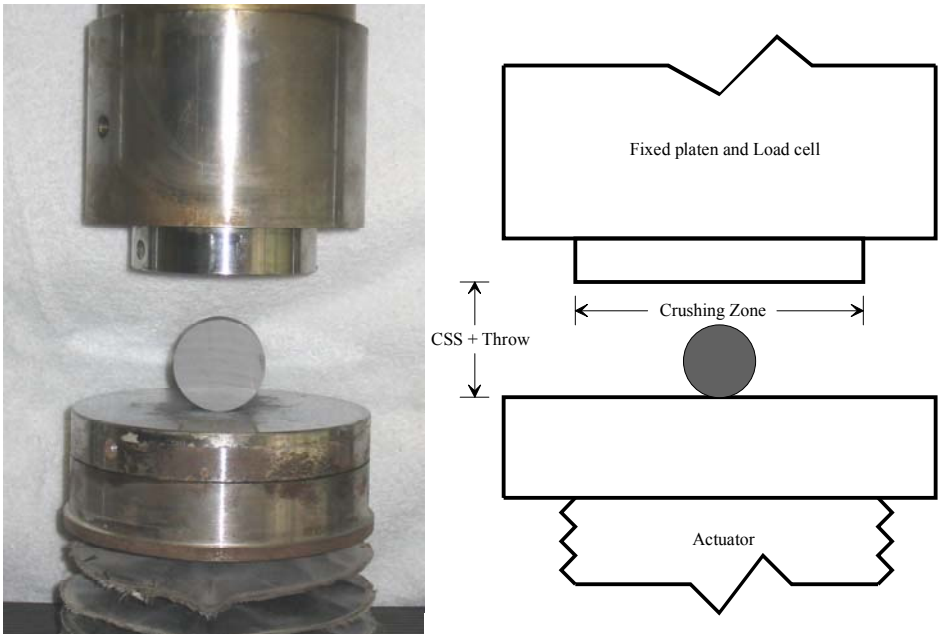

Figure 3.13 Schematic and picture of HECT loading configuration

The *DATA 6000* can be programmed manually or by using a program supplied by Allis-Chalmers. In each case the *DATA 6000* is configured to collect the raw data

after a certain "triggering" level has been met and to process the data according to the input program. For this study the *DATA 6000* is programmed to calculate the crushing energy from the force and displacement data. The *DATA 6000* differentiates the stroke/displacement signal in order to obtain the actuator velocity curve. The force data is multiplied by the velocity curve in order to determine the power curve. The *DATA 6000* then determines the points at which crushing began and ended. This interval is bounded by the first non-zero force value and the maximum displacement of the actuator (i.e., the point at which the actuator begins to retract). The waveform analyzer then integrates the power curve over this interval in order to determine the total crushing energy. Figure 3.14 illustrates a typical set of *DATA 6000* recorded and processed curves.

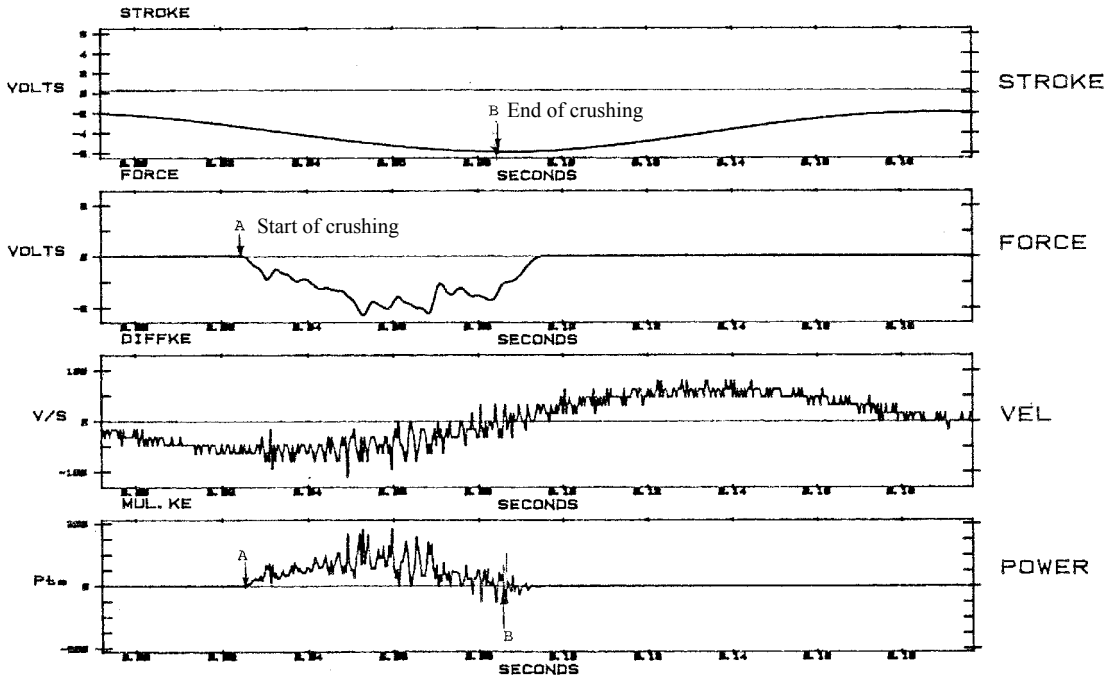

Figure 3.14 Recorded and processed curves from *DATA 6000*

After each breakage event an *HP 7470A* plotter produces a graph similar to Figure 3.14. In addition to the plot, the *DATA 6000* also provides numerical results for the total crushing energy and the peak crushing force. These values are recorded for each specimen. The crushing energy is given in "points", where 1 point is equal to one watt-second. The crushing energy is converted to specific comminution energy with units of kW-hours per metric ton. Using Equation 2.31 and the peak crushing force, the dynamic tensile strength of the specimen is calculated.

Upon completion of one series of testing (all specimens tested for a given closed size set/reduction ration), a sieve analysis is performed on the pooled breakage fragments. For this study a $\sqrt{2}$ series will be used with an initial sieve opening of 38.1 mm. The

material will be sieved down to 0.074 mm (200 mesh). A Ro-Tap sieve shaker is used to provide uniform circular tapping motion to the sieves. The particle-size distribution is recorded as the weight percentage retained on each of the sieves of decreasing size and the percentage passed of the finest size. This data is converted to the weight percentage passing each screen in order to determine the breakage function (see section 2.4.3). For the cylindrical disk specimens of this study the parent size is taken to be the diameter of the disk.

3.4 DATA REDUCTION AND MODEL DEVELOPMENT

The results of the Edge Notched Disk test and the High Energy Crushing Test will be compared in order to investigate and develop relationships between fracture toughness and specific comminution energy and fracture toughness and breakage distribution. Since the closed side set is the only HECT parameter that is variable, the specific comminution energy, E_c, and breakage function, B, are expected to be functions of fracture toughness and reduction ratio. Regression analysis will be performed using *Microcal Origin 6.0*.

The fracture toughness results will also be used to modify Equation 2.12, which is used to estimate capacity of a jaw crusher and is dependent upon a parameter related to the nature of the material crushed. It is proposed that fracture toughness can be used to define this parameter. Lab-scale crushing tests will be conducted in order to determine how fracture toughness can be used in this regard.

3.5 LABORATORY SCALE CRUSHING TESTS

The power of the models developed from analysis of the END test and HECT test results will be assessed by comparing the predicted and actual results generated from lab-scale crushing tests. The laboratory crusher results will also be used to develop a fracture toughness based model for the prediction of jaw crusher capacity.

3.5.1 CRUSHING EQUIPMENT

The tests will be performed using a 102 mm by 152 mm single-toggle, overhead eccentric, Blake-type, Morris jaw crusher with a feed opening of 75 mm.

3.5.2 ROCK SAMPLES

Rock samples from *Luck Stone's* Boscobel, Culpeper, Shadwell, and Spotsylvania operations will be used. The samples were collected from aggregate product piles. Figure 3.15 shows the feed size distribution of the four samples.

3.5.3 TEST PROCEDURE AND DATA ACQUISITION

Each test will use approximately 35 kg of material. The material is fed to the crusher and the time required to reduce the size of the feed material is recorded. The open and closed side sets of the crusher are noted. The crushed product is collected and a sieve analysis is conducted in order to determine the product size distribution.

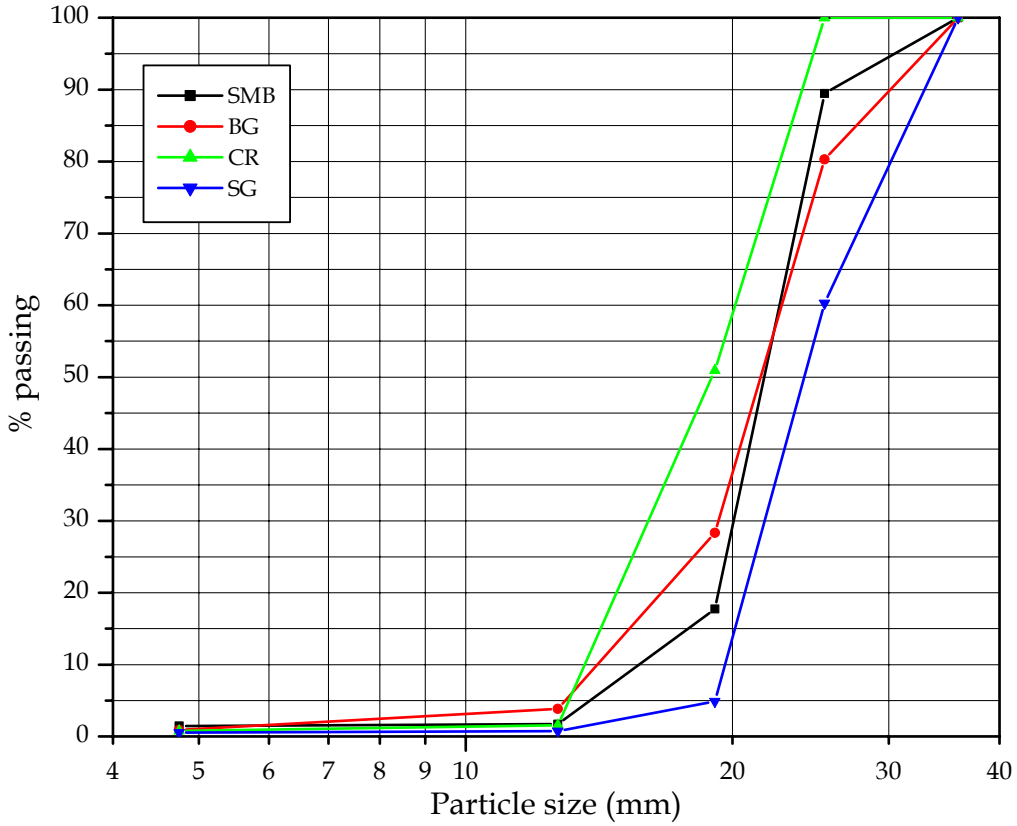

Figure 3.15 Feed size distribution of material fed to laboratory jaw

CHAPTER 4. EXPERIMENTAL RESULTS AND DISCUSSION

4.1 FRACTURE TOUGHNESS

Ten specimens of each rock type where tested in accordance with the END test procedure set forth in section 3.2. The results are shown in Table 4.1. Figure 4.1 displays the statistical scatter of test data for each rock (data points represent valid tests). Appendix I contains complete test data.

Table 4.1 Fracture toughness results

Rock Type	No. of specimens tested	No. of valid specimens	K_{Ic} (± SD) $MPa\sqrt{m}$
Shadwell Metabasalt (SMB)	10	7	1.411 ± 0.215
Boscobel Granite (BG)	10	5	0.601 ± 0.083
Culpeper Gray Siltstone (CRS)	10	10	1.454 ± 0.195
Culpeper Red Siltstone (CGS)	10	10	1.501 ± 0.262
Leesburg Diabase (LD)	10	10	1.254 ± 0.101
Thornburg Granite (TG)	10	10	1.045 ± 0.037
Spotsylvania Granite (SG)	10	8	0.843 ± 0.165

Of the seventy rock specimens tested, ten did not "qualify" as valid specimens. Three specimens of the Shadwell metabasalt and two specimens of the Spotsylvania granite did not meet the specimen size requirements set forth by Equation 2.40. The five invalid specimens of Boscobel granite did not fail at the notch (i.e., crack propagation ahead of the crack tip did not occur). This was due to the friable nature of the Boscobel granite, which consists of large grains with multiple planes of weakness. BG samples were difficult to prepare as often times the rock core would crumble or break apart while being sawed.

As was noted in section 2.5 and section 3.2, rock fracture toughness values show a dependence on grain size. The results in Table 4.1 support this trend. The Culpeper siltstone is a very fine-grained sedimentary rock and has the highest fracture toughness value. The metabasalt and diabase have slightly larger grain sizes and correspondingly have slightly lower K_{Ic} values. The granites follow in the same manner, with the Boscobel granite, consisting of fairly large grains, having the lowest fracture toughness. There may be a propensity for the K_{Ic} of coarse-grained rocks to be underestimated in comparison to fine-grained rocks when a notched specimen is used. This point will be considered when comparing fracture toughness and specific comminution energy.

Figure 4.1 indicates that the Culpeper siltstone rocks (red and gray) had very similar results. The mechanical properties given in Table 3.1 also show that the "two" rocks are virtually identical. Statistical analysis of the separate siltstone results shows that at a

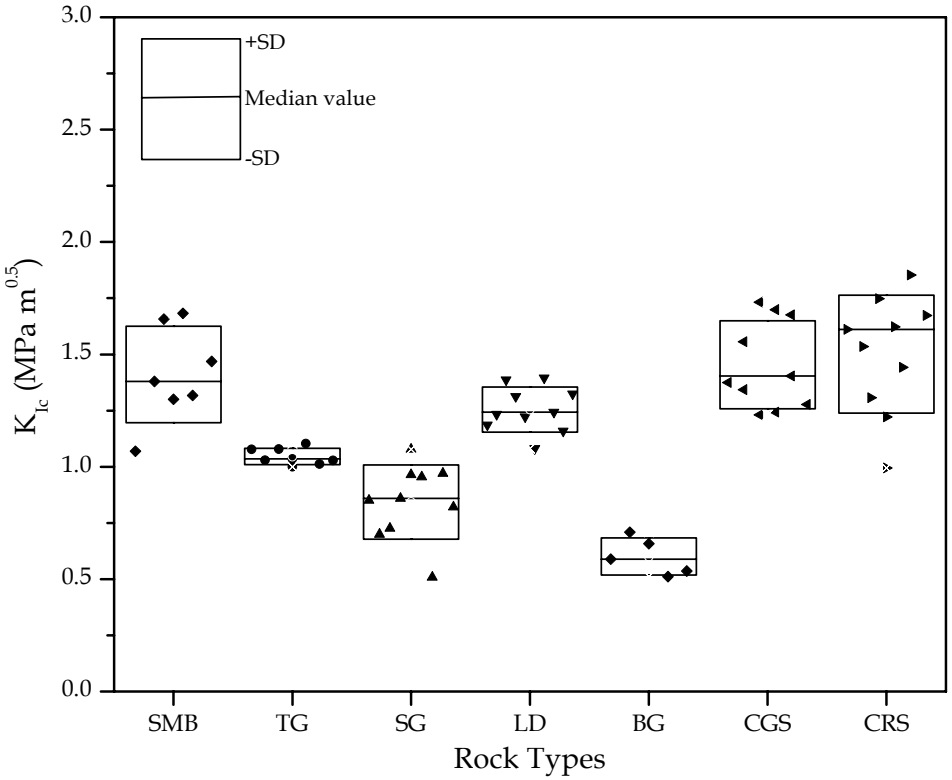

Figure 4.1 Fracture toughness data for all valid specimens

confidence level of 99% the average fracture toughness values are not significantly different. Unless significant differences in red and gray siltstone behavior are observed during single particle breakage, the test values of the two rocks will be pooled and the rocks considered as one type/sample.

For all valid test specimens fracture initiated at the notch tip. Fracture propagation did not always occur in a direction parallel to the notch tip nor was the crack surface planar. The crack surfaces of the Spotsylvania and Thornburg granites wandered towards planes of foliation but never directly along them. Crack propagation occurred along planes of weakness represented by narrow veins of mineral infilling in the Boscobel granite. The granites were more susceptible to changes in heterogeneity and the continuity of crack growth was affected by changes in local structure ahead of a crack tip. The metabasalt and diabase demonstrated somewhat more "parallel" crack propagation, with the Culpeper rocks almost always exhibiting parallel propagation. All the rocks had somewhat non-planar crack surfaces, most likely due to friction and inter-locking.

Figures 4.2 through 4.4 show the correlation between fracture toughness and the major mechanical properties of each rock (compressive strength, tensile strength, and elastic modulus). As would be expected, fracture toughness and tensile strength exhibit a strong correlation since tensile stresses are responsible for the opening of flaws or cracks

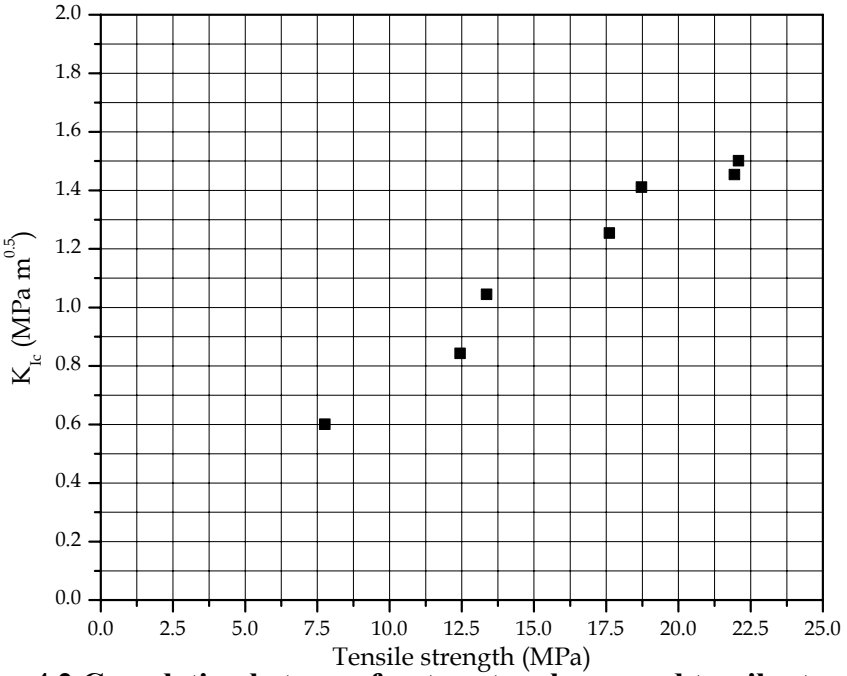

Figure 4.2 Correlation between fracture toughness and tensile strength

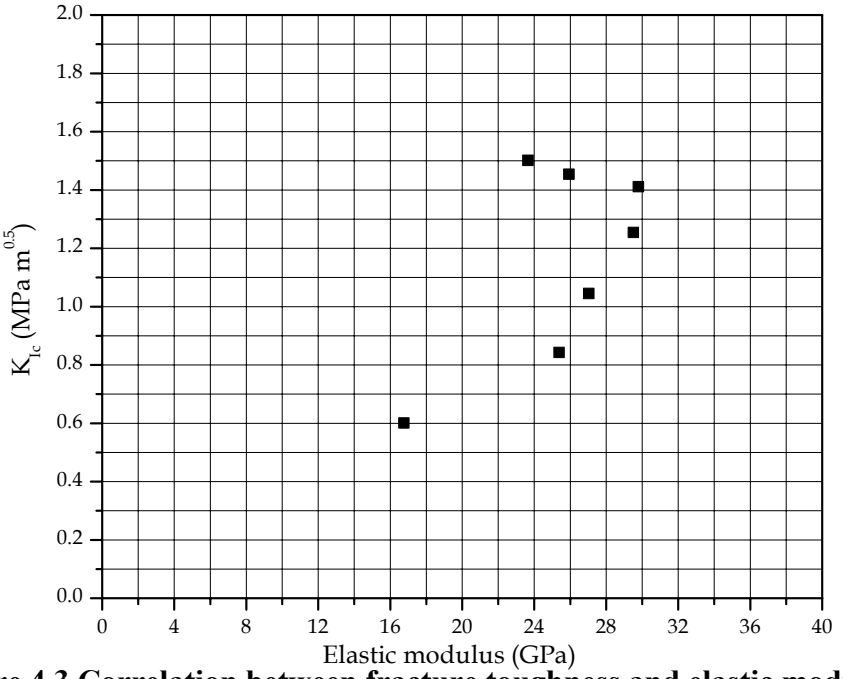

Figure 4.3 Correlation between fracture toughness and elastic modulus

within rock materials, particularly under conditions of point contact loading. There does not seem to be much of a link between K_{Ic} and elastic modulus but it is interesting to note that the Culpeper siltstones, with the highest fracture toughness values, are among the softer rocks or lower modulus rocks. Two vertical lines have been added to Figure 4.4,

one at 69 MPa and the other at 138 MPa. The lines represent the cut-offs for material ranked soft and material ranked average, for crushing applications, according to Table 2.2. Above 138 MPa rocks are considered hard and supposed to require full power draw. In Figure 4.4 it can be seen that five of the rocks would be considered hard but that the three rocks that showed the highest resistance to fracture are not the hardest according to the rankings.

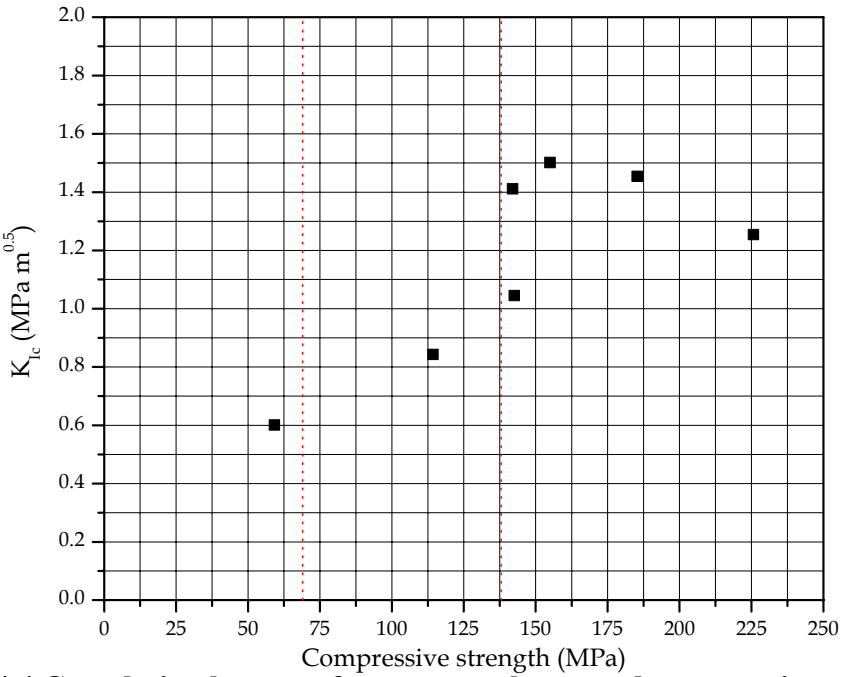

Figure 4.4 Correlation between fracture toughness and compressive strength

4.2 SINGLE PARTICLE BREAKAGE

High Energy Crushing Tests were conducted in accordance with the procedure set forth in section 3.3. Approximately twenty specimens of each rock were tested at each reduction ratio. The reduction ratio for the first series of tests was 1.50, corresponding to a closed side set of 31.75 mm. The second series of tests was conducted at a reduction ratio of 2.97 with the closed side set equal to 16.00 mm. Data collection included particle strength (tensile), specific comminution energy, and breakage size distribution. A comprehensive catalog of HECT data can be found in Appendix II and Appendix III.

Again, the red and gray Culpeper siltstones did not exhibit different behavior, with the data for each rock not statistically different. From this point forward the individual results for the red and gray siltstones will be shown since they were considered separate rocks when tested, but for comparative purposes (section 4.3) their results will be pooled and presented as one rock, Culpeper siltstone.

4.2.1 PARTICLE STRENGTH

Table 4.2 summarizes the dynamic tensile strength results from both HECT series. Particle strength data was collected in order to compare traditional rock properties collected under conditions of slow displacement with a strength property measured under the dynamic or high strain rate conditions seen in a jaw crusher. The compressive strength, tensile strength, and elastic modulus of each rock were tested under displacement control at a rate of 0.003 mm/s. As was mentioned in section 3.3, the crushing tests were conducted at a rate of 386 mm/s. Additionally the dynamic tensile strength was compared to the fracture toughness in order to verify that mode I crack opening is applicable to the crack displacement behavior of particles under point contact loading.

Table 4.2 Tensile strength measured in HECT tests

Rock Type	**Reduction Ratio 1**	**Reduction Ratio 2**
	Tensile Strength (± SD) *MPa*	**Tensile Strength** (± SD) *MPa*
Shadwell Metabasalt (SMB)	21.69 ± 4.10	24.80 ± 6.89
Boscobel Granite (BG)	11.90 ± 5.84	10.03 ± 3.46
Culpeper Gray Siltstone (CRS)	27.51 ± 3.22	26.29 ± 2.85
Culpeper Red Siltstone (CGS)	28.89 ± 3.69	26.41 ± 4.93
Leesburg Diabase (LD)	26.45 ± 3.93	25.72 ± 3.28
Thornburg Granite (TG)	17.60 ± 4.72	16.16 ± 2.88
Spotsylvania Granite (SG)	13.58 ± 4.13	15.71 ± 3.86

Care had to be taken when determining the load that caused initial fracture. The HECT/*DATA 6000* set-up only records the peak load, which in some instances occurred after fracture had already initiated and represented a smaller daughter fragment being loaded. In these instances the force curve produced by the *DATA 6000* acquisition system was used to distinguish the point at which fracture first initiated and the corresponding load on the disk specimen at that time. In all other instances the peak load recorded by the *DATA 6000* represented the failure load.

On average the increased displacement rate resulted in about a 29% increase in tensile strength for each rock. The data in table 4.2 indicates that, for each rock, there is little to no change in the dynamic tensile strength at the two reduction ratios. The change in reduction ratio would not be expected to influence the measured particle strength, as there is no change in strain rate between the ratios, only a change in total strain. The peak fracture load would be more affected by a change in either the crushing speed/frequency or the throw.

Figures 4.5 through 4.8 show the relationships between dynamic tensile strength and tensile strength, elastic modulus, compressive strength, and fracture toughness. Figures

4.5, 4.6, and 4.7 indicate that, for the rocks tested here, the relationships/correlations between dynamic tensile strength and tensile strength, elastic modulus, and compressive strength are almost identical to those between fracture toughness and those latter properties (compare to Figures 4.2 – 4.4). This is evident also by the strong correlation between dynamic tensile strength and fracture toughness seen in Figure 4.8. The strong correlations of dynamic tensile strength with tensile strength and fracture toughness again signify that fracture under point contact loading is due to induced tensile stresses. It is also clear that under rapid loading the magnitude of the induced tensile stresses increases but the fundamental mechanical behavior of rocks is unchanged (i.e., the increase in tensile strength is approximately proportional for all rocks).

The relationships among fracture toughness, dynamic tensile strength, and tensile strength highlight the application of fracture toughness as a strength parameter. When the proper crack opening displacement mode is identified for a given situation, fracture toughness effectively characterizes a material's resistance to fracture. In the case of jaw crushers, tensile stresses open cracks and the ability of mode I fracture toughness to assess a rock's resistance to breakage is shown by the strong correlation between fracture toughness and both tensile strength measurements. In other instances though, for example cone crushing, particles may also be subjected to shear stresses and mode III (mixed-mode/tearing) fracture toughness may be more applicable. The ability of fracture toughness to characterize a rock's resistance to fracture is dependent upon an understanding of the stress situation within the particle under the load action of the size reduction machine.

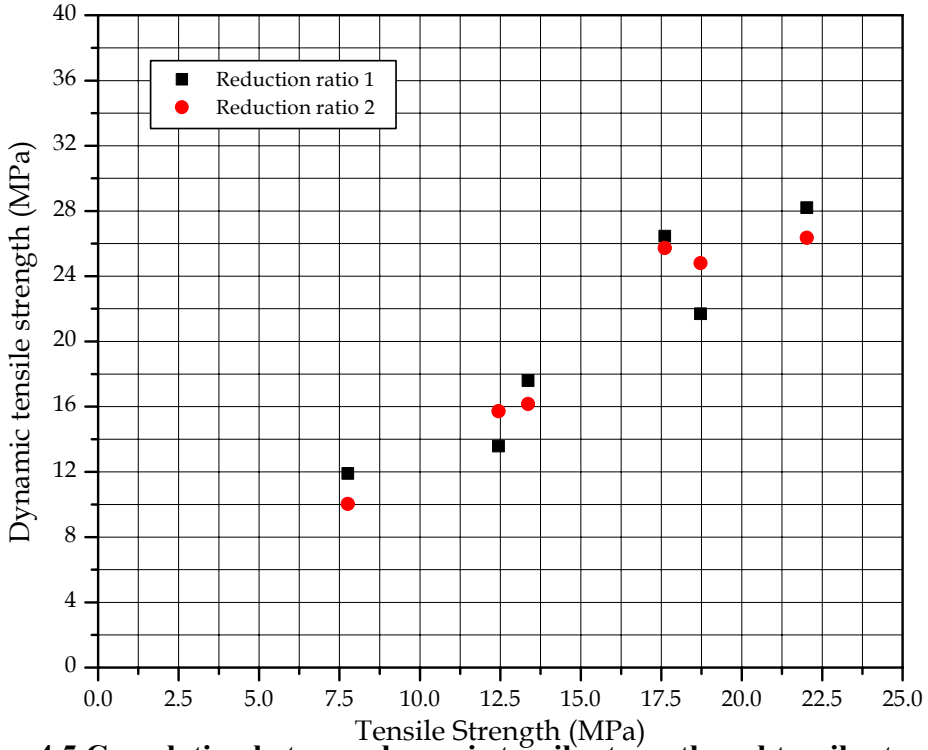

Figure 4.5 Correlation between dynamic tensile strength and tensile strength

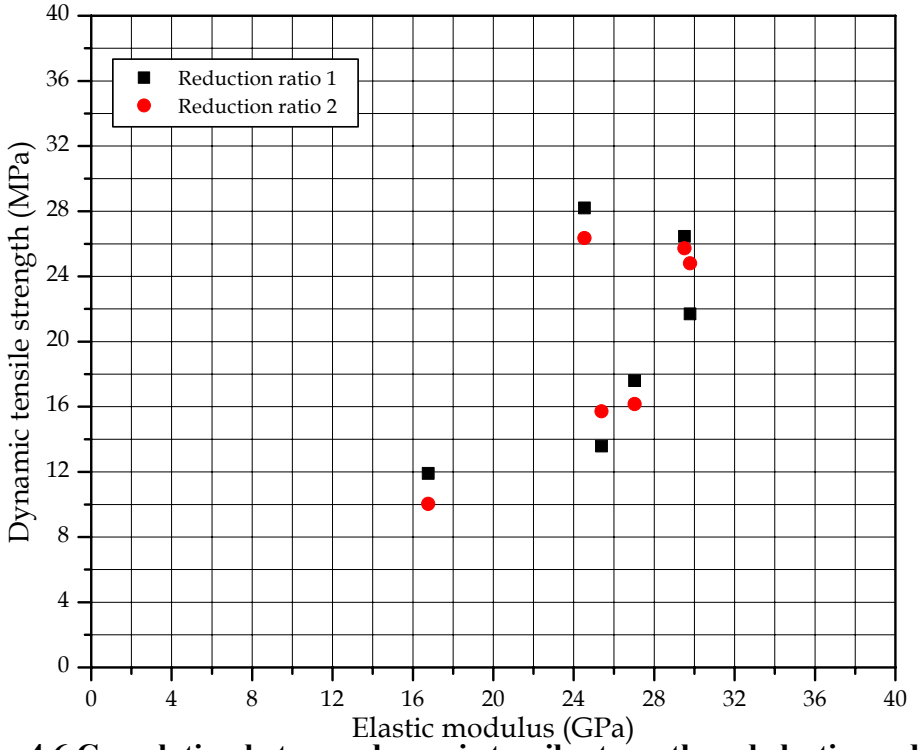

Figure 4.6 Correlation between dynamic tensile strength and elastic modulus

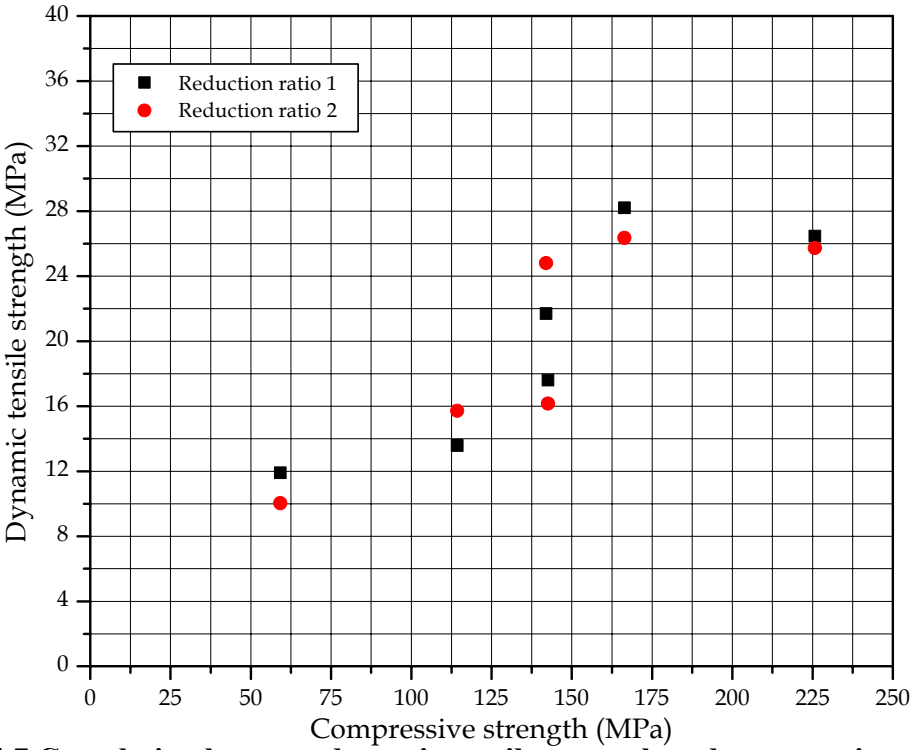

Figure 4.7 Correlation between dynamic tensile strength and compressive strength

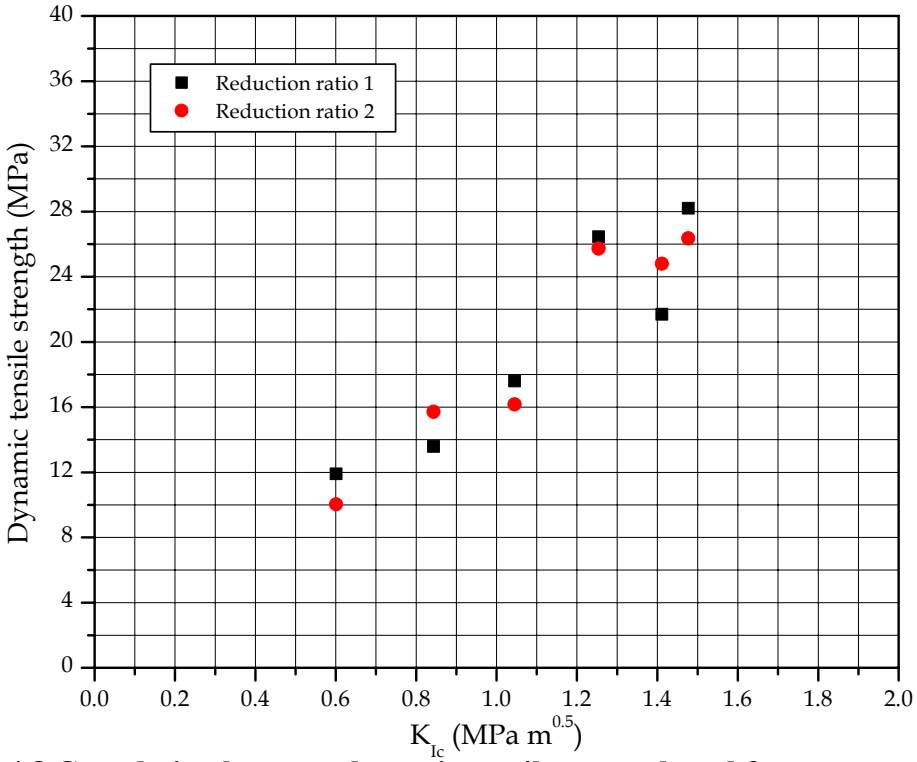

Figure 4.8 Correlation between dynamic tensile strength and fracture toughness

4.2.2 SPECIFIC COMMINUTION ENERGY

The *DATA 6000* waveform analyzer developed a power curve for each test specimen using the stroke and force input signals. The area under the power curve, initiating at the point of first fracture and ending at the moment the actuator began to retract, was calculated by the *DATA 6000* in order to determine the net crushing energy. The net crushing energy divided by the mass of the specimen is the specific comminution energy, the energy required to reduce the size of the particle for the given operating conditions (in kilowatt-hours per metric ton). Table 4.3 lists the specific comminution energy results for each rock at each reduction ratio. Individual specimen data can be found in Appendix II.

Figures 4.9 through 4.15 are sample HECT plots representing "typical/average" behavior for each rock at each reduction ratio. The visual quality of the plots is poor and the velocity curve developed by the DATA 6000 is quite ragged. This is a result of differentiation of the digitally recorded stroke signal processed from an analog input signal. Despite the ragged appearance there is little to no difference between the digitally processed velocity curve and one developed from direct differentiation of the analog signal (Allis-Chalmers, 1985). Also note that for the stroke signal (BUF.A1) one volt is equivalent to 10.16 mm and for the load signal (BUF.A2) one volt is equivalent to 15.57 kN.

Table 4.3 Specific comminution energy results from the HECT

Rock Type	Reduction Ratio 1	Reduction Ratio 2
	E_c *kWh/t*	E_c *kWh/t*
Shadwell Metabasalt	0.407	0.550
Boscobel Granite	0.105	0.230
Culpeper Grey Siltstone	0.292	0.350
Culpeper Red Siltstone	0.298	0.320
Leesburg Diabase	0.371	0.477
Thornburg Granite	0.272	0.384
Spotsylvania Granite	0.233	0.356

Figures 4.9 through 4.15 show the behavior of the rocks under jaw crusher conditions. At the start of the crushing cycle the actuator, which represents the swing jaw, moves towards the particle following the predefined haversine path. When the actuator comes in contact with the particle there is a sharp increase in the load and a corresponding increase in power consumption. Failure of the particle occurs quite rapidly (within approximately 1 μs) and is followed by a sharp decrease in load. The power also drops off after failure. Since particle failure requires only small amount of strain input the actuator continues to move upward (i.e., the crusher chamber continues to close). Fragmented particles remaining inside the crushing chamber (Figure 3.13) with dimensions greater then the closed side set are crushed under the continued displacement of the actuator. This is depicted by post-failure increases in the load and power signals. After traveling the throw distance the actuator begins to retract and particle crushing ends.

The HECT plots along with the results in Table 4.3 reveal that the rocks that required the most energy to crush also experienced the most secondary breakage. Secondary breakage is the crushing of daughter fragments after particle failure. The Culpeper siltstones exhibited the smallest amounts of secondary breakage. Even the Boscobel granite, which on average required less energy to crush than the siltstones, underwent more secondary crushing, i.e., a larger percentage of the total specific comminution energy was a result of secondary breakage. The siltstones required more energy to initiate fracture due to their high strength, low elastic modulus behavior, and thus more of the actuator displacement was "used" during particle failure. In comparison to the other rocks the Culpeper siltstones take approximately 43% to 94% more strain to fail (based on tensile strength and elastic modulus).

The strain at failure is very small in comparison to the total displacement of the actuator and a more significant explanation for the siltstone's behavior is needed. During testing it was observed that the siltstones tended to shatter producing thin, flat daughter fragments. This was a result of "ideal" disk splitting. Under diametrical compression

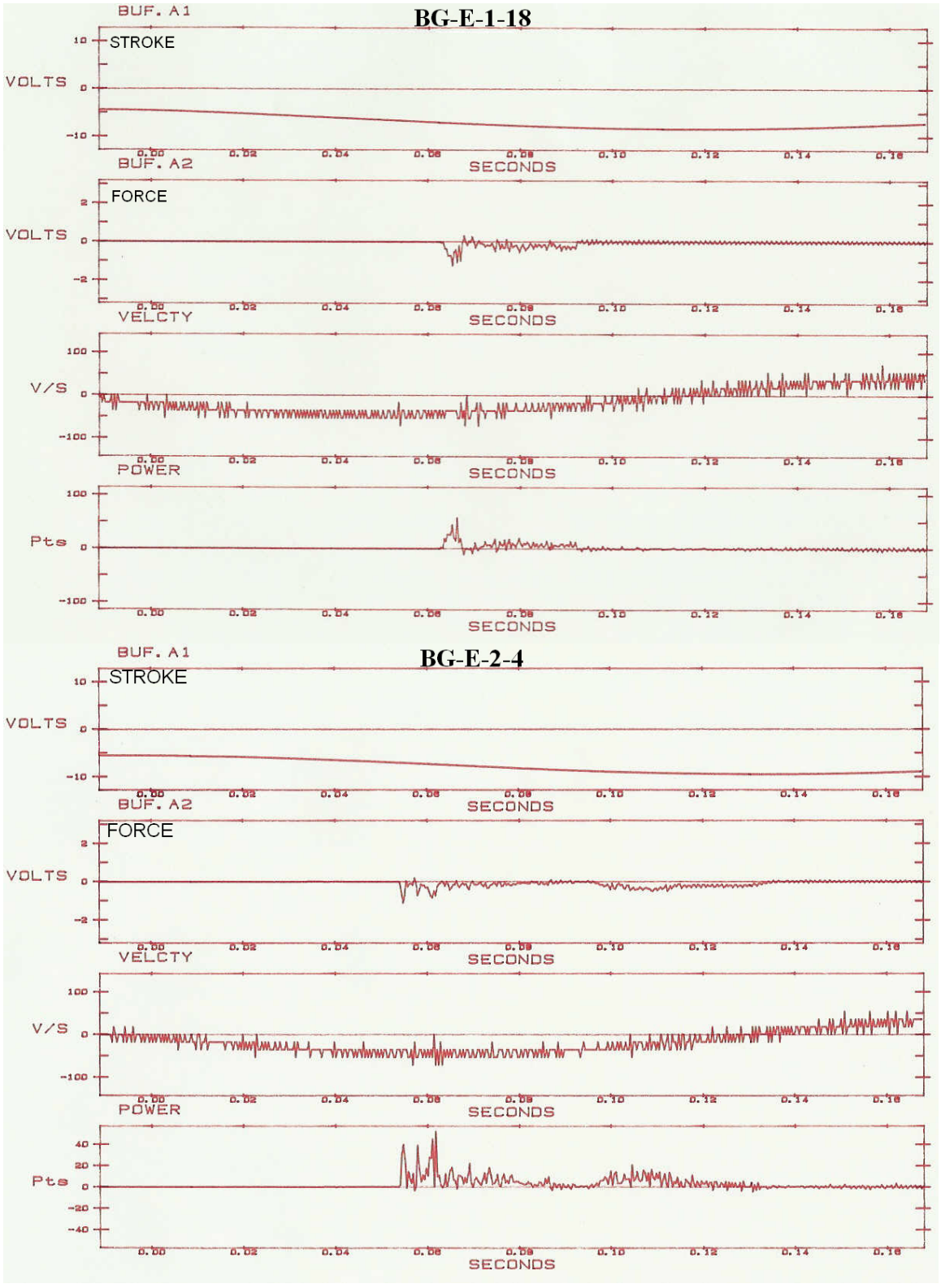

Figure 4.9 Typical BG HECT behavior: CSS 1 (top) and CSS 2 (bottom)

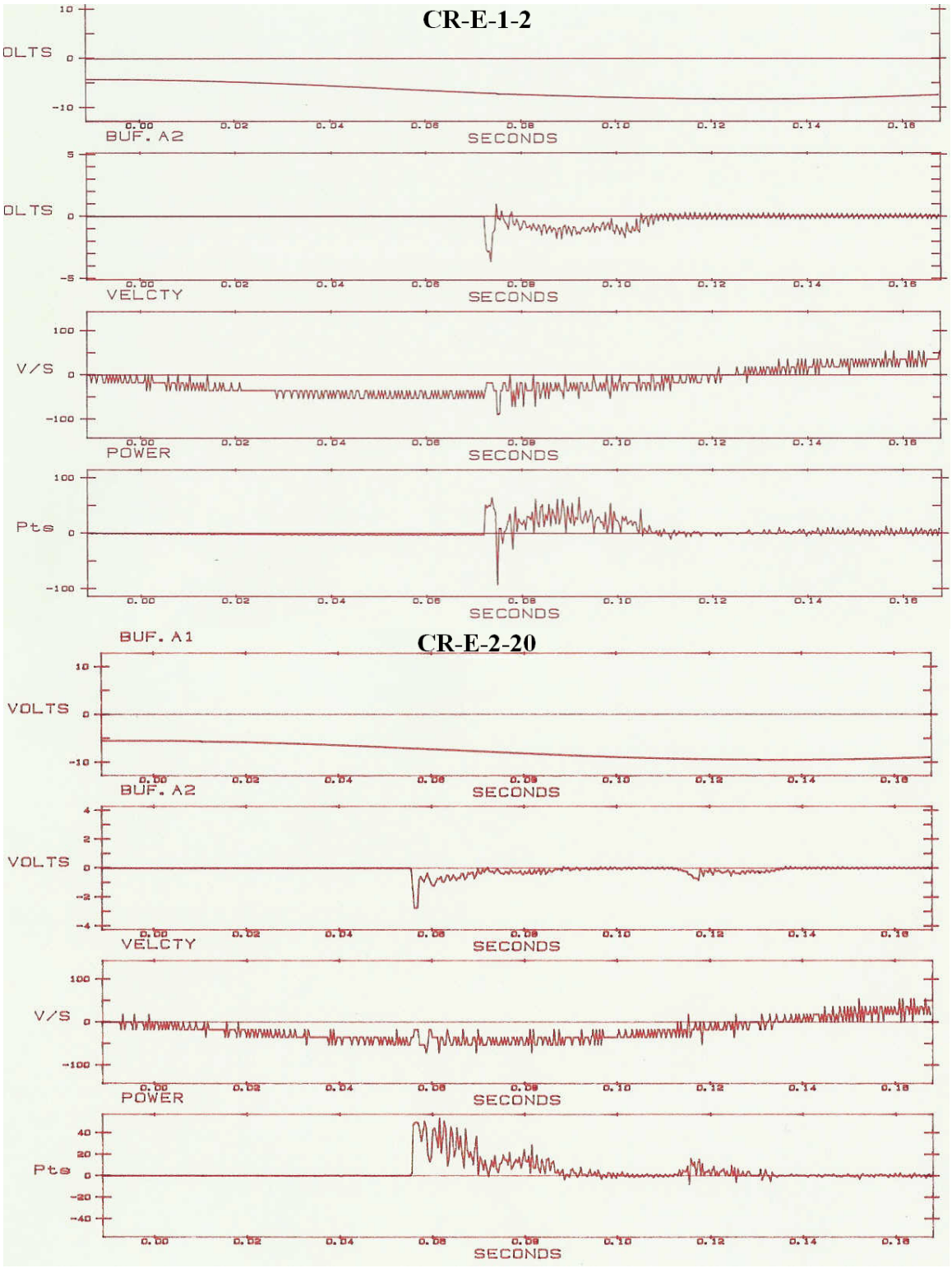

Figure 4.10 Typical CRS HECT behavior: CSS 1 (top) and CSS 2 (bottom)

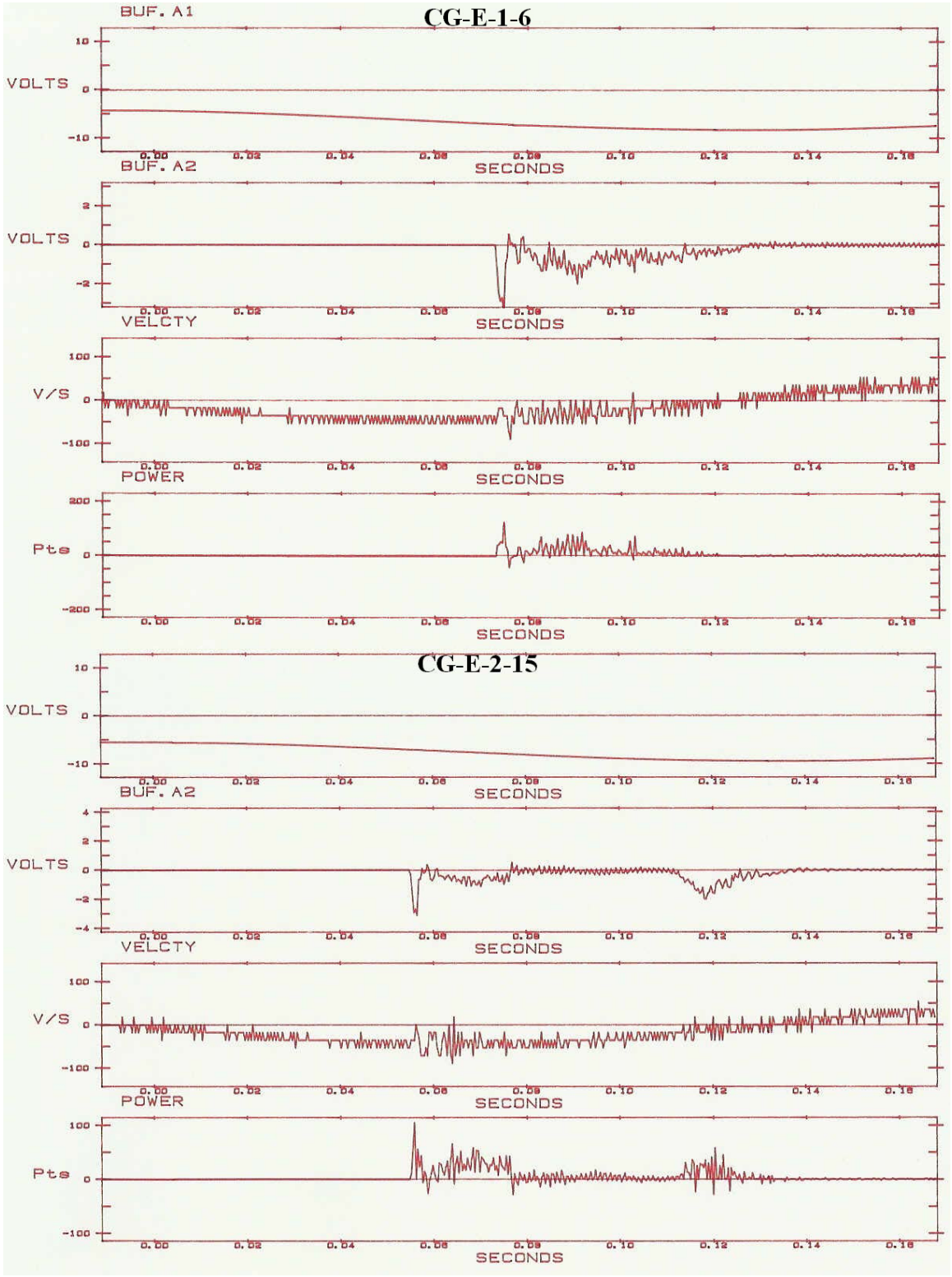

Figure 4.11 Typical CGS HECT behavior: CSS 1 (top) and CSS 2 (bottom)

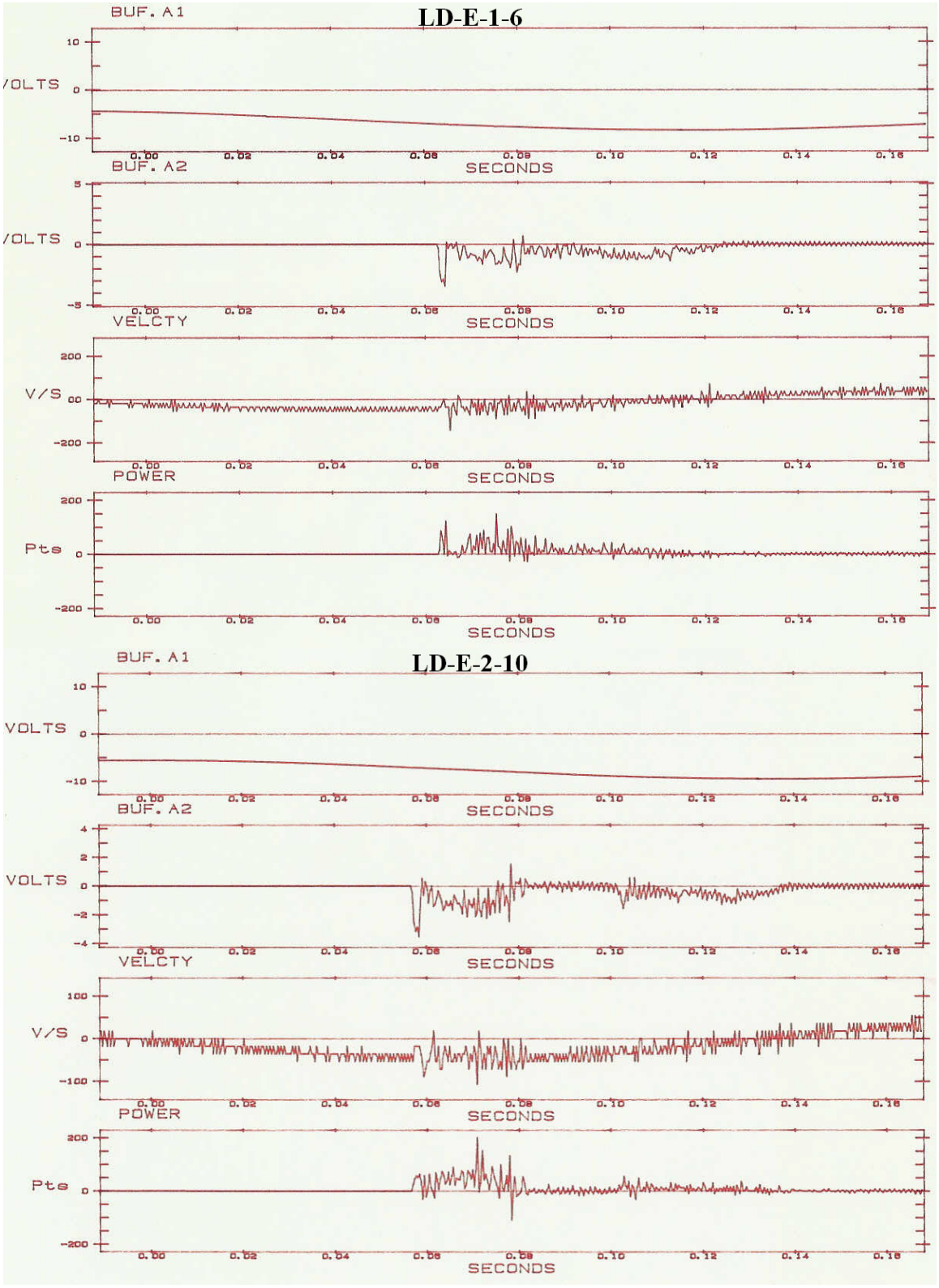

Figure 4.12 Typical LD HECT behavior: CSS 1 (top) and CSS 2 (bottom)

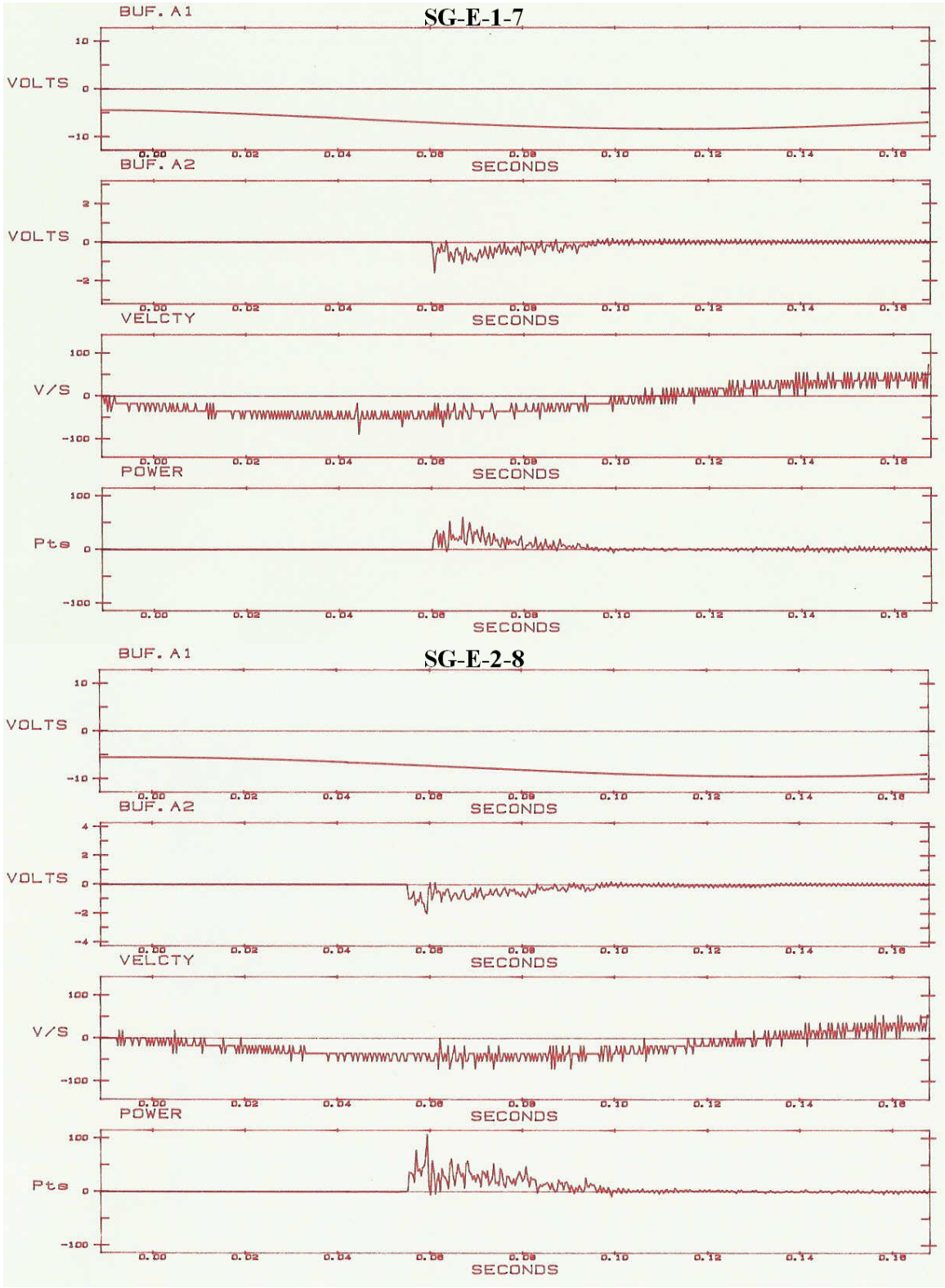

Figure 4.13 Typical SG HECT behavior: CSS 1 (top) and CSS 2 (bottom)

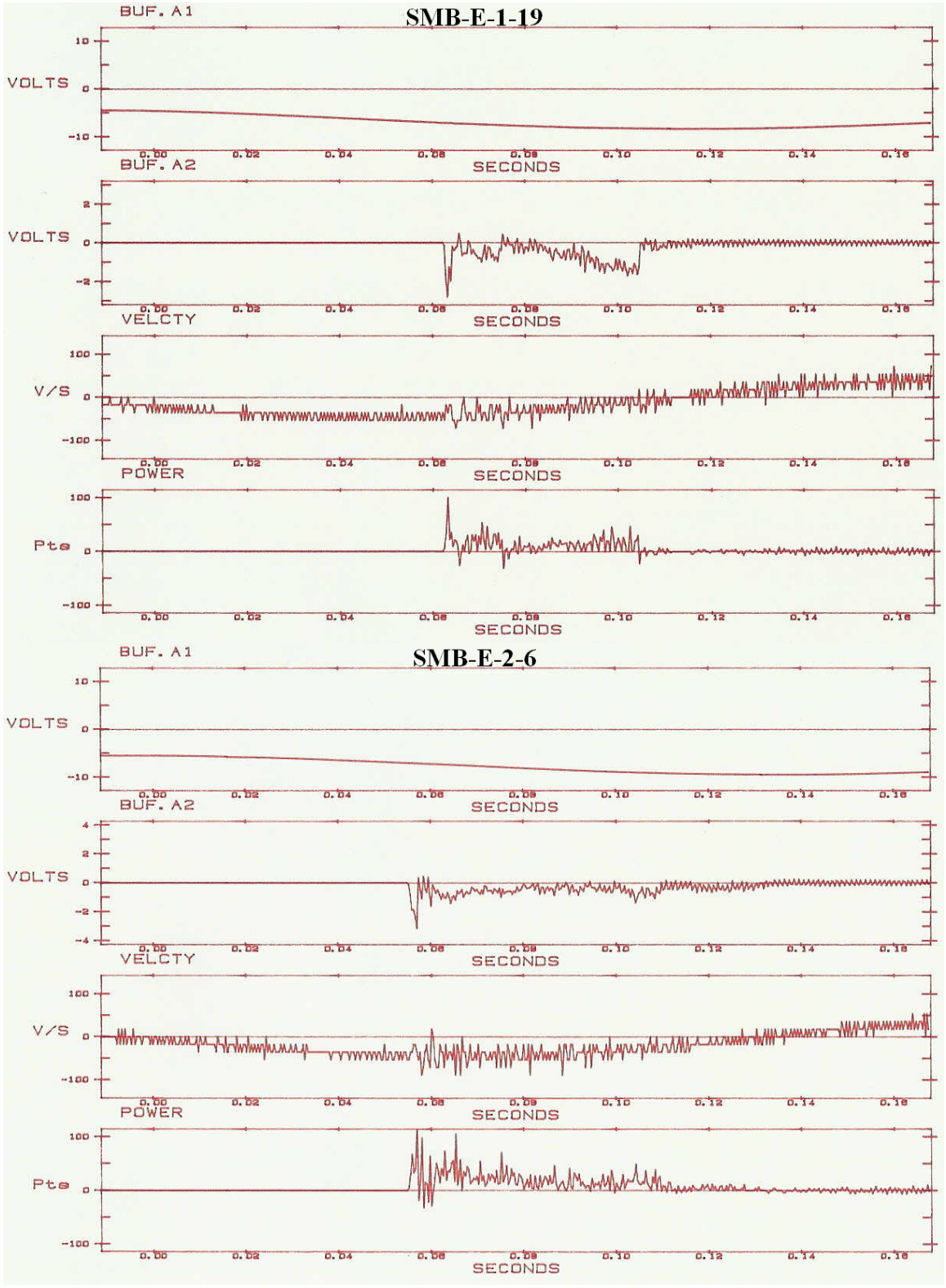

Figure 4.14 Typical SMB HECT behavior: CSS 1 (top) and CSS 2 (bottom)

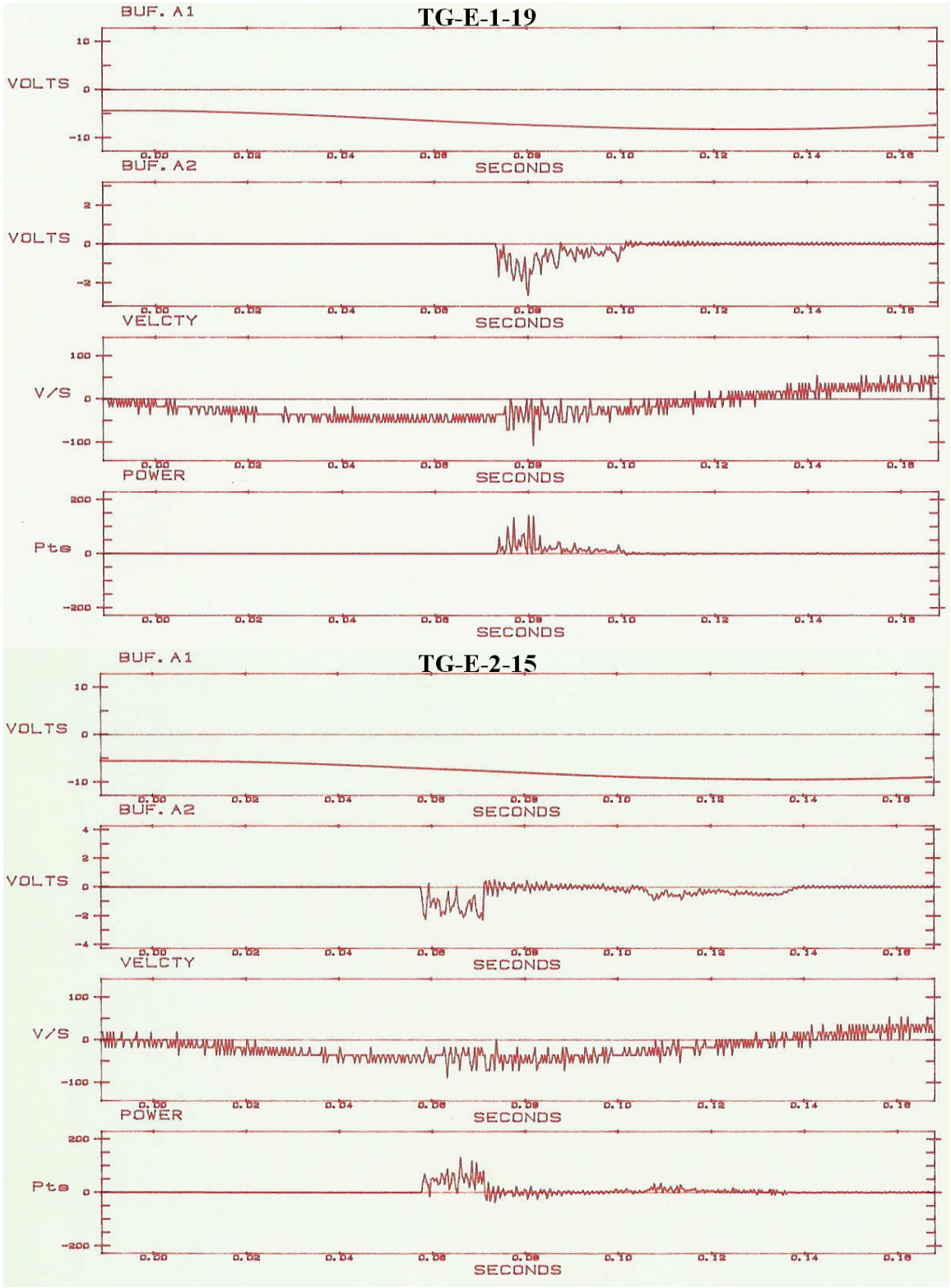

Figure 4.15 Typical TG HECT behavior: CSS 1 (top) and CSS 2 (bottom)

fracture initiates at the center of a disk and typically propagates in a straight line towards the load contact points. Additional displacement results in fracture planes on each side and parallel to the first plane. The result is rectangular plate-like fragments. Under rapid displacement rates of the HECT system these fragments move outward and away from the contact points at velocities greater than the velocity of the actuator. The daughter fragments of the Culpeper rocks either exited the crushing chamber or fell in such a way that their relative thinness, in comparison to the CSS, prevented any further crushing. Crack propagation in the other rocks, based on observations from fracture toughness testing, most likely did not occur in a straight path, resulting in larger and more irregularly shaped daughter fragments that were subject to additional breakage. These rocks experienced more cleavage fracture, particularly at the lower reduction ratio. This also implies that shatter and cleavage are not only functions of the type of crushing machine used but also of the fracture behavior of the material.

The increase in reduction ratio resulted in an increase in specific comminution energy. The increase in energy was due to the larger amount of secondary breakage that occurs at larger reduction ratios. Since the energy required for initial fracture essentially did not vary between reduction ratios (assuming load at first fracture and dynamic tensile strength are representative of the energy required to initiate fracture), the amount of crushing that occurs after initial breakage is dependent upon the post-failure strain input into the particle. A decrease in the closed side set of the HECT system results in more post-peak displacement and significant secondary crushing of daughter fragments.

Although an energy increase due to an increase in reduction ratio was seen for each rock changes in crusher reduction ratio (or CSS) cannot be expected to have a universal effect on all rocks. Table 4.3 indicates that the Culpeper siltstones saw the smallest increase in specific comminution energy, an average of 0.040 kWh/t. The other five rocks exhibited an increase that ranged between 0.106 - 0.143 kWh/t (average of 0.122 kWh/t). The dissimilar behavior, or variance in the degree of behavior, of the Culpeper siltstone is a result of the mechanical and fracture properties of the rock. Again the shattering behavior shown by the siltstones resulted in the exiting of daughter fragments from the crushing chamber. More secondary breakage of the siltstone is only possible if the crusher speed is increased such that the actuator is able to "close" in and make contact with daughter fragments before they exit the crushing chamber.

The specific comminution energy results were compared to the mechanical properties of the rocks, as well as the fracture toughness results and dynamic tensile strength results. Figures 4.16 - 4.20 show the correlations between E_c and these properties for each reduction ratio. The strongest correlations are between E_c and tensile strength and E_c and fracture toughness. Since tensile strength and mode I fracture toughness are most representative of the stress situation within a particle under point contact loading and the energy required for fracture is dependent upon, among other things, the stress applied to the particle, the strength of these correlations is not unexpected. More significantly, the correlation between E_c and K_{Ic} is stronger than that between tensile strength and E_c.

Assessing the fracture resistance of a rock particle in terms of a property that relates the fracture strength of the particle to the presence of flaws within the particle normalizes the effect and variation of stress magnitude. Tensile strength is an ultimate strength criterion and is based strictly on the magnitude of stress that a particle can withstand. It is very applicable to situations where tensile stresses lead to fracture by opening cracks and flaws but it is subject to more variation since no account is made for the presence or geometry of those flaws.

A limiting relationship between E_c and elastic modulus is evident in Figure 4.17, with a stronger correlation for the larger reduction ratio. The specific comminution energy seems to increase exponentially with elastic modulus, although more very stiff rocks (E > 28 GPa) would need to be tested in order to suggest such a relationship. Some correlation between specific comminution energy and compressive strength is indicated in Figure 4.18 for reduction ratio 1. The correlation loses its power significantly with an increase in reduction ratio. Compressive strength most likely correlates fairly well with E_c at low reduction ratios where power consumption is more dependent upon the material strength. At higher reduction ratios the specific comminution energy is more dependent on the fracture and elastic properties, i.e., fracture strength, crack propagation, and strain energy release rate. Figure 4.20 illustrates the relationship between E_c and dynamic tensile strength, which is more scattered than expected due to the low dynamic tensile strength of the Shadwell metabasalt.

The relationship between E_c and K_{Ic} in Figure 4.19 may be skewed somewhat by the results of the Edge Notched Disk test. It is widely accepted that rock fracture toughness measurements and values show a dependence on grain size. This dependency is evident in the fracture toughness values presented here and was discussed in section 4.1. The data presented in Figure 4.19 show that the Culpeper siltstones have the highest fracture toughness values yet the corresponding specific comminution energy values for those rocks fall in the middle to bottom third of the overall results. In fact the relationship between E_c and K_{Ic} is essentially linear except for the Culpeper siltstones. Based on the grain size effect, the fracture toughness values of the other, larger grained rocks may be underestimated, resulting in a left-shift of their data. If this is the case the correlation between E_c and K_{Ic} may in fact be stronger than is demonstrated.

The most important aspect of the HECT specific comminution energy results is that fracture toughness correlates the strongest with E_c in comparison to other rock properties. Based on the physics of fracture and the fact that the energy required to fracture a particle is dependent on the stresses applied to it, its mechanical properties, and the presence of flaws, it is no revelation that Mode I fracture toughness is related to the energy required to reduce the size of a particle under point contact loading. Another important result is that the relationship between E_c and K_{Ic} remains evident even when changes in reduction ratio are made. The energy required to crush rock material is a clearly function of its resistance to fracture and the amount of strain input by the crushing machine.

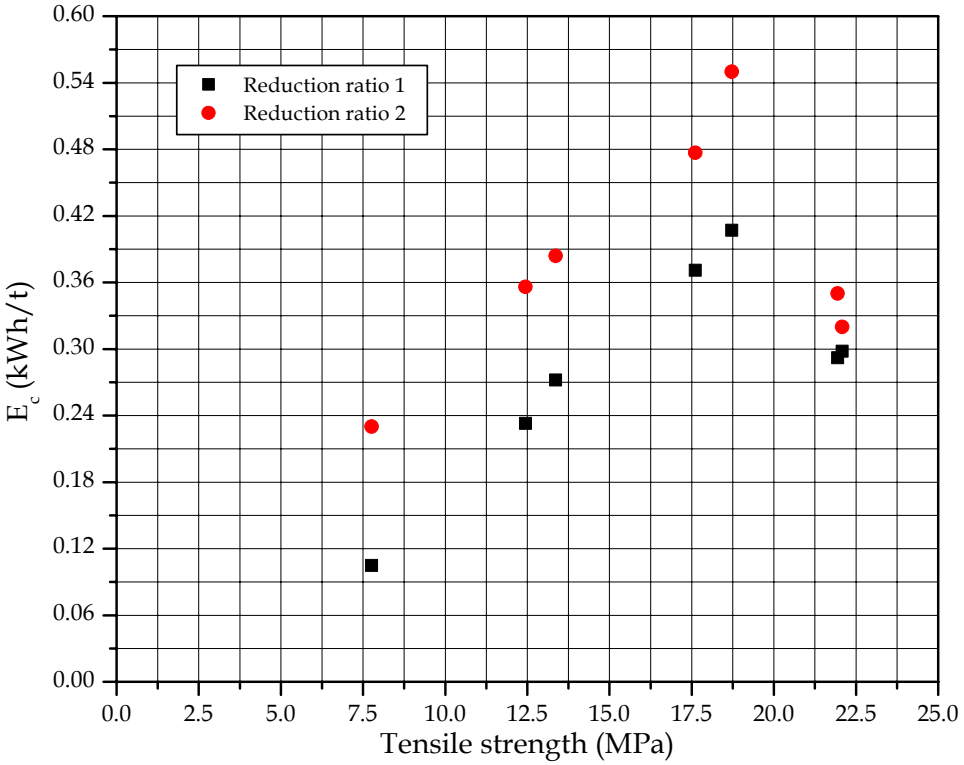

Figure 4.16 Correlation between E_c and tensile strength

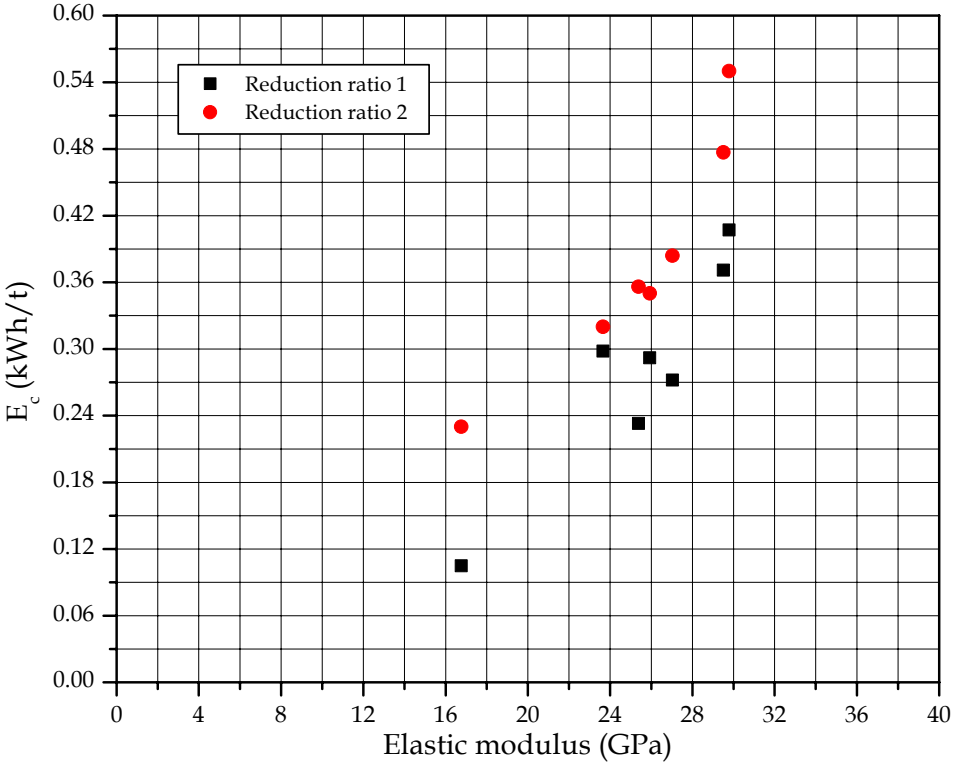

Figure 4.17 Correlation between E_c and elastic modulus

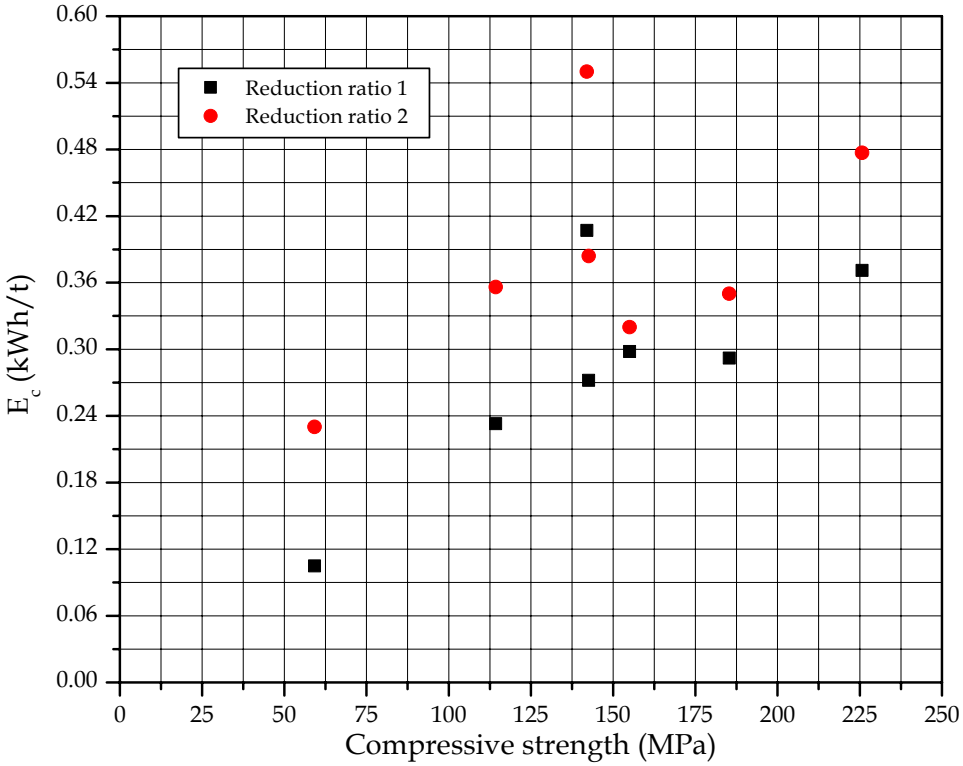

Figure 4.18 Correlation between E_c and compressive strength

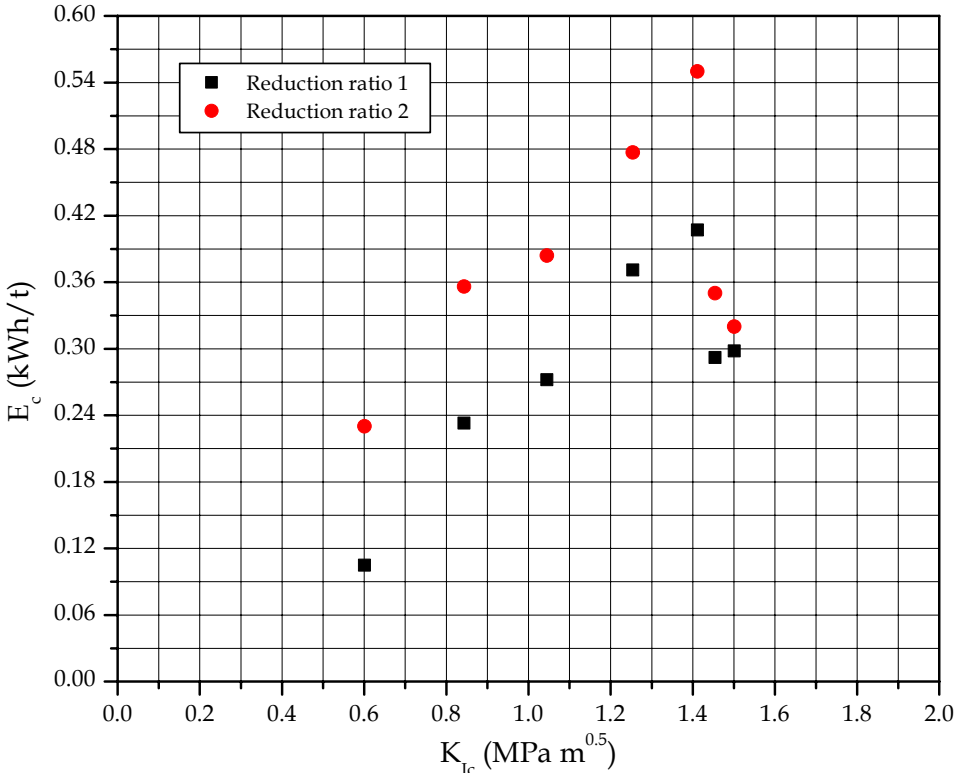

Figure 4.19 Correlation between E_c and fracture toughness

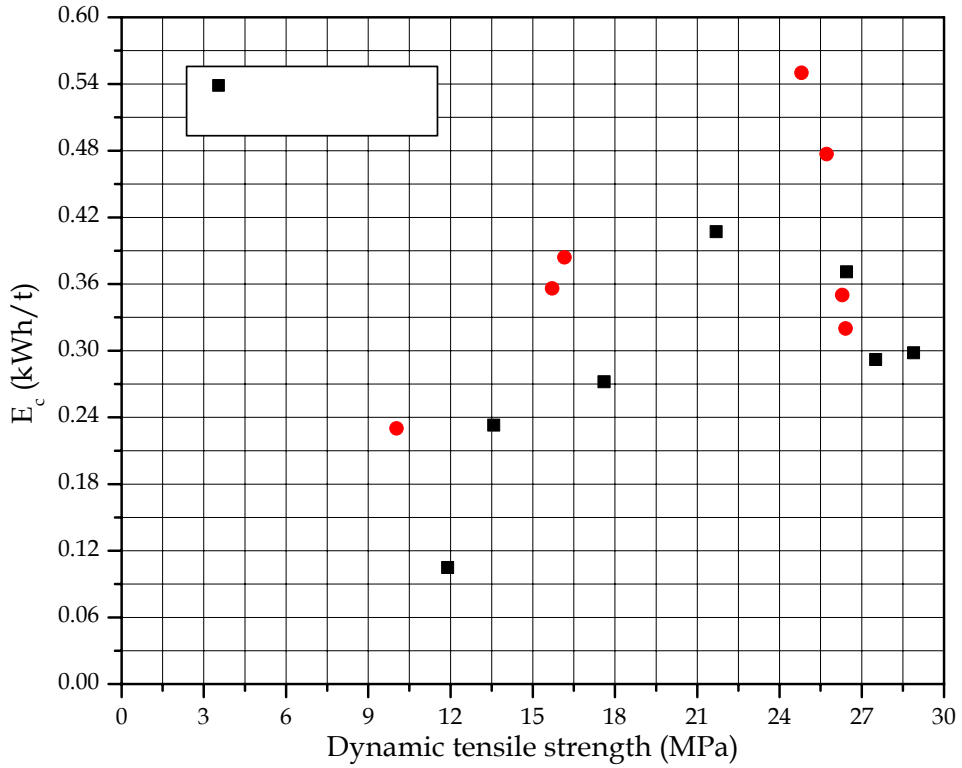

Figure 4.20 Correlation between E_c and dynamic tensile strength

4.2.3 BREAKAGE FUNCTION

After single particle breakage was conducted the pooled samples for each rock were sieved in order to determine the fragmented size distribution. A $\sqrt{2}$ sieve series was used starting with an initial opening size of 38.1 mm and finishing with a 0.075 mm mesh opening size. The breakage distribution was determined by normalizing the fragmented sizes with the parent size. The parent size was taken to be the average diameter of the tested specimens. Appendix III contains the fragmented size distribution data.

The breakage functions for each rock, and for both reduction ratios, are displayed in Figures 4.21 and 4.22. In each instance all material passed at a fragmented size of approximately 0.8 of the parent size. In fact for each rock 100% of the fragmented material would have passed at a size close to 0.54 of the parent size. This is because disk specimens with thicknesses approximately one half of their diameter were used in this study. Under (small displacement) point contact loading, a disk, with dimensions $D \times D \times t$, tends to split in half and the resultant fragments have approximate dimensions of $D \times 0.5D \times t$. When the thickness is close to the radius of the disk, 100% of the broken fragments are retained on a sieve that has an opening equal to one-half of the parent size. There was some debate as to whether or not this behavior is typical of what occurs in an actual crusher. If the irregular particles crushed in actual machines are idealized as

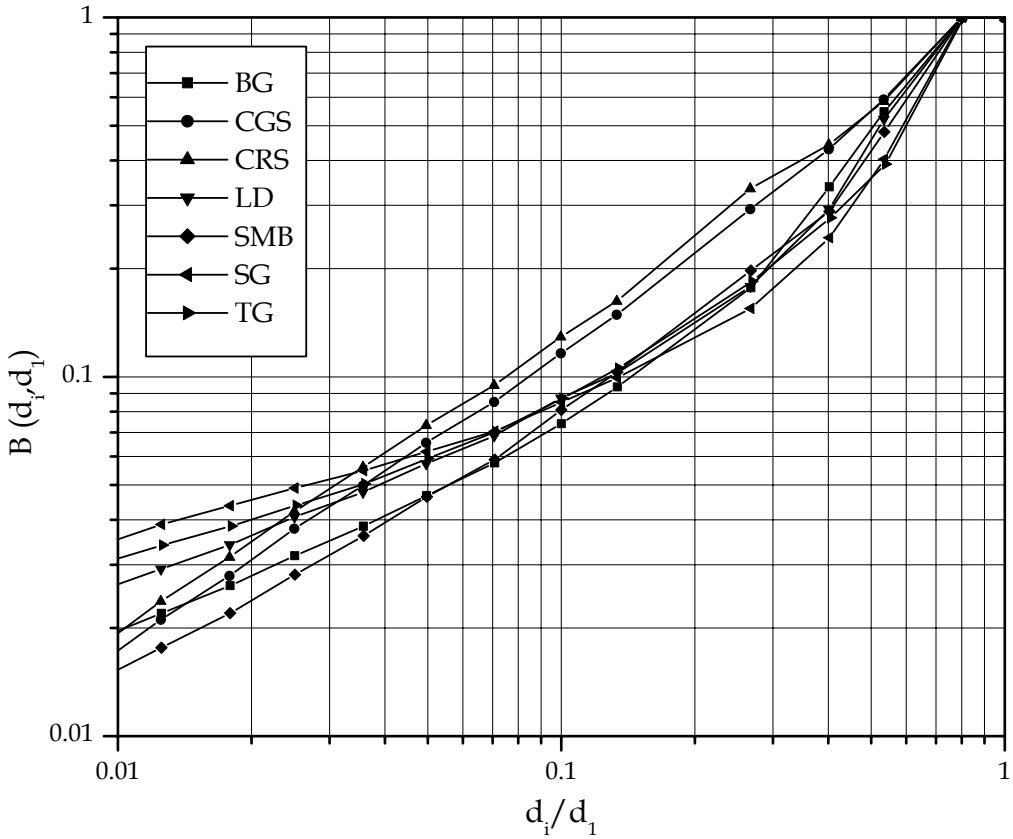

Figure 4.21 Breakage functions for each rock at reduction ratio 1

spheres, then disk specimens with thicknesses near one half of their diameters are also representative of irregular particles. Small displacement, point contact loading of a sphere will result in four "lune" pieces with dimensions $D \times 0.5D \times 0.5D$, which also results in 100% of the fragmented pieces being retained on a sieve that has an opening equal to one-half of the parent size. Of course a sphere, or an equivalent disk, may not adequately describe irregular particles so the results of this study may be limited/effected by the chosen test specimen.

For the smaller reduction ratio (Figure 4.21) it can be seen that the Boscobel, Shadwell, Leesburg, Spotsylvania, and Thornburg rocks exhibit similar distributions between the parent size and the 0.1 size. At sizes smaller than $1/10^{th}$ of the parent size the distributions diverge. At larger fragment sizes these rocks experience approximately the same degree of cleavage but the proportion of material in the smaller size ranges varies according to the degree of shatter each rock is subjected to. Figure 4.21 also touches upon the observation made in the previous section that fracturing of the Culpeper siltstones was a shatter-dominated event. The siltstones are shown to have a uniform distribution and their breakage functions are not a mixture of separate size populations. The other five rocks exhibit multi-modal behavior and their breakage functions are the more typical mixture of separate populations caused by shatter and cleavage.

Increasing the reduction ratio resulted in a breakage distributions consisting of a larger proportion of fine progeny sizes (i.e., the percent passing each progeny size increased). Figure 4.22 indicates that the distribution modulus of the larger progeny size populations is approximately the same for each rock but the proportion of fragmented material in the larger sizes is not. There is no consistency among the rock's distribution modulus or material proportion in the finer sizes (less than $1/10^{th}$ the parent size). The Culpeper siltstones again yielded fairly uniform breakage functions. The siltstones also did not experience as great of an increase in the percentage passing each fragment size. This is most likely a result of the small degree, relative to the other rocks, of secondary crushing the siltstones were exposed to and corresponds to the proposition made in the previous section that an increase in reduction ratio does not affect the siltstone's breakage behavior as much as the other rocks.

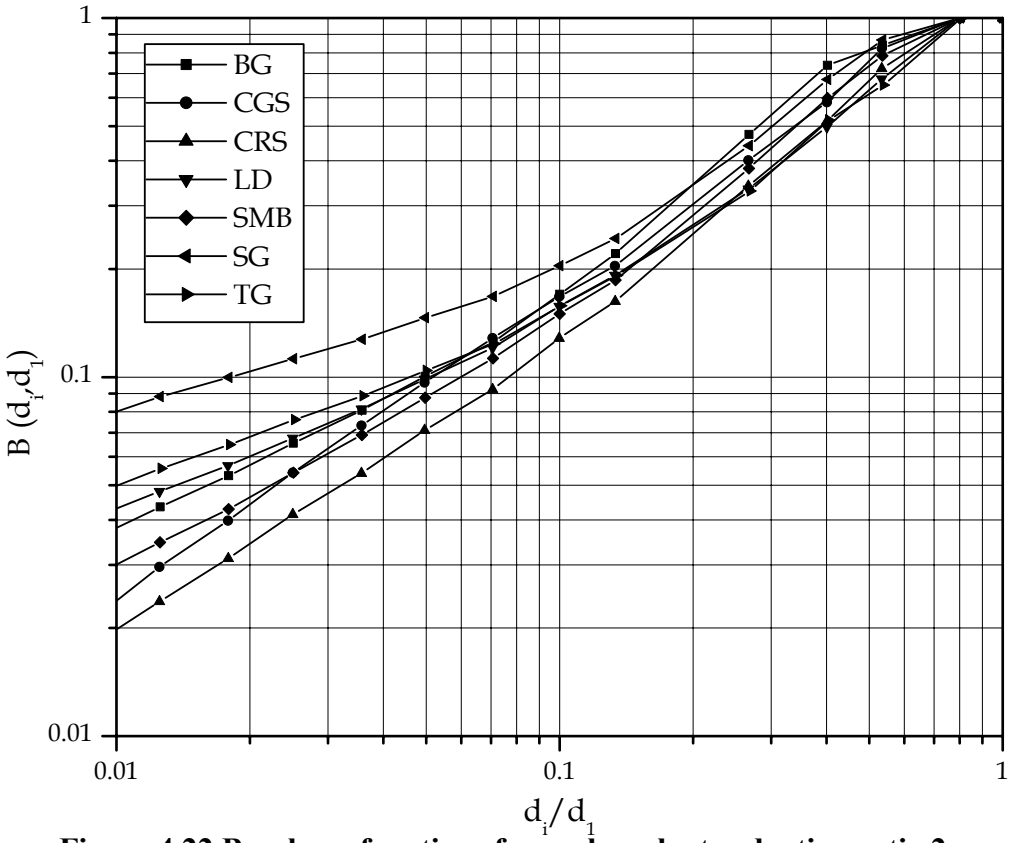

Figure 4.22 Breakage functions for each rock at reduction ratio 2

Figures 4.23 – 4.29 are the separate breakage functions for each rock at each reduction ratio. The change in breakage distribution with reduction ratio can be seen more clearly for each rock. At the lower reduction ratio the breakage functions are a mixture of two separate size populations, except for the Culpeper rocks as noted earlier. At the higher reduction ratio the larger size population becomes bimodal due to increased secondary breakage and shattering of progeny fragments.

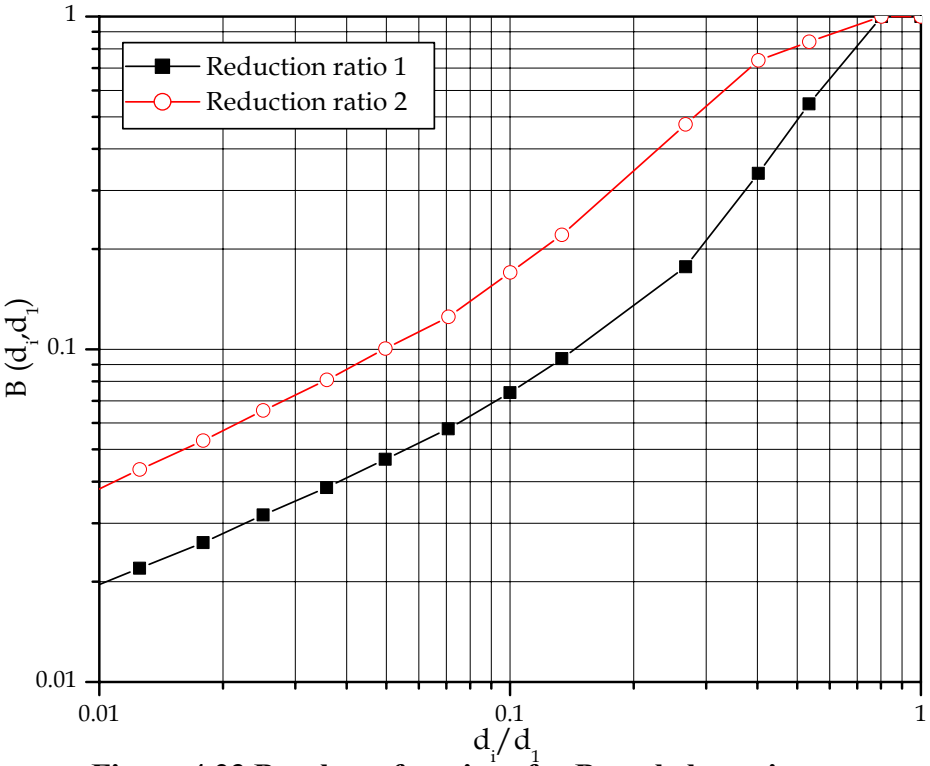

Figure 4.23 Breakage functions for Boscobel granite

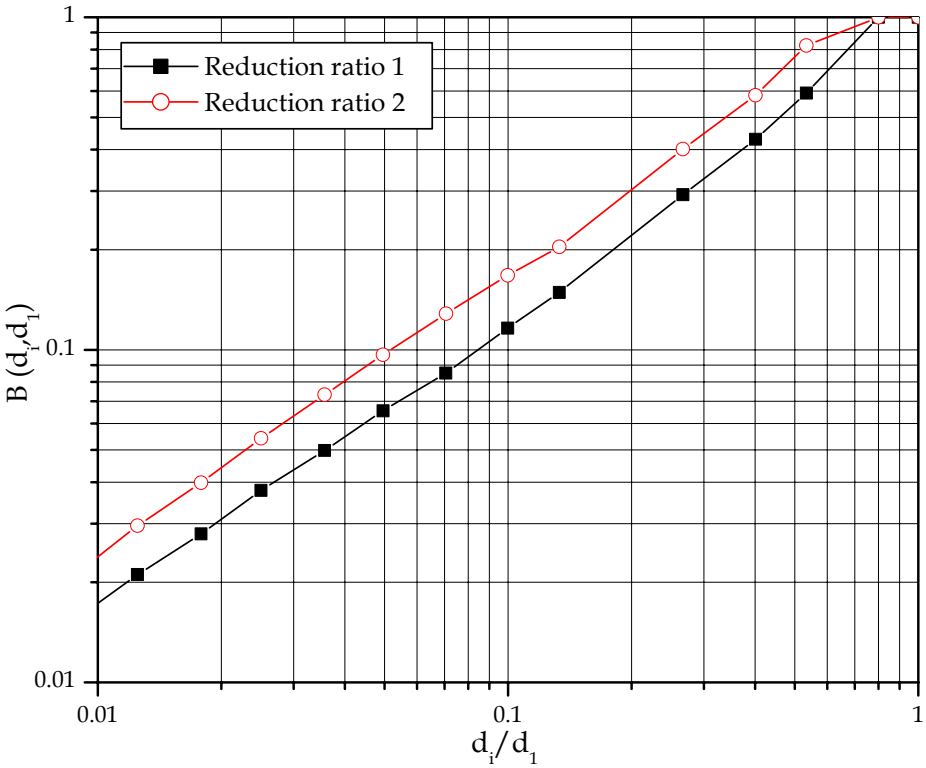

Figure 4.24 Breakage functions for Culpeper gray siltstone

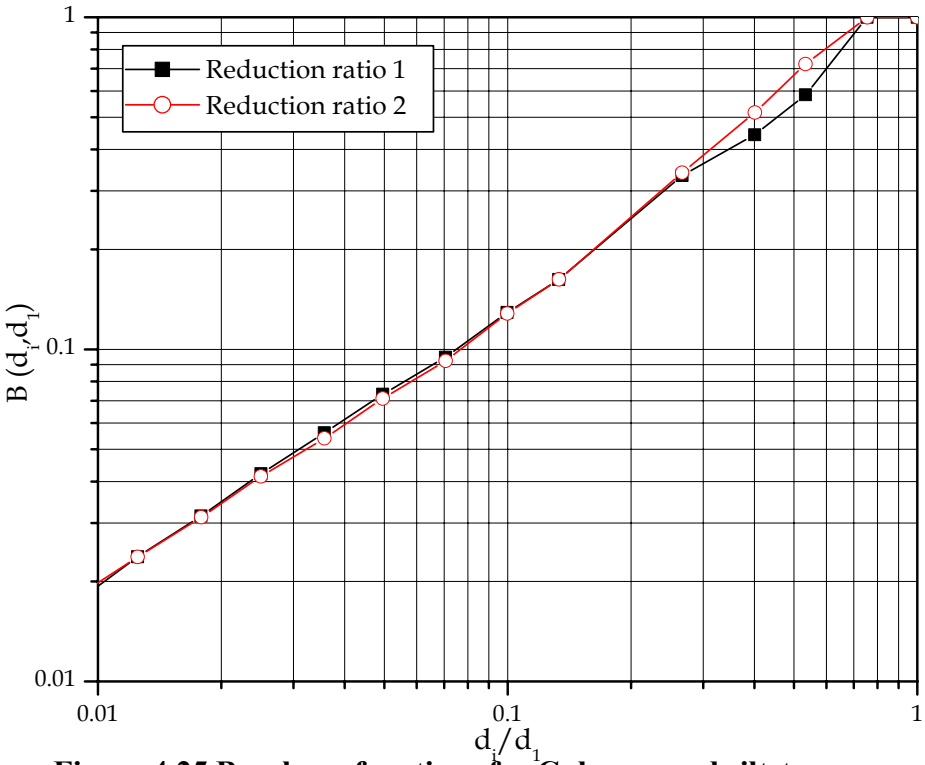

Figure 4.25 Breakage functions for Culpeper red siltstone

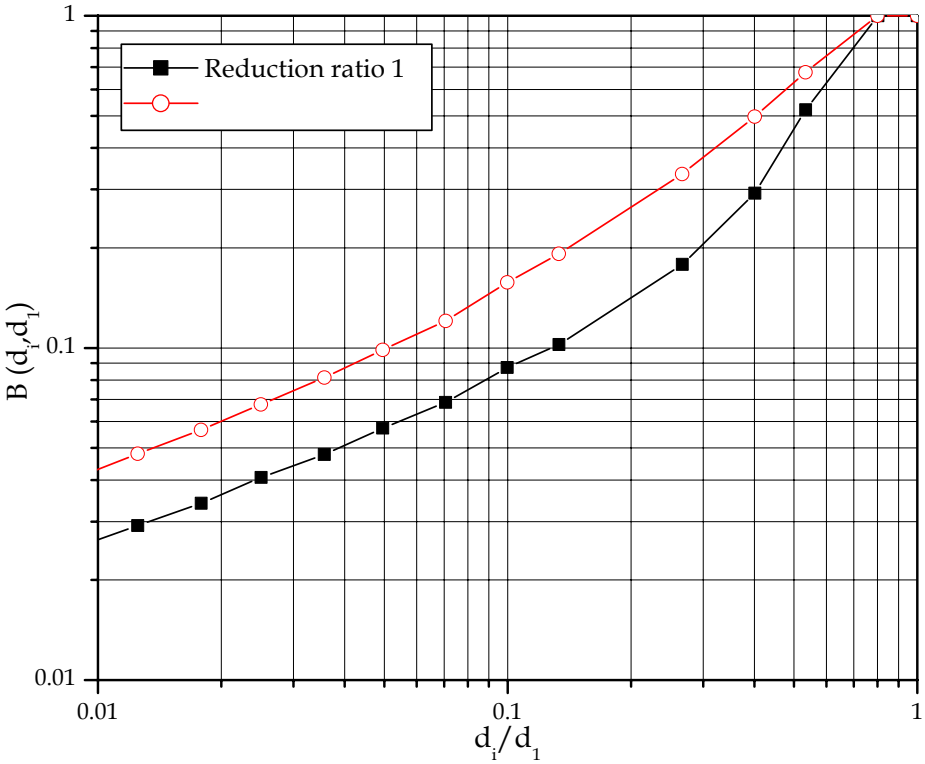

Figure 4.26 Breakage functions for Leesburg diabase

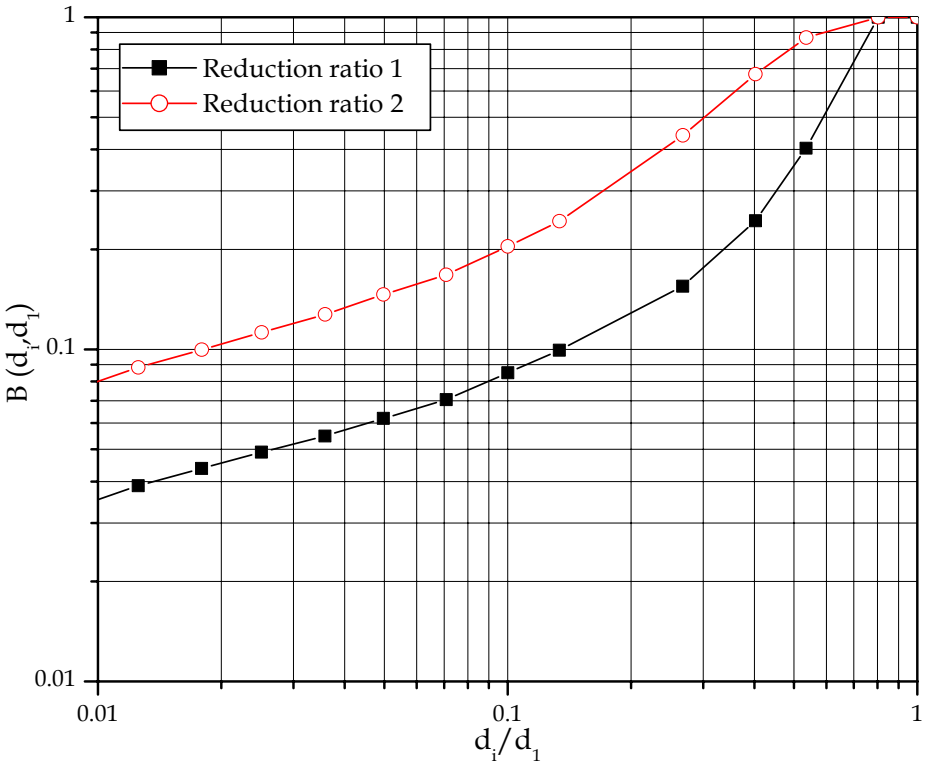

Figure 4.27 Breakage functions for Spotsylvania granite

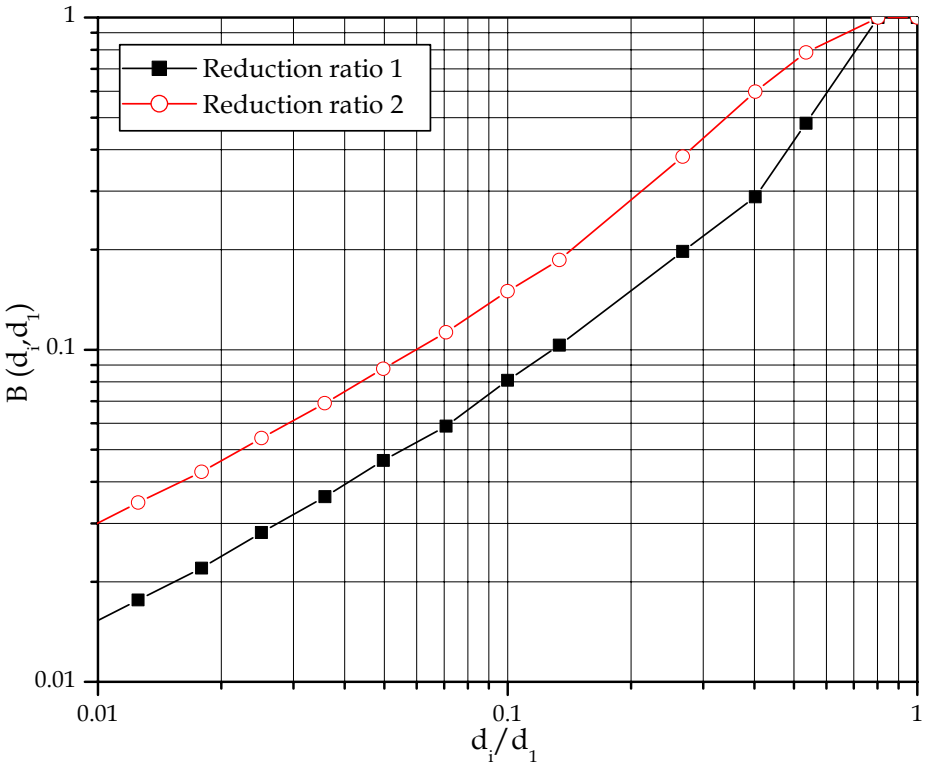

Figure 4.28 Breakage functions for Shadwell metabasalt

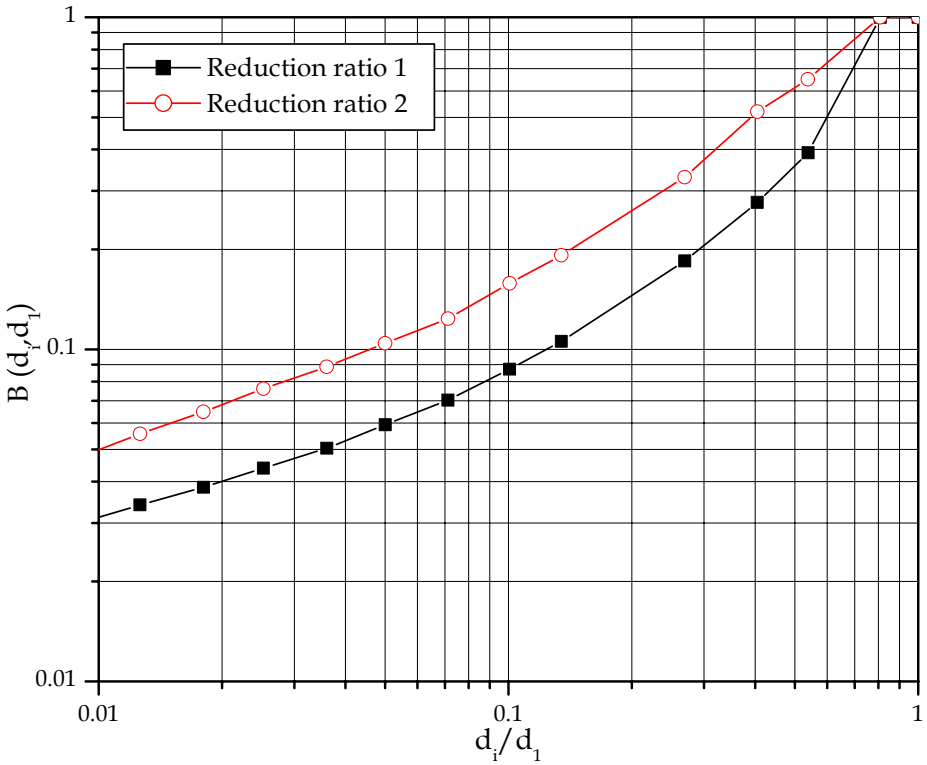

Figure 4.29 Breakage functions for Thornburg granite

Conventional wisdom, based on prior research (see section 2.4), dictates that an increase in energy intensity changes only the proportion of the separate populations that make up a breakage function and not their distribution. Agreement with this perception is found in the preceding figures. The distribution of the finer size population (sizes below 1/10th of the parent size) does not change but the proportion of material in that population does change. The proportion of material in the larger size fractions decreases because of rebreakage of cleavage progeny fragments. The distribution modulus does not change, although a change in the distribution above sizes half the parent size can be seen in some instances. This indicates that rebreakage of daughter particles initially produced by cleavage is occurring (note that the slope/distribution modulus above 0.5 is approximately the same as that of the fine size population).

In section 2.4.3 the t_{10} parameter was introduced. It is the percent of progeny particles passing a size one-tenth of the initial original particle size. t_{10} is employed as a characteristic size reduction parameter and has been related to the energy absorbed during a single particle breakage test. For crushing applications t_{10} is usually in the range of 10% to 20%. In order to determine t_{10}, and other t_n values, from the breakage distribution data, a *MathCAD* program was developed so that cubic spline interpolation of the measured data could be performed. Table 4.4 lists the value of t_{10} for each rock at each reduction ratio. As expected t_{10} increased with an increase in reduction ratio and the results fit close to the range of values typical of crushing. In conjunction with Table 4.3

the results listed below show that the rocks that had the largest percentage increase in E_c also had the largest percentage increase in t_{10}.

Table 4.4 Values of t_{10} for each rock and reduction ratio

Rock Type	Reduction Ratio 1	Reduction Ratio 2
	t_{10} %	t_{10} %
Shadwell Metabasalt	8.1	15.0
Boscobel Granite	7.4	17.0
Culpeper Grey Siltstone	11.7	16.8
Culpeper Red Siltstone	12.9	12.8
Leesburg Diabase	8.7	15.8
Thornburg Granite	8.7	15.7
Spotsylvania Granite	8.5	20.4

For each specific rock the t_{10} parameter is a function of the energy input. On the whole, looking at the grouped results for all rocks, t_{10} is more so a function of the reduction ratio. Figure 4.30 shows that t_{10} increases with an increase in reduction ratio but that at each reduction ratio it does not change significantly as E_c increases. This is because at a given reduction ratio specific comminution energy is a function of the material behavior. Thus a plot of t_{10} versus fracture toughness also shows that t_{10} varies

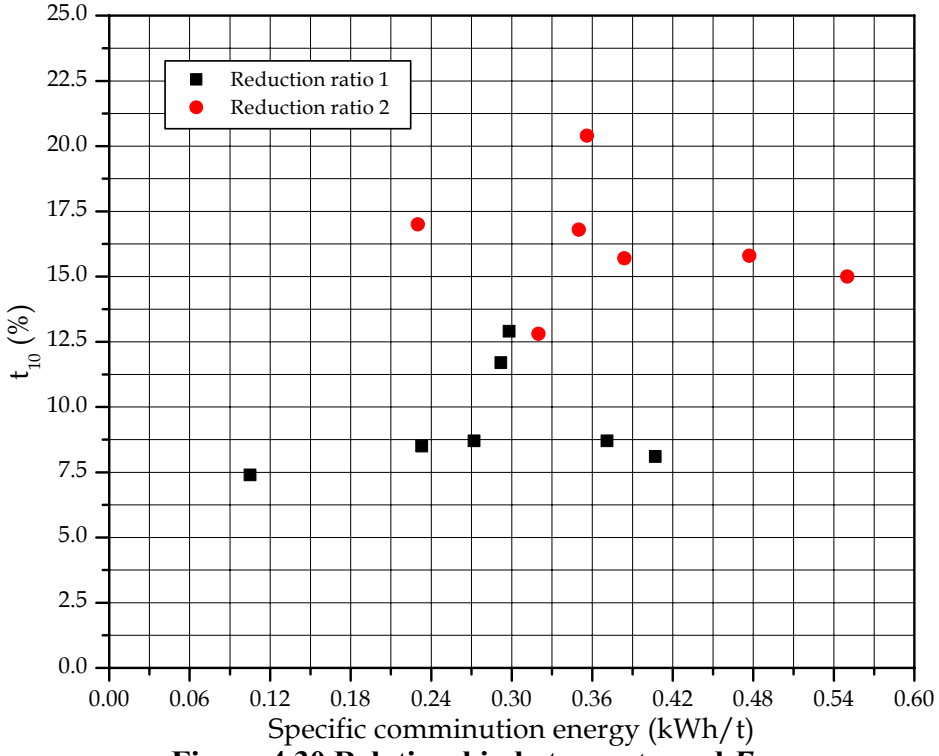

Figure 4.30 Relationship between t_{10} and E_c

very little as K_{Ic} changes, although the change in t_{10} with an increase in reduction ratio is still evident (Figure 4.31). Figures 4.32 and 4.33 indicate that other t_n values show similar behavior when compared to fracture toughness, particularly smaller values. t_2 and t_4 show a fairly wide degree of variation as fracture toughness changes. t_{25}, t_{50}, and t_{75} fluctuate in a manner similar to t_{10}.

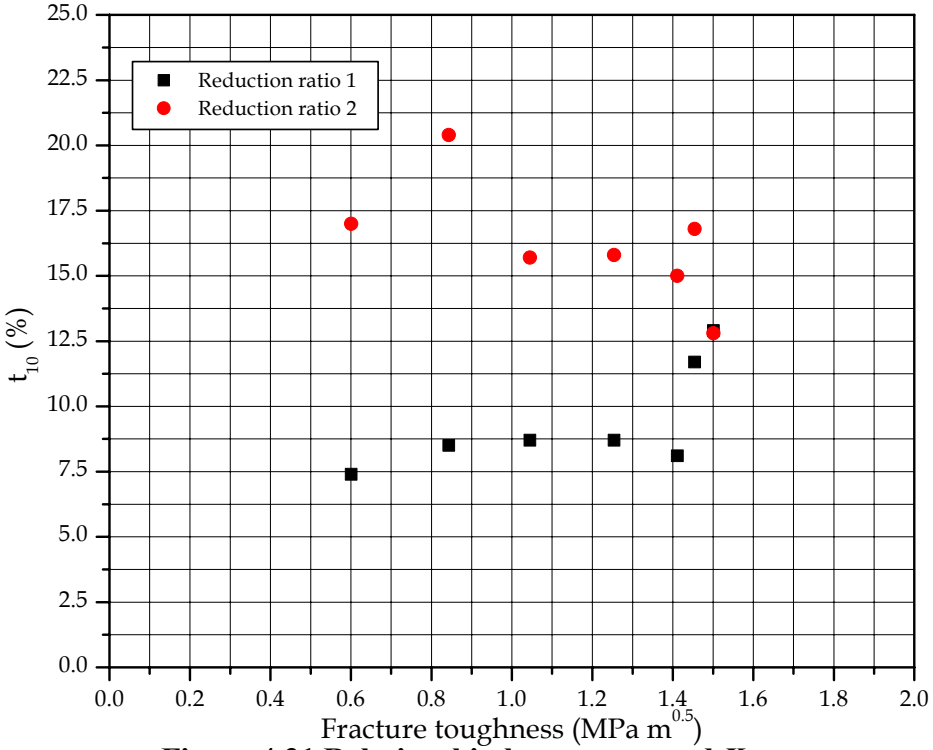

Figure 4.31 Relationship between t_{10} and K_{Ic}

It is difficult to observe any noticeable trend or correlation between t_n values and K_{Ic}. In regards to t_n and K_{Ic}, the conventional thinking would be that as fracture toughness increases the percent passing each t_n value decreases, or tougher rocks would fracture more coarsely. However, high fracture toughness rocks require more strain energy input in order to propagate flaws and thus tend to shatter upon fracture, which produces finer sized fragments. The siltstone is an example of this behavior and in Figures 4.32 and 4.33 it can be seen that more material passes at t_2 and t_4 for the "tough" siltstones. The relationship between t_n and K_{Ic} is complicated further by grain size. Rock fracture toughness has been shown to be dependent upon grain size (in this study and in the literature), as large grained rocks tend to have lower K_{Ic} values. Subsequently, on the one hand, large grained rocks are easy to fracture and should produce a more finely sized breakage distribution based on their fracture toughness. On the other hand, large grained rocks tend to fracture along grain boundaries and progeny fragment size will be dependent on the grain size and may end up being coarser in comparison to tougher, fine-grained rocks. The Boscobel granite is a good example of this behavior. In Figures 4.32

and 4.33 the Boscobel granite, which has the lowest fracture toughness, has the highest percentage passing at t_2 and t_4. This indicates that multiple crack surfaces, occurring as grain boundaries, are propagated upon fracture. However, at lower t_n values the Boscobel has a smaller percentage passing. These sizes are near the grain size of the granite and the progeny fragments at these sizes were most likely produced at first fracture or soon there after. In other words, large grained rocks shatter more upon initial fracture producing daughter fragments that are not subjected to secondary breakage. In order to determine a relationship between fracture toughness and breakage function, as represented by a series of t_n values, observation of the fracture behavior and structure/grain size of each rock is required.

A final observation from the breakage distribution results is that the t_{10} parameter measured under jaw crusher conditions can be applied in order to determine a complete size distribution. This is the one-parameter family of curves method described in section 2.4.3, where, using only a given value of t_{10}, the full product size distribution can be reconstructed. Figure 4.34 shows the HECT breakage results in terms of t_n versus t_{10}. The solid lines represent Narayanan's (1985) work presented previously in Figure 2.21. Narayanan's work was for tumbling mills and there seems to be some agreement, at least trend-wise, between that work and the results from this study. The t_n values from the HECT jaw crusher set-up are higher than those given by Narayanan, most likely because of the different size reduction application (jaw crusher vs. tumbling mill), different degrees of reduction ratio, and the fact that Narayanan's data represents only one type of material, where as the data in this study covers six different rock types (although Naraynan's relationships have since been verified for a range of rock/ore types). Despite these differences it is clear that t_{10} is mostly a function of reduction ratio, and not necessarily of energy input or size reduction machine, and that if t_{10} and fracture toughness can be related, then all other t_n values can be determined simply from t_{10}.

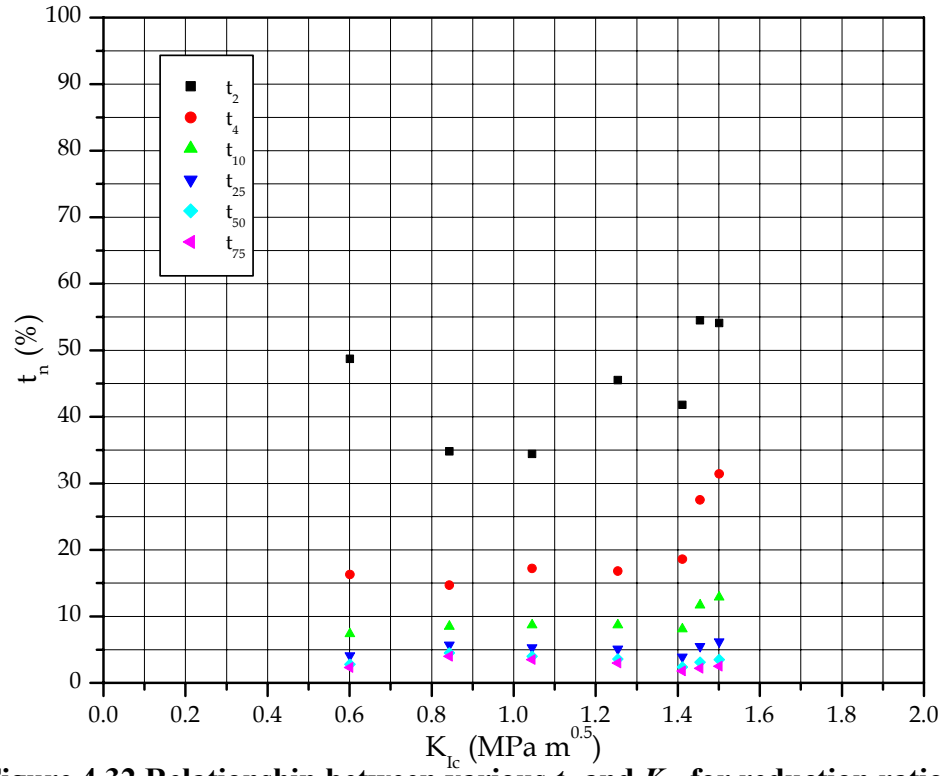

Figure 4.32 Relationship between various t_n and K_{Ic} for reduction ratio 1

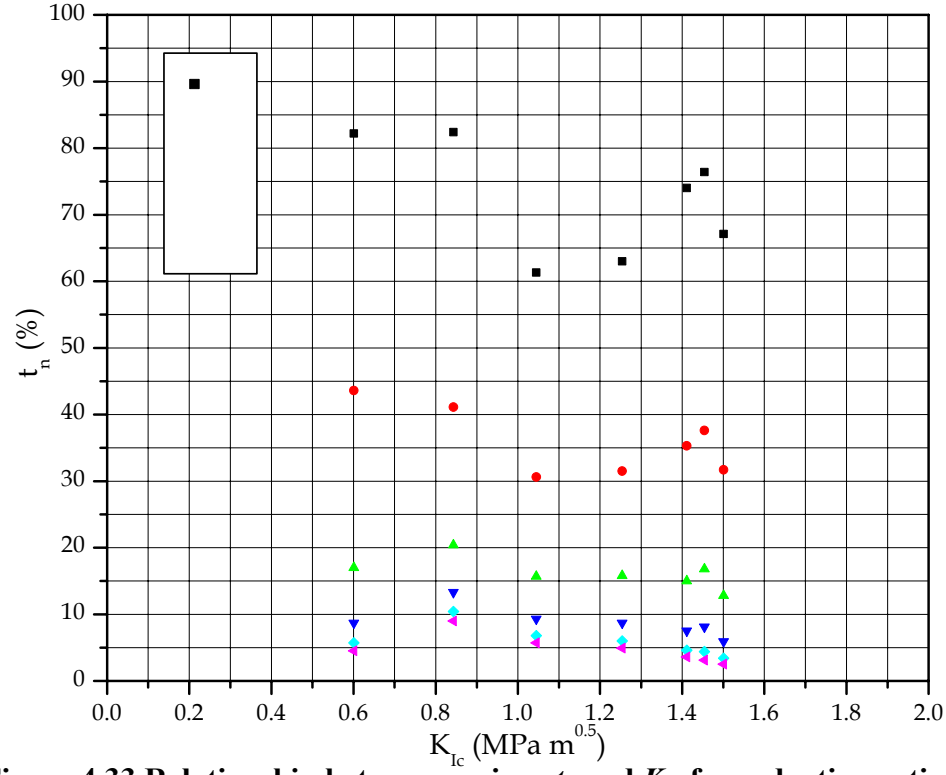

Figure 4.33 Relationship between various t_n and K_{Ic} for reduction ratio 2

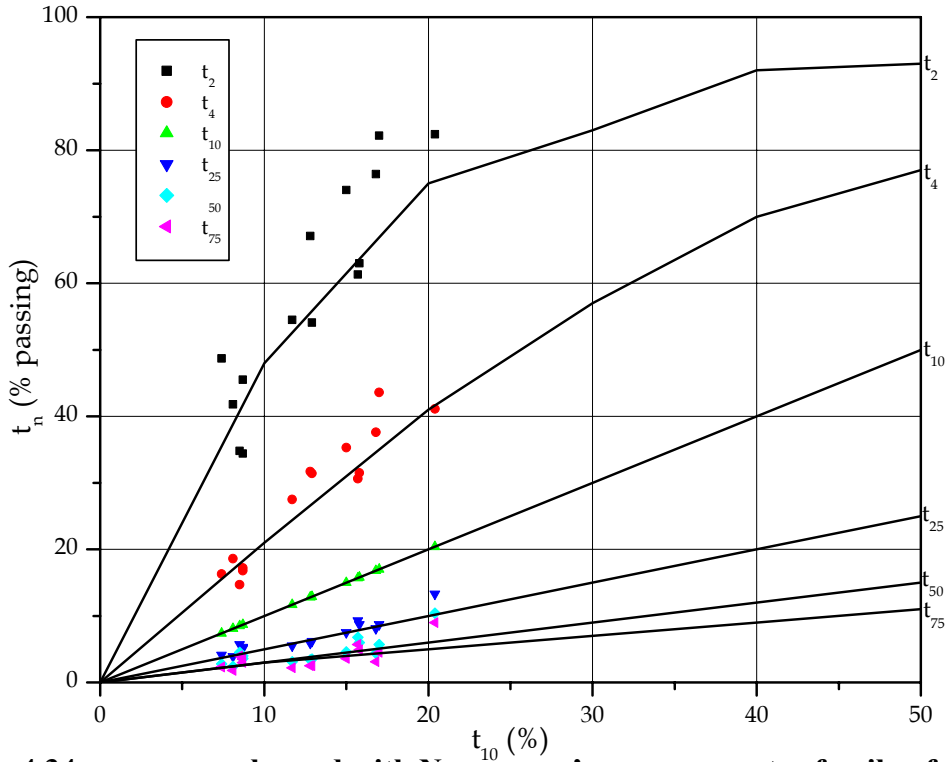

Figure 4.34 t_n vs. t_{10} overlapped with Narayanan's one-parameter family of curves

CHAPTER 5. MODEL DEVELOPMENT AND EXPERIMENTAL VERIFICATION

5.1 MODELS FOR JAW CRUSHER POWER CONSUMPTION AND PRODUCT SIZE

5.1.1 POWER CONSUMPTION

The results presented in section 4.1 indicated a strong correlation between fracture toughness, K_{Ic}, and specific comminution energy, E_c. This relationship can be used to develop an empirical model for the prediction of jaw crusher power consumption that can account for changes in reduction ratio.

As was noted earlier the Culpeper gray and red siltstones were tested separately but when no statistical difference was found between their mechanical properties or fracture toughness values it was decided that they would be considered as one rock. Therefore the HECT results for the gray and red siltstone have been pooled together and model development is based only on data for six rock types.

Figure 5.1 is a plot of specific comminution energy versus fracture toughness for reduction ratio 1. It displays a best-fit line of the data along with the upper and lower 95% confidence limits of the correlation. The linear fit has been forced through the origin based on the assumption that a material with no fracture toughness would not require energy in order to be fractured. The linear relationship between E_c and K_{Ic} is given by the following equation:

$$E_c = 0.255K_{Ic} \quad \{\text{for a reduction ratio of } 1.50\} \qquad [5.1]$$

The coefficient of determination for the relationship given in Equation 5.1 is 0.89. When the reduction ratio is increased the relationship between E_c and K_{Ic} also changes. This is seen in Figure 5.2. The same type of relationship holds, with E_c and K_{Ic} being linearly related. The relationship can be expressed by:

$$E_c = 0.342K_{Ic} \quad \{\text{for a reduction ratio of } 2.97\} \qquad [5.2]$$

The coefficient of determination for the relationship between E_c and K_{Ic} for reduction ratio 2 is 0.80. An increase in reduction ratio results in an increase in the slope, m, of Equation 5.1. In order to determine a model that is inclusive of all reduction ratios an expression relating the slopes of Equations 5.1 and 5.2 needs to be determined.

In addition to the two reduction ratios used in this study, it can be assumed that at a reduction ratio of one (i.e, the particle size equals the closed side set and no strain energy is input into the particle), the slope of the relationship between E_c and K_{Ic} is also zero. A plot of this data is given in Figure 5.3 and has been fit with two expressions, one for reduction ratios between 1 and 1.5 and the other for reduction ratios greater than or equal to 1.5 . The general relationship between E_c and K_{Ic}, covering all reduction ratios (RR), is then given by the following equation:

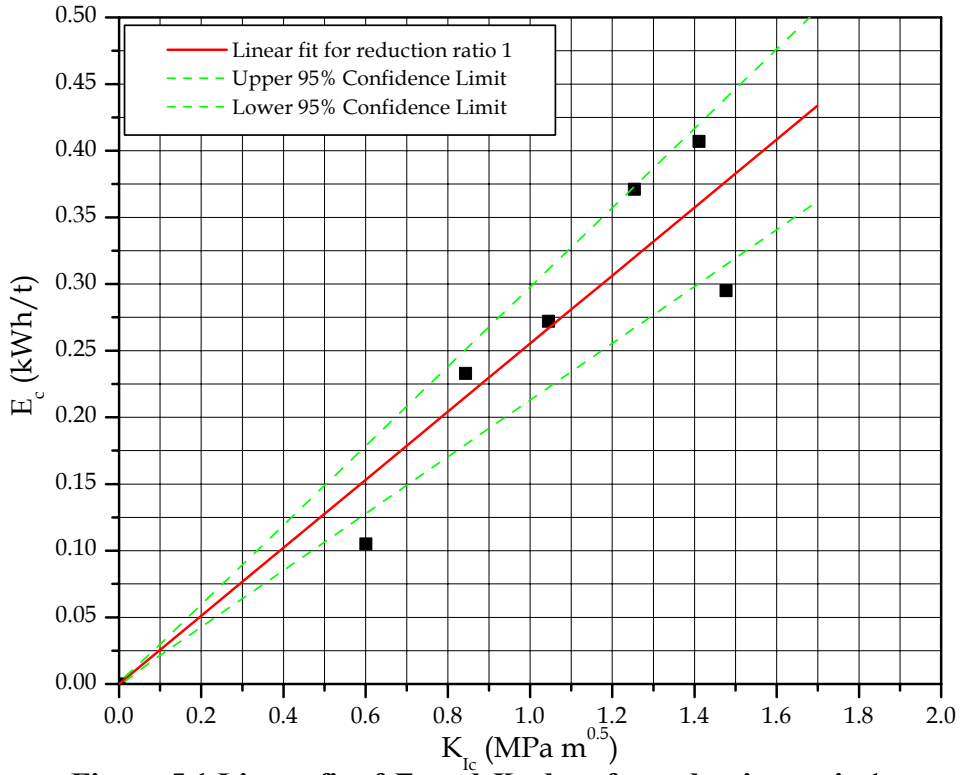

Figure 5.1 Linear fit of E_c and K_{Ic} data for reduction ratio 1

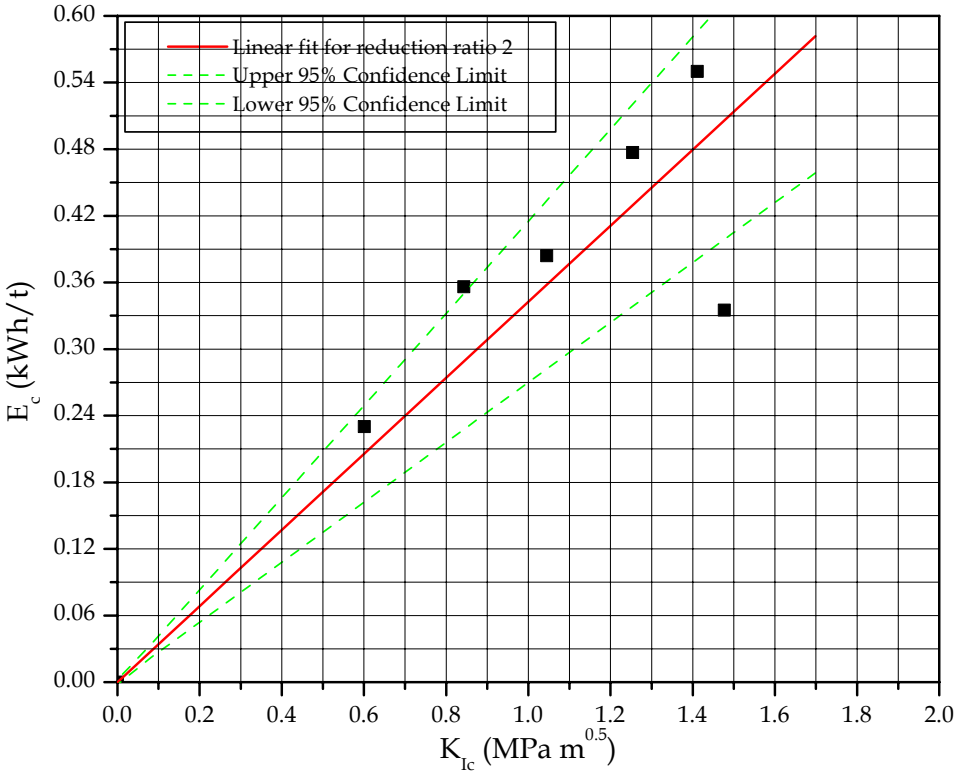

Figure 5.2 Linear fit of E_c and K_{Ic} data for reduction ratio 2

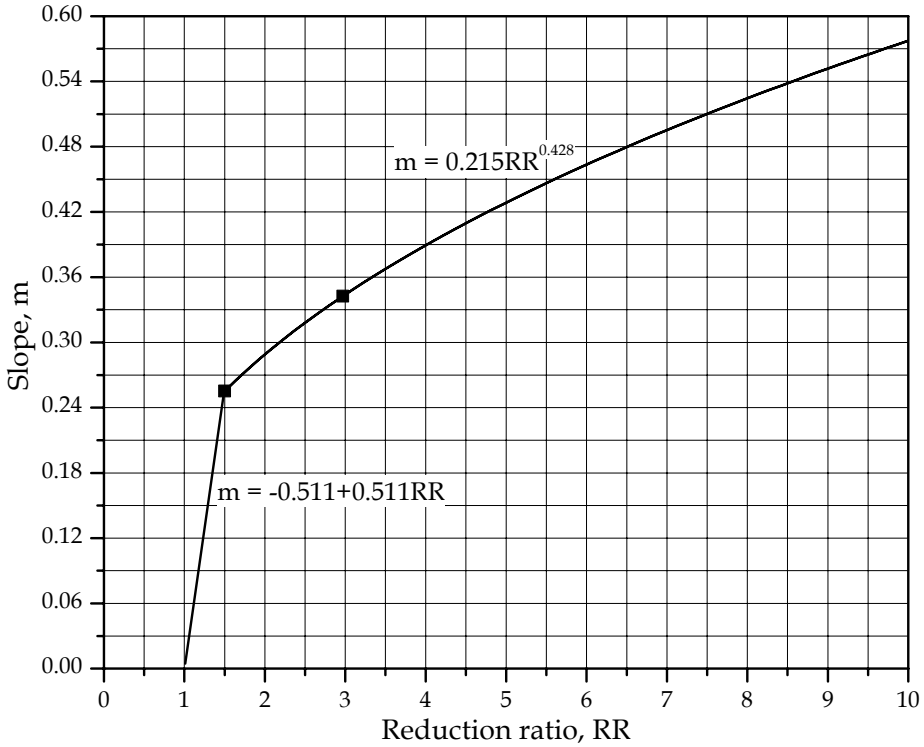

Figure 5.3 Change in coefficient *m* with reduction ratio

$$E_c = \left[-0.511 + 0.511RR\right] K_{Ic} \qquad \text{for } 1 \le RR < 1.5$$
$$E_c = \left[0.215RR^{0.428}\right] K_{Ic} \qquad \text{for } RR \ge 1.5 \qquad [5.3]$$

An allometric equation was chosen for reduction ratios greater than or equal to 1.5. Although the measured data only suggest a linear relationship between reduction ratios of 1.5 and 2.97 it has been assumed that a limiting power law, or possibly exponential, relationship between specific communution energy and reduction ratio exists at higher reduction ratios. This is mainly due to the fact that the rate of strain input decreases with increasing reduction ratio.

Equation 5.3 governs the relationship between fracture toughness and specific comminution energy based on the HECT results, where E_c is given in terms of kilowatt-hours per metric ton and reduction ratio is defined as the particle size divided by the closed side set. In order to determine the power consumption of a jaw crusher the feed size distribition would have to be known, as well as the mass flow at each size, and the the idling power of the crusher. Equation 5.3 can be adjusted to account for these variables and an equation for determining the power consumption of a jaw crusher, based on fracture toughness, can be written as:

$$P_c = \sum_{i=1}^{j} \left[-0.511 + 0.511 RR_i \right] K_{Ic} C_i x_i + P_n \quad \text{for } 1 \le RR < 1.5$$
$$P_c = \sum_{i=1}^{j} \left[0.215 RR_i^{0.428} \right] K_{Ic} C_i x_i + P_n \quad \text{for } RR \ge 1.5 \qquad [5.4]$$

where, P_c is the power consumption of the crusher in kW
RR_i is the reduction ratio for a particle of size i
C_i is the probability of breakage for particle size i
x_i is the mass flow of particle size i in metric tons per hour
P_n is the power drawn by the crusher under no load in kW.

Equation 5.4 accounts for the wide range of reduction ratios seen in a jaw crusher due to the non-uniformity of the feed size distribution. It is difficult in practice to sample the feed size entering a jaw crusher and often times the feed size distribution is unknown. In these instances Equation 5.4 is not applicable. If an estimate of the average reduction seen by the feed can be made, which infers some kowledge of the feed size distribution, then the following equation can be used to approximate the power consumption of a jaw crusher:

$$P_c = \left[-0.511 + 0.511 RR_{avg} \right] K_{Ic} T + P_n \quad \text{for } 1 \le RR < 1.5$$
$$P_c = \left[0.215 RR_{avg}^{0.428} \right] K_{Ic} T + P_n \quad \text{for } RR \ge 1.5 \qquad [5.5]$$

where, RR_{avg} is the avereage reduction ratio for the entire feed
T is the total mass flow in metric tons per hour.

Equation 5.4 is limited since the E_c and K_{Ic} relationship is based on six rocks and two reduction ratios. Figures 5.1 and 5.2 indicate that the relationship may be exponential or allometric, with a limiting amount of specific comminution energy required to crush high fracture toughness rocks (i.e., a "ceiling" is reached in terms of E_c). The strength of the linear relationships suggested in Equations 5.1 and 5.2 is influenced by the behavior of the Culpeper siltstone, which at each reduction ratio has E_c values outside the 95% confidence limit of the linear fit model. As discussed in section 4.2, the siltstone was not exposed to as much secondary breakage as the other rocks. This is mainly due to the low elastic modulus of the siltstone. Though the siltstone was the only "tough" rock that exhibited this type of behavior, it is believed that E_c also has a strong dependency on the elastic modulus and over the course of more testing, linear, or non-linear, relationships between E_c and K_{Ic} may be strengthened if they are defined for specific intervals of elastic modulus. Another option may be to use the strain energy release rate, G, which is dependent on fracture toughness and the elastic modulus (and in the case of plane strain, Poisson's ratio). G, or an estimate of G based on the measured K_{Ic} and elastic modulus values for each rock, was investigated for this study but the correlation, and the strength of the relationship, between strain energy release rate and E_c was not as significant as the one between E_c and K_{Ic}.

5.1.2 PRODUCT SIZE

A direct model for the product size appearing from a jaw crusher is not possible. Any prediction of product size is dependent upon the feed size, classification function, and the breakage function. The model developed here is strictly for the prediction of the breakage function, which in conjunction with the feed size distribution and classification function can be used to find the product size distribution from a jaw crusher.

In section 2.4.3 methods for describing the breakage function were covered. The most common method is to express the breakage function as a mixture of separate size populations. A second method is the one-parameter family of curves approach popularized by the JKMRC (Julius Kruttschnitt Mineral Research Center). Each method was given due consideration for the breakage data collected in this study but the final model used here employs an approach similar to that of the one parameter family of curves. For the mixed population approach, relationships between the coefficients K_i and n_i, used to describe different size populations, and fracture toughness were difficult to discern and curve fitting of the twelve measured breakage functions (2 for each rock) was arduous.

The model developed here is based on the characteristic size reduction parameter t_{10}. In section 4.2.3 a plot, inclusive of all reduction ratios, of t_n values versus t_{10} was presented that showed relationships exist between different t_n values and t_{10}. It was determined that if t_{10} is a function of fracture toughness and reduction ratio, then other t_n values can be determined using these relationships. Thus the one-parameter family of curves can be used to determine the breakage function for a rock given the fracture toughness and reduction ratio.

Figure 4.31 in section 4.2.3 showed the relationship between t_{10} and fracture toughness at each reduction ratio. A correlation between the two is hard to observe, even when the siltstone results are pooled and presented as one rock. This is most likely because the percent passing at a particle size one-tenth the parent size, or any size for that matter, is dependent upon the reduction ratio, the rock's fracture behavior, and the rock's grain size/structure. The data presented in section 2.4.3 indicated that at small t_n values the percent passing increases with increasing fracture toughness for the smaller reduction ratio. One explanation for this behavior is the increased presence of flaws in the weaker rocks that are activated upon fracture and produce progeny fragments that are not subjected to secondary breakage. This corresponds with the behavior observed at the higher reduction ratio that showed a decrease in percent passing with increased fracture toughness at the small t_n values. The effect of grain size/structure is nullified when significant amounts of secondary breakage occur. A second explanation is based on the "ability" of the rock particle to absorb energy. It is possible that before fracture occurs at the weakest flaw in a rock particle, excess energy can be applied such that fracture of many flaws occurs almost simultaneously. This process is shatter fracture and results in

finer progeny fragments. Again, at higher reduction ratios this behavior is "hidden" due large amounts of secondary breakage.

Based on the previous qualitative description, the effect of fracture behavior and microstructure on the breakage distribution should be accounted for when investigating the relationship between t_{10} and K_{Ic}. The only approach that can be taken here is to account for a rock particle's "ability" to absorb energy by estimating the strain energy release rate, G, of each rock. Recalling Equation 2.34, G can be calculated using fracture toughness, elastic modulus, and Poisson's ratio. For conditions of plane stress, only K_{Ic} and the elastic modulus are needed. Poisson's ratio for the rocks used in this study are not known thus a universal value of 0.3 was assumed since Poisson's ratios for rocks are fairly small and usually very comparable. Table 5.1 lists the G values for the rocks used in this study, along with their K_{Ic} values for reference.

Table 5.1 Strain energy release rate of each rock

Rock Type	G J/m^2	K_{Ic} $MPa\sqrt{m}$
Shadwell Metabasalt	60.15	1.411
Boscobel Granite	15.98	0.601
Culpeper Siltstone	79.54	1.477
Leesburg Diabase	47.95	1.254
Thornburg Granite	36.36	1.045
Spotsylvania Granite	25.22	0.843

Figures 5.4 and 5.5 are plots of t_{10} versus G for each reduction ratio. An allometric expression has been fit to the data in each case. For a reduction ratio of 1.50 t_{10} can be determined from:

$$t_{10} = 3.54\left(\frac{K_{Ic}}{E'}\right)^{0.251} \qquad [5.6]$$

where E' is the elastic modulus. For a reduction ratio of 2.97 the relationship between t_{10} and K_{Ic} can be written as:

$$t_{10} = 27.2\left(\frac{K_{Ic}}{E'}\right)^{-0.139} \qquad [5.7]$$

It is clear that the relationship between t_{10} and K_{Ic}^2/E' is not well defined but the coefficient of determination is higher than that for any relationship defined between t_{10} and K_{Ic}. The relationship shown in Figure 5.4 demonstrates that t_{10} increases with G. This is because for rocks with higher G values shatter fracture is more prevalent and more energy is released as new crack surface energy. Figure 5.5 indicates that as the reduction ratio is increased, the relationship between t_{10} and G inverses, and t_{10} decreases with increasing strain energy release rate. The low G rocks are subjected to more

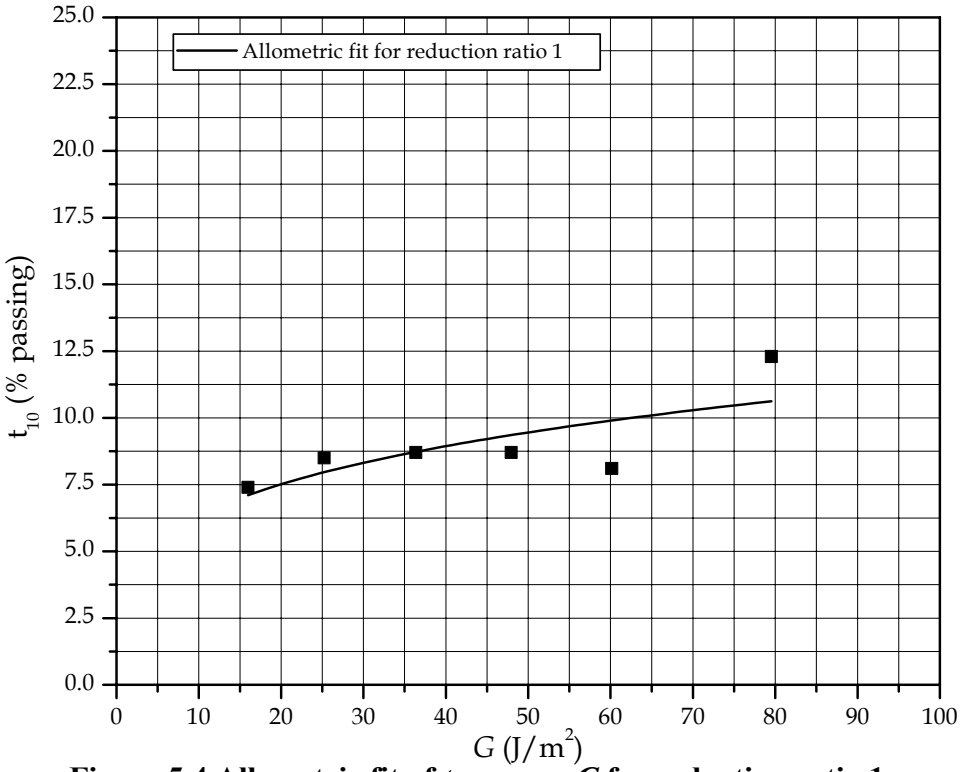

Figure 5.4 Allometric fit of t_{10} versus G for reduction ratio 1

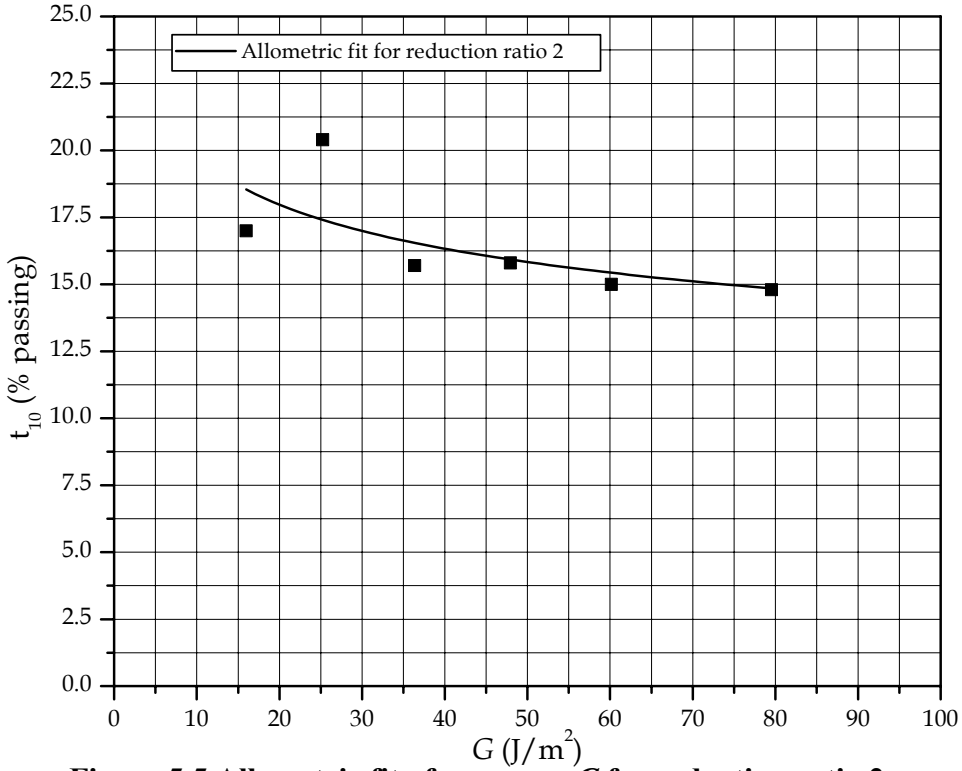

Figure 5.5 Allometric fit of t_{10} versus G for reduction ratio 2

secondary breakage than the higher *G* rocks because the low *G* rocks initially produce large progeny fragments as a result of cleavage. These progeny undergo additional breakage in comparison to the "first" fragments of the high *G* rocks, produced by shatter and having more particles of varying size.

The coefficients and exponents in Equations 5.6 and 5.7 are functions of the reduction ratio. Thus, as was done for the E_c model, general expressions relating them to the reduction ratio need to be determined. The coefficient, *a*, is plotted against reduction ratio in Figure 5.6. As was noted previously a reduction ratio of 1 means that no size reduction takes place, therefore no daughter fragments are produced and all t_n's are zero. Again, since no reduction ratios greater than 3 were used some assumptions have to be made about what occurs as the reduction ratio increases. In this instance it is known that t_{10} cannot exceed 100%, thus *a* has an upper limit as the reduction ratio increases. It is expected that *a* will increase at about the same rate as defined by the two measured data points up to a reduction ratios of about 5. Above a reduction ratio of 5, *a* will not increase as rapidly and will approach 100 at a reduction ratios greater than 10. Figure 5.6 shows the functions used to relate the coefficient *a* and the reduction ratio. Two expressions were used, one for reduction ratios between 1 and 1.5, and one for reduction ratios greater than or equal to 1.5.

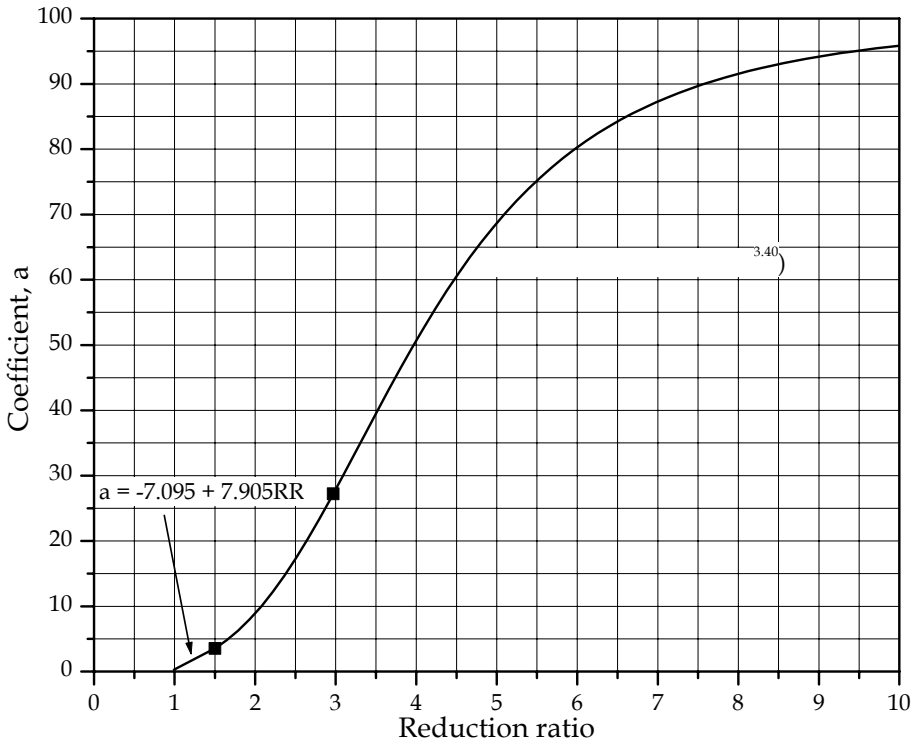

Figure 5.6 Change in coefficient *a* with reduction ratio

The exponent, defined as *b*, in Equations 5.6 and 5.7 is more difficult to relate to the reduction ratio. In this case *b* decreases and becomes negative between the reduction

ratios of 1.5 and 2.97. But for a reduction ratio of one *b* is zero, as is *a*, and at some large reduction ratio *b* equals zero again (in order to satisfy the t_{10} upper limit of 100%). For reduction ratios between 1 and 1.5 the change in *b* is assumed linear. For reduction ratios greater than 1.5 *b* decreases in a exponential/linear manner up to a reduction ratio of 3. Beyond a reduction ratio of 3 *b* increases and approaches zero in an exponential/linear manner. The functions governing the change in *b* with reduction are given in Figure 5.7.

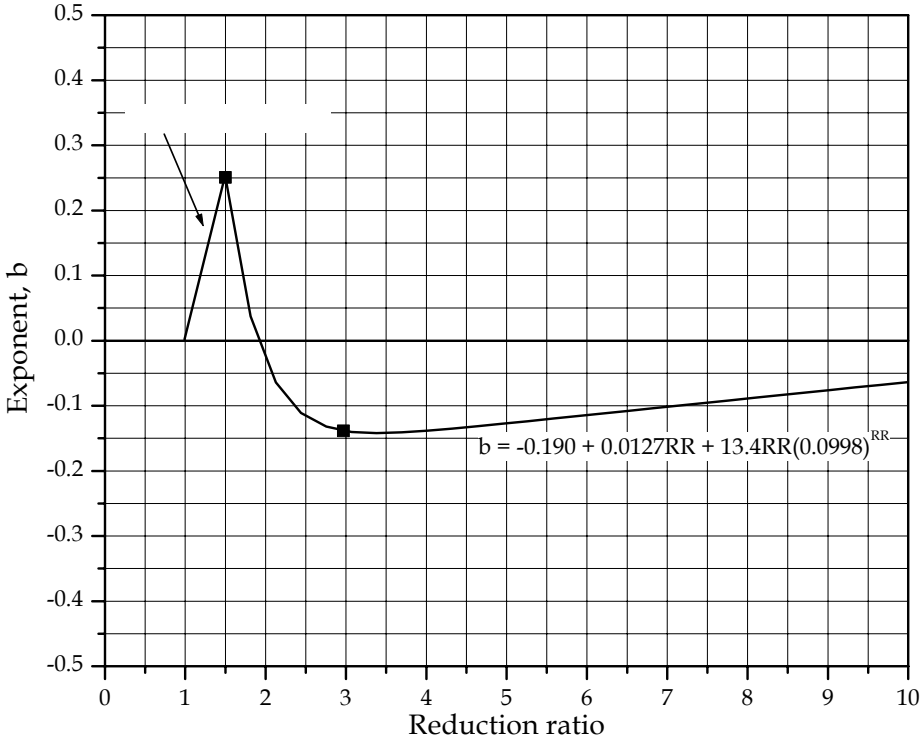

Figure 5.7 Change in exponent *b* with reduction ratio

Substituting the functions that relate the coefficient *a* and the exponent *b* to the reduction ratio into Equations 5.6 or 5.7 gives the following general expression relating t_{10} and K_{Ic}^2/E:

$$t_{10} = \left[-7.01 + 7.01RR\right]\left(\frac{K_{Ic}^{\,2}}{E'}\right)^{(-0.501+0.501RR)} \qquad \text{for } 1 \le RR < 1.5$$

$$t_{10} = \left[100 - \frac{100}{1+\left(\frac{RR}{3.97}\right)^{3.40}}\right]\left(\frac{K_{Ic}^{\,2}}{E'}\right)^{\left(-0.190+0.0127RR+13.4(0.0998)^{RR}\right)} \qquad \text{for } RR \ge 1.5 \qquad [5.8]$$

where, *RR* is the reduction ratio. Equation 5.8 is applicable only over the range of fracture toughness values determined in this study. What occurs outside of this range, at K_{Ic}^2/E' values approaching zero or values greater than 80 J/m^2, is hard to assess based on the given data. More testing is required in order to establish a wider ranging t_{10} and

K_{Ic}^2/E' relationship, as well as to strengthen or modify the suggested one. Additionally, HECT tests run at higher reduction ratios need to be performed in order to verify that the functions proposed in Figures 5.6 and 5.7 are acceptable. Despite these limitations it is believed t_{10} is dependent upon the fracture behavior of the rock as defined by either fracture toughness or the strain energy release rate, which is related to K_{Ic}. The fracture toughness of a rock is dependent upon the presence, distribution, and geometry of flaws within the rock, as well as the energy/stress applied to the rock. These factors also dictate the size and distribution of new crack surfaces present after fracture or breakage and are represented as t_n values. Further study will enhance the inter-relationship between fracture toughness and fractured size distribution.

Equation 5.8 defines t_{10} for a given reduction ratio, fracture toughness, and elastic modulus. In order to determine the complete breakage function more t_n values are needed. Using the one-parameter family of curves approach t_{10} can be related to other t_n values. Figure 4.34 showed the measured t_n versus t_{10} data. Curve fitting of that data was used to develop Figures 5.8 and 5.9, which show the relationships between various t_n values and t_{10}. The expressions describing those relationships are also given in Figures 5.8 and 5.9 and are:

$$\begin{aligned} t_{1.5} &= 40.9 t_{10}^{\,0.281} \\ t_2 &= 7.68 t_{10}^{\,0.800} \\ t_4 &= 2.17 t_{10} \\ t_{10} &= t_{10} \\ t_{25} &= 0.556 t_{10} \\ t_{50} &= 0.384 t_{10} \\ t_{75} &= 0.315 t_{10} \\ t_{100} &= 0.271 t_{10} \end{aligned} \qquad [5.9]$$

The series of equations given in 5.9 can be used along with Equation 5.8 to determine the complete breakage function for a rock of known fracture toughness exposed to a given level of size reduction in a jaw crusher. The breakage function can then be used in conjunction with feed size data and a classification function in order to predict the product size distribution produced by a jaw crusher when crushing the given rock material.

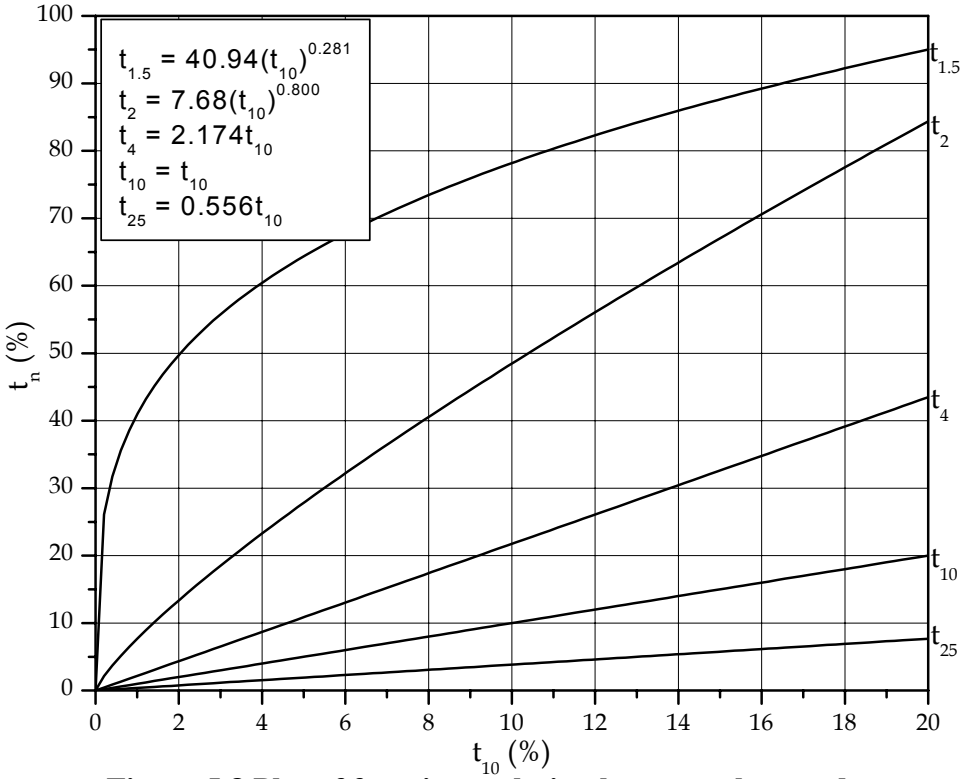

Figure 5.8 Plot of functions relating large t_n values and

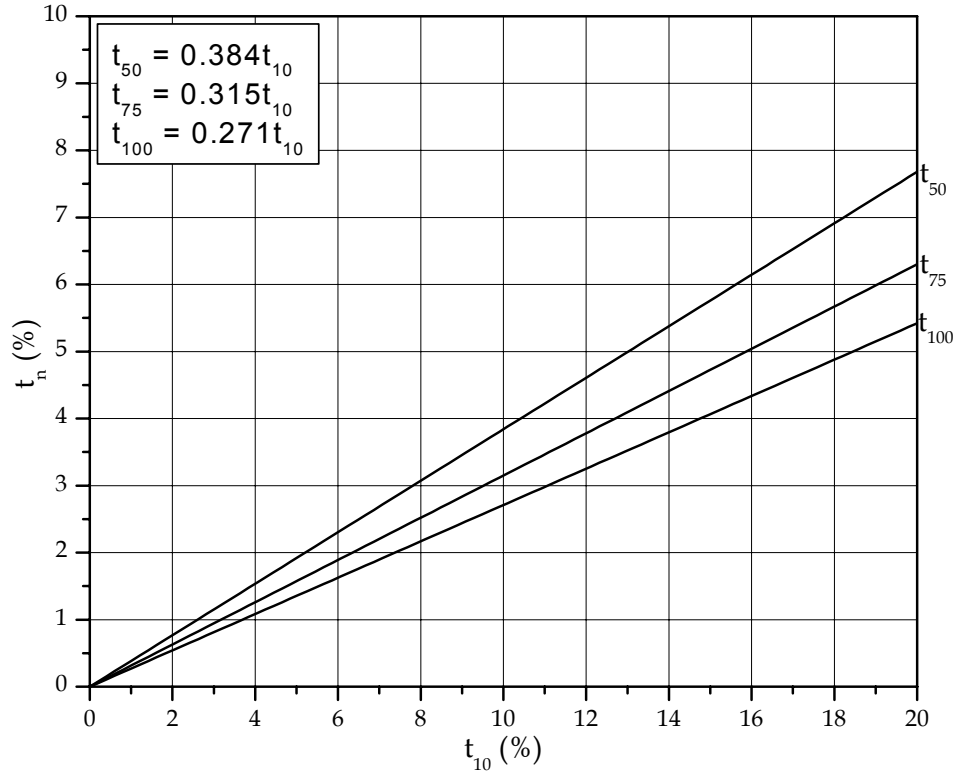

Figure 5.9 Plot of functions relating small t_n values and t_{10}

5.2 EXPERIMENTAL VERIFICATION OF MODELS

5.2.1 LABORATORY VERIFICATION OF E_C AND BREAKAGE FUNCTION MODELS

It was concluded that a brief assessment of the HECT derived E_c and breakage function models needed to be performed before laboratory jaw crushing was conducted. This allows for an investigation of the strength of the models strictly from a laboratory, or baseline, perspective before scale-up variables can have an effect on the predicted results (i.e, feed rate, jaw crusher geometry). Samples of dolomitic limestone where tested because it had been used in the development of the Edge Notched Disk fracture toughness test and a K_{Ic} value was available. The fracture toughness of the dolomitic limestone is 1.397 $MPa\sqrt{m}$ and it has an elastic modulus of 39.7 GPa.

Ten samples of the dolomitic limestone were tested in the High Energy Crushing Test system. Except for the closed side set, which was 35.2 mm, the conditions of the HECT system were exactly the same as used for the six *Luck Stone* rocks. The 10 samples were disk specimens with an average diameter of 50.22 mm and thickness of 24.82 mm. The average reduction ratio was 1.43. The average specific comminution energy of the ten samples was determined and the pooled fragments sieved for breakage function analysis. The specific comminution energy results are shown in table 5.2 along with the predicted value of E_c as given by Equation 5.3. The measured t_{10} value and the t_{10} value predicted by Equation 5.9 are also in Table 5.2. The actual breakage function and the predicted breakage function given by Equation 5.9 are shown in Figure 5.10.

Table 5.2 Actual and predicted E_c and t_{10} for dolomitic limestone

Parameter	Measured	Predicted
E_c	0.295 kWh/t	0.305 kWh/t
t_{10}	6.0 %	6.6 %

Table 5.2 indicates that the E_c model developed from the experimental program is fairly accurate for the given reduction ratio of 1.43. Since this reduction is within the bounds of the measured data it is not surprising the actual and predicted E_c values are in good agreement. It remains to be seen if the model holds at higher reduction ratios, which could not be tested here due to the limited availability of rocks and the re-configuration of the HECT system required for small closed side sets and intense secondary crushing.

The measured and predicted breakage functions also show fairly good agreement, particularly at the larger progeny sizes. As the daughter size decreases past 0.1 (which represents t_{10}) the deviation between the measured and predicted breakage distribution increases. This is because the relationships between t_{10} and the smaller t_n values ($t_{50,\ 75,\ 100}$) given in Equation 5.9 are not as strong as those between t_{10} and the larger t_n values.

The average coefficient of determination for the relationships between t_{10} and t_n's coarser than t_{10} is 0.85, and between t_{10} and the finer t_n's it is 0.60.

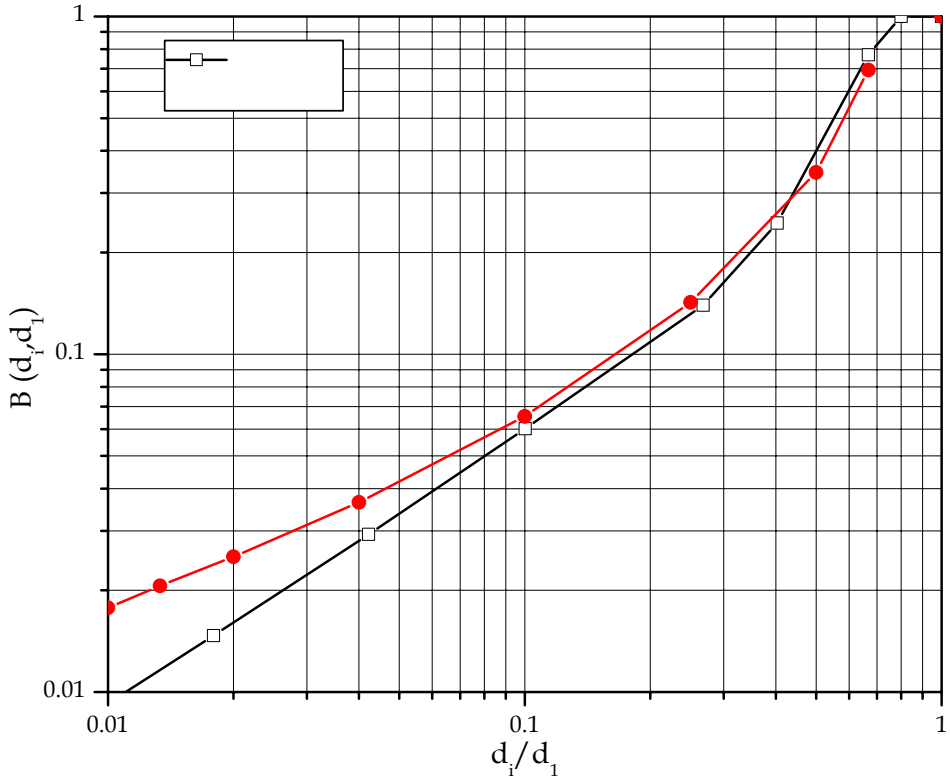

Figure 5.10 Measured and predicted breakage function for dolomitic limestone

5.2.2 Prediction of Product Size Using a Laboratory Jaw Crusher

A laboratory scale crusher was used to test the ability of the breakage function model, when used with the feed size distribution and a classification function, to predict the product size coming out of an actual jaw crusher. The lab-scale crusher was also used to develop a fracture toughness based model for the prediction of capacity. The crushing tests were conducted on rock samples from Boscobel, Culpeper, Shadwell, and Spotsylvania in accordance with the procedure outlined in section 3.5. Appendix IV contains data collected from the laboratory crushing trials.

Verification of breakage function (product size) model

The closed side set and open side set of the crusher were 7.94 mm and 14.29 mm respectively. The throw of the crusher was 6.35 mm and the crusher speed was approximately 300 rpm. Based on the feed size distributions shown in Figure 3.15 the maximum reduction ratio seen by any particle in the crusher was around 4. Using Whiten's crusher model, determined from mass balance equations, and given in Equation 2.4, the product size was predicted using the breakage function model given in the previous section along with a classification function and the feed size distribution. The

breakage function for each particle size in the feed was determined using Equations 5.8 and 5.9 where reduction ratio was defined as the particle size divided by the closed side set. The classification function was calculated for each feed particle using Equation 2.5. A *MathCAD* program was developed in order to perform matrix calculation of the product size using the feed size distribution (mass fraction in each size) vector, the diagonal classification function matrix, and the strictly lower triangular breakage function matrix. The product size distribution vector was determined in terms of the mass fraction retained in each size class. This vector in turn was converted to a percent passing distribution in order to compare it to the actual, measured size distribution of the product.

The actual product size distribution from the jaw was determined by sampling and sieve analysis. Approximately 9 kg of product material was sampled, sieved using a Ro-Tap, and weighed for each rock tested. The actual and predicted results are shown in Figures 5.11 through 5.14.

It can be seen from Figures 5.11 - 5.14 that the actual and predicted results are in fairly good agreement. The predicted product size distribution deviates at the 12.7 mm size due to the use of the cylindrical disk specimen during HECT testing. Since most of the feed material was in the 19.1 to 25.4 mm size range, the breakage function developed in this study using the disk specimen implies that a large portion, if not all, of the product will pass at sizes half of 19.1 to 25.4, or 9.5 to 12.7 mm. In each case 100% of the product was predicted to pass at 12.7 mm. If irregular particles were used during single particle breakage analysis more agreement would be expected between the actual and predicted distributions at the larger sizes. The "shapes" of the predicted and actual distributions are very similar in each case with the major difference between the two curves being in the proportion of material in each size class. The Boscobel granite product distributions showed the most deviation, with about a constant 5% difference (by % passing) between the actual and predicted percentage passing.

Based on the results of the laboratory jaw crushing experiment, the suggested fracture toughness based model for the determination of the breakage function seems reasonable. However, lab crushing is a small-scale attempt at reproducing very large-scale conditions. The feed size used may not be representative of what is seen in actual crushing conditions and the effects of jaw plate wear, throughput, and other operating conditions are minimal. The rocks crushed in the lab jaw were also the same as ones used in the development of the breakage function model, thus the applicability of the model to rocks outside the measured data range is still in question. In the same vein, the maximum reduction seen in the lab crushing experiments was about 4, which is outside the range used in model development but not too far (maximum HECT reduction ratio was 3). Since jaw crushers can see higher reduction ratios up the applicability of the breakage function to all jaw crushing reduction ratios remains to be tested. Despite these limitations the fracture toughness based breakage function model can be used to provide a reasonable estimate of the product size coming out of a jaw crusher given the feed size distribution and the closed side set of the crusher.

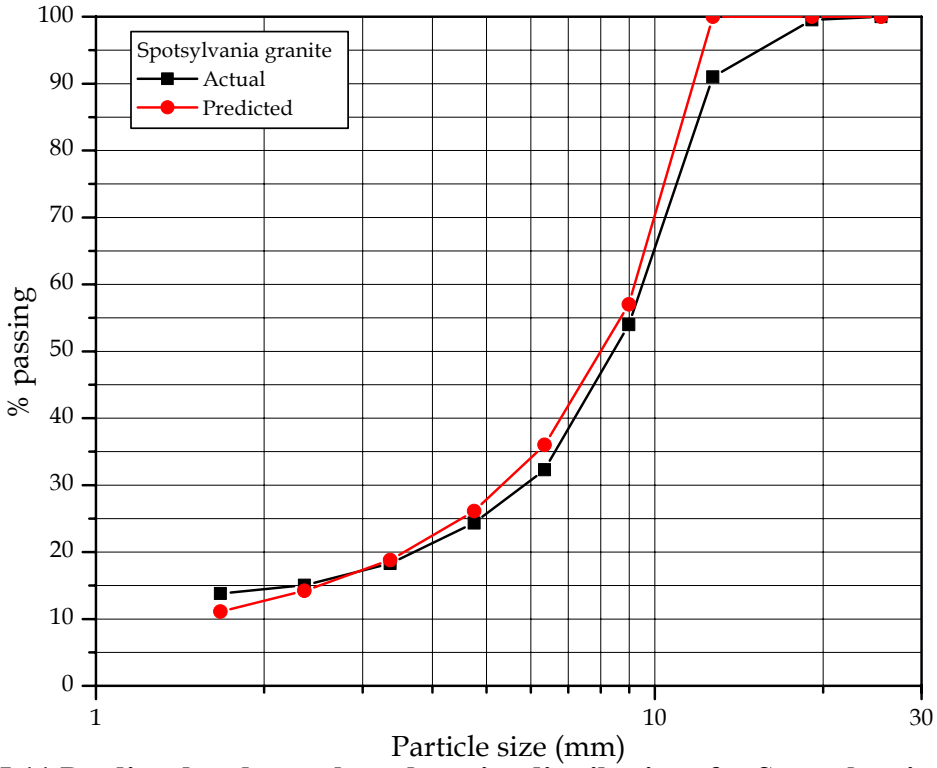

Figure 5.11 Predicted and actual product size distributions for Spotsylvania granite

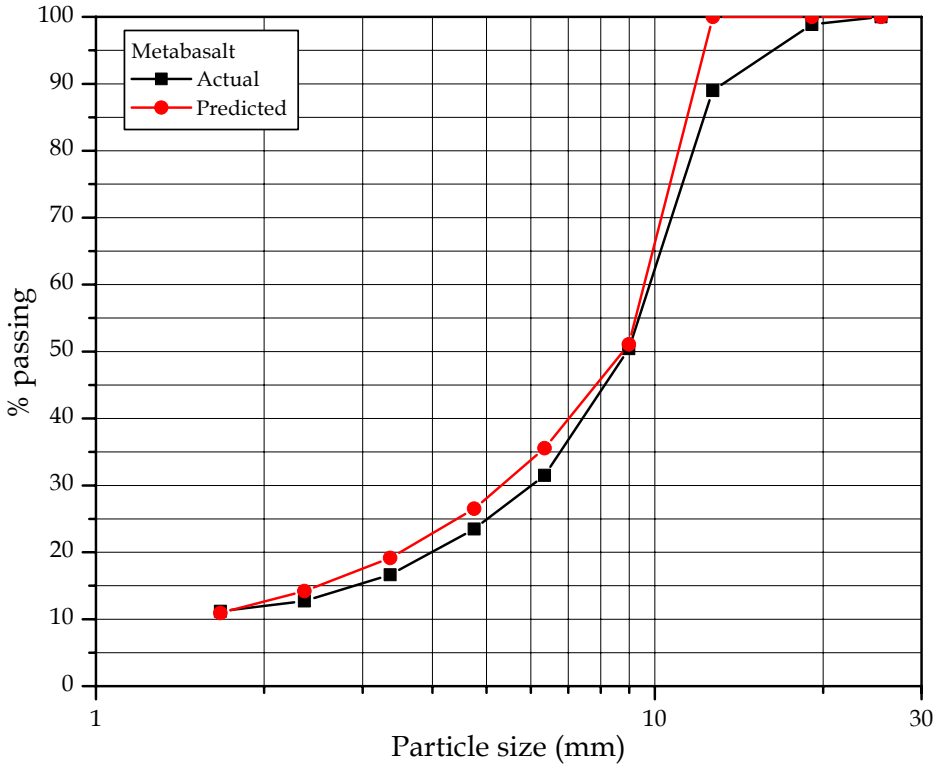

Figure 5.12 Predicted and actual product size distributions for Shadwell metabasalt

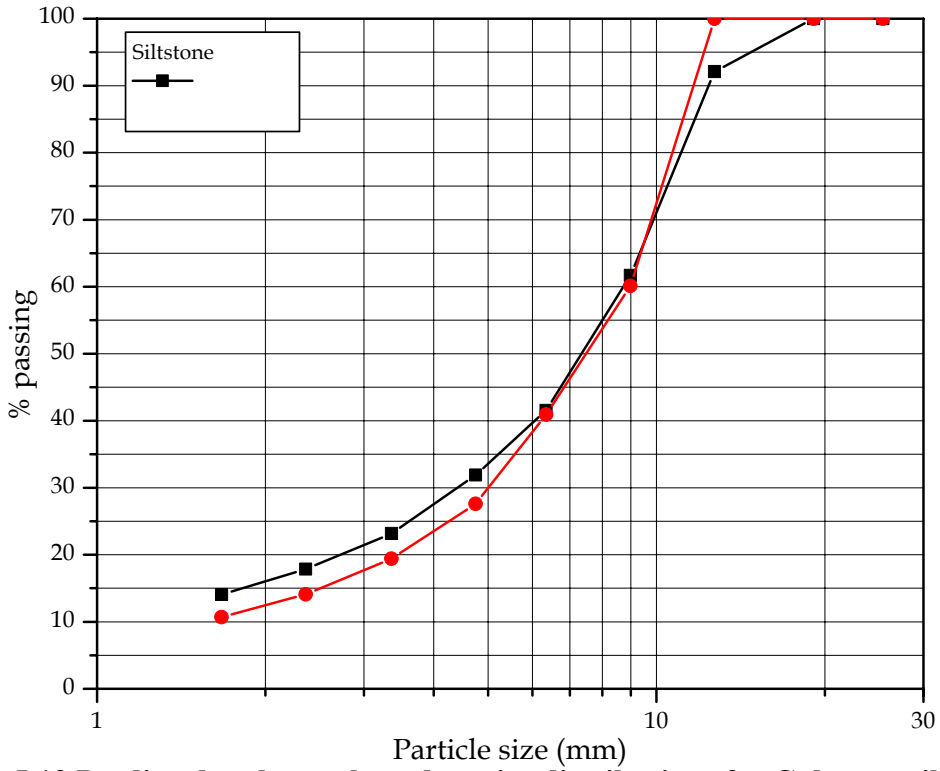

Figure 5.13 Predicted and actual product size distributions for Culpeper siltstone

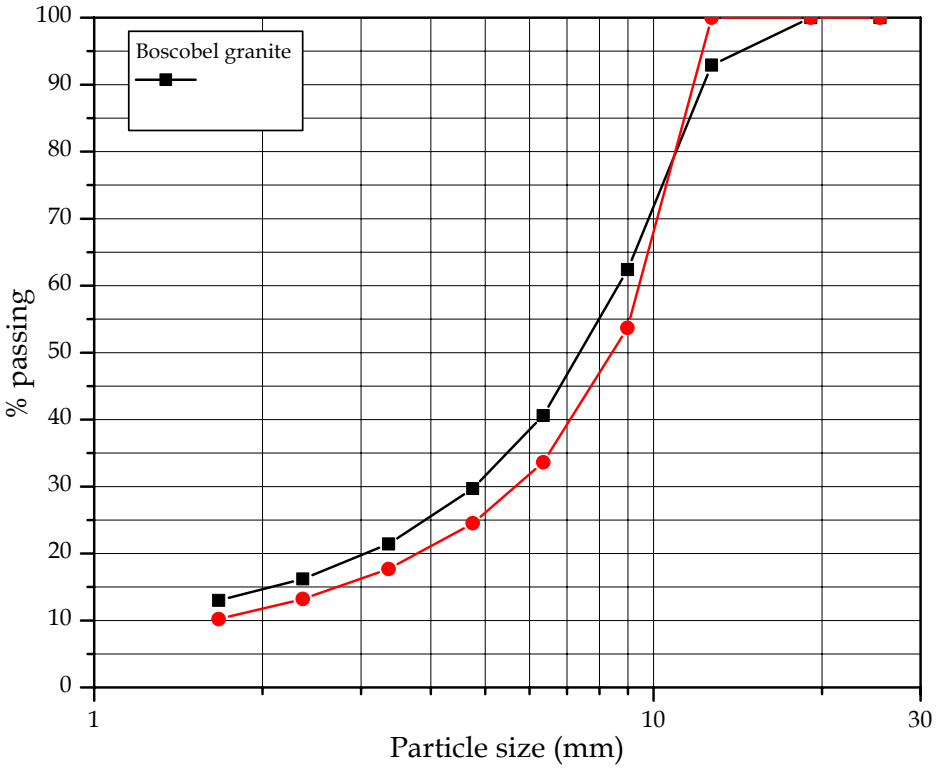

Figure 5.14 Predicted and actual product size distributions for Boscobel granite

5.3 MODEL FOR VOLUMETRIC CAPACITY OF A JAW CRUSHER

In section 2.1.3 equations were given for the volumetric capacity of a jaw crusher based on the dimensions of the crusher, its operational settings (closed side set and throw), its speed, the average feed size, and an undefined parameter related to the nature of the material. The laboratory jaw crusher trials were used to determine the actual volumetric capacity of the jaw, for a given rock, with the expectation that the K_3 parameter could be defined in terms of fracture toughness.

For each rock the average particle size and bulk density of the feed were determined, and the time required to crush the feed material was recorded. The volumetric capacity for each rock was then calculated. Table 5.3 lists the measured capacities for each rock.

Table 5.3 Rock specific volumetric capacities of laboratory jaw crusher

Rock Type	Bulk density kg/m^3	Mass kg	Volume m^3	Time sec	Vol. capacity m^3/hr
Culpeper siltstone	1702	38.80	0.0228	160	0.513
Shadwell metabasalt	1837	45.97	0.0250	195	0.462
Spotsylvania granite	1691	42.97	0.0254	169	0.541
Boscobel granite	1670	47.14	0.0282	172	0.591

Equation 2.12 gives the volumetric capacity of a jaw crusher. The predicted capacity is the "ideal" capacity (i.e., strictly a function of the crusher geometry and operational settings) normalized by three parameters, K_1, K_2, and K_3, which are functions of the feed size, throw and gape, and the nature of the material, respectively. Since K_3 is undefined it is assumed that the deviation between the predicted capacity and the actual capacity measured using the lab crusher is a function of K_3. This can be expressed as (Sastri, 1994):

$$K_3 = \frac{V_{actual}}{V_{predicted}} \qquad [5.10]$$

where (recalling Equations 2.12 and 2.13),

$$V_{predicted} = 60Nw\left(CSS + 0.5T\right)\left(\frac{450g}{N^2}\right)K_1K_2$$

$$K_1 = 0.85 - \left(\frac{F_{avg}}{G}\right)^{2.5} \qquad [5.11]$$

$$K_2 = 1.92 \times 10^{\frac{-6.5T}{G}}$$

and, N is the speed of the crusher in rpm
w is the width of the jaws in m
CSS is the closed side set in m
T is the throw in m

D is the vertical depth between the jaws in m
G is the crusher gape in m
g is gravitational acceleration in m/s^2.

Equation 5.10 was used to determine the predicted volumetric capacity for each rock, which in turn was compared to the actual volumetric capacity using Equation 5.11. It was anticipated that K_3 would be a function of either fracture toughness or strain energy release rate. Figure 5.15 is plot of K_3 versus fracture toughness. It can be seen that K_3 decreases with fracture toughness, or in other words, the volumetric capacity decreases

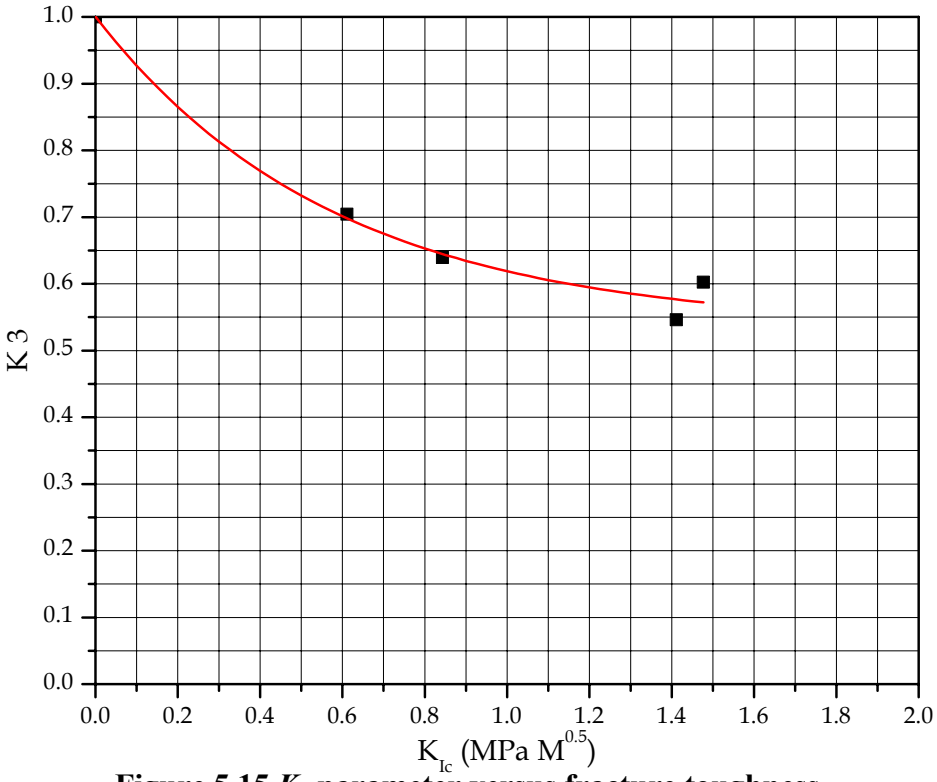

Figure 5.15 K_3 parameter versus fracture toughness

with increasing fracture toughness. K_3 decreases from a value of one since it is expected that the capacity of a material with little to no "hardness" is strictly a function of the crusher geometry, operational settings, and feed size. Again, the Culpeper siltstone shows unique behavior in that it has the highest fracture toughness yet its value of K_3, and in turn the volumetric capacity, was not the lowest among the four rocks crushed. The upward trend is a result of the large amount of shatter occurring in the siltstone particles upon fracture. This behavior has been discussed in detail in the previous sections. The increased shatter occurring in the siltstone results in a uniform progeny size distribution consisting of more finely sized fragments. In regards to volumetric capacity, these fragments pass through the crusher without experiencing much secondary breakage and exit the crushing chambering rather quickly. Additionally, the lack of large fragments that result primarily from cleavage enables more feed material to enter the crushing chamber. Based on this observation K_3 was plotted against the strain energy release rate,

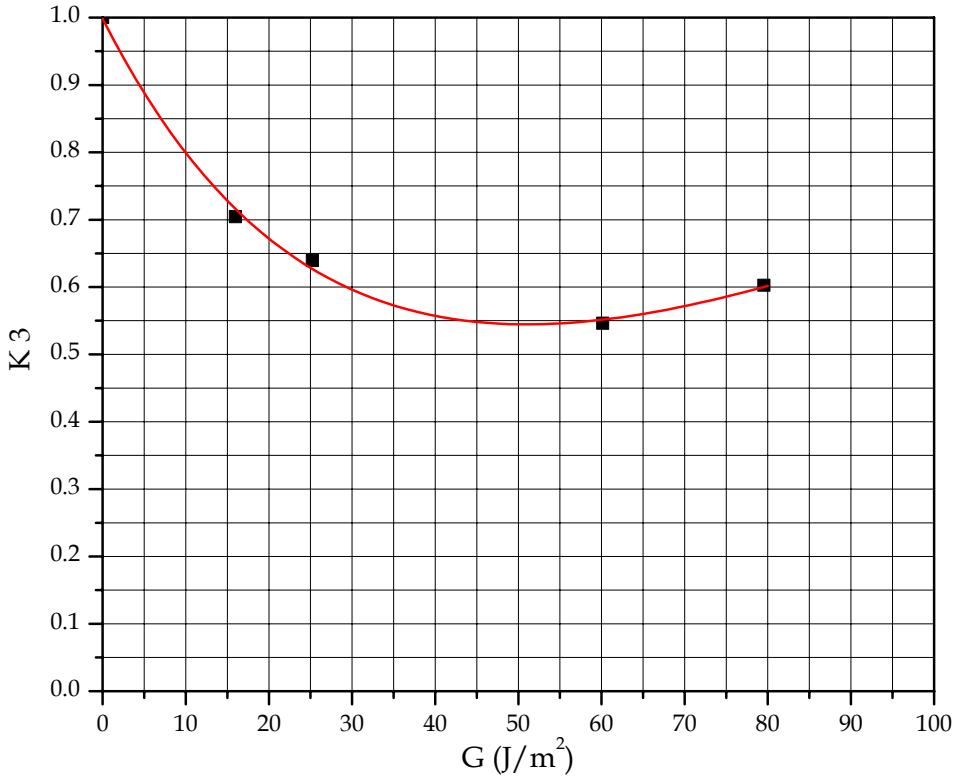

Figure 5.16 K_3 parameter versus strain energy release rate

which was previously related to the product size and takes into account the dominant "type" of fracturing seen in a rock (i.e, cleavage, shatter). Figure 5.16 shows K_3 versus G for the four rocks crushed.

Figure 5.16 indicates that the volumetric capacity decreases with an increase in strain energy release rate to a limiting value (which corresponds to K_3 equal to 0.54) and then begins to increase as the strain energy release rate increases past 50 J/m^2. The relationship between K_3 and G (where G equals K_{Ic}^2/E') can be fit with an exponential expression of the following form:

$$K_3 = 0.0987 + 0.0055\left(\frac{K_{Ic}^{\,2}}{E'}\right) + 0.8995\left(0.9674\right)^{K_{Ic}^2/E'} \qquad [5.12]$$

The volumetric capacity of a jaw crusher can be determined by substituting Equation 5.12 into Equation 2.12.

The relationship given in 5.12 is limited by the small number of rock types (4) crushed in the laboratory jaw crusher. Verification of the fracture toughness based K_3 and volumetric capacity models were not performed. Additional testing on the laboratory scale, or even on a large scale using actual jaw crushers, needs to be performed in order to assess the applicability of the given model.

CHAPTER 6. CONCLUSIONS AND RECOMMENDATIONS

6.1 CONCLUSIONS

In today's crushing environment the need for optimization of jaw crusher selection and operation to meet the economic requirements of quarrying has become imperative. Aggregate processing plants require rugged, massive, and expensive equipment, and misjudgments in design are difficult and expensive to correct. The selection of a jaw crusher for application in the aggregate industry is primarily based on technical literature provided by crusher manufacturers, experience, and cost. Charts and graphs provide data on electric power requirements, crusher size, as well as expected capacities for a given material and closed side set. These charts and graphs have also been incorporated into computer programs to aid in crusher selection. Jaw crusher selection is also heavily influenced by the subjective judgment/experience of individuals, which results in the conservative selection and operation of jaw crushers.

In order to account for material variations manufacturers rely on a suite of laboratory tests. The uniaxial compression and Bond impact crushability test are two of the most common tests used to rank materials relative to their hardness/crushability. Each of these tests has limitations and neither adequately describes a material's resistance to fracture or the breakage process that occurs in a jaw crusher. The plates of a jaw crusher are used to apply compressive forces that induce tensile stresses within particles, causing fracture. Any description of the nature of rock material, relative to jaw crushing, should be based on, at the very least, tensile strength. Although jaw crushers are used extensively the lack of understanding relative to their operational characteristics, as well as a reliance on an inappropriate, single set of material properties, makes selection of a proper machine difficult, and optimization of in-place crushers almost non-existent.

The focus of jaw crusher selection should be on the prediction of power consumption, product size, and capacity. Each of these parameters is a function of the mechanical aspects of the jaw crusher as well as the rock material being crushed, and prediction of these parameters requires the proper characterization of the mechanical nature of rock in regards to the jaw crushing environment and operational settings. This will allow for the rapid estimation of power consumption, product size, and capacity for a given rock being crushed under a given set of operating conditions.

Consideration of the physics of particle fracture and the mechanisms that drive fracture initiation is necessary in the evaluation and improvement of jaw crushing operations. Rocks broken in jaw crushers fail at stress levels well below what is predicted based on stress-strain behavior or compressive strength, due to induced tensile stresses (rocks are much weaker in tension than compression) and the presence of cracks. Rocks by their nature contain inherent flaws in the form of grain boundaries, voids/pores, bedding planes, foliations, etc., on both small and large scales. These cracks act as stress

concentrators, and the increase in stress at these locations is proportional to the geometry of the crack.

Griffith's theory expounds a relationship between crack size and fracture stress. Griffith hypothesized that fracture occurs when the energy supplied by an external force, or by the release of stored strain energy, is greater than the energy of the new crack surface. Griffith's work defined a constant critical value that when equal to the product of the applied stress and crack length will result in fracture. The importance in terms of jaw crushing operations is that fracture is dependent on applied loads (i.e., energy) and the presence, distribution, and size of flaws, and both need to be accounted for when characterizing a rock materials' resistance to fracture.

The mechanisms of fracture also control the distribution of progeny particle sizes and specific fracture mechanisms produce specific fragment sizes, and thus particle physics is the foundation for describing size reduction processes. Energy-size reduction relationships are related to Griffith's energy criterion and the presence of Griffith cracks. The energy criterion states that enough potential energy must be released in order to overcome a material's resistance to crack propagation, requiring an increase in the work done by external forces acting on the material. This is the amount of energy input into reducing the size of a particle. Therefore the energy required for fracture and the amount of size reduction achieved, or the size distribution resulting from fracture, are both dependent upon the presence and distribution of Griffith flaws.

Modifications to Griffith's theory have led to the development of the field of fracture mechanics. Fracture mechanics provides quantitative methods for characterizing the behavior of an intact material as it fractures due to crack growth. Fracture mechanics is applicable to problems of rock breakage since the presence of inherent flaws and discontinuities within geologic materials result in failure. These flaws control the fracture of rocks, and establishing a relationship between flaw geometry and fracture strength is the most fundamental aspect of fracture mechanics. This relationship is defined by fracture toughness, the critical level above which crack extension occurs. Mode I fracture toughness properly characterizes the crack opening displacements that occur in particles being broken in a jaw crusher. Induced tensile stresses open pre-existing flaws and ultimately lead to crack propagation and particle failure. When considering jaw crushing, mode I fracture toughness is the material property most representative of the breakage process occurring due to point contact loading and it is dependent upon the same parameters (applied stress/energy input, flaw distribution and geometry) that control the power consumption and product size of jaw crushers.

In order to relate rock fracture toughness to the power consumption, product size, and volumetric capacity of jaw crushers, a series of laboratory experiments, comprised of fracture toughness testing, single particle breakage, and small scale jaw crushing, had to be undertaken. In addition a new fracture toughness test had to be developed and verified so that rapid, and representative, estimation of rock fracture toughness could be achieved.

A major drawback in studying size reduction processes from a fracture mechanics point of view has been the difficulty and complexity of rock fracture toughness testing.

The Edge-Notched Disk Wedge Splitting test yields representative fracture toughness values (in accordance with Level I testing) using a simple, core based specimen. It requires little specimen preparation time since it employs a straight-through notch. Testing, load application, and data collection are straightforward. The test enables a large number of rock types and specimens to be tested allowing for quick indexing and comparison. When compared to the Semi-Circular bend test, a more common and accepted fracture toughness test, the END test yields almost identical results.

Seven rocks, provided by aggregate producer *Luck Stone Corporation*, were tested for fracture toughness, specific comminution energy, and breakage function. Specific comminution energy and breakage function were determined using a unique single particle breakage device, the High Energy Crushing Test (HECT) system. The HECT system is a specially configured materials testing system that is capable of simulating a wide range of crushing operations. For this study the HECT system was configured to deliver a sinusoidal crushing blow at a speed of 225 rpm, "average" jaw crushing conditions. Since power consumption and product size are functions of the crusher settings as well as the material being crushed, the closed side set of the HECT system was varied, resulting in single particle breakage tests run at two reduction ratios, 1.5 and 3. Core based, disk specimens were employed in the HECT system in order to eliminate the effect of microstructure changes due to blasting (since the END test also used rock core). Although some size/geometry dependency was seen in the breakage function results, the experimental program performed in this study provides a unique core based approach that can be used to determine the jaw crushing requirements of a given rock.

The results of the fracture toughness and HECT system tests indicate a strong, proportional relationship between fracture toughness and specific comminution energy. Additionally, fracture toughness was shown to be related to specific comminution energy more strongly than any other material property tested, including tensile strength. For the rocks tested in this study a linear relationship most adequately describes the relationship between fracture toughness and specific comminution energy. As fracture toughness increases so does the energy required to achieve a certain amount of size reduction (as defined by the reduction ratio, the ratio of the initial particle size to the closed side set). As the reduction ratios increases so does the specific comminution energy. Therefore, the specific comminution energy is function of both the fracture toughness of the rock material and the operational characteristics of the jaw crusher, as defined by the closed side set.

Of the rocks tested only one, a siltstone, did not fall within the 95% confidence limit for the suggested linear relationship between fracture toughness and specific comminution energy. The siltstone had the highest fracture toughness yet was "middle of the road" in terms of required breakage energy. It was observed during HECT breakage

of the siltstone that the rock tended to shatter upon fracture, producing a wide range of progeny sizes. The lack of daughter fragments created by cleavage resulted in less secondary crushing and consequently lower levels of specific comminution energy. This observation was substantiated quantitatively by the uniform distribution of progeny particles seen in the siltstone's breakage function.

When the the feed size distribution, the mass flow at each size, the probability of breakage and the idling power are taken into account, the relationship between fracture toughness and specific comminution energy can be used to define a model for the prediction of jaw crusher power consumption, given by:

$$P_c = \sum_{i=1}^{j} \left[-0.511 + 0.511 RR_i \right] K_{Ic} C_i x_i + P_n \quad \text{for } 1 \le RR < 1.5$$

$$P_c = \sum_{i=1}^{j} \left[0.215 RR_i^{0.428} \right] K_{Ic} C_i x_i + P_n \quad \text{for } RR \ge 1.5$$

where, P_c is the power consumption of the crusher in kW
RR_i is the reduction ratio for a particle of size I
K_{Ic} is the fracture toughness of the rock being crushed in $MPa\sqrt{m}$
C_i is the probability of breakage for particle size i
x_i is the mass flow of particle size i in metric tons per hour
P_n is the power drawn by the crusher under no load in kW.
Since the maximum reduction ratio used in this study was 3, assumptions had to be made in regards to what occurs at higher reduction ratios, and the applicability of the power consumption model to higher reduction ratios remains to be tested.

The relationship between breakage function and fracture toughness was not as strong or as evident as the one between fracture toughness and specific comminution energy. The common procedure of expressing breakage functions as mixtures of separate size populations (fine and coarse) was not employed due to the lack of a relationship between the size proportion and distribution parameters and fracture toughness. Instead, the one-parameter family curves approach was used. In this case a relationship between t_{10}, the characteristic size reduciton parameter, and fracture toughness was evident but only when the elastic modulus, E', of the rock was taken into account. Additional relationships between t_{10} and various t_n values were also evident, thus allowing for the determination of a rock's breakage function based soley on its fracture toughness and elastic modulus.

The relationship demonstrated by the data shows that t_{10} increases with K_{Ic}^2/E', which is the strain energy release rate of the rock. This is because for rocks with higher strain energy release rates shatter fracture is more prevalent and more energy is released as new crack surface energy. As the reduction ratio is increased, the relationship between t_{10} and K_{Ic}^2/E' inverses, and t_{10} decreases with increasing strain energy release rate. The low strain energy release rate rocks are subjected to more secondary breakage than the higher K_{Ic}^2/E' rocks because the low K_{Ic}^2/E' rocks initially produce large progeny fragments as a result of cleavage. These progeny undergo additional breakage in

comparison to the fragments of the high strain energy release rate rocks, which are produced by shatter and have more particles of varying size.

The model for the breakage function is:

$$t_{10} = \left[-7.01 + 7.01RR\right]\left(\frac{K_{Ic}{}^2}{E'}\right)^{(-0.501+0.501RR)} \qquad \text{for } 1 \le RR < 1.5$$

$$t_{10} = \left[100 - \frac{100}{1+\left(\frac{RR}{3.97}\right)^{3.40}}\right]\left(\frac{K_{Ic}{}^2}{E'}\right)^{\left(-0.190+0.0127RR+13.4(0.0998)^{RR}\right)} \qquad \text{for } RR \ge 1.5$$

$$t_{1.5} = 40.9t_{10}{}^{0.281}$$

$$t_2 = 7.68t_{10}{}^{0.800}$$

$$t_4 = 2.17t_{10}$$

$$t_{10} = t_{10}$$

$$t_{25} = 0.556t_{10}$$

$$t_{50} = 0.384t_{10}$$

$$t_{75} = 0.315t_{10}$$

$$t_{100} = 0.271t_{10}$$

where, t_{10} is the percent passing at a progeny size 1/10th of the parent size
K_{Ic} is the fracture toughness of the rock being crushed in $MPa\sqrt{m}$
t_n values are percent passing at a progeny size 1/nth of the parent size
and, E' is given by,

$$E' = E \qquad \text{for conditions of plane stress}$$

$$E' = \frac{E}{1-v^2} \qquad \text{for conditions of plane strain}$$

where, v is Possion's ratio.
As is the case with the power consumption model, the applicability of the breakage function model to high reduction ratios is based strictly on assumptions. Additionally, since the relationship between t_{10} and $K_{Ic}{}^2/E'$ is not well defined the given breakage function model is only recommended for rocks with strain energy release rates that fall within the range measured in this study. More testing is required in order to establish a wider ranging t_{10} and $K_{Ic}{}^2/E'$ relationship, as well as to strengthen/modify the suggested one.

The strain energy release rate was also used in the development of the volumetric capacity model. Although volumetric capacity was shown to decrease with increasing fracture toughness, the siltstone once again displayed deviatoric behavior, as the ability of the laboratory jaw crusher to handle the siltstone actually increased compared to less

"tough" rocks. When using strain energy release rate it was observed that the volumetric capacity initially decreases with increasing K_{Ic}^2/E' but begins to level off and then increase as the strain energy release rate increases beyond 50 J/m^2. Again, this is due to the propensity for high strain energy release rate rocks to shatter upon fracture. The increased shatter occurring in the siltstone resulted in more finely sized daughter fragments. These fragments passed through the crusher without incurring secondary breakage and exited the crushing chambering rather quickly. The lack of large fragments that result primarily from cleavage also allowed more feed material to enter the crushing chamber.

Using K_{Ic}^2/E' the previously undefined parameter K_3 in Sastri's volumetric capacity equation was defined. The adjusted model for volumetric capacity of a jaw crusher is:

$$V = 60Nw\left(CSS + 0.5T\right)\left(\frac{DT}{G-\left(CSS+T\right)}\right)K_1K_2K_3 \qquad \text{at low speeds}$$

$$V = 60Nw\left(CSS + 0.5T\right)\left(\frac{450g}{N^2}\right)K_1K_2K_3 \qquad \text{at high speeds}$$

where, N is the speed of the crusher in rpm
w is the width of the jaws in m
CSS is the closed side set in m
T is the throw in m
D is the vertical depth between the jaws in m
G is the crusher gape in m
and, K_1, K_2, K_3 are given by,

$$K_1 = 0.85 - \left(\frac{F_{avg}}{G}\right)^{2.5}$$

$$K_2 = 1.92\times10^{\frac{-6.5T}{G}}$$

$$K_3 = 0.0987 + 0.0055\left(\frac{K_{Ic}^{\ 2}}{E'}\right) + 0.8995\left(0.9674\right)^{K_{Ic}^2/E'}$$

where, F_{avg} is the average feed size in m.

Full verification of the models for power consumption and volumetric capacity were not performed. Verification of the model strictly for specific comminution energy was performed, along with verification of the breakage function model using the HECT system. The breakage functon model was tested further using the laboratory jaw crusher, by comparing the actual product size distribution with the predicted product size distribution based on Whiten's crusher model and the breakage function.

For the HECT system verification experiment, dolomitic limestone, which had previously been tested for fracture toughness using the END test, was used. The fracture toughness based models for specific comminution energy and t_{10} predicted that the

dolomitic limestone would require 0.305 kWh per metric ton of energy to crush, with brekage resulting in a t_{10} value of 6.6%. The actual values were 0.295 kWh/ton and 6.0%, respectively. The entire predicted breakage function also showed good agreement with the measured function, with some deviation occurring at large t_n values since the breakage function model loses power with increasing t_n.

The prediction of product size for the laboratory scale jaw crusher was performed using four rock types. Employing Whiten's crusher model, based on a mass balance approach, the product size was predicted using the breakage function, classification function, and feed size distribution. The predicted product size showed good agreement with the actual product size produced by the crusher. There is some deviation at larger sizes due to the effect of the disk specimen used to develop the breakage function model. In two cases the predicted percent passing was slightly higher than measured, and in the other two instances it was slightly lower. Overall the predicted product size distribution was within ± 5%, in terms of percent passing (by weight) a given particle size.

Unfortunately full scale verification, using jaw crushers in operation at *Luck Stone* sites, could not be performed. One reason is because the feed size distribution entering *Luck Stone's* jaw crushers has never been determined. Secondly, *Luck Stone* employs essentially the same size jaw crusher at each of its operations and comparison of the predicted power consumption to the installed electric drive would be baseless since the same drive is used at each operation. But at the same time this is the argument for using a new approach to selecting jaw crushers. Based on the model suggested here, the toughest rock tested would consume 230% more power than the weakest for the same feed size and average reduction ratio. In turn, a smaller crusher, driven by a smaller motor, could be used for the weaker rock as long as it is able to meet production requirements. This would result in lower capital cost and lower operating costs. It is important to realize that this would also require a shift away from avoiding secondary breakage at all costs, the main reason large crushers are employed almost universally. Or it would require a change in blast specifications such that the feed material entering the jaw crusher will not bridge.

For cases such as *Luck Stone's*, where jaw crushers are already in place, the breakage function and volumetric capacity models developed in this study can be used to determine feed size distributions and operational settings (i.e., closed side set) that optimize the product size and production capacity. This would improve downstream processes since control over their feed sizes would be excercised. Blasting would also be improved since guidelines for muck size disitribution, which becomes the feed material, could be given.

This study clearly demonstrates that a fracture mechanics approach to the study of size reduction processes is appropriate, and most thoroughly characterizes the process of rock fragmentation in crushing equipment. Rock fracture toughness is related to the amount of energy required to reduce a particle to a given size. It can also be related to

the resultant fractured size distribution and the volumetric capacity of a jaw crusher. Equipment selection and optimization can now be performed using a material property that properly represents the fracture process occurring in a jaw crusher. Fracture toughness can be rapidly determined using the END test, and along with feed size data, and the average amount of size reduction, K_{Ic} can be used to determine the power consumption, product size, and the volumetric capacity of a jaw crusher processing a given rock. The process can also be reversed so that fracture toughness, along with product size and/or desired capacity, can be used to optimize the feed size or closed side set of the crusher.

6.2 RECOMMENDATIONS

All size reduction processes are dependent upon the mechanical parameters of the size reduction and the nature of the rock being broken. Therefore all size reduction and rock fragmentation processes, beginning with blasting, should be analyzed using fracture mechanics, with the nature of the rock being characterized using some measure of its ability to resist fracture, either fracture toughness or strain energy release rate.

Although the applicability of the Edge Notched Disk test was verified in this study, there is some evidence that the results are dependent on grain size and notch radius. Additional refinement of the END test needs to be performed, particularly in regards to using a chevron notch instead of a straight through notch.

The models for power consumption and the breakage function developed in this study need to either verified or modified, based on additional testing, for reduction ratios greater than 3. The breakage function model also requires more testing in order to further clarify the relationship between fragmented product size and fracture toughness/strain energy release rate. Testing at higher reduction ratios will also improve the relationships between t_{10} and other t_n vales used to determine the breakage size distribution. Since only 6 rock types were used in this study the models proposed could be strengthened/adjusted simply by testing more rocks that are both inside and outside of the measured range. Specifically, more sedimentary rocks types should be tested in order to determine the how representative of sedimentary rocks the Culpeper siltstone is.

All the models proposed here require full-scale verification. Similar models for the power consumption of cone crushers require scale-up factors, and the same may be expected for the jaw crusher power consumption model. The volumetric capacity model is based only on the results of lab-scale crushing of four rocks, and it too may be subject to a scale-up factor since actual jaw crushers are on the order of 10 times bigger than the lab jaw used in this study. The feed size distribution used in the lab crushing experiments was fairly narrow and the scale-up effect of feed size and distribution must also be accounted for.

This investigation relied solely on the testing of rock core specimens (except for the laboratory jaw tests). In reality, rocks fed to a jaw crusher have undergone a change in their microstructure due to blasting. Although it would be expected that similar relationships hold between fracture toughness, specific comminution energy, and breakage function, a similar study should be undertaken using rock specimens prepared from blasted rock. The effect of blasting on the distribution and size of flaws, and thus fracture toughness, can be examined.

Likewise, single particle breakage testing should be done on irregular particles that more closely resemble those found in the feed. The influence of the disk specimen geometry on the breakage distribution can then be determined, as well as it ability to mimic an irregular particle under point contact loading.

It is clear that fracture mechanics and fracture toughness can be used to model and predict the behavior of both rock and machine when considering jaw crushing applications. Jaw crushers can now be selected or optimized based on only a few parameters as long as the fracture toughness of the rock being broken is known. Proper characterization of the rock, along with the exclusion of overemphasized factors such as design experience and secondary breakage, allows for the selection of suitably sized equipment and/or the optimization of the product and production capacity. This results in reduced capital costs, reduced operating costs, efficient production, and an overall improvement in the entire size reduction process.

It is also apparent that this study is just the beginning, and that more effort in studying size reduction from a rock fracture mechanics point of view needs to be carried out in order to refine and verify the findings outlined here, as well as to widen the application of fracture mechanics to other size reduction applications.

REFERENCES

Akram, M. (1991) *The Effect of Zero Point of Charge Environment On Rock Fracture Behavior*, MS Thesis - Virginia Tech, Blacksburg, VA.

Allis-Chalmers (1985) *Allis-Chalmers High Energy Crushing Test System User Manual*, Version 1.0.

Andersen, J.S. (1988) *Development of a Cone Crusher Model*, MEng Thesis – University of Queensland, Australia.

Andersen, J.S. and Napier-Munn, T.J. (1988) Power Prediction for Cone Crushers, *3rd Mill Operators Conference*, AusIMM, Cobar, Australia.

Andersen, J.S. and Napier-Munn, T.J. (1990) The Influence of Liner Condition on Cone Crusher Performance, *Minerals Engineering*, Vol. 3, No. 1-2, pp. 105-116.

Arbiter, N., Harris, C.C., and Stamboltzis, G.A. (1969) Single Fracture of Brittle Spheres, *Transactions of SME/ AIME*, Vol. 244, AIME, New York, pp. 118-133.

Austin, L.G. and Brame, K. (1983) A Comparison of the the Bond Method for Sizing Wet Tumbling Ball Mills With An SMB Simulation Model, *Powder Technology*, Vol. 34, pp. 261-274.

Barker, L.M. (1977) A Simplified Method for Measuring Plane Strain Fracture Toughness, *Engineering Fracture Mechanics*, Vol. 9, pp. 361-369.

Barton, C.C. (1983) Variables in Fracture Energy and Toughness of Rock, *Proceedings of the 24th U.S. Symposium On Rock Mechanics*, Berkeley, CA, pp. 449-462.

Bearman, R.A., Pine, R.J., and Wills, B.A. (1989) Use of Fracture Toughness Testing in Characterizing the Comminution Potential of Rock, *Proceedings of MMIJ/IMM Joint Symposium*, Kyoto, pp. 161-170.

Bearman, R.A., Barley, R.W., and Hitchcock, A., (1990) The Development of a Comminution Index for Rock and The Use of an Expert System to Assist The Engineer in Predicting Crushing Requirements, *Minerals Engineering*, Vol. 3, No. 1-2, pp. 117-127.

Bearman, R.A., Barley, R.W., and Hitchcock, A. (1991) Prediction of Power Consumption and Product Size in Cone Crushing, *Minerals Engineering*, Vol. 4, No. 12, pp. 1243-1256.

Bearman, R.A., Briggs, C.A., and Kojovic, T. (1997) The Application of Rock Mechanics Parameters to the Prediction of Comminution Behavior, *Minerals Engineering*, Vol. 10, No. 3, pp. 255-264.

Bearman, R.A. (1998) The Use of the Point Load Test for the Rapid Estimation of Mode I Fracture Toughness, *International Journal of Rock Mechanics and Mining Sciences*, Vol. 36, pp. 257-263.

Bergstrom, B.H., Sollenberger, C.L., and Mitchell, W. (1962) Energy Aspects of Single Particle Crushing, *Transactions AIME*, Vol. 223, pp. 367-372.

Bergstrom, B.H. and Sollenberger, C.L. (1962) Kinetic Energy Effect in Single Particle Crushing, *Transactions AIME*, Vol. 223, pp. 373-379.

Bergstrom, B.H. (1965) Energy and Size Distribution Aspects of Single Particle Crushing, *Proceedings of 5th Rock Mechanics Symposium*, pp. 155-172.

Berry, P., Dantini, E.M., and Masacci, P. (1984) Influences of Mechanical Characteristics of Rock on Size Reduction Processing, *Proceedings of Mineral Processing and Extractive Metallurgy*, Beijing, pp. 15-26.

Beke, Bela. (1964) *Principles of Comminution*, Akademiai Kiado, Budapest.

Black, R.A. and Hoek, E. (1967) Status of Rock Mechanics as Applied to Mining, *Proceedings of the 9th Symposium on Rock Mechanics*, AIME, Colorado School of Mines, Golden, CO.

Bond, F.C. (1952) The Third Theory of Comminution, *Transactions of AIME/SME*, Vol. 193, pp. 4884-494.

Bourgeois, F., King, R.P., and Herbst, J.A. (1992) Low-Impact-Energy Single-Particle Fracture, *Comminution – Theory and Practice*, ch. 8, (edited by S. Komar Kawatra). SME, Littleton, CO, pp. 99-108.

Bowers, L.R., Broaddus, W.R., Dwyer, J., Hines, J., and Stansell, R. (1991) Processing Plant Principles, *The Aggregate Handbook,* ch. 8, (edited by Richard D. Barksdale), NSA, Washington D.C.

Briggs, C.A. and Bearman, R.A. (1996) An Investigation of Rock Breakage and Damage in Comminution Equipment, *Minerals Engineering*, Vol. 9, No. 5, pp. 489-497.

Bubsey, R.T., Munz, D., Pierce, W.S., Shannon, J.L. (1982) Compliance Calibration of the Short Rod Chevron-Notch Specimen for Fracture Toughness Testing of Brittle Materials, *International Journal of Fracture*, Vol. 18, no. 2, pp. 125-133.

Carey, W.F. and Bosanquet, C.H. (1933) A Study of Crushing Brittle Solids, *Journal of the Society of Glass Technology*, Vol. 17, pp. 348.

Charles, R.J. (1957) Energy-Size Relationships in Comminution, *Transactions AIME/SME*, Vol. 208, pp. 80-88.

Choi, Woo-Zin. (1982) *Comminution and Liberation Studies of Complex Sulfide Ores*, MS Thesis – Virginia Tech, Blacksburg, VA.

Chong, K.P. (1980) Effects of Strain Rate on Oil Shale Fracturing, *International Journal of Rock Mechanics, Mining Science, and Geomechanics Abstracts*, Vol. 17, pp. 35-43.

Chong, K.P. and Kuruppu, M.D. (1984) New Specimen for Fracture Toughness Determination of Rock and Other Materials, *International Journal of Fracture*, Vol. 26, pp. R59-R62.

Chong, K.P., Kuruppu, M.D., and Kuszmaul, J.S. (1987) Fracture Toughness Determination of Rocks with Core Based Specimens, *SEM/RILEM International Conference on Fracture of Concrete and Rock*, Houston, pp. 13-25.

Clark, C.B. (1987) *Principles of Rock Fragmentation*, Wiley and Sons, New York.

Csoke, B., Petho, S., Foldesi, J., and Meszaros, L. (1996) Optimization of Stone-Quarry Technologies, *International Journal of Mineral Processing*, Vol. 44-45, pp. 447-459.

DeDiemar, R.B. (1990) New Concepts in Crusher Technology, *Minerals Engineering*, Vol. 3, No. 1-2, pp. 67-74.

Deliac, E.P. (1986) *Optimization Des Machines D'abattage a Pics*, PhD Thesis – University of Paris, France.

Donovan, J.G. and Karfakis, M.G. (2003) Adaptation of a Simple Wedge Test for the Rapid Determination of Mode I Fracture Toughness and the Assessment of Relative Fracture Resistance, *International Journal of Rock Mechanics and Mining Sciences*, Technical Note, In Press.

Dowling, N.E. (1999) *Mechanical Behavior of Materials – Engineering Methods for Deformation, Fracture, and Fatigue*, Prentice Hall, Upper Saddle River, NJ.

Duthoit, Vincent (2000) Crushing and Grinding, *Aggregates*, ch. 9, (edited by Louis Primel and Claude Tourenq). Balkema, Rotterdam.

Eloranta, J. (1997) The Efficiency of Blasting Versus Crushing and Grinding, *Proceedings of the 23rd Annual Conference on Explosives and Blasting Techniques*, Las Vegas, pp. 157-163.

Fairs, G.L. (1954) A Method of Predicting the Performance of Commercial Mills in the Fine Grinding of Brittle Materials, *Transactions of the Institute of Mining and Metallurgy*, Vol. 63, pp. 211-240.

Fenghui, W. (2000) Prediction of Intrinsic Fracture Toughness for Brittle Materials From the Apparent Toughness of Notched-Crack Specimen, *Journal of Materials Science*, Vol. 35, pp. 2443-2546.

Gaudin, A.M. and Hukki, R.T. (1946) Principles of Comminution, *Transactions AIME/SME*, Vol. 223, pp. 40-43.

Gaudin, A.M. and Meloy, T.P. (1962) Model and a Comminution Distribution Equation, *Transactions AIME*, Vol. 169, pp. 67-87.

Gilvarry, J.J. (1961) Fracture of Brittle Solids – Distribution Function for Fragment Size in Single Fracture (Theoretical), *Journal of Applied Physics*, Vol. 32, pp 391-399.

Gilvarry, J.J. and Bergstrom, B.H. (1962) Fracture and Comminution of Brittle Solids: Further Experimental Results, *Transactions AIME/SME*, Vol. 226, pp. 412-422.

Gregory, R.D. (1979) The Edge-Cracked Circular Disc Under Symmetric Pin-Loading, *Mathematical Proceedings of the Cambridge Philosophical Society*, Vol. 85, pp. 523-538.

Griffith, A.A. (1921) The Phenomenon of Rupture and Flow in Solids, *Philosophical Transactions of the Royal Physical Society*, Vol. 221, pp. 163-198.

Guo, H. (1990) *Rock Cutting Using Fracture Mechanics Principles*, PhD Thesis - The University of Wollongong, Australia.

Hanish, J. and Schubert, H. (1986) Compressive Comminution of Particle Beds, *Aufbereitungs Technik*, No. 10, pp. 535-539.

Herbst, J.A. and Fuersternau, D.W. (1972) Influence of Mill Speed and Ball Loading on the Parameters of the Batch Grinding Equation, *Transactions AIME/SME*, Vol. 252, pp. 169-176.

Herbst, J.A. and Lo, Y.C. (1992) Microscale Comminution Studies for Ball Mill Modeling, *Comminution – Theory and Practice*, ch. 11, (edited by S. Komar Kawatra). SME, Littleton, CO, pp. 137-152.

Hersam, E.A. (1923) Factors Controlling the Capacity of Rock Crushers, *Transactions AIME*, Vol. 68, pp. 463-476.

Hofler, Andreas. (1990) *Fundamental Breakage Studies of Mineral Particles With An Ultrafast Load Cell Device*, PhD Dissertation – University of Utah, Salt Lake City, UT.

Holmes, J.A. (1957) A Contribution to the Study of Comminution – A Modified Form of Kick's Law, *Transactions of the Institute of Chemical Engineers*, Vol. 35, pp. 125-156.

Hondros, J.R. (1959) The Evaluation of Poisson's Ratio and the Modulus of Materials of a Low Tensile Resistance by the Brazilian (Indirect Tensile) Test With Particular Reference to Concrete, *Australian Journal of Applied Science*, no. 10, pp. 243-268.

Hukki, R.T. (1961) Proposal for a Solomonic Settlement Between the Theories of von Rittenger, Kick, and Bond, *Transactions of AIME/SME,* Vol. 220, pp. 403-408.

Ingraffea, A.R., Gunsallus, K.L., Beech, J.F., Nelson, P. (1982) A Fracture Toughness Testing System for Prediction of Tunnel Boring Machine Performance, *Proceedings of the 23rd U.S. Symposium on Rock Mechanics*, The University of California, pp. 463-470.

Institution of Chemical Engineers (1974) *Comminution: A Report by the Institution of Chemical Engineers' Working Party Concerned With the Theory and Practice of the Size Reduction of Solid Materials*, (edited by V.C. Marshall), I. Chem. E. Services, London.

Inglis, C.E. (1913) Stresses in a plate Due to the Presence of Cracks and Sharp Corners, *Transactions of the Institute of Naval Architects*, pp. 219-230.

Irwin, G.R. (1948) Fracture Dynamics, *Fracturing of Metals - American Society of Metals Symposium*, Chicago, pp. 147-166.

Irwin, G.R. (1957) Analysis of Stresses and Strains Near the End of a Crack Transversing a Plate, *Journal of Applied Mechanics*, Vol. 24, pp. 361-364.

Isida, M., Imai, R., and Tsuru, H. (1979) *Symmetric Plane Problems of Arbitrarily Shaped Plates With an Edge Crack*, Transactions of the Japanese Society of Mechanical Engineers, Vol. 45, 395A, pp. 743-749.

ISRM (1988) Suggested Methods for Determining the Fracture Toughness of Rocks, (coordinator F. Ouchterlony), *International Journal of Rock Mechanics and Geomechanics Abstracts*, Vol. 25, pp. 73-96.

Jomoto, K. and Majima, H. (1972) Criterion of Comminution, *CIM Transactions*, Vol. 75, pp. 326-331.

Jowett A. and van der Waerden, N.M. 91982) Adaptation of Single Particle Hardness Test for Application to Iron Ores and Associated Rocks, *Powder Technology*, Vol. 32, pp. 9-19.

Karfakis, M.G., Chong, K.P., and Kuruppu, M.D. (1986) A Critical Review of Fracture Toughness Testing of Rocks, *Proceedings of the 27th U.S. Symposium on rock Mechanics*, University of Alabama, SME, pp. 3-10.

Karra, V.J. (1982) A Process Performance Model for Cone Crushers, *XIV International Mineral Processing Congress: Worldwide Industrial Application of Mineral Processing Technology*, Toronto, paper III-6.

Kelly, E.G and Spottiswood, D.J. (1982) *Introduction to Mineral Processing*, John Wiley and Sons, New York.

Kelly, E.G and Spottiswood, D.J. (1990) The Breakage Function; What Is It Really?, *Minerals Engineering*, Vol. 3, No. 5, pp. 405-414.

Kelsall, D.F. and Reid, K.J. (1965) The Derivation of a Mathematical Model for Breakage in Small, Continuous Wet Ball Mill, *Joint AIChE and Institute of Chemical Engineers Meeting*, London, Paper 4.2.

Khan, K. and Al-Shayea, N.A. (2000) Effect of Specimen Geometry and testing Method on Mixed-Mode I-II Fracture Toughness of a Limestone Rock From Saudi Arabia, *Rock Mechanics and Rock Engineering*, Vol. 33, no. 3, pp. 179-206.

Kick, F. (1883) The Law of Proportional Resistance and Its Application to Sand and Explosions, *Dinglers Journal*, Vol. 250, pp. 141-145.

King, R.P. (2001) *Modeling and Simulation of Mineral Processing Systems*, Butterworth-Heinemann, Boston.

Kojovic, T., Napier-Munn, T.J., and Andersen, J.S. (1997) Modeling Cone and Impact Crushers Using Laboratory Determined Energy-Breakage Functions, *Comminution Practices*, ch. 25, (edited by S. Komar Kawatra), SME, Littleton, CO.

Klimpel, R.R. and Austin, L.G. (1965) The Statistical Theory of Primary Breakage Distribution for Brittle Materials, *Transactions AIME/SME*, Vol. 232, pp. 88-94.

Knott, J.F. (1972) *Fundamentals of Fracture Mechanics*, John Wiley and Sons, New York.

Krough, S.R. (1980) Determination of Crushing and Grinding Characteristics Based On Testing of Single Particles, *AIME Transactions*, Vol. 266, pp. 1957-1962.

Lim, I. L., Johnston, I. W., Choi, S. K., Boland, J. N. (1994) Fracture Testing of a Soft Rock With Semicircular Specimens Under Three Point Bending - Part 1, *International Journal of Rock Mechanics, Mining Sciences, and Geomechanics Abstracts*, Vol. 31, pp. 185-197.

Lowrison, G.C. (1974) Crushing and Grinding, CRC Press, Cleveland, Ohio.

Luck Stone Corporation (2003) *http://www.luckstone.com/crushed*.

Lynch, A.J. (1977) *Mineral Crushing and Grinding Circuits: Their Simulation, Optimization, Design, and Control*, Elsevier, New York.

Manca, P.P, Massacci G., and Rossi, G. (1983) Energy Requirements of Rock Breaking in Mining Operations – Considerations and Proposals, *1st International Symposium on Rock Fragmentation by Blasting*, Lulea, Sweden, pp. 705-724.

Mehrim, M.R. and Khalaf, F. 91980) Kinetics of Comminution in Slow Compression, *21st U.S Symposium on Rock Mechanics*, pp. 410-419.

Metso Minerals (2003) *Nordberg C Series Jaw Crushers*, Technical publication.

Metso Minerals (2003a) *Your Comprehensive Source for Aggregate Processing*, Technical literature.

Moore, D.C. (1982) Prediction of Crusher Power Requirements and Product Size Analysis, *Design and Installation of Comminution Circuits*, (edited by A.L. Mular and G.V. Jergensen), SME/AIME, pp. 218-227.

Morrell, S., Napier-Munn, T.J., and Andersen, J.S. (1992) The Prediction of Power Draw for Comminution Machines, *Communition – Theory and Practice*, (edited by S. Komar Kawatra), AIME, pp. 405-426.

Murakami, Y. (1987) *Stress intensity Factors Handbook*, Pergamon Press, New York.

Muskhelishvili, N.I. (1963) *Some Basic Problems of the Mathematical Theory of Elasticity; Fundamental Equations, Plane Theory of Elasticity, Torsion, and Bending*, Groningen P. Noordhoff.

Narayanan, S.S. (1985) *Development of a Laboratory Single Particel Breakage Technique and Its Application to Ball Mill Modeling and Scale-Up*, PhD Dissertation – University of Queensland.

Narayanan, S.S. and Whiten, W.J. (1988) Determination of Characteristics from Single Particle Breakage Test and Its Application in Ball Mill Scale-up, *Transactions of IMM*, 97, Section C, pp. C1115-C124.

Napier-Munn, T.J., Morrell, S., Morrison, R.D., Kojovic, T. (1999) *Mineral Comminution Circuits – Their Operation and Optimization*, Julius Kruttschnitt Mineral Research Center, Queensland.

Nelson, P.P. and Fong, F.L.C. (1986) Characterization of Rock For Boreability Evaluation Using Fracture Material Properties, *Proceedings of the 27th U.S. Symposium on Rock Mechanics*, pp. 846-852.

Nolen-Hoeksema, R.C. and Gordon, R.B. (1987) Optical Detection of Crack Patterns in the Opening Mode Fracture of Marble, *International Journal of Rock Mechanics, Mining Sciences, and Geomechanics Abstracts*, Vol. 24, no. 2, pp. 135-144.

Nordberg (1995) Compression Test, *Laboratory Test Guidelines*, pp. 3-9.

Oka, Y. and Majima, W. (1970) A Theory of Size Reduction Involving Fracture Mechanics, *Canadian Metallurgical Quarterly*, Vol. 9, pp. 429-339.

Orowan, E. (1949) Fracure and Strength of Solids, *Reports on Progress in Physics*, Vol. 12, pp. 185.

Ouchterlony, F. (1980) *A New Core Specimen for the Fracture Toughness Testing of Rock*, SveDeFo Report DS1980:17, Swedish Detonic Research Foundation, Stockholm.

Ouchterlony, F. and Sun, Z. (1983) New Methods of Measuring Fracture toughness on Rock Cores, *1st International Symposium on Rock Fragmentation By Blasting*, Lulea, Sweden, pp. 199-223.

Ouchterlony, F. (1989) Fracture Toughness Testing of Rock With Core Based Specimens - The Development of an ISRM Standard, *Fracture Toughness and Fracture Energy*, (edited by Mihashi et al.), Balkema, Rotterdam, pp. 231-251.

Ouchterlony, F. (1989a) On the Background to the Formula and Accuracy of Rock Fracture Toughness Measurements Using ISRM Stnadard Core Specimens, *International Journal of Rock Mechanics, Mining Science, and Geomechanics Abstracts*, Vol. 26, no. 1, pp. 13-23.

Pauw, O.G. and Mare, M.S. (1988) The Determination of Optimum Impact Breakage Routes for an Ore, *Powder technology*, vol. 54, pp. 3-13.

Pennsylvania Crusher Corporation (2003) Crusher Selection, *Handbook of Crushing* - http://penncrusher.com/1sol1_3.html.

Peter Rit A., Hagg, H., and van Brakel, J. (1983) Characterization of Mechanical Strength of Coal Particles, *Instiution of Chemical Engineers EME Symposium Series 69, POWTECH '83 - 9th International Powder Bulk Solids Technical Exhibit and Conference*, Birmingham, UK, pp. 1-19.

Pook, L.P. (2000) *Linear Elastic Fracture Mechanics for Engineers: Theory and Applications*, WIT Press, Boston.

Prasher, C.L. (1987) *Crushing and Grinding Process Handbook*, John Wiley and Sons, New York.

Rimmer, H.W., Swaroop, S., Flavel, M.D., Leverance, N.C. (1986) Equipment Sizing and Process Design Procedures for Crushing and Screening Circuits, *Advances in Mineral Processing*, (edited by P. Somasundaran), SME/AIME, pp. 575-593.

von Rittenger, P.R. (1867) *Lehrbuch der Aufbereitungskonde*, Berlin.

Rooke, D.P. and Cartwright, D.J. (1976) *Compendium of Stress Intensity Factors*, H.M.S.O, London.

Rumpf, H. (1966) Auferbereitungs-Technik, Vol. 7, pp. 421.

Santurbao, R. and Fairhurst, C. (1991) Fracture Mechanics In the Context of Rock Crushing: preliminary Experimental Results Concerning the Impact of Limestone Spheres, *Rock Mechanics as a Multidisciplinary Science Proceedings of the 32nd U.S. Symposium* (edited by Roegiers), Balkema, Rotterdam, pp. 441-449

Sastri, S.R (1994) Capacities and Performance Characteristics of Jaw Crushers, *Minerals and Metallurgical Processing*, Vol. 11, No. 2, pp. 80-86.

Schmidt, R.A. (1980) A Microcrack Model and Its Significance to Hydraulic fracturing and Fracture toughness Testing, *Proceedings of the 21st U.S. Symposium on Rock Mechanics*, pp. 581-590.

Schmidt, R.A and Rossmantihm H.P (1983) Basics of Rock Fracture Mechanics, *Rock Fracture Mechanics*, ch. 1, (edited by H.P. Rossmanith), Springer-Verlag, New York, pp. 2-29.

Schoenert, K. (1972) Role of Fracture Physics in Understanding Comminution Phenomena, *Transactions SME/AIME*, Vol. 252, pp. 21-26.

Schoenert, K. (1979) Aspects of the Physics of Breakage Relevant to Comminution, *4th Tewksbury Symposium*, Melbourne, pp. 3.1-3.30.

Schoenert, K. (1987) Advances in the Physical Fundamentals of Comminution, *Advances in Mineral Processing*, ch. 1, (edited by Somasundaran), SME, Littleton, CO, pp. 19-32.

Schoenert, K. (1991) Advances in Comminution Fundamentals and Impacts on Technology, *Aufbereitungs Technik*, Vol,. 32, No. 9, pp. 487-494.

Shockey, D., Curran, D., Seaman, L., Rosenberg, J, and Ptersen, C. (1974) Fragmentation of Rock Under Load, *International Journal of Rock Mechanics Science and Geoemachanics Abstracts*, Vol. 11, pp. 303-317.

Sih, G.C. (1973) *Handbook of Stress Intensity Factors for Researchers and Engineers*, Institute of Fracture and Solid Mechanics - Lehigh University.

Stansell, B. (2003) Private communication.

Sun, Z. and Ouchterlony, F. (1986) Fracture Toughness of Stripa Granite Cores, *International Journal of Rock Mechanics, Mining Sciences, and Geomechanics Abstracts*, Vol. 23, no. 6, pp. 399-409.

Svensson, A. and Steer, J.F. (1990) New Cone Crusher Technology and Developments In Comminution Circuits, *Minerals Engineering*, Vol. 3, No. 1-2, pp. 83-103.

Tada, H., Paris, P.C., and Irwin, G.R. (2000) *The Stress Analysis of Cracks Handbook*, ASME Press, New York.

Tkacova, K. (1989) *Mechanical Activation of Minerals*, Elsevier, New York.

Virginia Department of Mines, Minerals, and Energy (DMME) (2003) Division of Mineral Resources, http://www.mme.state.va.us/dmr/DOCS/Geol/vageo.html.

Wagner, W.J., (1990) Rating Crushers By Formula, *Rock Products*, February, pp. 48-51.

Weibull, W. (1939) A Statistical Theory of the Strength of Materials, *Ing Vet Akad*, Vol. 151, pp. 1-39.

Weichert, R. and Herbst, J.A. (1986) An Ultrafast load Cell Device for Measuring Particle Breakage, *Proceedings of the 1st World Congress on Particle Technology*, Nurnber, pp. 3-14.

Weiss, N.L. (1985) Jaw Crushers, SME Mineral Processing Handbook, ch. 3B-1, (edited by N.L. Weiss), SME/AIME, New York.

Whiten, W.J. (1972) *Simulation and Model Building for Mineral Processing*, PhD Dissertation - University of Queensland, Australia.

Whiten, W.J. (1972a) The Simulation of Crushing Plants with models Developed Using Multiple Spline Regression, *The 10th International Symposium on the Application of Computer Methods in the Mineral Industry*, Johannesburg, pp. 317-323.

Whiten , W.J. (1984) Models and Control Techniques for Crushing Plants, *Control '84* (edited by J.A. Herbst), SME, pp. 217-224.

Whittaker, B.N., Singh, R.N., and Sun, G. (1992) *Rock Fracture Mechanics – Principles, Design and Applications*, Elsevier, New York.

Wills, B.A. (1992) *Mineral Processing Technology*, Pergamon Press, New York.

Yashima, S., Morohashi, S., and Saito, F. (1979) Single Particel Crushing Under Slow Rate of Loading, *Scientific Reports of the Research Institute – Tohoku University*, No. 1, pp. 116-133.

APPENDIX I

END RESULTS: FRACTURE TOUGHNESS

Table A1.1 Fracture toughness results for Boscobel granite

Specimen	D	t	a	F_v	F_w	K_{Ic}
	mm	*mm*	*mm*	*N*	*N*	*MPa m$^{1/2}$*
BG-W-1	47.498	25.375	21.920	73	73	0.129
BG-W-2	47.447	25.095	21.920	367	367	0.657
BG-W-3	47.473	26.289	21.920	416	416	0.709
BG-W-4	47.473	24.511	21.920	48	48	0.088
BG-W-5	47.498	25.502	22.047	289	289	0.511
BG-W-6	47.498	24.790	22.123	23	23	0.042
BG-W-7	47.473	25.603	21.971	131	131	0.229
BG-W-8	47.523	26.416	22.123	344	344	0.589
BG-W-9	47.498	25.121	21.996	109	109	0.195
BG-W-10	47.447	24.841	22.123	294	293	0.536
					AVG	0.601
Did not fracture at notch					**STDEV**	0.083

Table A1.2 Specimen size requirements for Boscobel granite

Specimen	Requirement	t	a	D	D - a	Size of FPZ
	mm	*mm*	*mm*	*mm*	*mm*	*mm*
BG-W-1	0.628	OK	OK	OK	OK	0.010
BG-W-2	16.157	OK	OK	OK	OK	0.257
BG-W-3	18.871	OK	OK	OK	OK	0.301
BG-W-4	0.289	OK	OK	OK	OK	0.005
BG-W-5	9.792	OK	OK	OK	OK	0.156
BG-W-6	0.067	OK	OK	OK	OK	0.001
BG-W-7	1.974	OK	OK	OK	OK	0.031
BG-W-8	13.027	OK	OK	OK	OK	0.207
BG-W-9	1.426	OK	OK	OK	OK	0.023
BG-W-10	10.772	OK	OK	OK	OK	0.172

Table A1.3 Fracture toughness results for Culpeper gray siltstone

Specimen	D	t	a	F_v	F_w	K_{Ic}
	mm	*mm*	*mm*	*N*	*N*	*MPa m$^{1/2}$*
CG-W-1	47.600	25.121	20.676	749	748	1.243
CG-W-2	47.600	24.790	20.574	736	735	1.231
CG-W-3	47.574	25.527	20.599	862	861	1.404
CG-W-4	47.574	25.044	20.701	805	804	1.343
CG-W-5	47.625	25.248	20.701	1028	1027	1.699
CG-W-6	47.574	25.070	20.599	1044	1043	1.732
CG-W-7	47.650	25.298	20.726	1016	1014	1.676
CG-W-8	47.625	24.943	20.726	762	761	1.277
CG-W-9	47.574	25.146	20.726	935	934	1.556
CG-W-10	47.574	24.232	20.650	799	798	1.375
					AVG	1.454
					STDEV	0.195

Table A1.4 Specimen size requirements for Culpeper gray siltstone

Specimen	Requirement	t	a	D	D - a	Size of FPZ
	mm	*mm*	*mm*	*mm*	*mm*	*mm*
CG-W-1	8.035	OK	OK	OK	OK	1.023
CG-W-2	7.876	OK	OK	OK	OK	1.003
CG-W-3	10.242	OK	OK	OK	OK	1.304
CG-W-4	9.380	OK	OK	OK	OK	1.194
CG-W-5	15.008	OK	OK	OK	OK	1.911
CG-W-6	15.587	OK	OK	OK	OK	1.985
CG-W-7	14.602	OK	OK	OK	OK	1.859
CG-W-8	8.474	OK	OK	OK	OK	1.079
CG-W-9	12.582	OK	OK	OK	OK	1.602
CG-W-10	9.824	OK	OK	OK	OK	1.251

Table A1.5 Fracture toughness results for Culpeper red siltstone

Specimen	D	t	a	F_v	F_w	K_{Ic}
	mm	*mm*	*mm*	*N*	*N*	*MPa m$^{1/2}$*
CR-W-1	47.625	24.130	22.250	863	862	1.623
CR-W-2	47.600	25.451	22.200	686	685	1.221
CR-W-3	47.600	28.550	22.885	792	791	1.307
CR-W-4	47.574	24.917	22.250	958	957	1.748
CR-W-5	47.549	25.578	22.225	1043	1041	1.853
CR-W-6	47.523	24.460	22.276	823	822	1.535
CR-W-7	47.625	24.943	22.225	921	919	1.673
CR-W-8	47.625	25.451	22.250	558	557	0.995
CR-W-9	47.625	23.063	22.225	734	733	1.442
CR-W-10	47.549	25.121	22.098	897	895	1.611
					AVG	1.501
					STDEV	0.262

Table A1.6 Specimen size requirements for Culpeper red siltstone

Specimen	Requirement	t	a	D	D - a	Size of FPZ
	mm	*mm*	*mm*	*mm*	*mm*	*mm*
CR-W-1	14.373	OK	OK	OK	OK	0.610
CR-W-2	8.131	OK	OK	OK	OK	0.345
CR-W-3	9.318	OK	OK	OK	OK	0.395
CR-W-4	16.679	OK	OK	OK	OK	0.708
CR-W-5	18.726	OK	OK	OK	OK	0.795
CR-W-6	12.853	OK	OK	OK	OK	0.546
CR-W-7	15.271	OK	OK	OK	OK	0.648
CR-W-8	5.398	OK	OK	OK	OK	0.229
CR-W-9	11.349	OK	OK	OK	OK	0.482
CR-W-10	14.156	OK	OK	OK	OK	0.601

Table A1.7 Fracture toughness results for Leesburg Diabase

Specimen	D	t	a	F_v	F_w	K_{Ic}
	mm	*mm*	*mm*	*N*	*N*	*MPa m$^{1/2}$*
LD-W-1	47.600	26.060	21.768	588	636	1.081
LD-W-2	47.574	25.527	21.768	650	704	1.222
LD-W-3	47.574	25.908	21.742	754	816	1.395
LD-W-4	47.625	24.841	21.742	682	738	1.313
LD-W-5	47.625	25.730	21.793	667	722	1.243
LD-W-6	47.600	25.959	21.742	753	814	1.387
LD-W-7	47.574	24.968	21.742	604	654	1.159
LD-W-8	47.625	26.441	21.819	679	734	1.233
LD-W-9	47.574	26.238	21.768	724	784	1.324
LD-W-10	47.600	26.086	21.742	647	700	1.186
					AVG	1.254
					STDEV	0.101

Table A1.8 Specimen size requirements for Leesburg diabase

Specimen	Requirement	t	a	D	D - a	Size of FPZ
	mm	*mm*	*mm*	*mm*	*mm*	*mm*
LD-W-1	9.435	OK	OK	OK	OK	0.400
LD-W-2	12.048	OK	OK	OK	OK	0.511
LD-W-3	15.696	OK	OK	OK	OK	0.666
LD-W-4	13.917	OK	OK	OK	OK	0.591
LD-W-5	12.473	OK	OK	OK	OK	0.529
LD-W-6	15.533	OK	OK	OK	OK	0.659
LD-W-7	10.835	OK	OK	OK	OK	0.460
LD-W-8	12.259	OK	OK	OK	OK	0.520
LD-W-9	14.141	OK	OK	OK	OK	0.600
LD-W-10	11.359	OK	OK	OK	OK	0.482

Table A1.9 Fracture toughness results for Shadwell metabasalt

Specimen	D	t	a	F_v	F_w	K_{Ic}
	mm	*mm*	*mm*	*N*	*N*	*MPa m$^{1/2}$*
SMB-W-1	47.447	24.486	21.920	710	709	1.300
SMB-W-2	47.447	24.409	21.946	750	749	1.380
SMB-W-3	47.447	25.197	21.844	1221	1219	2.163
SMB-W-4	47.447	24.105	21.920	1274	1272	2.370
SMB-W-5	47.447	24.917	21.996	729	727	1.317
SMB-W-6	47.396	24.232	21.946	576	575	1.069
SMB-W-7	47.346	24.892	21.946	930	928	1.683
SMB-W-8	47.422	24.917	21.996	812	811	1.469
SMB-W-9	47.422	24.816	21.971	914	912	1.657
SMB-W-10	47.396	24.994	21.971	983	982	1.772
					AVG	1.411
					STDEV	0.215

Failed to meet specimen size reqiurements

Table A1.10 Specimen size requirements for Shadwell metabasalt

Specimen	Requirement	t	a	D	D - a	Size of FPZ
	mm	*mm*	*mm*	*mm*	*mm*	*mm*
SMB-W-1	12.166	OK	OK	OK	OK	0.376
SMB-W-2	13.701	OK	OK	OK	OK	0.424
SMB-W-3	33.672	**NO**	**NO**	OK	**NO**	1.041
SMB-W-4	40.425	**NO**	**NO**	OK	**NO**	1.250
SMB-W-5	12.481	OK	OK	OK	OK	0.386
SMB-W-6	8.220	OK	OK	OK	OK	0.254
SMB-W-7	20.396	OK	OK	OK	OK	0.631
SMB-W-8	15.539	OK	OK	OK	OK	0.480
SMB-W-9	19.767	OK	OK	OK	OK	0.611
SMB-W-10	22.601	OK	**NO**	OK	OK	0.699

Table A1.11 Fracture toughness results for Spotsylvania granite

Specimen	D	t	a	F_v	F_w	K_{Ic}
	mm	*mm*	*mm*	*N*	*N*	*MPa m$^{1/2}$*
SG-W-1	47.473	25.806	21.971	554	553	0.965
SG-W-2	47.447	25.375	21.971	485	484	0.859
SG-W-3	47.447	25.273	21.895	608	608	1.078
SG-W-4	47.473	25.095	22.022	531	530	0.954
SG-W-5	47.498	24.740	21.971	400	400	0.726
SG-W-6	47.473	24.765	22.022	279	279	0.508
SG-W-7	47.371	25.248	21.920	392	392	0.699
SG-W-8	47.498	25.222	22.123	541	540	0.971
SG-W-9	47.473	25.222	21.946	479	478	0.851
SG-W-10	47.523	25.222	22.047	460	459	0.821
					AVG	0.843
					STDEV	0.165

Table A1.12 Specimen size requirements for Spotsylvania granite

Specimen	Requirement	t	a	D	D - a	Size of FPZ
	mm	*mm*	*mm*	*mm*	*mm*	*mm*
SG-W-1	14.533	OK	OK	OK	OK	0.617
SG-W-2	11.525	OK	OK	OK	OK	0.489
SG-W-3	18.144	OK	OK	OK	OK	0.770
SG-W-4	14.194	OK	OK	OK	OK	0.602
SG-W-5	8.235	OK	OK	OK	OK	0.350
SG-W-6	4.032	OK	OK	OK	OK	0.171
SG-W-7	7.621	OK	OK	OK	OK	0.323
SG-W-8	14.714	OK	OK	OK	OK	0.624
SG-W-9	11.314	OK	OK	OK	OK	0.480
SG-W-10	10.528	OK	OK	OK	OK	0.447

Table A1.13 Fracture toughness results for Thornberg granite

Specimen	D	t	a	F_v	F_w	K_{Ic}
	mm	*mm*	*mm*	*N*	*N*	*MPa m$^{1/2}$*
TG-W-1	47.193	26.162	21.285	636	619	1.035
TG-W-2	47.142	25.883	21.311	654	636	1.079
TG-W-3	47.168	25.756	21.234	829	807	1.368
TG-W-4	47.168	25.654	21.234	666	648	1.103
TG-W-5	47.168	25.806	21.234	813	791	1.339
TG-W-6	47.219	24.917	21.184	589	573	1.000
TG-W-7	47.092	24.460	21.184	592	576	1.029
TG-W-8	47.142	25.603	21.234	609	593	1.012
TG-W-9	47.168	25.959	21.260	657	640	1.077
TG-W-10	47.142	25.679	21.209	622	605	1.028
					AVG	1.045
					STDEV	0.037

Failed to meet specimen size reqiurements

Table A1.14 Specimen size requirements for Thornburg granite

Specimen	Requirement	t	a	D	D - a	Size of FPZ
	mm	*mm*	*mm*	*mm*	*mm*	*mm*
TG-W-1	14.998	OK	OK	OK	OK	0.637
TG-W-2	16.296	OK	OK	OK	OK	0.692
TG-W-3	26.194	**NO**	**NO**	OK	**NO**	1.112
TG-W-4	17.052	OK	OK	OK	OK	0.724
TG-W-5	25.093	OK	**NO**	OK	OK	1.065
TG-W-6	13.991	OK	OK	OK	OK	0.594
TG-W-7	14.827	OK	OK	OK	OK	0.629
TG-W-8	14.345	OK	OK	OK	OK	0.609
TG-W-9	16.257	OK	OK	OK	OK	0.690
TG-W-10	14.807	OK	OK	OK	OK	0.628

APPENDIX II

HECT RESULTS: SPECIFIC COMMINUTION ENERGY

Table AII.1 HECT results for Boscobel granite at reduction ratio 1

Specimen	D *mm*	t *mm*	Mass *g*	F *kN*	E *pts*	T *MPa*	P *kWh/t*
BG-E-1-1	47.473	25.654	115.3	10.898	42.665	5.697	0.103
BG-E-1-2	47.473	25.603	116.3	14.887	67.242	7.798	0.161
BG-E-1-3	47.473	25.984	123.4	35.993	8.889	18.576	0.020
BG-E-1-4	47.422	25.984	123.4	41.936	87.393	21.666	0.197
BG-E-1-5	47.473	25.705	115.3	18.975	39.197	9.899	0.094
BG-E-1-6	47.498	26.035	123.4	43.693	7.809	22.493	0.018
BG-E-1-7	47.473	25.832	117.4	24.909	0.463	12.931	0.001
BG-E-1-8	47.549	25.552	117.4	19.073	3.205	9.994	0.008
BG-E-1-9	47.447	25.806	122.4	51.281	70.323	26.662	0.160
BG-E-1-10	47.574	25.324	113.3	15.764	46.524	8.330	0.114
BG-E-1-11	47.473	25.502	119.4	17.516	59.564	9.211	0.139
BG-E-1-12	47.549	25.070	111.3	13.233	18.058	7.067	0.045
BG-E-1-13	47.549	25.781	117.4	17.125	59.472	8.893	0.141
BG-E-1-14	47.473	25.171	115.3	24.326	82.403	12.960	0.198
BG-E-1-15	47.498	25.730	113.3	12.067	24.360	6.286	0.060
BG-E-1-16	47.473	25.654	114.3	21.604	85.755	11.293	0.208
BG-E-1-17	47.498	25.375	115.3	21.697	61.704	11.461	0.149
BG-E-1-18	47.498	25.806	118.4	19.269	46.797	10.008	0.110
BG-E-1-19	47.498	25.756	113.3	16.738	32.339	8.710	0.079
BG-E-1-20	47.473	26.035	114.3	15.666	38.749	8.069	0.094
					AVG	**11.900**	**0.105**
					STDEV	**5.840**	**0.065**

1 pts =	1 watt sec
FREQ =	3.8 Hz
SPAN =	284
THROW =	50.80 mm
SET PT =	410
CSS =	31.75 mm

D = Specimen diameter
t = Specimen thickness
M = Specimen mass
F = Peak crushing force
E = Total crushing energy
T = Tensile strength
P = Mass specific crushing energy

Table AII.2 HECT results for Boscobel granite at reduction ratio 2

Specimen	D *mm*	t *mm*	W *g*	F *kN*	E *pts*	T *MPa*	P *kWh/t*
BG-E-2-1	47.523	25.654	110.3	11.676	42.032	6.097	0.106
BG-E-2-2	47.295	26.543	115.3	14.207	88.610	7.205	0.213
BG-E-2-3	47.371	26.441	113.3	9.634	13.547	4.897	0.033
BG-E-2-4	47.320	25.756	111.3	17.418	92.112	9.098	0.230
BG-E-2-5	47.447	26.162	120.4	23.379	155.383	11.990	0.359
BG-E-2-6	47.498	26.187	120.4	24.615	133.220	12.598	0.307
BG-E-2-7	47.473	25.705	116.3	15.470	63.534	8.071	0.152
BG-E-2-8	47.422	26.060	117.4	12.748	135.602	6.567	0.321
BG-E-2-9	47.523	25.502	115.3	12.748	57.332	6.696	0.138
BG-E-2-10	47.523	26.111	119.4	23.641	39.300	12.129	0.091
BG-E-2-11	47.473	25.705	117.4	20.238	75.158	10.558	0.178
BG-E-2-12	47.523	26.416	120.4	17.027	145.752	8.635	0.336
BG-E-2-13	47.523	25.781	119.4	34.957	72.519	18.164	0.169
BG-E-2-14	47.523	25.908	118.4	25.594	72.192	13.233	0.169
BG-E-2-15	47.523	26.162	120.4	27.151	135.790	13.902	0.313
BG-E-2-16	47.498	26.543	120.4	25.496	196.590	12.874	0.454
BG-E-2-17	47.447	26.416	121.4	21.697	165.771	11.021	0.379
BG-E-2-18	47.498	25.933	119.4	23.739	91.050	12.269	0.212
BG-E-2-19	47.473	26.314	120.4	19.073	122.132	9.720	0.282
BG-E-2-20	47.396	25.527	113.3	9.243	60.464	4.863	0.148
					AVG	**10.029**	**0.230**
					STDEV	**3.456**	**0.110**

1 pts =	1 watt sec
FREQ =	3.8 Hz
SPAN =	224
THROW =	50.80 mm
SET PT =	406
CSS =	16.00 mm

D = Specimen diameter
t = Specimen thickness
M = Specimen mass
F = Peak crushing force
E = Total crushing energy
T = Tensile strength
P = Mass specific crushing energy

Table AII.3 HECT results for Culpeper gray siltstone at reduction ratio 1

Specimen	D *mm*	t *mm*	W *g*	F *kN*	E *pts*	T *MPa*	P *kWh/t*
CG-E-1-1	47.625	26.822	129.8	65.875	146.230	32.830	0.313
CG-E-1-2	47.727	26.492	128.8	52.740	NA	26.555	NA
CG-E-1-3	47.574	26.721	128.8	57.117	157.110	28.604	0.339
CG-E-1-4	47.600	25.832	122.7	50.792	93.486	26.298	0.212
CG-E-1-5	47.600	26.111	123.7	70.741	174.160	36.234	0.391
CG-E-1-6	47.650	26.695	127.8	53.349	136.560	26.700	0.297
CG-E-1-7	47.600	26.949	128.8	46.028	147.640	22.843	0.318
CG-E-1-8	47.625	26.695	127.8	53.518	153.410	26.799	0.334
CG-E-1-9	47.600	26.518	127.8	53.714	104.140	27.091	0.226
CG-E-1-10	47.625	26.695	129.8	47.389	137.093	23.729	0.293
CG-E-1-11	47.625	26.899	130.8	65.292	42.735	32.447	0.091
CG-E-1-12	47.625	26.314	126.8	57.802	52.096	29.362	0.114
CG-E-1-13	47.625	26.848	130.8	52.157	80.812	25.969	0.172
CG-E-1-14	47.625	27.229	131.8	53.714	236.690	26.370	0.499
CG-E-1-15	47.625	26.594	129.8	55.560	NA	27.927	NA
CG-E-1-16	47.600	26.924	128.8	52.059	219.860	25.860	0.474
CG-E-1-17	47.650	26.721	128.8	55.075	198.612	27.537	0.428
CG-E-1-18	47.650	26.721	129.8	54.879	123.510	27.439	0.264
CG-E-1-19	47.625	26.137	126.8	50.787	182.050	25.975	0.399
CG-E-1-20	47.600	26.111	125.8	46.219	41.576	23.674	0.092
					AVG	**27.512**	**0.292**
					STDEV	**3.219**	**0.123**

1 pts =	1 watt sec
FREQ =	3.8 Hz
SPAN =	284
THROW =	50.80 mm
SET PT =	410
CSS =	31.75 mm

D = Specimen diameter
t = Specimen thickness
M = Specimen mass
F = Peak crushing force
E = Total crushing energy
T = Tensile strength
P = Mass specific crushing energy

Table AII.4 HECT results for Culpeper gray siltstone at reduction ratio 2

Specimen	D *mm*	t *mm*	W *g*	F *kN*	E *pts*	T *MPa*	P *kWh/t*
CG-E-2-1	47.650	24.892	121.4	45.152	177.472	24.234	0.406
CG-E-2-2	47.600	25.933	126.4	45.152	105.540	23.286	0.232
CG-E-2-3	47.650	25.425	122.4	45.632	205.113	23.978	0.466
CG-E-2-4	47.650	25.578	124.4	65.479	146.622	34.202	0.327
CG-E-2-5	47.650	25.705	124.4	46.415	170.931	24.124	0.382
CG-E-2-6	47.600	24.587	119.4	50.009	196.981	27.203	0.458
CG-E-2-7	47.625	25.730	124.4	53.323	188.210	27.702	0.420
CG-E-2-8	47.600	25.730	125.4	46.708	140.070	24.279	0.310
CG-E-2-9	47.625	25.197	122.4	49.235	244.950	26.120	0.556
CG-E-2-10	47.600	24.511	118.4	47.776	131.061	26.069	0.308
CG-E-2-11	47.625	25.552	123.4	51.183	102.832	26.776	0.232
CG-E-2-12	47.574	25.375	123.4	50.890	116.780	26.837	0.263
CG-E-2-13	47.600	26.162	126.4	50.890	227.050	26.016	0.499
CG-E-2-14	47.600	25.781	125.4	43.497	142.160	22.565	0.315
CG-E-2-15	47.625	25.375	123.4	48.554	158.700	25.578	0.357
CG-E-2-16	47.600	25.781	125.4	47.825	249.290	24.810	0.552
CG-E-2-17	47.625	25.400	123.4	52.936	46.233	27.859	0.104
CG-E-2-18	47.650	27.559	132.4	60.230	153.372	29.199	0.322
CG-E-2-19	47.625	26.060	126.4	61.200	139.650	31.392	0.307
CG-E-2-20	47.650	25.171	122.4	44.275	81.963	23.500	0.186
					AVG	**26.286**	**0.350**
					STDEV	**2.854**	**0.119**

1 pts =	1 watt sec
FREQ =	3.8 Hz
SPAN =	224
THROW =	50.80 mm
SET PT =	406
CSS =	16.00 mm

D = Specimen diameter
t = Specimen thickness
M = Specimen mass
F = Peak crushing force
E = Total crushing energy
T = Tensile strength
P = Mass specific crushing energy

Table AII.5 HECT results for Culpeper red siltstone at reduction ratio 1

Specimen	D *mm*	t *mm*	W *g*	F *kN*	E *pts*	T *MPa*	P *kWh/t*
CR-E-1-1	47.574	26.848	131.4	55.707	183.590	27.766	0.388
CR-E-1-2	47.600	25.908	125.4	55.756	142.040	28.783	0.315
CR-E-1-3	47.625	26.289	127.4	61.204	147.412	31.121	0.321
CR-E-1-4	47.625	26.187	127.4	60.146	90.996	30.701	0.198
CR-E-1-5	47.625	26.238	127.4	71.911	92.529	36.636	0.202
CR-E-1-6	47.650	26.721	128.4	56.632	33.229	28.316	0.072
CR-E-1-7	47.549	27.051	131.4	54.395	92.853	26.922	0.196
CR-E-1-8	47.650	26.035	125.4	52.446	34.285	26.914	0.076
CR-E-1-9	47.650	26.670	128.4	45.828	72.848	22.957	0.158
CR-E-1-10	47.650	26.848	130.4	59.843	56.112	29.780	0.120
CR-E-1-11	47.650	24.740	121.4	55.164	154.000	29.790	0.352
CR-E-1-12	47.625	26.949	130.4	70.149	68.577	34.795	0.146
CR-E-1-13	47.676	25.908	126.4	52.446	142.793	27.031	0.314
CR-E-1-14	47.574	27.305	130.4	57.215	302.560	28.040	0.645
CR-E-1-15	47.650	25.883	125.4	48.070	192.811	24.813	0.427
CR-E-1-16	47.701	25.298	123.4	66.751	201.000	35.214	0.453
CR-E-1-17	47.600	26.619	130.4	48.848	172.720	24.543	0.368
CR-E-1-18	47.650	25.730	125.4	58.869	NA	30.567	NA
CR-E-1-19	47.650	26.822	130.4	58.994	240.730	29.385	0.513
CR-E-1-20	47.650	26.035	125.4	46.219	180.122	23.718	0.399
					AVG	**28.890**	**0.298**
					STDEV	**3.691**	**0.156**

1 pts =	1 watt sec
FREQ =	3.8 Hz
SPAN =	284
THROW =	50.80 mm
SET PT =	410
CSS =	31.75 mm

D = Specimen diameter
t = Specimen thickness
M = Specimen mass
F = Peak crushing force
E = Total crushing energy
T = Tensile strength
P = Mass specific crushing energy

Table AII.6 HECT results for Culpeper red siltstone at reduction ratio 2

Specimen	D *mm*	t *mm*	W *g*	F *kN*	E *pts*	T *MPa*	P *kWh/t*
CR-E-2-1	47.600	25.629	123.4	63.055	61.943	32.906	0.139
CR-E-2-2	47.600	25.171	122.4	57.606	65.419	30.608	0.149
CR-E-2-3	47.523	26.416	127.4	52.157	169.870	26.450	0.370
CR-E-2-4	47.600	26.162	126.4	24.424	158.400	12.486	0.348
CR-E-2-5	47.574	25.654	124.4	54.782	19.440	28.575	0.043
CR-E-2-6	47.625	25.832	125.4	62.374	NA	32.277	NA
CR-E-2-7	47.676	25.959	128.4	38.924	142.820	20.023	0.309
CR-E-2-8	47.574	26.340	127.4	63.344	214.040	32.181	0.467
CR-E-2-9	47.600	25.121	121.4	56.534	43.105	30.099	0.099
CR-E-2-10	47.625	25.629	126.4	46.121	189.552	24.056	0.417
CR-E-2-11	47.701	25.527	125.4	49.044	214.000	25.641	0.474
CR-E-2-12	47.625	24.994	123.4	51.570	88.018	27.581	0.198
CR-E-2-13	47.549	25.883	126.4	47.287	305.770	24.461	0.672
CR-E-2-14	47.574	25.400	122.4	46.415	195.310	24.453	0.443
CR-E-2-15	47.625	25.679	126.4	43.884	NA	22.844	NA
CR-E-2-16	47.625	25.883	128.4	55.756	76.973	28.796	0.167
CR-E-2-17	47.523	26.340	127.4	51.179	317.941	26.029	0.693
CR-E-2-18	47.650	25.095	124.4	46.415	34.331	24.710	0.077
CR-E-2-19	47.574	26.060	125.4	61.787	174.622	31.727	0.387
CR-E-2-20	47.650	26.035	127.4	43.497	144.390	22.321	0.315
					AVG	**26.411**	**0.320**
					STDEV	**4.932**	**0.192**

1 pts =	1 watt sec
FREQ =	3.8 Hz
SPAN =	224
THROW =	50.80 mm
SET PT =	406
CSS =	16.00 mm

D = Specimen diameter
t = Specimen thickness
M = Specimen mass
F = Peak crushing force
E = Total crushing energy
T = Tensile strength
P = Mass specific crushing energy

Table AII.7 HECT results for Leesburg diabase at reduction ratio 1

Specimen	D *mm*	t *mm*	W *g*	F *kN*	E *pts*	T *MPa*	P *kWh/t*
LD-E-1-1	47.752	25.781	138.4	50.987	173.160	26.366	0.348
LD-E-1-2	47.803	27.229	145.4	48.750	220.864	23.844	0.422
LD-E-1-3	47.549	27.203	145.4	51.668	170.274	25.430	0.325
LD-E-1-4	47.574	26.975	144.4	57.290	238.110	28.420	0.458
LD-E-1-5	47.574	27.381	145.4	46.219	150.700	22.588	0.288
LD-E-1-6	47.574	26.594	140.4	53.518	183.330	26.930	0.363
LD-E-1-7	47.549	26.746	142.4	61.302	300.290	30.687	0.586
LD-E-1-8	47.625	27.000	144.4	59.794	NA	29.603	NA
LD-E-1-9	47.625	26.568	141.4	59.794	NA	30.084	NA
LD-E-1-10	47.625	26.899	143.4	45.272	NA	22.498	NA
LD-E-1-11	47.600	26.873	142.4	50.111	118.630	24.940	0.231
LD-E-1-12	47.574	27.381	146.4	49.920	213.943	24.397	0.406
LD-E-1-13	47.650	26.949	144.4	59.648	190.881	29.570	0.367
LD-E-1-14	47.600	27.280	146.4	62.957	341.770	30.866	0.648
LD-E-1-15	47.523	26.772	143.4	47.776	15.401	23.906	0.030
LD-E-1-16	47.549	27.127	144.4	68.308	343.380	33.714	0.660
LD-E-1-17	47.625	26.975	145.4	53.420	332.040	26.472	0.634
LD-E-1-18	47.600	26.975	144.4	55.271	122.160	27.404	0.235
LD-E-1-19	47.600	27.229	145.4	58.189	233.731	28.582	0.446
LD-E-1-20	47.625	27.178	144.4	45.734	14.111	22.494	0.027
LD-E-1-21	47.193	23.089	107.3	26.274	93.826	15.351	0.243
LD-E-1-22	47.523	22.454	121.4	46.317	141.230	27.633	0.323
					AVG	**26.445**	**0.371**
					STDEV	**3.929**	**0.182**

1 pts =	1 watt sec
FREQ =	3.8 Hz
SPAN =	284
THROW =	50.80 mm
SET PT =	410
CSS =	31.75 mm

D = Specimen diameter
t = Specimen thickness
M = Specimen mass
F = Peak crushing force
E = Total crushing energy
T = Tensile strength
P = Mass specific crushing energy

Table AII.8 HECT results for Leesburg diabase at reduction ratio 2

Specimen	D *mm*	t *mm*	W *g*	F *kN*	E *pts*	T *MPa*	P *kWh/t*
LD-E-2-1	47.600	25.527	137.4	48.946	67.404	25.644	0.136
LD-E-2-2	47.625	26.137	139.4	46.820	NA	23.946	NA
LD-E-2-3	47.625	26.035	140.4	NA	NA	NA	NA
LD-E-2-4	47.549	25.959	138.4	48.167	219.020	24.843	0.440
LD-E-2-5	47.625	26.391	141.4	52.082	NA	26.380	NA
LD-E-2-6	47.600	26.340	140.4	37.826	NA	19.207	NA
LD-E-2-7	47.574	26.187	139.4	47.193	290.021	24.116	0.578
LD-E-2-8	47.625	26.035	138.4	49.528	304.533	25.430	0.611
LD-E-2-9	47.625	26.162	139.4	65.973	326.283	33.708	0.650
LD-E-2-10	47.549	26.238	140.4	55.075	240.430	28.104	0.476
LD-E-2-11	47.625	26.365	141.4	63.735	135.390	32.314	0.266
LD-E-2-12	47.600	26.264	140.4	52.740	211.564	26.857	0.419
LD-E-2-13	47.625	25.857	138.4	50.013	251.110	25.855	0.504
LD-E-2-14	47.650	26.060	139.4	47.487	76.479	24.345	0.152
LD-E-2-15	47.574	26.137	139.4	47.585	253.400	24.363	0.505
LD-E-2-16	47.676	25.375	135.4	48.265	203.254	25.399	0.417
LD-E-2-17	47.625	26.518	141.4	53.714	299.070	27.077	0.587
LD-E-2-18	47.625	25.603	136.4	40.188	236.360	20.982	0.481
LD-E-2-19	47.625	25.857	137.4	47.678	344.290	24.648	0.696
LD-E-2-20	47.549	25.705	137.4	49.044	355.170	25.545	0.718
					AVG	**25.724**	**0.477**
					STDEV	**3.275**	**0.174**

1 pts =	1 watt sec
FREQ =	3.8 Hz
SPAN =	224
THROW =	50.80 mm
SET PT =	406
CSS =	16.00 mm

D = Specimen diameter
t = Specimen thickness
M = Specimen mass
F = Peak crushing force
E = Total crushing energy
T = Tensile strength
P = Mass specific crushing energy

Table AII.9 HECT results for Shadwell metabasalt at reduction ratio 1

Specimen	D *mm*	t *mm*	W *g*	F *kN*	E *pts*	T *MPa*	P *kWh/t*
SMB-E-1-1	47.447	26.289	132.4	52.059	217.710	26.570	0.457
SMB-E-1-2	47.473	25.629	122.4	46.900	96.723	24.540	0.220
SMB-E-1-3	47.549	25.883	124.4	44.652	201.453	23.098	0.450
SMB-E-1-4	47.574	25.705	121.4	48.542	198.755	25.270	0.455
SMB-E-1-5	47.422	26.010	131.4	46.121	200.700	23.805	0.424
SMB-E-1-6	47.371	26.314	131.4	33.389	275.846	17.052	0.583
SMB-E-1-7	47.473	25.756	124.4	53.445	226.807	27.827	0.507
SMB-E-1-8	47.498	26.086	132.4	45.948	231.300	23.608	0.485
SMB-E-1-9	47.523	25.832	124.4	42.224	215.783	21.897	0.482
SMB-E-1-10	47.447	26.060	131.4	45.152	187.250	23.247	0.396
SMB-E-1-11	47.498	25.578	121.4	44.641	145.765	23.392	0.334
SMB-E-1-12	47.523	25.781	122.4	45.126	187.956	23.448	0.427
SMB-E-1-13	47.473	25.654	120.4	40.068	200.047	20.945	0.462
SMB-E-1-14	47.549	25.425	120.4	30.358	120.210	15.986	0.277
SMB-E-1-15	47.473	25.984	123.4	41.353	129.331	21.342	0.291
SMB-E-1-16	47.473	26.035	132.4	46.117	216.691	23.754	0.455
SMB-E-1-17	47.422	26.111	131.4	45.632	196.410	23.461	0.415
SMB-E-1-18	47.473	25.781	121.4	24.037	54.397	12.503	0.125
SMB-E-1-19	47.473	26.162	124.4	43.688	112.980	22.394	0.252
SMB-E-1-20	47.396	26.010	131.4	51.962	225.980	26.834	0.478
SMB-E-1-21	47.498	25.171	127.4	33.280	161.384	17.721	0.352
SMB-E-1-22	47.473	26.035	132.4	58.674	271.380	30.222	0.569
SMB-E-1-23	47.473	26.010	132.4	54.003	223.073	27.843	0.468
					AVG	**22.816**	**0.407**
					STDEV	**4.102**	**0.112**

1 pts =	1 watt sec
FREQ =	3.8 Hz
SPAN =	284
THROW =	50.80 mm
SET PT =	410
CSS =	31.75 mm

D = Specimen diameter
t = Specimen thickness
M = Specimen mass
F = Peak crushing force
E = Total crushing energy
T = Tensile strength
P = Mass specific crushing energy

Table AII.10 HECT results for Shadwell metabasalt at reduction ratio 2

Specimen	D *mm*	t *mm*	W *g*	F *kN*	E *pts*	T *MPa*	P *kWh/t*
SMB-E-2-1	47.498	26.238	124.4	32.301	157.010	16.500	0.351
SMB-E-2-2	47.549	25.933	125.4	22.378	108.620	11.553	0.241
SMB-E-2-3	47.422	25.883	131.4	51.468	381.332	26.695	0.806
SMB-E-2-4	47.523	25.781	124.4	45.343	411.740	23.560	0.920
SMB-E-2-5	47.447	26.264	133.4	43.977	178.293	22.467	0.371
SMB-E-2-6	47.447	25.908	124.4	49.235	243.370	25.498	0.544
SMB-E-2-7	47.447	26.060	125.4	47.967	174.430	24.696	0.386
SMB-E-2-8	47.523	26.314	131.4	46.806	77.250	23.828	0.163
SMB-E-2-9	47.574	26.060	129.4	29.388	143.030	15.090	0.307
SMB-E-2-10	47.447	25.908	123.4	54.879	320.174	28.421	0.721
SMB-E-2-11	47.473	26.162	127.4	79.695	690.190	40.850	1.505
SMB-E-2-12	47.523	25.959	126.4	57.606	147.130	29.727	0.323
SMB-E-2-13	47.447	26.213	133.4	48.065	129.262	24.603	0.269
SMB-E-2-14	47.473	26.086	132.4	63.242	329.730	32.511	0.692
SMB-E-2-15	47.473	26.264	132.4	43.693	280.570	22.310	0.589
SMB-E-2-16	47.473	26.111	132.4	47.967	449.760	24.635	0.944
SMB-E-2-17	47.447	26.238	126.4	72.102	331.470	36.871	0.729
SMB-E-2-18	47.498	26.162	128.4	37.559	187.190	19.242	0.405
SMB-E-2-19	47.473	26.365	133.4	41.936	216.980	21.330	0.452
SMB-E-2-20	47.473	26.264	131.4	50.111	138.500	25.587	0.293
					AVG	**24.799**	**0.550**
					STDEV	**6.885**	**0.323**

1 pts =	1 watt sec
FREQ =	3.8 Hz
SPAN =	224
THROW =	50.80 mm
SET PT =	406
CSS =	16.00 mm

D = Specimen diameter
t = Specimen thickness
M = Specimen mass
F = Peak crushing force
E = Total crushing energy
T = Tensile strength
P = Mass specific crushing energy

Table AII.11 HECT results for Spotsylvania granite at reduction ratio 1

Specimen	D *mm*	t *mm*	W *g*	F *kN*	E *pts*	T *MPa*	P *kWh/t*
SG-E-1-1	47.447	26.848	131.4	31.430	167.524	15.707	0.354
SG-E-1-2	47.549	27.127	133.4	25.785	137.333	12.726	0.286
SG-E-1-3	47.473	26.670	127.4	8.562	NA	4.305	NA
SG-E-1-4	47.422	27.178	127.4	42.514	159.812	21.000	0.348
SG-E-1-5	47.422	26.492	124.4	23.641	150.570	11.980	0.336
SG-E-1-6	47.422	26.543	124.4	33.858	118.760	17.124	0.265
SG-E-1-7	47.447	24.028	114.3	24.726	96.719	13.807	0.235
SG-E-1-8	47.473	27.483	135.4	NA	NA	NA	NA
SG-E-1-9	47.473	27.051	132.4	27.827	227.321	13.795	0.477
SG-E-1-10	47.422	26.899	133.4	18.099	95.680	9.033	0.199
SG-E-1-11	47.422	25.933	120.4	25.687	33.569	13.297	0.077
SG-E-1-12	47.447	27.229	133.4	22.769	130.452	11.220	0.272
SG-E-1-13	47.447	27.203	131.4	35.900	31.810	17.707	0.067
SG-E-1-14	47.473	27.076	132.4	34.441	93.259	17.058	0.196
SG-E-1-15	47.473	26.822	127.4	12.744	30.655	6.371	0.067
SG-E-1-16	47.498	26.797	130.4	26.755	62.013	13.382	0.132
SG-E-1-17	47.447	25.375	124.4	27.827	113.524	14.714	0.254
SG-E-1-18	47.447	27.076	133.4	35.513	118.510	17.598	0.247
SG-E-1-19	47.422	27.000	126.4	21.017	85.165	10.450	0.187
SG-E-1-20	47.447	26.619	123.4	33.271	89.760	16.770	0.202
					AVG	**13.581**	**0.233**
					STDEV	**4.126**	**0.108**

1 pts =	1 watt sec
FREQ =	3.8 Hz
SPAN =	284
THROW =	50.80 mm
SET PT =	410
CSS =	31.75 mm

D = Specimen diameter
t = Specimen thickness
M = Specimen mass
F = Peak crushing force
E = Total crushing energy
T = Tensile strength
P = Mass specific crushing energy

Table AII.12 HECT results for Spotsylvania granite at reduction ratio 2

Specimen	D *mm*	t *mm*	W *g*	F *kN*	E *pts*	T *MPa*	P *kWh/t*
SG-E-2-1	47.422	26.340	122.4	33.596	160.440	17.123	0.364
SG-E-2-2	47.473	27.051	126.4	45.539	191.473	22.575	0.421
SG-E-2-3	47.498	26.086	129.4	26.657	169.610	13.697	0.364
SG-E-2-4	47.396	25.781	119.4	43.813	219.350	22.826	0.510
SG-E-2-5	47.447	26.391	130.4	24.037	148.560	12.221	0.316
SG-E-2-6	47.396	25.629	121.4	33.765	183.120	17.696	0.419
SG-E-2-7	47.422	26.187	128.4	28.316	184.861	14.516	0.400
SG-E-2-8	47.371	25.654	119.4	31.043	195.880	16.262	0.456
SG-E-2-9	47.396	25.883	122.4	25.105	87.930	13.028	0.200
SG-E-2-10	47.422	26.492	132.4	43.786	218.544	22.188	0.459
SG-E-2-11	47.447	25.984	124.4	29.188	122.543	15.072	0.274
SG-E-2-12	47.447	26.162	130.4	23.161	208.560	11.878	0.444
SG-E-2-13	47.396	25.248	125.4	21.893	167.030	11.647	0.370
SG-E-2-14	47.422	26.213	121.4	34.058	74.480	17.443	0.170
SG-E-2-15	47.422	25.832	121.4	25.687	126.260	13.349	0.289
SG-E-2-16	47.473	26.619	129.4	29.775	244.413	15.000	0.525
SG-E-2-17	47.473	25.629	124.4	20.238	33.833	10.590	0.076
					AVG	**15.712**	**0.356**
					STDEV	**3.855**	**0.123**

1 pts =	1 watt sec
FREQ =	3.8 Hz
SPAN =	224
THROW =	50.80 mm
SET PT =	406
CSS =	16.00 mm

D = Specimen diameter
t = Specimen thickness
M = Specimen mass
F = Peak crushing force
E = Total crushing energy
T = Tensile strength
P = Mass specific crushing energy

Table AII.13 HECT results for Thornburg granite at reduction ratio 1

Specimen	D *mm*	t *mm*	W *g*	F *kN*	E *pts*	T *MPa*	P *kWh/t*
TG-E-1-1	47.168	27.051	127.4	43.742	76.249	21.825	0.166
TG-E-1-2	47.244	26.746	125.4	32.986	111.243	16.619	0.246
TG-E-1-3	47.168	26.873	126.4	45.734	NA	22.970	NA
TG-E-1-4	47.193	26.695	124.4	24.010	NA	12.133	NA
TG-E-1-5	47.168	27.102	126.4	34.543	134.870	17.203	0.296
TG-E-1-6	47.193	27.229	128.4	46.806	89.711	23.189	0.194
TG-E-1-7	47.168	26.568	122.4	34.445	NA	17.498	NA
TG-E-1-8	47.066	27.153	127.4	29.290	150.820	14.591	0.329
TG-E-1-9	47.168	26.568	123.4	31.136	215.930	15.817	0.486
TG-E-1-10	47.142	26.416	123.4	21.213	77.514	10.844	0.175
TG-E-1-11	47.142	27.153	126.4	33.280	148.490	16.552	0.326
TG-E-1-12	47.219	26.949	126.4	27.733	76.644	13.875	0.168
TG-E-1-13	47.193	27.254	128.4	31.136	72.996	15.411	0.158
TG-E-1-14	47.219	26.949	125.4	43.203	109.430	21.614	0.242
TG-E-1-15	47.193	22.962	107.3	45.343	270.472	26.638	0.700
TG-E-1-16	47.142	27.229	127.4	48.265	192.031	23.937	0.419
TG-E-1-17	47.168	27.229	128.4	17.321	30.161	8.586	0.065
TG-E-1-18	47.168	26.899	126.4	34.156	106.990	17.139	0.235
TG-E-1-19	47.168	26.772	125.4	40.966	125.354	20.653	0.278
TG-E-1-20	47.193	26.772	126.4	29.481	65.774	14.855	0.145
					AVG	**17.597**	**0.272**
					STDEV	**4.718**	**0.152**

1 pts =	1 watt sec
FREQ =	3.8 Hz
SPAN =	284
THROW =	50.80 mm
SET PT =	410
CSS =	31.75 mm

D = Specimen diameter
t = Specimen thickness
M = Specimen mass
F = Peak crushing force
E = Total crushing energy
T = Tensile strength
P = Mass specific crushing energy

Table AII.14 HECT results for Thornburg granite at reduction ratio 2

Specimen	D *mm*	t *mm*	W *g*	F *kN*	E *pts*	T *MPa*	P *kWh/t*
TG-E-2-1	47.193	26.187	121.4	23.730	177.611	12.224	0.407
TG-E-2-2	47.142	26.289	122.4	23.521	222.123	12.082	0.504
TG-E-2-3	47.168	26.416	121.4	42.425	365.982	21.677	0.838
TG-E-2-4	47.168	26.264	118.4	36.976	NA	19.002	NA
TG-E-2-5	47.193	25.984	121.4	34.058	195.280	17.681	0.447
TG-E-2-6	47.168	26.010	118.4	32.502	126.730	16.866	0.297
TG-E-2-7	47.168	26.010	119.4	31.234	92.050	16.208	0.214
TG-E-2-8	47.219	25.756	117.4	29.290	108.204	15.333	0.256
TG-E-2-9	47.142	26.035	120.4	36.100	194.480	18.725	0.449
TG-E-2-10	47.193	26.365	121.4	32.399	41.661	16.577	0.095
TG-E-2-11	47.142	25.883	118.4	28.707	147.312	14.978	0.346
TG-E-2-12	47.193	26.010	120.4	24.130	NA	12.515	NA
TG-E-2-13	47.193	25.781	118.4	22.089	44.743	11.558	0.105
TG-E-2-14	47.269	26.416	121.4	26.759	103.990	13.643	0.238
TG-E-2-15	47.219	25.883	119.4	35.322	174.910	18.399	0.407
TG-E-2-16	47.219	25.705	117.4	26.857	144.524	14.087	0.342
TG-E-2-17	47.219	25.908	120.4	33.280	278.404	17.319	0.643
TG-E-2-18	47.193	26.035	120.4	36.002	139.790	18.654	0.323
TG-E-2-19	47.219	26.289	121.4	39.507	326.520	20.261	0.747
TG-E-2-20	47.219	26.060	118.4	29.775	109.230	15.404	0.256
					AVG	**16.160**	**0.384**
					STDEV	**2.878**	**0.201**

1 pts =	1 watt sec
FREQ =	3.8 Hz
SPAN =	224
THROW =	50.80 mm
SET PT =	406
CSS =	16.00 mm

D = Specimen diameter
t = Specimen thickness
M = Specimen mass
F = Peak crushing force
E = Total crushing energy
T = Tensile strength
P = Mass specific crushing energy

APPENDIX III

HECT RESULTS: BREAKAGE SIZE DISTRIBUTION

Table AIII.1 Breakage distribution results for Boscobel granite at RR1

Size *mm*	Sieve Weight *g*	Sieve + Sample Weight *g*	Weight Retained *g*	Fraction Passing
47.492			0.00	1.0000
38.100			0.00	1.0000
25.400	651.0	1713.5	1062.5	0.5466
19.100	665.0	1154.5	489.5	0.3377
12.700	632.5	1009.5	377.0	0.1769
6.350	615.5	810.5	195.0	0.0937
4.750	543.5	589.5	46.0	0.0740
3.360	506.5	545.0	38.5	0.0576
2.360	489.5	515.0	25.5	0.0467
1.700	475.0	494.5	19.5	0.0384
1.190	427.0	442.5	15.5	0.0318
0.850	433.5	446.5	13.0	0.0262
0.595	449.0	459.0	10.0	0.0220
0.425	434.5	442.5	8.0	0.0186
0.300	426.0	432.0	6.0	0.0160
0.210	450.0	456.5	6.5	0.0132
0.150	409.5	418.0	8.5	0.0096
0.105	384.5	386.0	1.5	0.0090
0.075	391.0	398.5	7.5	0.0058
pan	366.0	379.5	13.5	0.0000

Table AIII.2 Breakage distribution results for Boscobel granite at RR2

Size *mm*	Sieve Weight *g*	Sieve + Sample Weight *g*	Weight Retained *g*	Fraction Passing
47.464			0.00	1.0000
38.100			0.00	1.0000
25.400	651.0	1026.0	375.0	0.8401
19.100	665.0	903.0	238.0	0.7385
12.700	632.5	1252.5	620.0	0.4741
6.350	615.5	1209.5	594.0	0.2207
4.750	543.5	662.0	118.5	0.1702
3.360	506.5	612.0	105.5	0.1252
2.360	489.5	547.5	58.0	0.1004
1.700	475.0	521.0	46.0	0.0808
1.190	427.0	463.0	36.0	0.0655
0.850	433.5	462.5	29.0	0.0531
0.595	449.0	471.5	22.5	0.0435
0.425	434.5	453.0	18.5	0.0356
0.300	426.0	439.5	13.5	0.0299
0.210	450.0	462.5	12.5	0.0245
0.150	409.5	429.5	20.0	0.0160
0.105	384.5	388.0	3.5	0.0145
0.075	391.0	404.0	13.0	0.0090
pan	361.0	382.0	21.0	0.0000

Table AIII.3 Breakage distribution results for Culpeper gray siltstone at RR1

Size *mm*	Sieve Weight *g*	Sieve + Sample Weight *g*	Weight Retained *g*	Fraction Passing
47.624			0.00	1.0000
38.100			0.00	1.0000
25.400	650.5	1694.3	1043.8	0.5915
19.100	663.9	1077.0	413.1	0.4298
12.700	631.7	982.1	350.4	0.2927
6.350	614.3	982.0	367.7	0.1488
4.750	542.3	625.2	82.9	0.1163
3.360	505.6	585.2	79.6	0.0852
2.360	488.6	538.8	50.2	0.0655
1.700	474.4	514.4	40.1	0.0498
1.190	426.2	456.9	30.8	0.0378
0.850	432.9	458.0	25.2	0.0279
0.595	448.6	466.1	17.5	0.0211
0.425	433.6	447.5	14.0	0.0156
0.300	425.2	435.3	10.1	0.0117
0.210	449.4	457.3	7.8	0.0086
0.150	408.9	418.7	9.9	0.0048
0.105	384.0	385.4	1.4	0.0042
0.075	390.3	394.5	4.3	0.0025
pan	365.2	371.6	6.5	0.0000

Table AIII.4 Breakage distribution results for Culpeper gray siltstone at RR2

Size *mm*	Sieve Weight *g*	Sieve + Sample Weight *g*	Weight Retained *g*	Fraction Passing
47.621			0.00	1.0000
38.100			0.00	1.0000
25.400	651.0	1093.0	442.0	0.8220
19.100	665.0	1259.5	594.5	0.5826
12.700	632.5	1083.0	450.5	0.4012
6.350	615.5	1105.5	490.0	0.2039
4.750	543.5	634.0	90.5	0.1675
3.360	506.5	603.5	97.0	0.1284
2.360	489.5	568.5	79.0	0.0966
1.700	475.0	533.0	58.0	0.0733
1.190	427.0	474.5	47.5	0.0542
0.850	433.5	469.0	35.5	0.0399
0.595	449.0	474.5	25.5	0.0296
0.425	434.5	455.0	20.5	0.0213
0.300	426.0	441.0	15.0	0.0153
0.210	450.0	461.5	11.5	0.0107
0.150	409.5	422.0	12.5	0.0056
0.105	384.5	387.0	2.5	0.0046
0.075	391.0	397.5	6.5	0.0020
pan	365.5	370.5	5.0	0.0000

Table AIII.5 Breakage distribution results for Culpeper red siltstone at RR1

Size *mm*	Sieve Weight *g*	Sieve + Sample Weight *g*	Weight Retained *g*	Fraction Passing
47.631			0.00	1.0000
38.100			0.00	1.0000
25.400	650.5	1710.2	1059.7	0.5845
19.100	663.9	1025.6	361.7	0.4426
12.700	631.7	908.7	277.0	0.3340
6.350	614.3	1052.1	437.8	0.1623
4.750	542.3	626.9	84.6	0.1292
3.360	505.7	593.7	88.0	0.0947
2.360	488.5	543.1	54.6	0.0733
1.700	474.2	518.1	43.9	0.0560
1.190	426.2	461.5	35.3	0.0422
0.850	432.9	460.2	27.3	0.0315
0.595	448.5	468.2	19.7	0.0238
0.425	433.7	449.8	16.1	0.0174
0.300	425.3	436.3	11.0	0.0131
0.210	449.5	457.6	8.1	0.0099
0.150	408.8	420.8	12.0	0.0052
0.105	384.0	384.5	0.6	0.0050
0.075	390.3	395.7	5.4	0.0029
pan	360.7	368.1	7.4	0.0000

Table AIII.6 Breakage distribution results for Culpeper red siltstone at RR2

Size *mm*	Sieve Weight *g*	Sieve + Sample Weight *g*	Weight Retained *g*	Fraction Passing
47.605			0.00	1.0000
38.100			0.00	1.0000
25.400	651.0	1346.5	695.5	0.7230
19.100	665.0	1183.5	518.5	0.5165
12.700	632.5	1075.0	442.5	0.3403
6.350	615.5	1062.0	446.5	0.1625
4.750	543.5	629.5	86.0	0.1282
3.360	506.5	596.5	90.0	0.0924
2.360	489.5	543.0	53.5	0.0711
1.700	475.0	518.0	43.0	0.0540
1.190	427.0	458.5	31.5	0.0414
0.850	433.5	459.0	25.5	0.0313
0.595	449.0	468.0	19.0	0.0237
0.425	434.5	448.5	14.0	0.0181
0.300	426.0	437.0	11.0	0.0137
0.210	450.0	459.0	9.0	0.0102
0.150	409.5	421.0	11.5	0.0056
0.105	384.5	386.5	2.0	0.0048
0.075	391.0	401.5	10.5	0.0006
pan	365.5	367.0	1.5	0.0000

Table AIII.7 Breakage distribution results for Leesburg diabase at RR1

Size *mm*	Sieve Weight *g*	Sieve + Sample Weight *g*	Weight Retained *g*	Fraction Passing
47.587			0.00	1.0000
38.100			0.00	1.0000
25.400	650.5	2135.6	1485.1	0.5213
19.100	664.0	1374.8	710.8	0.2922
12.700	631.8	984.7	352.9	0.1784
6.350	614.3	850.6	236.3	0.1023
4.750	542.4	588.9	46.5	0.0873
3.360	505.7	563.9	58.2	0.0685
2.360	488.7	523.4	34.7	0.0573
1.700	474.3	504.1	29.8	0.0477
1.190	426.3	448.1	21.8	0.0407
0.850	432.9	453.6	20.6	0.0341
0.595	448.5	463.6	15.1	0.0292
0.425	433.6	446.0	12.4	0.0252
0.300	425.2	434.9	9.7	0.0221
0.210	449.5	459.3	9.8	0.0189
0.150	408.9	419.4	10.6	0.0155
0.105	384.0	390.5	6.5	0.0134
0.075	390.3	401.1	10.8	0.0099
pan	365.2	395.9	30.7	0.0000

Table AIII.8 Breakage distribution results for Leesburg diabase at RR2

Size *mm*	Sieve Weight *g*	Sieve + Sample Weight *g*	Weight Retained *g*	Fraction Passing
47.608			0.00	1.0000
38.100			0.00	1.0000
25.400	651.0	1551.5	900.5	0.6763
19.100	665.0	1162.5	497.5	0.4974
12.700	632.5	1088.0	455.5	0.3336
6.350	615.5	1009.5	394.0	0.1920
4.750	543.5	639.5	96.0	0.1575
3.360	506.5	609.0	102.5	0.1206
2.360	489.5	550.5	61.0	0.0987
1.700	475.0	523.0	48.0	0.0814
1.190	427.0	465.5	38.5	0.0676
0.850	433.5	464.0	30.5	0.0566
0.595	449.0	473.0	24.0	0.0480
0.425	434.5	454.5	20.0	0.0408
0.300	426.0	441.0	15.0	0.0354
0.210	450.0	464.5	14.5	0.0302
0.150	409.5	429.0	19.5	0.0232
0.105	384.5	385.0	0.5	0.0230
0.075	391.0	416.5	25.5	0.0138
pan	361.5	400.0	38.5	0.0000

Table AIII.9 Breakage distribution results for Shadwell metabasalt at RR1

Size *mm*	Sieve Weight *g*	Sieve + Sample Weight *g*	Weight Retained *g*	Fraction Passing
47.477			0.00	1.0000
38.100			0.00	1.0000
25.400	651.0	1962.5	1311.5	0.4801
19.100	665.0	1148.0	483.0	0.2886
12.700	632.5	862.0	229.5	0.1976
6.350	615.5	854.0	238.5	0.1031
4.750	543.5	599.5	56.0	0.0809
3.360	506.5	562.0	55.5	0.0589
2.360	489.5	521.0	31.5	0.0464
1.700	475.0	501.0	26.0	0.0361
1.190	427.0	447.0	20.0	0.0281
0.850	433.5	449.0	15.5	0.0220
0.595	449.0	460.0	11.0	0.0176
0.425	434.5	443.0	8.5	0.0143
0.300	426.0	432.0	6.0	0.0119
0.210	450.0	455.5	5.5	0.0097
0.150	409.5	419.5	10.0	0.0057
0.105	384.5	388.5	4.0	0.0042
0.075	391.0	395.0	4.0	0.0026
pan	361.5	368.0	6.5	0.0000

Table AIII.10 Breakage distribution results for Shadwell metabasalt at RR2

Size *mm*	Sieve Weight *g*	Sieve + Sample Weight *g*	Weight Retained *g*	Fraction Passing
47.481			0.00	1.0000
38.100			0.00	1.0000
25.400	651.0	1202.0	551.0	0.7853
19.100	665.0	1144.5	479.5	0.5985
12.700	632.5	1189.5	557.0	0.3815
6.350	615.5	1116.5	501.0	0.1862
4.750	543.5	636.5	93.0	0.1500
3.360	506.5	602.0	95.5	0.1128
2.360	489.5	554.0	64.5	0.0877
1.700	475.0	523.0	48.0	0.0690
1.190	427.0	465.0	38.0	0.0542
0.850	433.5	462.5	29.0	0.0429
0.595	449.0	470.0	21.0	0.0347
0.425	434.5	451.5	17.0	0.0281
0.300	426.0	440.0	14.0	0.0226
0.210	450.0	468.5	18.5	0.0154
0.150	409.5	422.5	13.0	0.0103
0.105	384.5	389.0	4.5	0.0086
0.075	391.0	407.0	16.0	0.0023
pan	365.5	371.5	6.0	0.0000

Table AIII.11 Breakage distribution results for Spotsylvania granite at RR1

Size *mm*	Sieve Weight *g*	Sieve + Sample Weight *g*	Weight Retained *g*	Fraction Passing
47.454			0.00	1.0000
38.100			0.00	1.0000
25.400	650.6	2179.0	1528.4	0.4035
19.100	663.9	1073.0	409.1	0.2438
12.700	631.6	859.0	227.4	0.1551
6.350	614.2	757.0	142.8	0.0993
4.750	542.2	579.0	36.8	0.0850
3.360	505.6	542.5	36.9	0.0706
2.360	488.9	511.0	22.1	0.0620
1.700	474.2	492.5	18.3	0.0548
1.190	426.0	440.9	14.9	0.0490
0.850	432.7	446.2	13.4	0.0438
0.595	448.4	460.9	12.5	0.0389
0.425	433.3	446.6	13.3	0.0337
0.300	425.3	439.8	14.6	0.0280
0.210	449.4	463.3	14.0	0.0226
0.150	408.8	425.2	16.4	0.0162
0.105	383.9	391.9	8.0	0.0131
0.075	390.2	401.9	11.6	0.0085
pan	365.1	386.9	21.8	0.0000

Table AIII.12 Breakage distribution results for Spotsylvania granite at RR2

Size *mm*	Sieve Weight *g*	Sieve + Sample Weight *g*	Weight Retained *g*	Fraction Passing
47.431			0.00	1.0000
38.100			0.00	1.0000
25.400	651.0	931.0	280.0	0.8686
19.100	665.0	1078.5	413.5	0.6745
12.700	632.5	1130.0	497.5	0.4410
6.350	615.5	1037.0	421.5	0.2431
4.750	543.5	626.5	83.0	0.2042
3.360	506.5	584.0	77.5	0.1678
2.360	489.5	535.5	46.0	0.1462
1.700	475.0	515.0	40.0	0.1274
1.190	427.0	459.0	32.0	0.1124
0.850	433.5	460.5	27.0	0.0997
0.595	449.0	473.5	24.5	0.0882
0.425	434.5	459.5	25.0	0.0765
0.300	426.0	450.5	24.5	0.0650
0.210	450.0	477.0	27.0	0.0523
0.150	409.5	442.5	33.0	0.0368
0.105	384.5	395.0	10.5	0.0319
0.075	391.0	417.5	26.5	0.0195
pan	365.5	407.0	41.5	0.0000

Table AIII.13 Breakage distribution results for Thornburg granite at RR1

Size *mm*	Sieve Weight *g*	Sieve + Sample Weight *g*	Weight Retained *g*	Fraction Passing
47.174			0.00	1.0000
38.100			0.00	1.0000
25.400	650.3	2173.4	1523.1	0.3908
19.100	663.9	948.5	284.6	0.2770
12.700	631.7	863.1	231.4	0.1845
6.350	614.3	811.1	196.8	0.1058
4.750	542.4	588.8	46.4	0.0872
3.360	505.8	547.8	42.0	0.0704
2.360	488.6	516.4	27.8	0.0593
1.700	474.3	496.5	22.2	0.0504
1.190	426.2	442.5	16.3	0.0439
0.850	433.0	446.6	13.6	0.0384
0.595	448.5	459.5	11.1	0.0340
0.425	433.6	443.5	9.9	0.0301
0.300	425.2	434.5	9.3	0.0264
0.210	449.5	459.4	9.9	0.0224
0.150	408.9	422.0	13.1	0.0171
0.105	384.0	391.5	7.5	0.0141
0.075	390.3	401.0	10.7	0.0099
pan	360.7	385.4	24.7	0.0000

Table AIII.14 Breakage distribution results for Thornburg granite at RR2

Size *mm*	Sieve Weight *g*	Sieve + Sample Weight *g*	Weight Retained *g*	Fraction Passing
47.192			0.00	1.0000
38.100			0.00	1.0000
25.400	651.0	1487.5	836.5	0.6509
19.100	665.0	979.0	314.0	0.5198
12.700	632.5	1087.5	455.0	0.3299
6.350	615.5	946.0	330.5	0.1920
4.750	543.5	625.0	81.5	0.1580
3.360	506.5	588.5	82.0	0.1237
2.360	489.5	536.0	46.5	0.1043
1.700	475.0	512.5	37.5	0.0887
1.190	427.0	457.0	30.0	0.0762
0.850	433.5	460.5	27.0	0.0649
0.595	449.0	471.0	22.0	0.0557
0.425	434.5	454.5	20.0	0.0474
0.300	426.0	444.0	18.0	0.0399
0.210	450.0	468.5	18.5	0.0321
0.150	409.5	443.0	33.5	0.0182
0.105	384.5	387.0	2.5	0.0171
0.075	391.0	407.0	16.0	0.0104
pan	361.5	386.5	25.0	0.0000

APPENDIX IV

LABORATORY JAW CRUSHING RESULTS

Table AIV.1 Feed size data for lab jaw crusher

Size	Fraction passing			
mm	**SMB**	**BG**	**CR**	**SG**
35.92	1.0000	1.0000	1.0000	1.0000
25.40	0.8947	0.8030	1.0000	0.6028
19.10	0.1776	0.2833	0.5093	0.0489
12.70	0.0170	0.0385	0.0157	0.0075
4.75	0.0147	0.0090	0.0076	0.0056
0.00	0.0000	0.0000	0.0000	0.0000

Table AIV.2 Volumetric capacity results from lab jaw crusher tests

Rock Type	Bulk density kg/m^3	Mass kg	Volume m^3	Time sec	Vol. capacity m^3/hr	Avg. Feed Size m	K1	Predicted Capacity m^3/hr
Culpeper siltstone	1702	38.80	0.02280	160	0.5130	0.0157	0.8389	0.8515
Shadwell metabasalt	1837	45.97	0.02502	195	0.4618	0.0185	0.8333	0.8457
Spotsylvania granite	1691	42.97	0.02541	169	0.5413	0.0182	0.8340	0.8464
Boscobel granite	1670	47.14	0.02823	172	0.5909	0.0212	0.8266	0.8389

Closed side set (*m*)	0.0079
Throw (*m*)	0.0064
Gape (*m*)	0.0953
Jaw width (*m*)	0.1461
Jaw length (*m*)	0.2096
RPM	300
K2	0.7079

Table AIV.3 Measured product size of Boscobel granite

Size *mm*	Sieve Weight *g*	Sieve + Sample Weight *g*	Weight Retained *g*	Fraction Passing
19.10	579.5	579.5	0.0	1.0000
12.70	552.5	910.0	357.5	0.9292
6.35	599.5	3243.5	2644.0	0.4059
4.75	533.5	1083.5	550.0	0.2971
3.36	480.5	898.5	418.0	0.2143
2.36	489.5	754.0	264.5	0.1620
pan	366.0	1184.5	818.5	0.0000

Table AIV.4 Measured product size of Culpeper siltstone

Size *mm*	Sieve Weight *g*	Sieve + Sample Weight *g*	Weight Retained *g*	Fraction Passing
19.10	579.5	579.5	0.0	1.0000
12.70	552.5	984.0	431.5	0.9211
6.35	599.5	3364.0	2764.5	0.4154
4.75	533.5	1061.0	527.5	0.3189
3.36	480.5	958.0	477.5	0.2316
2.36	489.5	779.5	290.0	0.1785
pan	366.0	1342.0	976.0	0.0000

Table AIV.5 Measured product size of Shadwell metabasalt

Size *mm*	Sieve Weight *g*	Sieve + Sample Weight *g*	Weight Retained *g*	Fraction Passing
19.10	579.5	640.0	60.5	0.9884
12.70	552.5	1443.0	890.5	0.8184
6.35	599.5	3235.5	2636.0	0.3150
4.75	533.5	954.0	420.5	0.2347
3.36	480.5	839.0	358.5	0.1662
2.36	489.5	694.0	204.5	0.1272
pan	366.0	1032.0	666.0	0.0000

Table AIV.6 Measured product size of Spotsylvania granite

Size *mm*	Sieve Weight *g*	Sieve + Sample Weight *g*	Weight Retained *g*	Fraction Passing
19.10	579.5	600.5	21.0	0.9952
12.70	552.5	926.0	373.5	0.9103
6.35	599.5	3181.5	2582.0	0.3230
4.75	533.5	883.0	349.5	0.2435
3.36	480.5	746.5	266.0	0.1830
2.36	489.5	633.5	144.0	0.1502
pan	366.0	1026.5	660.5	0.0000

APPENDIX V

EQUILIBRIUM ANALYSIS OF WEDGE FORCES

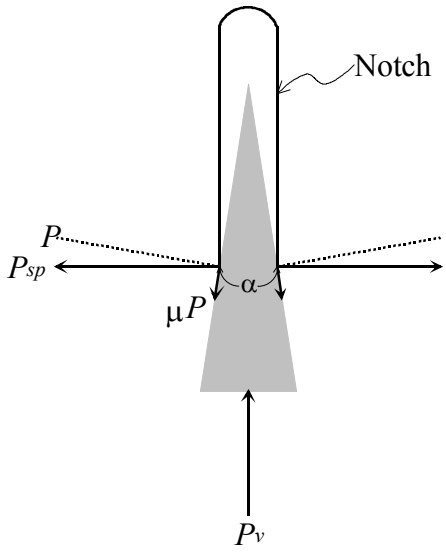

Summing forces in the x and y directions:

$$\sum F_x : P_{sp} = P\cos\left(\alpha/2\right) - \mu P\sin\left(\alpha/2\right)$$

$$\sum F_x : P = \frac{P_{sp}}{\cos\left(\alpha/2\right) - \sin\left(\alpha/2\right)} \qquad \text{[EQ. 1]}$$

$$\sum F_y : \frac{P_v}{2} = P\sin\left(\alpha/2\right) + \mu P\cos\left(\alpha/2\right)$$

$$\sum F_y : P = \frac{P_v}{2\sin\left(\alpha/2\right) + 2\mu\cos\left(\alpha/2\right)} \qquad \text{[EQ. 2]}$$

Setting Equation 1 equal to Equation 2:

$$P_{sp} = \frac{P_v\left[\cos\left(\alpha/2\right) - \mu\sin\left(\alpha/2\right)\right]}{2\sin\left(\alpha/2\right) + 2\mu\cos\left(\alpha/2\right)}$$

$$P_{sp} = \frac{P_v\left[1 - \mu\tan\left(\alpha/2\right)\right]}{2\left(1+\mu\right)}$$

$$P_{sp} = \frac{P_v}{2\tan\left(\alpha/2\right)} \times \frac{1 - \mu\tan\left(\alpha/2\right)}{1 + \mu\cot\left(\alpha/2\right)}$$

VITA

James Donovan was born on June 24, 1975 in Manalapan, NJ. He graduated from St. John Vianney High School in 1993, where upon he enrolled at Virginia Tech. He earned his Bachelor of Science degree in Mining Engineering in 1997. During his undergraduate years he spent his summers working for New Hope Crushed Stone. In 1999 he earned his Master of Science degree in Mining Engineering from Virginia Tech and completed a thesis entitled "*The Effects of Backfilling on Ground Control and Recovery in Thin-Seam Coal Mining"*. He stayed on at Virginia Tech as a doctoral research and teaching assistant, and completed his PhD requirements in the summer of 2003. He currently resides in Christiansburg, Virginia with his beautiful wife, Erin, and his glorious son, Quinn.